Designing Nanostructured Titanium Dioxide-Based Potentiometric Sensors for the Analysis of Chromium(III) and Iron(III) Ions

By

Maryam Hariri

A Thesis Submitted to the Faculty of Graduate Studies
In Partial Fulfillment of the Requirements
for the Degree of

Doctor of Philosophy

Graduate Program in Chemistry
YorkUniversity
Toronto, Ontario

August 2016

Abstract

The objective of the first part of this study was to introduce a novel solid-state Cr(III)-selective potentiometric sensor based on Schiff base glyoxal bis(2-hydroxyanil) (GBHA) ionophores adsorbed onto nanostructured TiO_2 electrodes, with the aim of eliminating the drawbacks associated with the conventional polymer based Cr(III)-selective membrane potentiometric sensors.

The assembled sensor showed the best response characteristics with Nernstian behavior for Cr^{3+} (Nernstian slope of 19.45 ± 0.44 mV per decade of Cr^{3+} concentration) over a wide working concentration range 1.000×10^{-7} to 1.000×10^{-2} M, and a low detection limit of 3.000×10^{-8} M. Also this sensor displayed an improved selectivity towards Cr^{3+} with respect to all the other tested ions.

In addition the objective of the second part of this work was to fabricate novel solid-state Fe(III)-selective potentiometric sensors based on desferal ionophores physisorbed and chemisorbed onto the surface of nanostructured TiO_2 electrodes. For the sensors designed based on desferal-chemisorbed onto TiO_2 electrodes, carboxyl-terminated alkyl phosphonic acids with different alkyl chain lengths (short chain (3-C), medium chain (6-C), and long chain (11-C)) were used as linkers to anchor to the surfaces of nanostructured TiO_2 electrodes. The results of the designed sensors, based on ionophores physisorbed and chemisorbed on TiO_2 electrodes, were then compared with each other and with some of the best ferric-selective sensors reported in other studies.

It was concluded that chemically anchoring the desferal ligand onto the surface of functionalized TiO_2 electrodes using the SAMs of medium alkyl chain length PAs (6-C), gave the best performance.

In addition, the fabricated sensor based on desferal-chemisorbed 6-C PA-modified TiO_2 electrode showed the best response characteristics with Nernstian behavior for Fe^{3+} (Nernstian slope of 19.44 ± 0.46 mV per decade of Fe^{3+} concentration) over a wide working concentration range 1.000×10^{-7} to 4.500×10^{-1} M, and a low detection limit of 2.820×10^{-9} M.

The fabricated Cr(III)-selective and Fe(III)-selective sensors showed superior behavior, compared to the previously reported sensors, which can be ascribed to the higher stability of the solid substrates. These sensors could successfully eliminate the weaknesses related to conventional membrane sensors.

Acknowledgements

Firstly, I want to express my deepest gratitude to my supervisor Prof. S. Morin for her patience, guidance, and encouragements throughout this journey. She has always been very helpful to me throughout my research and provided me with valuable insight into this project. Her instructions have not only helped me benefit from her extensive knowledge, but also have motivated me to learn a lot along my research process. Secondly, I would like to thank members of my supervising and reading committee, Prof. P. G. Potvin and Prof. R Fournier for their instructions, advice, and comments on my project. I am truly grateful for the opportunity to have had such a dynamic and capable thesis committee. Thirdly, I would like to thank M. Baket, the chemistry graduate program assistant and M. Mamais the administrative assistant of the department of chemistry for their time, constant care and considerations. I would like to extend my deepest thanks to my father Amir, my mother Shahnaz, my sister Elika, Nima, as well as all my colleagues, and friends for their love and encouragement. Each of you can share in this accomplishment, for without your support it would not have been possible. Last but not least, I would like to acknowledge the Natural Science and Engineering Research Council (NSERC) of Canada, Ontario Graduate Scholarship (OGS) and the Granting Agencies for their financial support.

Statement of Collaboration

The organic compound, GBHA used in the work on "Designing a Potentiometric Sensor Based on Glyoxal-bis(2-hydroxyanil) adsorbed onNanostructured Titanium Dioxide for the Analysis of Chromium(III) Ions in Solution", was prepared in Prof. P. G. Potvin's lab, Department of Chemistry, York University.

The organic compound desferal, used in the work on "Functionalization of Nanostructured Titanium Dioxide Surface with Self Assembled Monolayers (SAMs) of Alkanephosphonic Acids and the Comparisons of the Performances of the Fabricated Potentiometric Sensors forthe Analysis of Iron(III) Ions Based on Desferal-Chemisorbed and Physisorbed TiO_2 Electrode", was prepared inDr. M. Elhabir's lab, Department of Chemistry and Bioorganic Medicine, European school of Chemistry, Polymers and Materials (ECPM), University of Strasbourg, Strasbourg, France.

I would like to thank Dr. Darcy Burns and Dr. Sergiy Nokhrin from the University of Toronto, and Dr. Howard Hunter from York University for their assistance with the ^{31}Phosphorus NMR measurements. I would also like to express my gratitude to Karen Rethoret, form York University for her help with the Scanning Electron Microscopy and Energy Dispersive X-ray analysis.

Table of Contents

Chapter One:

Chapter Two:

Chapter Three:

Chapter Four:

Chapter Five:

List of Tables

List of Figures

List of Acronyms

AAS	Atomic Absorption Spectrometry
AFM	Atomic Force Microscopy
ATM	Auto Tune & Match
Bicarb	Potassium Bicarbonate
BTMMT	4-(5-bromothiophen-2-Carboxylidene Amino)-3-Methyl-5-Mercapto-s-triazole
CNT	Carbon Nanotube
CPE	Carbon Paste Electrode
CWE	Coated Wire Electrode
DCC	N,N'-Dicyclohexyl Carbodiimide
DCM	Dichloromethane
DFT	Density Functional Theory
DRI	Dietary Reference Intake
EANQ	9-ethylacenaphtho[1,2-b]quinoxaline
ECPM	European School of Chemistry, Polymers and Materials
EMF	Electromotive Force
ESADDI	Estimated Safe and Adequate Daily Dietary Intake
FEG-FIB	Field Emission-Focused Ion Beam
FET	Field Effect Transistor

FTIR	Fourier Transform Infrared Spectroscopy
GBHA	Glyoxal bis 2-hydroxyanil
HPLC	High Performance Liquid Chromatography
ICP-AES	Inductively Coupled Plasma-Atomic Emission Spectroscopy
ICP-MS	Inductively Coupled Plasma Mass spectroscopy
IR	Infrared Spectroscopy
ISE	Ion-Selective Electrodes
IUPAC	International Union of Pure And Applied Chemistry
LMCT	Ligand-to-Metal Charge Transfer
LOD	Limit of Detection
MAS	Magic Angle Spinning
MCPE	Modified Carbon Paste Electrodes
MMCHH	2-methyl-6-(4-methylenecyclohex -2-en-1-yl)hept-2-en-4-one
MPM	Matched Potential Method
MSPE	Modified Screen Printed Electrode
NAS	National Academy of Science
NHS	*N*-Hydroxysuccinimide

NMR	Nuclear Magnetic Resonance
OCP	Open Circuit Potential
OCV	Open Circuit Voltage
PA	Phosphonic Acid
PME	Polymeric Membrane Electrode
PSPD	Position-Sensitive four-Quadrant Photodiode Detector
PVC	Poly(Vinyl Chloride)
SAM	Self-Assembled Monolayers
SCE	Saturated Calomel Electrode
SEM-EDX	Scanning Electron Microscopy-Energ Dispersive X-ray Spectroscopy
SSNMR	Solid-State Nuclear Magnetic Resonance
THF	Tetrahydrofuran
XRF	X-Ray Fluorescence

1. Introduction

1.1. Motivation of the Study

The determinations of biologically, clinically, environmentally, and industrially important metal ions in different samples have always been of significant interest to scientists and are increasingly demanding by analytical chemists [1]. Among different methods available for trace level determination of metal ions, potentiometric sensing methods by ion-selective electrodes (ISEs) hold an outstanding position owing to their numerous advantages [2]. ISEs offer simple, low cost, and fast analysis procedures with no need of special equipment. Moreover, this method, which is non-destructive, requires low sample volumes and no sample pretreatments [3-10]. ISEs have reached the commercialization stage [11], and have important applications in the fields of biological, clinical, industrial, environmental, and agricultural analyses [1].

This study was initiated with the aim of introducing a novel potentiometric sensing technique based on nanostructured titanium dioxide electrodes which eliminates the drawbacks associated with the conventional (i.e., poly(vinyl chloride) (PVC)-membrane-based) ISE sensors. These TiO_2-based nanosensors are expected to be highly sensitive due to the large surface-to-volume ratio of the nanostructure, show improved selectivity and stability, and be cost-effective, with the hope of using them for the in-place analyses of metal ions.

The present work has focused on the fabrication of potentiometric sensors for the determination of Cr^{3+} and Fe^{3+} ions using selective ionophores adsorbed on nanostructured TiO_2 electrodes. The importance of measuring these ions in various environments will be explained in the following sections

1.1.1. The Importance of Measuring Chromium

Chromium is an essential metal for human health in small amounts while toxic in larger quantities. It's a mineral that affects insulin, carbohydrate, fat, and protein levels in the body. Recommended chromium intakes are provided in the Dietary Reference Intakes (DRIs) developed by the Institute of Medicine of the National Academy of Sciences (NAS) [13]. Serum chromium levels normally range from less than 0.05 up to 0.5 micrograms/milliliter (μg/mL); in addition, the Estimated Safe and Adequate Daily Dietary Intake (ESADDI) for chromium in adults is between 50 –200 μg per day [14, 15].

Chromium blood test is performed in laboratories to diagnose this mineral's poisoning or deficiency [16]. In addition chromium can be measured in hair, urine, serum, and red blood cells [17]. On the one hand, chromium deficiency may lead to diabetes and cardio-vascular diseases including elevated circulating insulin, glucose, triglycerides, total cholesterol, and impaired immune function. On the other hand, its high concentration can cause epigastria pain, nausea, vomiting, diarrhea, and hemorrhage. Chromium compounds are also well known for their carcinogenic effects [18].

Exposure to Cr(III) can happen through natural sources of chromium via inhaling (i.e., Cr^{3+} dust particles in the air), drinking (i.e., Cr^{3+} in well water near a waste site containing chromium), and swallowing (i.e., Cr^{3+} in food). Chromium has been also used extensively in steel manufacturing, leather tanning, wood treatment, electroplating, paint and pigment, metal finishing, and alloy manufacturing industries [19]. Therefore exposure to this ion also can occur through industrial sources, such as dermal exposure (i.e., during the use of consumer products that contain chromium, like wood treated with copper dichromate or leather tanned with chromic

sulphate), and occupational exposure (i.e., from chromate production, stainless-steel production, chrome plating, and working in the tanning industries) [17, 20].

Due to the vital importance of Cr(III) in complex biological and industrial systems, as well as environmental samples [21-23], a narrow window of concentration between essentiality and toxicity warrants the determination of this ions. Therefore for medical, industrial, and environmental reasons, it is of great importance to determine how much of this metal ion is present in various samples, such as water, food, and pharmaceutical products.

Although sophisticated analytical techniques, such as atomic absorption spectrometry (AAS), X-ray fluorescence (XRF), high performance liquid chromatography (HPLC), and inductively coupled plasma-atomic emission spectroscopy (ICP-AES) have been generally employed for the trace level determination of chromium ions, they are disadvantageous in terms of cost and unsuitable for routine analysis. These techniques are also time consuming as they require sample preparation and pretreatment [18, 21-23]. Therefore, there is critical need for the development of selective, portable and inexpensive diagnostic tools for the determination of chromium ions. Potentiometric detection of chromium ions is a promising alternative owing to the several advantages that it offers [18, 24-27].

1.1.2. The Importance of Measuring Iron

With only a few possible exceptions in the bacterial world, there will be no life without iron [28]. Iron is believed to be the sixth most abundant element in the universe and the fourth most abundant on earth [29]. It is also one of the most essential elements in the human body [30], which is present in many biological organisms at various concentration levels. In biological

processes, iron is likely an integral part of metabolism, e.g. it has an effective role as oxygen carrier (in haemoglobin and myoglobin), in oxygen storage, and also in electron transport [31-33]. The enzymes, which play a role in the synthesis of amino acids, hormones, and neurotransmitters, need Fe^{3+}. It is recommended that adults ingest 10-15 mg of iron in their food daily intake, and studies report that the normal subject assimilate only 10% of the recommended daily intake of iron from food [34].

The concentration of ferric ions in human body has to be efficiently balanced as both its deficiency and overdose can cause various health hazards [34]. Deficiency of iron causes a reduction in the number of red blood cells in the body and can be a cause of anemia, especially in babies. In addition, iron overload can be inherited (genetic) or acquired by receiving numerous blood transfusions, getting iron shots or injections, or consuming high levels of supplemental iron. The excess amount of iron is stored in the heart, liver, kidney, and other organs [35, 36]. As it cannot be spontaneously released from the body, it can put other organs at risk of impairment [37]. Surplus or deficiency of iron in the human body can contribute to a high incidence of cancer (e.g. breast cancer) [38, 39]. In addition, illnesses such as hemochromatosis are linked to high level of iron in the body [40-42].

Iron is also a vital element in environmental systems as well as industries. The same iron limit-importance holds for environmental systems, such as fresh and seawaters, in which the iron concentration is claimed to be of crucial relevance [43]. Therefore, it is essential to efficiently determine the amount of Fe^{3+} ions in various biological, clinical, environmental, and industrial systems using sensitive analytical techniques.

As of today, several analytical methods have been applied for the quantification analysis of iron ions such as AAS, and inductively coupled plasma-Mass spectroscopy (ICP-MS) [29, 44-48]. However these methods have some limitations, such as being time consuming as they involve

multiple sample manipulations, instability if a large number of samples analysis is needed [49], and high cost [50]. These issues have raised the demand for the advent of an analytical technique that is not only cost-effective, sensitive, rapid, durable, highly selective, and easy to perform, but also does not have the disadvantages of other analytical methods. Potentiometric sensing technology is particularly suited with the aim of meeting these demands especially for *in-situ* applications.

Selective molecular receptors that can indicate the concentration of iron(III) in the presence of other metal ions have many potential applications, ranging from medical analysis and biochemical research to environmental monitoring [51]. The most Fe(III) selective molecular receptors developed to date have been those that mimic siderophores (from the Greek word for "iron carriers") to optimise the affinity and selectivity for iron(III) ions [52].

1.2. Chemical Sensors

Generally speaking, sensors can be categorised into two main groups. There are physical sensors, which are sensitive to physical responses, such as temperature, pressure, and magnetic field. Then there are chemical sensors, which rely on a particular chemical reaction for their response [53].

A chemical sensor can be described as an analytical device that transforms chemical information, ranging from the concentration of a specific sample component to total composition analyses, into an analytically useful signal. Generally speaking, this chemical information may originate from a chemical reaction of the analyte or from a physical property of the system, and the output is a measurable physical signal correlated with the concentration of the analyte [54,

55]. Chemical sensors consist of two main parts, a receptor, and a transducer. Some sensors may include a separator between the parts, for instance a membrane.

In the receptor part of a sensor the chemical information is transformed into a form of energy, which can be converted to a measurable analytical signal by the transducer. The transducer part is responsible for transforming the energy carrying the chemical information about the sample into a useful analytical output signal [54, 55].

Chemical sensors may be classified according to the operating principle of the transducer. A visual review of the types of chemical sensors is shown in figure 1.1.

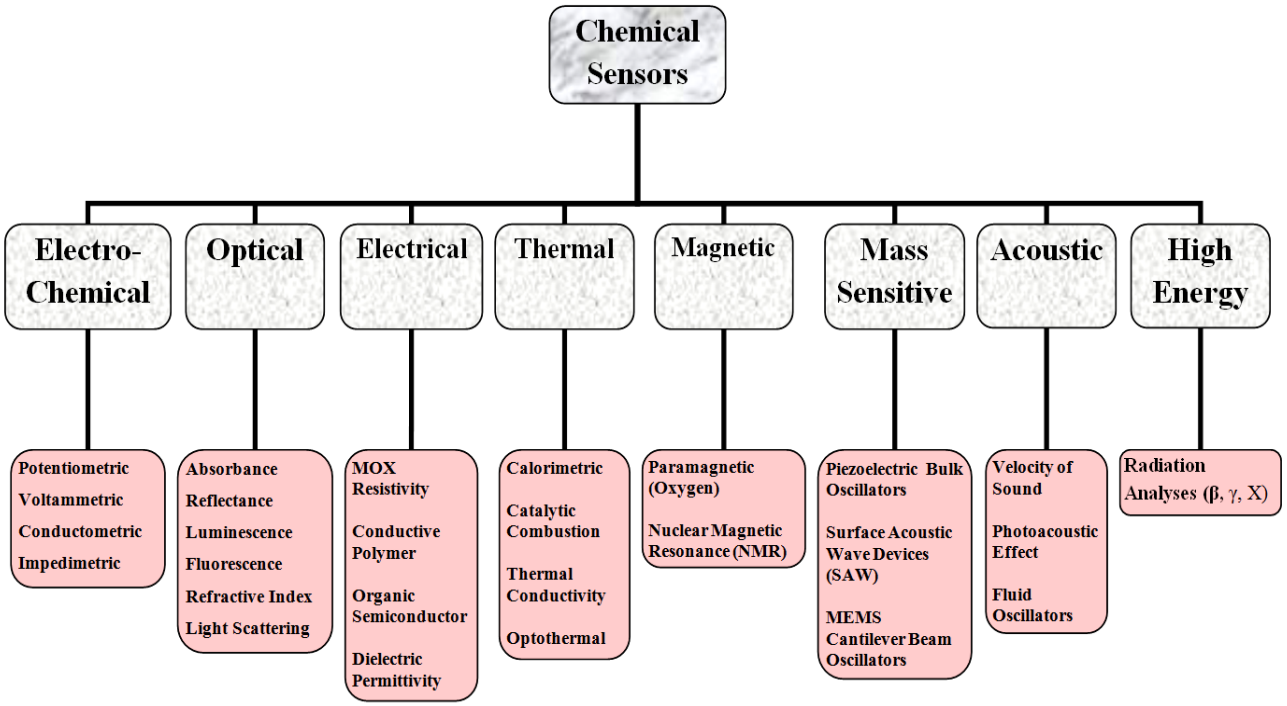

Figure 1.1. A possible classification of chemical sensors [56].

1.3. Electrochemical Sensors

Electrochemical sensors are the most versatile and highly developed chemical sensors. They are divided into several types: 1. Potentiometric sensors; in which the potential of an indicator is measured against a reference electrode; 2. Voltammetric sensors, including amperometric devices, in which current is measured as a function of the applied potential; 3. Conductometric sensors that work based on measuring electrolytic conductivity; and 4. Impedimetric sensors, in which the measuring parameter is impedance [54].

Electrochemical sensing always requires a closed circuit [57]. Since a closed loop is needed at least two electrodes are required. An ideally nonpolarizable reference electrode provides a constant potential, while an indicator electrode shows a potential dependence with the concentration of the analytes [58]. These sensors have found a dominant position among all the presently available sensors that have reached the commercialization stage with a vast range of important applications in different fields [59]. So far, many solid-state electrochemical sensors have been commercialized, such as glucose monitors for diabetes and ion sensors for blood electrolytes [12].

1.4. Potentiometric Sensors

Potentiometric sensors are the simplest type of electrochemical sensors with various analytical applications. These types of sensors are very attractive owing to the low cost and ease of use of the instruments employed [12]. The best-known examples of this type of sensor are the common glass electrodes used for pH measurements, which were the first developed potentiometric sensors [60-62].

Potentiometric sensors are used to determine the analytical concentration of an analyte in a gas or a solution by measuring the equilibrium potential of an electrode when no current is flowing (zero current potential, or open circuit potential (OCP)). As an absolute potential value cannot be measured, the signal obtained is the potential difference (voltage) between the working or indicator electrode and a reference electrode (figure 1.2). The working electrode's potential depends on the concentration of the analyte in the gas or solution phase, while the reference electrode is needed to provide a defined reference potential. The voltage is theoretically dependent on the logarithm of the ionic concentration, according to the Nernst equation, which will be described subsequently [12].

Besides the advantages already given in favour of potentiometric based sensing methods, they also offer simple instrumentation, speed and ease of preparation and procedure, relatively fast response time, high selectivity, wide dynamic range, non-destructivity, feasibility of ‘online’ analysis, and very low detection limits for ions detection. Moreover, the instrumental response does not depend on the area of the electrode; therefore potentiometric devices could be readily miniaturized without losing their determination capabilities [12, 63].

Various independent achievements in the mid-1960s marked the starting point of modern potentiometry [64]. During the last decade, the capabilities of potentiometric analyses have changed dramatically in that the lower limit of detection (LOD) of ion selective electrodes has improved by a factor of up to one million [12].

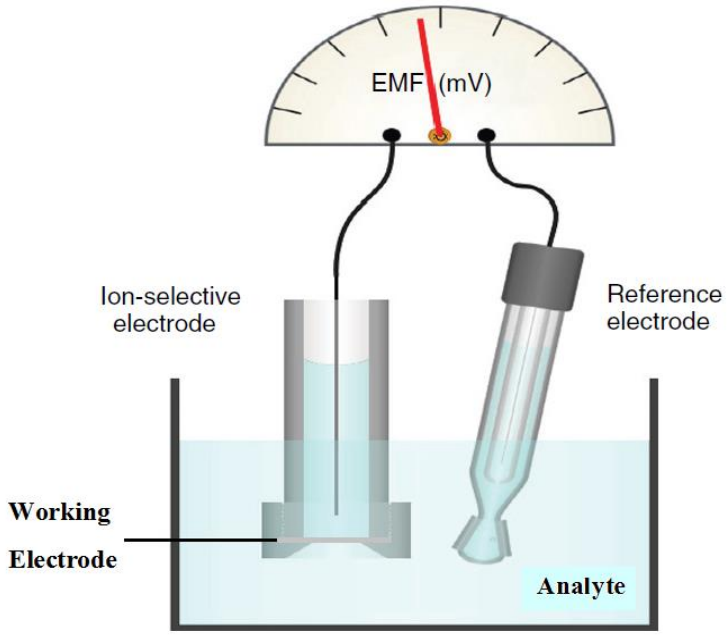

Figure 1.2. Schematic of a potentiometric sensor set-up.

Potentiometric sensors have become the standard technique in the clinical analyses of ions, including Na^+, Ca^{2+}, K^+ and Cl^-. Today more than 10 companies sell blood gas analysers with potentiometric detectors for the analyses of relevant gases, such as oxygen and carbon dioxide, using on the order of 100µl blood serum or plasma [65]. Moreover, potentiometric sensors are now widely used for the detection of trace level of various drugs [66-73].

Potentiometric devices can be divided into the following types: 1) coated wire electrodes (CWEs), 2) carbon paste electrodes (CPEs), 3) field effect transistors (FETs), and 4) ion selective

electrodes (ISEs) [12]. As this study has focused on the fabrication of ISEs for Cr^{3+} and Fe^{3+}ions, this group of potentiometric sensors will be described further in the following section.

1.5. Ion Selective Electrodes (ISEs)

In ISEs, some selective chemistry takes place at the surface of the electrode producing an interfacial potential. Species recognition is achieved with a potentiometric chemical sensor through a chemical equilibrium reaction at the sensor's surface. Thus the surface must contain a component that will react chemically and reversibly with the analyte [12].

Nowadays ISEs can be used for trace level measurements in a number of fields, such as clinical, environmental, process monitoring, as well as more novel approaches such as microfluidic-based systems and micro/nanoprobes [74, 75].

Ionophore-based sensors provide a stable, portable, simple, and relatively cheap method of analysis. They can be improved by the development of enhanced electrode design and through introducing new methodologies of data acquisition and interpretation [75]. ISEs are classified into the following two categories: 1) ISEs with solid substrates/membranes, and 2) ISEs with liquid substrates/membranes.

Another classification based on the membranes used in ISEs is as follow: 1) glass membranes, 2) sparingly soluble inorganic salt membranes, 3) polymer-immobilized ionophore membranes, and 4) gel-immobilized and chemically bonded enzyme membranes [12].

As our measuring electrode in this work is a ligand-modified nanostructured TiO_2 layer deposited on a Fluorine doped Tin Oxide (FTO) glass, which belongs to the group of “ion-

selective electrodes with solid substrates", these types of sensors will be briefly explained in the following section.

1.6. Ion-Selective Electrodes with Solid Substrates

The substrate can be either homogeneous (a single crystal, a crystalline substance or a glass), which is considered to be a solid with regard to the immobility of the ion-recognition element, or heterogeneous, for example a crystalline substance built into a matrix made from a suitable polymer [12].

1.7. Chromium(III) Ion-Selective Potentiometric Sensors

To date, many Cr(III) selective electrodes with polymeric membrane, based on various neutral ionophores have been introduced [76-78]. However, reported sensors suffer from the disadvantages of significant interferences from foreign ions [79-81], deviations from Nernstian behaviour, long response times, narrow working concentration ranges, and narrow pH ranges of operations [82-88].

Therefore, fabrication of novel solid-state ISEs for measuring Cr^{+3} ions with high selectivity and sensitivity, wide linear concentration range, long lifetime, good reproducibility and low cost has been of great importance to analytical chemists. These potentiometric sensors do not possess the disadvantages associated with the conventional membrane sensors and show improved sensitivity due to the higher stability of the solid substrates. The main objective of the first part of

this study was to introduce a novel solid-state Cr(III)-selective potentiometric sensor based on physisorbed ionophores onto the surface of TiO_2 electrodes, which does not have the weaknesses of the above-mentioned Cr(III)-selective membrane sensors.

1.8. Iron(III) Ion-Selective Potentiometric Sensors

To date, numerous studies have reported the analysis of heavy metals using ISEs [89, 90]. However only a few studies discuss the use of solid-state ISEs for the determination of Fe^{3+}. In addition most of the studies for Fe(III)-selective membrane based sensors have some drawbacks, such as low selectivity, narrow working pH range, as well as short lifetime and little stability [91-97]. In order to achieve wider applicability of ISEs, these limitations need to be eliminated. Therefore, it is necessary to develop highly selective electrodes with higher sensitivity for the determination of the Fe^{3+} concentrations which do not possess the flaws of the Fe(III)-selective membrane sensors [91-97]. The main goal of the second part of this study is to fabricate novel solid-state Fe(III)-selective potentiometric sensors based on physisorbed and chemisorbed ionophores onto the surface of TiO_2 electrodes, and to compare their performances.

1.9. Ion Recognition Elements (Ionophores)

An ionophore or ion carrier (also known as electroactive ingredient, sensing material, or analyte recognition element) is a chemical species that reversibly binds ions [98]. Some ionophores such as siderophores are synthesized by microorganisms to improve uptake of ions into their cells. In addition Synthetic ionophores have been used in sensors assemblies [12, 98]. Carrier based ion sensors provide a suitable means for selective quantification of one or more analytes within a complex mixture [23]. Neutral carriers have characteristics of being uncharged, lipophilic, undergoing reversible complexation with selected ions, and hence promoting cation and anion transfers between the aqueous phase and the organic layer phase by means of carrier transport [99].

One of the most critical steps in the development of a chemical sensor is the rational choice and preparation of electroactive materials. Most of the key properties of a sensor, such as selectivity and sensitivity strongly depend on the characteristics of the sensing materials. These electroactive species enable the sensor to respond selectively to a particular analyte of interest without the interferences of other substances [12].

Since the introduction of valinomycin as an ionophore for K^+ [12], ISEs have become one of the best studied and understood analytical devices. In recent years, researches have used a variety of ligands as ionophores in the preparation of new ion-selective electrodes [12, 100, 101]. Schiff bases, ion association complexes, macrocyclic compounds, porphyrins, calixarenes, calixresorcinarenes, crown ethers, and other ligands have been studied for their use as ionophores in ISEs. The application of supramolecular compounds as ionophores in ISEs is getting more attention because of its molecular recognition properties, which can be attributed to the three

dimensional nature of their molecular chemistry [102]. Calixarenes and calixresorcinarenes were studied as hosts for an extensive spectrum of guests. Calixarenes are used in commercial applications as Na^+ selective electrodes for the measurement of sodium levels in blood. Metalloporphyrins offer almost unique opportunities to design artificial receptors for chemical sensors [103]. Electrochemical molecular recognition is an expanding research area at the interface of electrochemistry and supramolecular chemistry [104, 105].

A Schiff base (named after Hugo Schiff) is a type of chemical compound containing a carbon-nitrogen double bond as functional group, where the nitrogen atom is connected to an aryl or alkyl group (R) but not to a hydrogen (i.e., the general structure R' R"C=NR, where R’ is H or alkyl group, R” is phenyl or substituted phenyl, and R is phenyl or alkyl group which makes the Schiff base a stable imine). This kind of ligand is able to coordinate metal ions through the imine nitrogen and another group, usually linked to R” [106].

The Schiff base is synonymous of an azomethine and can be considered a sub-class of imines. Schiff bases are common ligands in coordination chemistry and are regarded as a very important class of organic compounds having wide range of applications, e.g. as visual pigments, and in quantitative analytical chemistry [106]. One of the interesting applications of Schiff's bases is their use as an effective corrosion inhibitor, which is based on their ability to spontaneously form a monolayer on the surface to be protected. [107].

Nowadays different active and well designed Schiff base ligands are synthesized by chemists. These compounds are considered to be "privileged ligands" [108] as they are very good chelating agents and are easily prepared and characterized [106]. Bridged Schiff’s bases have been synthesized (with the general structure R' R"C =N-X-N=C R' R"), which contain many functional groups able to change according to the purpose required.

When two equivalents of salicylaldehyde are combined with a diamine, a particular chelating Schiff base is produced, called Salen ligand that has four coordinating sites. Although the term Salen was used originally only to describe the tetradentate Schiff bases derived from ethylenediamine, the more general term Salen-type is used in literature to describe the class of [O,N,N,O] tetradentate Schiff base ligands [108]. The ionophore we used as a Chromium(III)-selective ion-carrier in this work, is a tetradentate Schiff base.

As the bioavailability of iron in many environments such as the soil or sea is limited by the very low solubility of Fe^{3+} ions, microorganisms such as bacteria, fungi and grasses, have developed their own method to release siderophores to scavenge iron from their living environment by the formation of soluble Fe^{3+} complexes [109].

Siderophores are small, high-affinity iron chelating compounds that usually form a stable, hexadentate, octahedral complex preferentially with Fe^{3+} ions. As Fe^{3+} is a hard Lewis acid, it prefers to coordinate with hard Lewis bases such as anionic or neutral oxygen atoms. Microbes usually release the iron from the siderophore by reduction to Fe^{2+} which has little affinity to these ligands [110]. Siderophores are usually classified by the ligands used to chelate the ferric iron. The major groups of siderophores include the catecholates (phenolates), hydroxamates, and carboxylates (e.g. derivatives of citric acid) [111]. These iron-carriers are amongst the strongest soluble Fe^{3+} binding agents known. The most effective siderophores are those that have three bidentate binding units per molecule, forming a hexadentate complex. The ionophore we used as an iron(III)-selective ion-carrier in this work, is a hexadentate microbial siderophore which is a member of hydroxamate siderophore [112].

1.9.1. The GBHA Ionophore

In order to develop highly selective and sensitive potentiometric sensors for Cr(III) ions, we took advantage of a Schiff base glyoxal bis(2-hydroxyanil) (GBHA) as an excellent ionophore for the determination of these ions in sample solutions (figure 1.3 (a)). GBHA has four binding atoms (two nitrogen and two oxygen atoms) in its structure and was expected to act as a suitable ion carrier within the proposed sensor's framework and therefore to be a good ionophore candidate for the quantification analyses of Cr(III) ions. Figure 1.3 (b) shows the proposed binding of GBHA ionophore to Cr^{3+}.

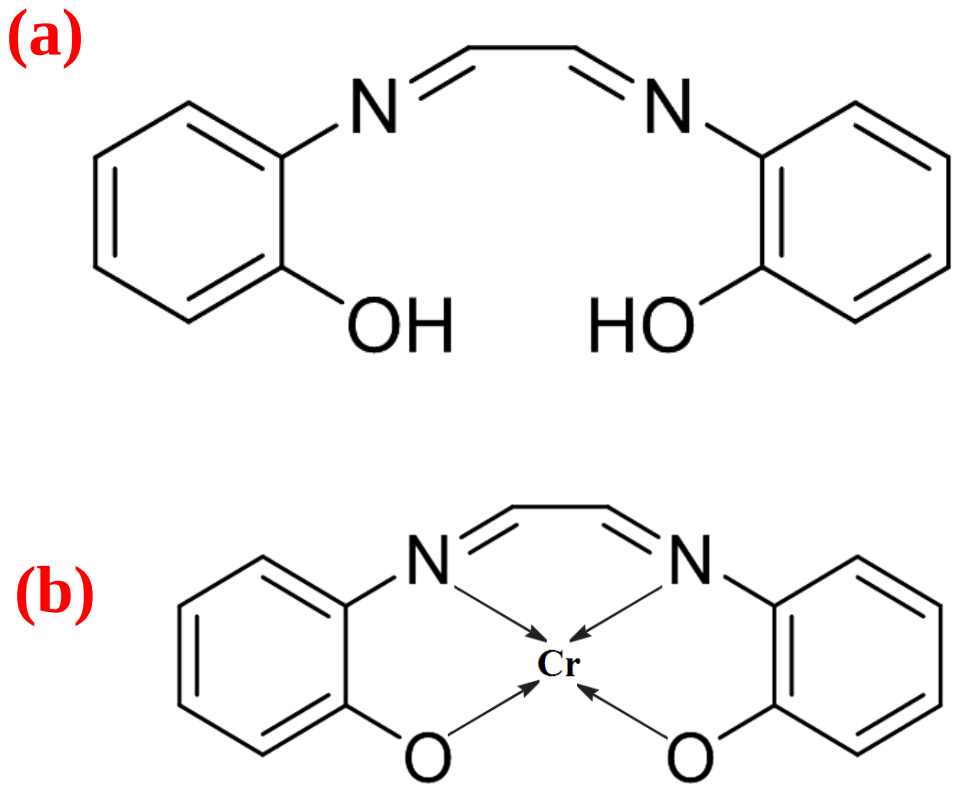

Figure 1.3. (a) The chemical structure of glyoxal bis(2-hydroxyanil) (GBHA) ligand, **(b)** The proposed binding of GBHA ligand to Cr^{3+}.

1.9.2. The Deferoxamine Ionophore

Deferoxamine ligand (also known as desferrioxamine B, deferoxamine B, DFO-B, or desferal) (figure 1.4) is a microbial siderophore which belongs to the important group of hydroxamate siderophores [112]. Deferoxamine binding to iron(III), makes it water soluble, and thereby enables cellular uptake (figure 1.5). This ligand has also medical applications as a chelating agent used to remove excess iron from the body. The mesylate salt of DFO-B is commercially available and is approved by the FDA [113].

Desferal as a chelating agent forms complexes predominantly with ferric irons with the complex formation constant of 10^{31}. The affinity of desferal for divalent ions such as Fe^{2+}, Cu^{2+}, Zn^{2+} is substantially lower (complex formation constants 10^{14} or below). Chelation occurs on a 1:1 molar basis, so that 1 gram desferrioxamine theoretically can bind 85 mg ferric iron [114].

Deferoxamine is used to treat acute iron poisoning especially in small children by forming a complex with iron in the blood, which will be then removed from the body by the kidneys. Also, deferoxamine injection is used to remove excess iron from the body (chronic iron overload), which can occur due to multiple transfusions in patients with β-thalassaemia or other types of chronic anemia [113].

In this work, we report the assembly of novel Fe^{3+}-selective potentiometric sensors using desferal as an ionophore physisorbed and chemisorbed onto the surface of nanostructured TiO_2 electrodes as our ISEs' solid substrate. Also, the performances of the fabricated sensors based on the physisorption and chemisorption of desferal molecules onto the surface of the TiO_2 substrates, will be compared.

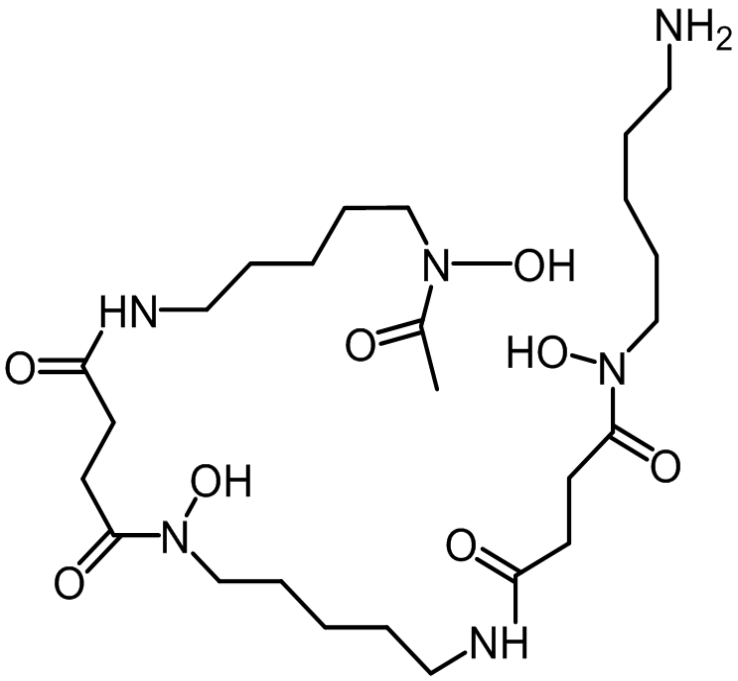

Figure 1.4. The chemical structure of Deferoxamine (Desferal) ligand.

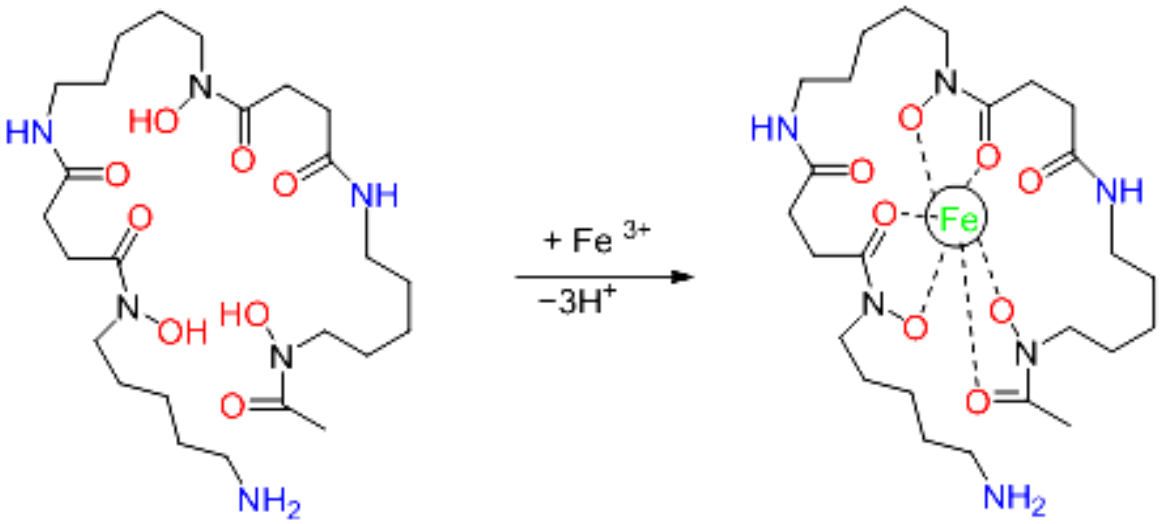

Figure 1.5. The reaction of desferrioxamine-B (Desferal) with iron(III). Reproduced from open access Ref. [114]. Copyright © 2009 RCS.

1.10. Analysis Methodology and the Nernst Equation

Walther H. Nernst (1864-1941) was a German physical chemist who received the Nobel Prize in 1920 for formulating the Nernst equation for the very first time [115]. His contribution to chemical thermodynamics led to the well-known equation correlating chemical energy and the electric potential of a galvanic cell or battery. In electrochemistry, the Nernst equation (Equation 1) relates the reduction potential of a half cell, or the total voltage (electromotive force (EMF) of the full cell, at any point to the standard electrode potential, temperature, concentration, and reaction quotient of the underlying reactions and species used [116, 117], which can be written as shown in equation 1.

$$E = E'_0 + \frac{RT}{nF}\ln\left(\frac{C_O}{C_R}\right) \qquad \textbf{Equation 1}$$

where $\boldsymbol{E}$ is the electrode potential, $\boldsymbol{E'_0}$ is the formal electrode potential at a standard state, $\boldsymbol{R}$ is the gas constant, $\boldsymbol{T}$ is the temperature, $\boldsymbol{n}$ is the number of electrons involved, $\boldsymbol{F}$ is the Faraday constant, $\boldsymbol{C_O}$ is the oxidant concentration, and $\boldsymbol{C_R}$ is the reduced product concentration [116, 117].

This equation is normally expressed with activities (i.e. a_O and a_R, where $a_i = C_i \times \gamma_i$, and γ_i is the activity coefficient of the species. Since in this work the concentration of the test solutions are very dilute (1.000×10^{-8} to 6.0000×10^{-1} M), the activity coefficients approach one ($\gamma_i \approx 1$), therefore the activities of the test solutions are approximated to be equal to their concentrations.

At room temperature (25 °C), *RT/F* may be treated like a constant and replaced by 25.693 mV for cells. The Nernst equation is frequently expressed in terms of base 10 logarithms (i.e.,

common logarithms) rather than natural logarithms, in which case it is written, for a cell at *25 °C* as [117]:

$$E = E'_0 + \frac{59mV}{n}\log_{10}(\frac{C_o}{C_R}) \qquad \textbf{Equation 2}$$

The Nernst equation only applies when there is no net current flow through the electrode (open circuit voltage (OCV)). This is because the concentration/activity of ions at the electrode surface changes when current flows, and there are additional overpotential and resistive loss terms which contribute to the measured potential [115].

An electrode is said to behave "Nernstially" if the equilibrium electrode potential obeys the Nernst equation [118]. In other words, Nernstian behaviour refers to the slope of the electrode response with respect to concentration. 10-fold changes in concentration yield electrode potential changes of (59.2 mV/n), where n is the number of electrons involved in the redox reaction [119].

For the potentiometric sensors response analysis, the zero current potential applied between the working and the reference electrodes are recorded as a function of the concentrations of target analytes in a logarithmic manner [120]. If a potentiometric sensor behaves Nernstially towards the detection of a singly charged, doubly charged, and a triply charged cation/anion, the corresponding graphs should be straight lines with slopes (absolute values) of nearly 59 ± 1 , 29.5 ± 1, and 19.7 ± 1 mV per decade of the ion concentration/activity, respectively (figure 1.6). Throughout this thesis, the slopes of the calibration graphs are reported as absolute values. An electrode is said to behave "non-Nernstially" if the equilibrium electrode potential does not obey the Nernst equation when the concentration of a species involved in the electrode reaction changes.

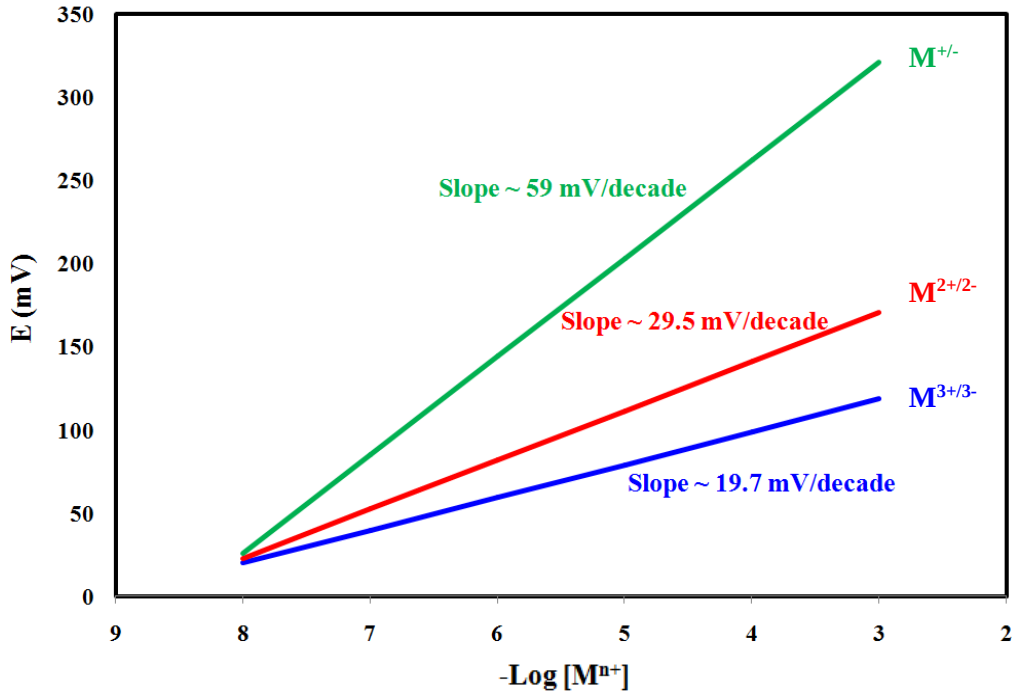

Figure 1.6. Typical Nernst plot used as potentiometric calibration curve in the analysis of the cation/anion of interest.

In ISEs, the potential difference at the electrode-electrolyte interface arising from unbalanced concentrations of species (*i)* in the electrolyte phase (*s*) and the electrode phase (*β*) is related by the Nernst equation with $C_o = C_i^s$ and $C_R = C_i^\beta$ .The generated potential can be related to the selective ion exchange between the ions in the complexes and the sample solution [12]. The measured potential is an electrostatic potential, which can be related to the charge crossing the interface between the electrolyte and the electrode phases.

1.11. Electrode Material

In recent years, an increasing number of researchers have explored the production of novel nano-scale metal oxides, metal-doped metal oxides, metal oxide-carbon nanotubes (CNTs) nanocomposites, and metal oxide-polymer composites [120].

Novel analytical devices based on nanostructured metal oxides are cost-effective, highly sensitive due to the large surface-to-volume ratio of the nanostructure, and show excellent selectivity when coupled to recognition molecules with simple design [121-124]. Nanostructured metal-oxides such as TiO_2, SiO_2, MnO_2, ZrO_2, CeO_2, ZnO, and other metal-oxides, have been extensively explored to develop biosensors with high sensitivity, fast response time, and high stability, for example for the determination of glucose by potentiometric methods [120]. Moreover, nanoscale-based materials exhibit distinctive physical and chemical properties [125]. Figure 1.7 illustrates the configuration of a potentiometric glucose sensor using glucose oxidase (GOx) modified ZnO nanowire as a working electrode [120].

In ISEs, a meticulous choice of electrode material can give good selectivity to one particular species, often , with minimal interference from other ions [126]. Among various nanoparticles, nano TiO_2 has been used vastly in industrial applications due to its unique optical and catalytic properties as well as its nontoxicity, biocompatibility, and high mechanical and chemical stability [127]. Browsing the literature demonstrated that only few reports are available for the detection of heavy metals using chemically modified TiO_2 films with chelating groups.

Nanocrystalline TiO_2 films were employed for naked-eye colorimetric detection of mercury in aqueous solution using N719 dye [128-130]. Besides, mesoporous TiO_2 is supposed to be a potentially active substrate for designing optical sensors using different fluoroionophores, due to its excellent surface area and high optical transparency in the visible part of the spectrum [131]. In sensing applications, mesoporosity provides the desired high accessible surface area and easier movement of metal ions for efficient binding.

Later on in this work, we will report the fabrication of novel potentiometric sensors for quantitative analysis of Cr^{3+} as well as Fe^{3+} ions, using GBHA and desferal molecular receptors grafted- nanostructured TiO_2 electrodes, respectively.

In this study, we employed nanostructured TiO_2 electrodes, with the aim of providing a large surface area for better adsorption of the applied ionophore molecules. This can facilitate the reversible binding of the analytes (i.e. Cr^{3+} and Fe^{3+}) to the ionophores, which leads to rapid exchange between these ions in the aqueous phase and the adsorbed layer phase. Therefore these fabricated sensors are expected to be highly sensitive and show very low limit of detections.

However, full optimization of the nanostructured material such as varying particle size, porosity, and thickness, was outside the scope of this thesis.

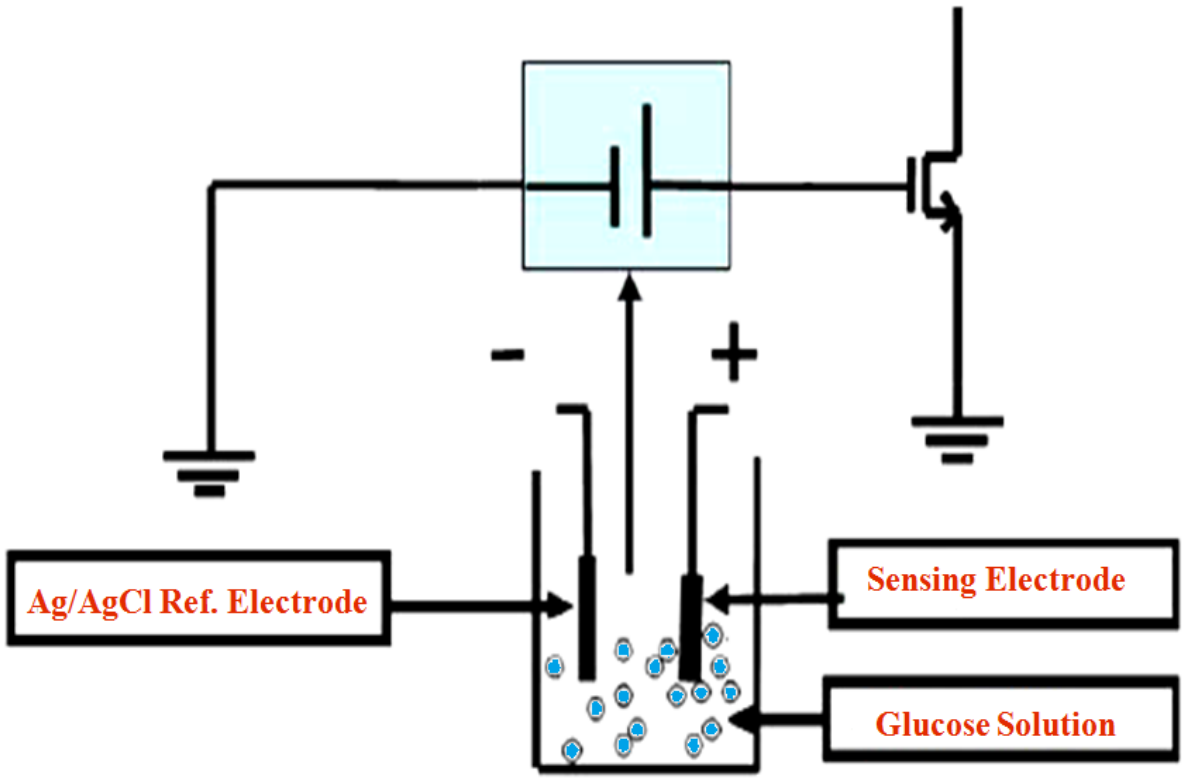

Figure 1.7. Schematic illustration of the configuration of a glucose sensor using GOx functionalized-ZnO nanowire as the working electrode and Ag/AgCl as the reference electrode. Reproduced with permission from Ref. [58], [www.mdpi.com/journal/sensors]. Copyright © [2010] Jae-Joon Lee *et al***.** MDPI.

1.12. Performance Factors

In this section the key performance factor of an ISE will be defined quantitatively to ensure that the reader is well aware of the methodology and terminology employed in this thesis.

1.12.1. Linear Concentration Range and Detection Limit

In ISEs the linear concentration range refers to the concentration range of the analyte for which the sensor behaves in a Nernstian manner. The calibration curve is plotted using the linear concentration range, and the signals (potentiometric or emf responses) associated with each of the sample concentrations within that range. This emf response is a linear function of the logarithm of the concentration of the free ions in solution [12]. The broader the working concentration range of an ISE, the better the performance of the sensor.

The limit of detection (LOD) or detection limit, is a term used to describe the smallest concentration of a substance which can be reliably measured by an analytical procedure. According to the International Union of Pure and Applied Chemistry (IUPAC)'s recommendations, the detection limit of an ion selective electrode is defined as the concentration of the analyte ion at the point of cross-section of the two linear segments where one represents the response of ISEs in a Nernstian fashion, while the other is the response of the electrode in the absence of ion of interest (LOD_{IUPAC}) [132, 133] as illustrated in figure 1.8.

In ISEs the LOD appears as the apparent loss of Nernstian slope of electrode response at low primary ion concentrations and can be related to two factors: 1) interference of competitive

sample ions (such as H^+ ions which is present in all aqueous samples) that affects the electrode response and causes deviations from the Nernstian slope, and 2) the perturbation of the interfacial sample concentration by the electrode. The most likely reason for this can be the constant release of low amounts of primary ions from the electrode into the sample [134].

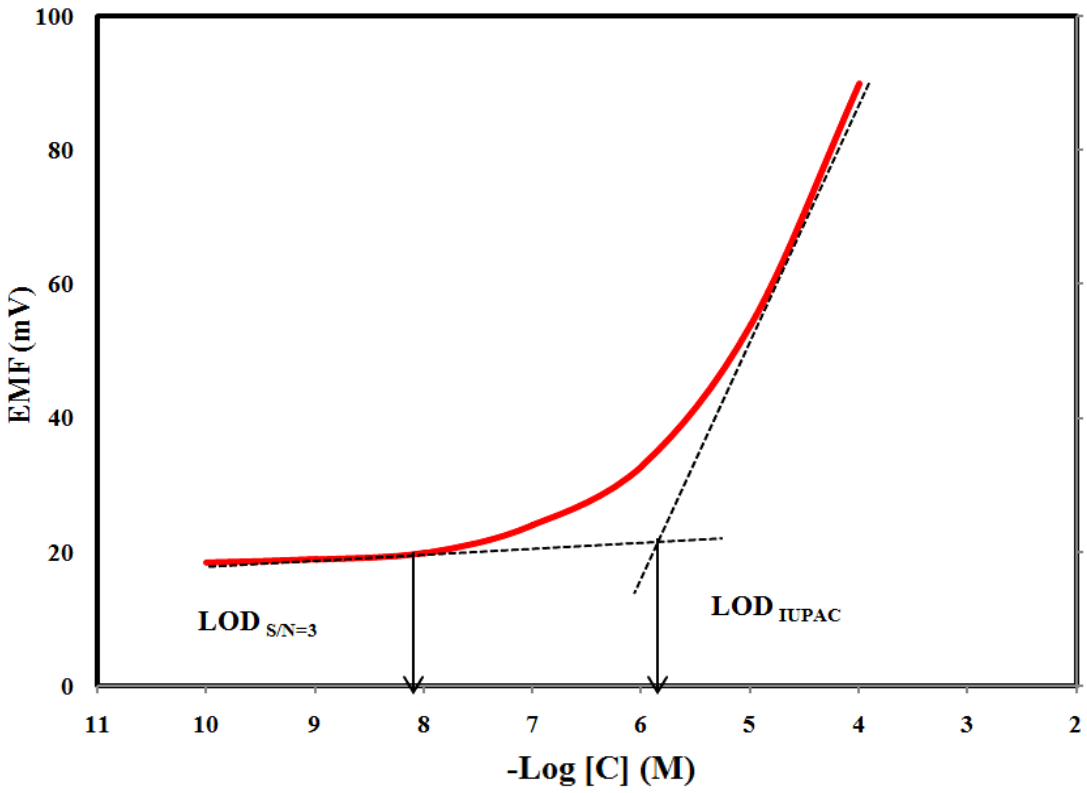

Figure 1.8. IUPAC definition of detection limit in ISEs.

1.12.2. Selectivity

In ISEs, the selectivity behavior of a sensor, which can be explained as the preference of an ion-selective electrode for the primary ion relative to interfering ions, or specificity towards the

primary ion in the presence of interfering ions, is one of the most important characteristics. Selectivity has been always one of the main challenges for the developers of ISEs; interferences by other sample ions are mainly dictated by their competitive extraction into electrode phase [134].

The two main factors determining the selectivity of a sensor are complexation of the target ions by the ligand, and electrode-solution ionic exchange. If some other ions are also complexed by the ionophore in addition to the primary ions, selectivity is attributed to the difference in stability constants of ion-ionophore complexes [134].

The selectivity of a sensor is controlled mainly by the complexation specificity of the receptor involved [22]. Therefore, in order to improve the selective properties of ISEs, one possible approach is to prepare ionophores that have zero or very low sensitivity towards other ions that may be present in the working atmosphere. Nonetheless, it is usually very difficult to achieve an absolutely selective ISE in practice, and most of the materials possess cross-sensitivity to other interfering ions [12, 135]. The higher the selectivity of an ISE towards an analyte of interest, the better the performance of the sensor.

In this study, the potentiometric selectivity coefficients, describing the preference of the carrier-based sensors for the ions of interest (A), relative to an interfering ion (B), were determined by the Matched Potential Method (MPM), which is recommended by IUPAC [136]. According to the MPM, the selectivity coefficient is defined as the concentration ratio of the primary ion and the interfering ion, which gives the same potential change in a reference solution. Subsequently, the potential change should be measured upon changing the primary ion concentration. Then, the interfering ion would be added to an identical reference solution until the same potential change would be obtained. The MPM selectivity coefficient, K_{MPM}, is then given by the resulting primary ion to the interfering ion concentration ratio, $K_{MPM} = c_A/c_B$ [136].

1.12.3. Response of the Electrode (Slope)

The slope of the calibration curve also called the response characteristic of the electrode is the main feature of a potentiometric sensor. Below the detection limit, it has a constant value which is ideally defined by the response of the sensor to other interfering ions [137]. The accepted deviation in the slopes of calibration graphs to be considered having a Nernstian behaviour is ± 1 mV decade^{-1} of the ion concentration [12].

1.12.4. pH Effect on the Electrode Response

The pH of the test solutions plays a key role in the potential response of ISEs. Special care must be taken in adjusting the pH of the test solutions within the suitable working pH range of the sensors' electrodes, because a small difference in pH may cause a significant change in the potential, and that will result in an error in the measurements [12]. Varying the pH can influence the formation of protonated and unprotonated species of the same substance, and also can cause the formation of hydroxyl complexes of the ions. The wider the working pH of a sensor is, the broader its application in different environments will be.

1.12.5. Dynamic Response Time

Dynamic response time is a critically important factor for analytical applications of any ISE, and is defined as the average time required for a electrode to reach a steady potential response within ± 1 mV of its final equilibrium value after successive addition of a series of M^{n+} solutions, each having a 10 fold-difference in concentration (IUPAC method) [138]. In ISEs, response time depends on concentrations as well as stability of the compounds formed between the analyte and the ligand at the electrode-solution interface [12, 139].The shorter the dynamic response of a sensor, the better its performance.

1.12.6. Life Time and Stability

The life time of a sensor refers to the period of time during which the sensor can be used for the determination of the analyte. It is determined by the stability of the selective material onto the electrode's surface. Once the end of an ISE's life time is reached, the slope and detection limit of the sensor decrease or increase. The main factor limiting the lifetime of an ISE in potentiometric measurements is the stability of the applied ionophore onto the electrode's surface [12].

It is accepted that the primary reasons for the limited life time of the ionophore-based sensors can be the loss of ionophore from the electrode's surface as a result of leaching into the sample, or lacking binding sites on the ionophore as a result of consecutive reversible complexation with the ions of interest [12]. The higher the stability of an ionophore onto the

surface of sensor's electrode, the longer the lifetime of the sensor, and therefore the better the performance of the sensor.

1.13. Self-Assembled Monolayers (SAMs)

Surfaces of metals and metal oxides have a tendency to adsorb foreign organic materials willingly because these adsorbates lower the free energy of the interface between the metal or metal oxide and the ambient environment [140]. These organic materials can act as physical or electrostatic barriers against aggregation and therefore decrease the reactivity of the surface atoms which leads to the formation of Self-Assembled Monolayers (SAMs). They can also act as an electrically insulating film.

SAMs are ordered organic assemblies [141, 142], formed by the adsorptions (chemisorptions) of molecular constituents from solution or the gas phase onto the surface of solids (inorganic materials). These adsorbates organize spontaneously into ordered structures and can have a significant influence on the stability of nanostructures of metals and metal oxides [140, 143]. A SAM is a properly organized layer of amphiphilic molecules that have a chemical functionality, or “head group” at the end with a specific affinity for a substrate. On the other end there is a terminal functional group connected by a “tail” (figure 1.9). There are a number of head groups that bind to specific metals, metal oxides, and semiconductors [140]. The end functional groups (tail groups) could be modulated as needed and appropriately chosen to improve hydrophilic and hydrophobic properties of the substrates [140].

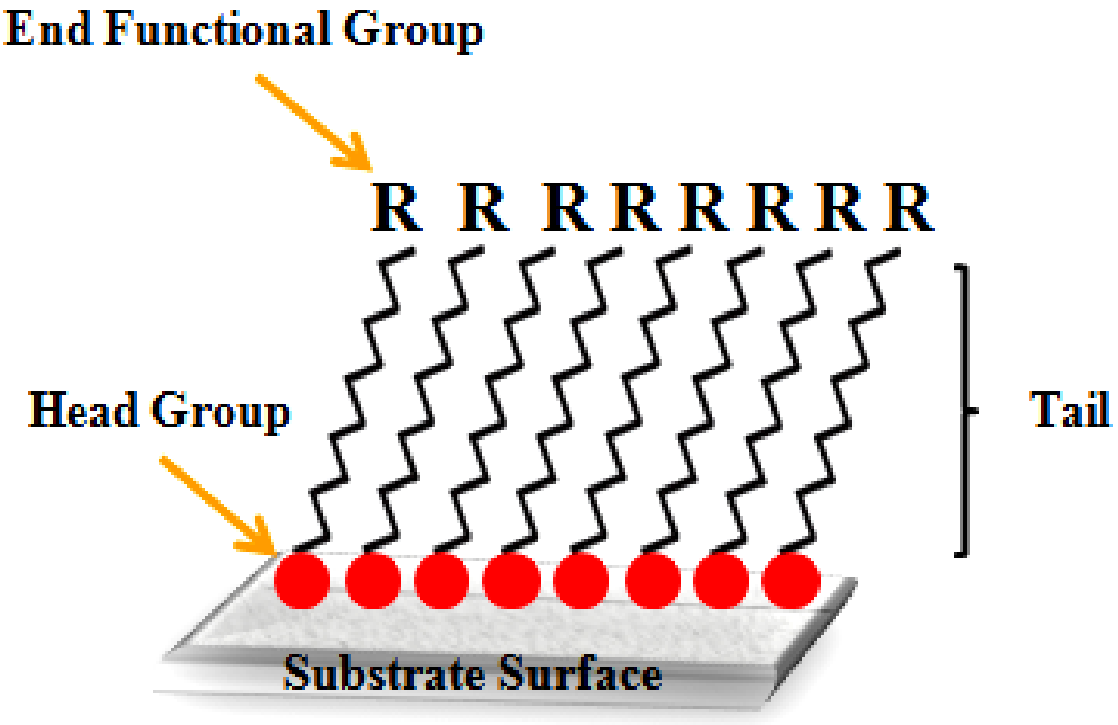

Figure 1.9. Schematic of a self-assembled monolayer.

In SAMs organization, firstly the hydrophilic head-groups of SAM molecules chemisorb onto a substrate as a disordered mass of molecules or in an initial "lying down phase". This is subsequently followed by rearrangement into a "standing-up phase", which completes the monolayer and results in highly ordered, two-dimensional structures. The final organization properties are dependent on the chain length, the adsorbate, and the substrate. While chain length influences SAM thickness [144, 145], steric hindrance and substrate properties affect the packing film density. Also the formation of well-ordered, stable monolayers depends on the purity of the adsorbates being used and the cleanness of the adsorbents. The presence of even low levels of

contaminants can result in disordered, non-ideal monolayer. The absorption of various kinds of unwanted molecules makes SAMs highly unstable [143].

As modification of surfaces of solids with SAMs enables researchers to tune various properties of the surface, it has found extensive applications in different fields such as chemical sensing, corrosion inhibition, semiconductor passivation, patterning, as well as control of surface properties like wettability, and so forth [146-148]. SAM molecules have been widely used in the literature during the last twenty years especially in the field of nanotechnology [149].

Depending on the type of the substrate, SAMs with different anchoring head groups can be used. Meticulous choice of SAM molecules can directly influence the surface modification properties such as the strength of SAMs chemisorption, as well as their stability, packing order, and aggregations, for example silanes/siloxanes are the best known SAM molecules used for modifications of silicon-containing substrates, such as SiO_2 [150].

1.14. Self-Assembled Monolayers (SAMs) of Phosphonic Acids on TiO_2 Electrodes

Phosphonic acids/phosphonates and silanes/siloxanes are the most commonly used organic reagents for titanium containing substrates [143]. Phosphonic acids (PAs) are compounds which contain R-$PO(OH)_2$ groups (where R=alkyl, aryl). The structure of a phosphonic acid compound features a tetrahedral phosphorus center, in which the phosphorous atom is bound to two hydroxyl groups with P-O single bonds, one R group (P-R bonds), as well as a double–bonded oxygen (P=O, known as a phosphoryl group). PAs are usually solids at room temperature and stable under harsh conditions such as high temperature over long periods of time. These organophosphorus coupling molecules tend to be soluble in polar solvents, such as ethanol. They

are sometimes soluble in water. However this is highly dependent on the R–group attached to the phosphonic acid [149].

PAs are attracting increasing attention, as they bind strongly to a wide variety of metal [151] and metal oxide substrates [152, 153]. Also, the presence of hydroxyl groups on the surface of TiO_2 allows for bonding other materials to this metal-oxide, which makes them a good candidate substrate for PAs attachment. PAs monolayers on TiO_2 surfaces have been particularly studied. PAs have been used to anchor dyes to TiO_2 anatase thin films in the preparation of solar cells, and also to modify TiO_2 membranes [154-156],

It is usually accepted that PAs form SAMs on TiO_2 surfaces by the formation of Ti-O-P bonds resulting from the condensation between P-OH and surface Ti-OH groups and from the coordination of the phosphoryl oxygen to the surface Lewis acidic sites on the surface (Ti atoms). In addition, remaining P-OH and P=O groups would probably be involved in hydrogen bonds with adjacent mono- or bidentate phosphonate units, or with surface hydroxyl or oxo groups [157]. Different binding scenarios have been proposed for the adsorption of PAs on transition metal oxide surfaces, which can use one, two, or three oxygen atoms bound to the surface, as well as both bridging and chelating configurations. The chelating binding mode with two oxygen atoms binding to the same metal is very uncommon [157-159]. In other words, PAs can bind to a metal oxide surface in either a monodentate, bidentate, or tridentate fashion as illustrated in figure 1.10 below [149, 155].

Recent Density Functional Theory (DFT) computations [160] suggested that the most stable adsorption arrangement for phosphonic acids to a titania surface would be a monodentate binding mode involving the coordination of the P=O groups, stabilized by two hydrogen bonds between the remaining POH groups and surface oxo bridges (figure 1.10 (h)). The binding of phosphonic

acids to titanium oxide surfaces is not easy to assess experimentally and the few studies reported may appear contradictory [155].

Advantages of phosphonic acid SAMs compared to silane ones are their higher hydrolytic stability under physiological conditions, their robust binding on the surface, and the fact that no surface conditioning (for example acid treatment) is required to obtain high coverage [143]. In addition, in contrast to silane SAMs, SAMs of PAs are not capable of cross linking, which leads to the formation of uniform monolayers of these molecules onto the surface of TiO_2 substrates [160].

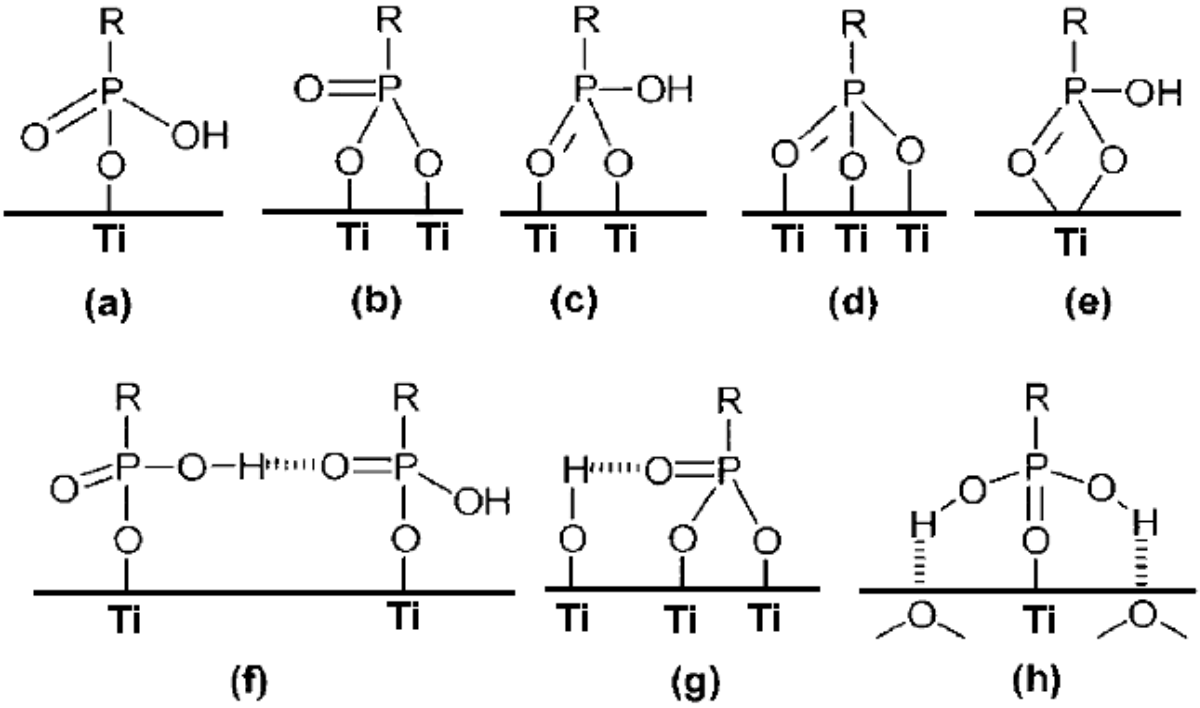

Figure 1.10. Different possible binding modes between PAs and nano TiO_2: **(a)** monodentate, **(b, c)** bridging bidentate, **(d)** bridging tridentate, **(e)** chelating bidentate, **(f-h)** additional hydrogen-bonding interactions Reprinted with permission from Ref. [160], [http://pubs.acs.org/doi/abs/10.1021/cm8012683]. Copyright © [2008] American Chemical Society.

In the current study, we took advantage of carboxyl-terminated alkyl phosphonic acids ($HO_2C(CH_2)_nPO_3H_2$ (n=3, 6, 11), with different alkyl chain lengths (short chain (3-C), medium chain (6-C), and long chain (11-C)) as linkers, to anchor to the surfaces of nanostructured TiO_2 electrodes as our sensors' substrates. These PAs bind selectively by the phosphonic end onto the surface of TiO_2, leaving the carboxylic acid as a free pendant group [150]. These surface modifications were performed with the aim of immobilizing the desferal ligand as our Fe(III)-selective ionophore onto the surface of TiO_2 by chemically binding the amino-terminal groups of this ligand to the carboxylic-terminal functional groups of the PAs linkers. The results of the desferal physisorbed-nanostructured TiO_2 electrodes were then compared with those of desferal chemisorbed-nanostructured TiO_2 substrates, by comparing the Nernstian responses of the fabricated nanosensors' electrodes.

1.15. A Brief Review On the Reported Cr(III)- and Fe(III)-Selective Sensors Using Different Ionophores

This part of the thesis encompasses a brief review on some of the best available ISEs in terms of performance factors, based on different ion-carriers for the analysis of Cr(III) as well as Fe(III) ions.

1.15.1. Reported Cr(III)-Selective Sensors

Abu-Shawish *et al.* developed a Chromium (III)-selective modified carbon paste electrode based on N,N-bis(salicylidene)-o-phenylenediamine as the ionophore [21]. The sensor exhibited a Nernstian behaviour (with a slope of 20.1 ± 0.6 mV decade^{-1}) for the linear concentration range of

$7.5 \times 10^{-6} – 1.0 \times 10^{-2}$ mol L^{-1} with a detection limit of 1.8×10^{-6} mol L^{-1}. It illustrated a relatively fast response time in the whole concentration range (5 - 10 s), and could be used in the pH range of 4.5 - 7.7. The fabricated sensor could be used for several months without any deterioration or change in the response of the electrode.

A new chromium(III) PVC membrane sensor incorporating p-tertiary-butyl calix[4]arene as ionophore was developed by Sadeghi *et al*. [22]. The electrode showed a good Nernstian slope of 20.0 ± 0.5 mV $decade^{-1}$ in the concentration range of 1.0×10^{-7} to 1.0×10^{-1} mol L^{-1} with a detection limit of 5.0×10^{-8} mol L^{-1}. The fabricated sensor exhibited a short response time (<15 s), and could be used for about 1 month in the pH range of 3.0 – 8.0.

Kumar *et al*. [23] fabricated a membrane all solid state electrochemical sensor containing synthesized triazole compound namely 4-(5-bromothiophen-2-carboxylidene amino)-3-methyl-5-mercapto-s-triazole (BTMMT) as an electroactive material for the determination of Cr^{3+} ions. The sensor exhibited Nernstian slope of 19.8 ± 0.2 mV $decade^{-1}$ in the working concentration range of $2.0 \times 10^{-7} – 1.0 \times 10^{-1}$ mol L^{-1} Cr(III) with a detection limit of 9.0×10^{-8} M and in the pH range of 2.2 – 5.0. The sensor also demonstrated a fast response time of 10 - 15 s, and could be used for at least 3 months without any considerable divergence in potentials.

In a study carried out by Gupta *et al*. [18], Tri-*o*-thymotide (I) was used as an electroactive material in PVC matrix for fabrication of a Cr(III)-selective sensor. The developed sensor displayed the working concentration range of 4.0×10^{-6} to 1.0×10^{-1} mol L^{-1} with a Nernstian slope of 20.0 ± 0.1 mV $decade^{-1}$ of Cr(III) concentration in the pH range of 2.8 – 5.1. The detection limit of this sensor was 2.0×10^{-7} M, and the electrode exhibited a fast response time of 15 s. This sensor could be successfully used for 5 months without showing any significant drifts in its response characteristics.

The figures below summarizes the ionophores mentioned above and their proposed binding to Cr^{3+} (see figure 1.11 (a-d)). [18, 21-23].

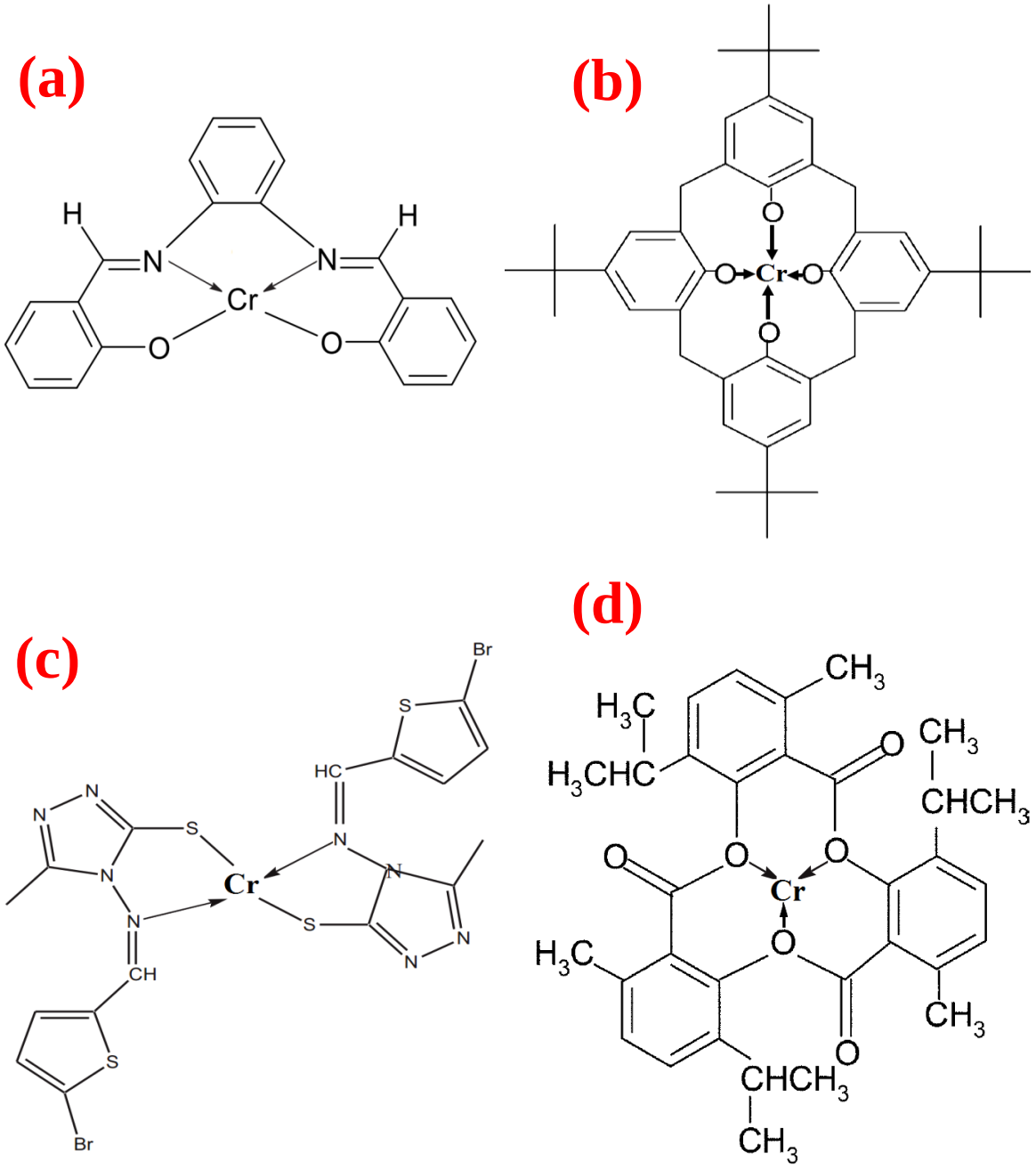

Figure 1.11 (a-d). The structures of the ionophores applied in references 21-23, and 18, respectively, and their proposed binding to Cr^{3+}.

1.15.2. Reported Fe(III)-Selective Sensors

Vlascici *et al*. designed a PVC-based membrane sensor for monitoring Fe^{3+} ions based on 5-(4-carboxyphenyl)-10,15,20-tris(4-phenoxyphenyl)-porphyrin as the ionophore [31]. The sensor showed a linear working range from 1×10^{-7} - 1×10^{-1} M with a slope of 21.6 mV/decade. It had a short response time of 20 and showed to work in a pH range from 2.0 – 3.8. The fabricated sensor could be used over a period of six weeks without observing any significant change in the sensor's response characteristics.

A membrane sensor for Fe^{3+} ions was developed by Mizani *et al*. based on 9-ethylacenaphtho[1,2-b]quinoxaline (EANQ) as the active component in a PVC polymer [33]. The PVC-based polymeric membrane electrode (PME) displayed a Nernstian behaviour (19.5 ± 0.3 mV $decade^{-1}$) over a wide range of Fe^{3+} ion concentrations 2.3×10^{-7} to 5.0×10^{-2} mol L^{-1} with very low limits of detection (9.6×10^{-8} M). The potentiometric response of this sensor was independent of the pH of the test solutions from 2.9 - 7.1 pH units. The electrode showed a relatively fast response time (<25 s) and could be used for at least 5 months without any remarkable deviations from the Nernstian behaviour.

Fe(III) ion-selective carbon paste and screen-printed sensors based on 2-methyl-6-(4-methylenecyclohex-2-en-1-yl)hept-2-en-4-one (MMCHH) were developed by Ali *et al*. [29]. The electrodes displayed a linear potential response over a broad concentration range from 4.3×10^{-7} to 1×10^{-2} mol L^{-1} and 1×10^{-7} to 1×10^{-2} mol L^{-1} with a LOD of 4.3×10^{-7} and 1×10^{-7} M for sensors fabricated based on modified carbon paste electrodes (MCPE) and modified screen-printed electrodes (MSPE), respectively. The slopes of the correlated calibration graphs were 18.5 ± 0.9 mV $decade^{-1}$ for MCPE, and 19.1 ± 0.2 mV $decade^{-1}$ for MSPE, and the electrodes showed

stable and reproducible potential over a period of 55 days (MCPE) and 130 days (MSPE). Also, the sensors exhibited short response times of <12 s and <7 s, and working pH ranges of 1.8 - 6.0 and 1.5 - 6.5 for MCPE and MSPE, respectively.

Isildak *et al* [161], developed a solid-state PVC Fe(III)-selective electrode based on ionophore (2-Hydroxymethyl-15-crown-5) for the determination of Fe^{3+} ions. The linear dynamic range of this Fe^{3+}-selective sensor was between 1.0×10^{-1} to 8.0×10^{-6} mol L^{-1} Fe^{3+} concentrations. The detection limit of this sensor was about 1.2×10^{-6} mol L^{-1} and the response time was shorter than 8 s. It also displayed good operational stability for at least two months keeping in dry conditions at 4–6°C, and it was stable in the pH range of 3-7.

The figures below summarizes the ionophores mentioned above and the proposed binding to Fe^{3+} for some of them (see figure 1.12 (a-d). [29, 31, 33, 161].

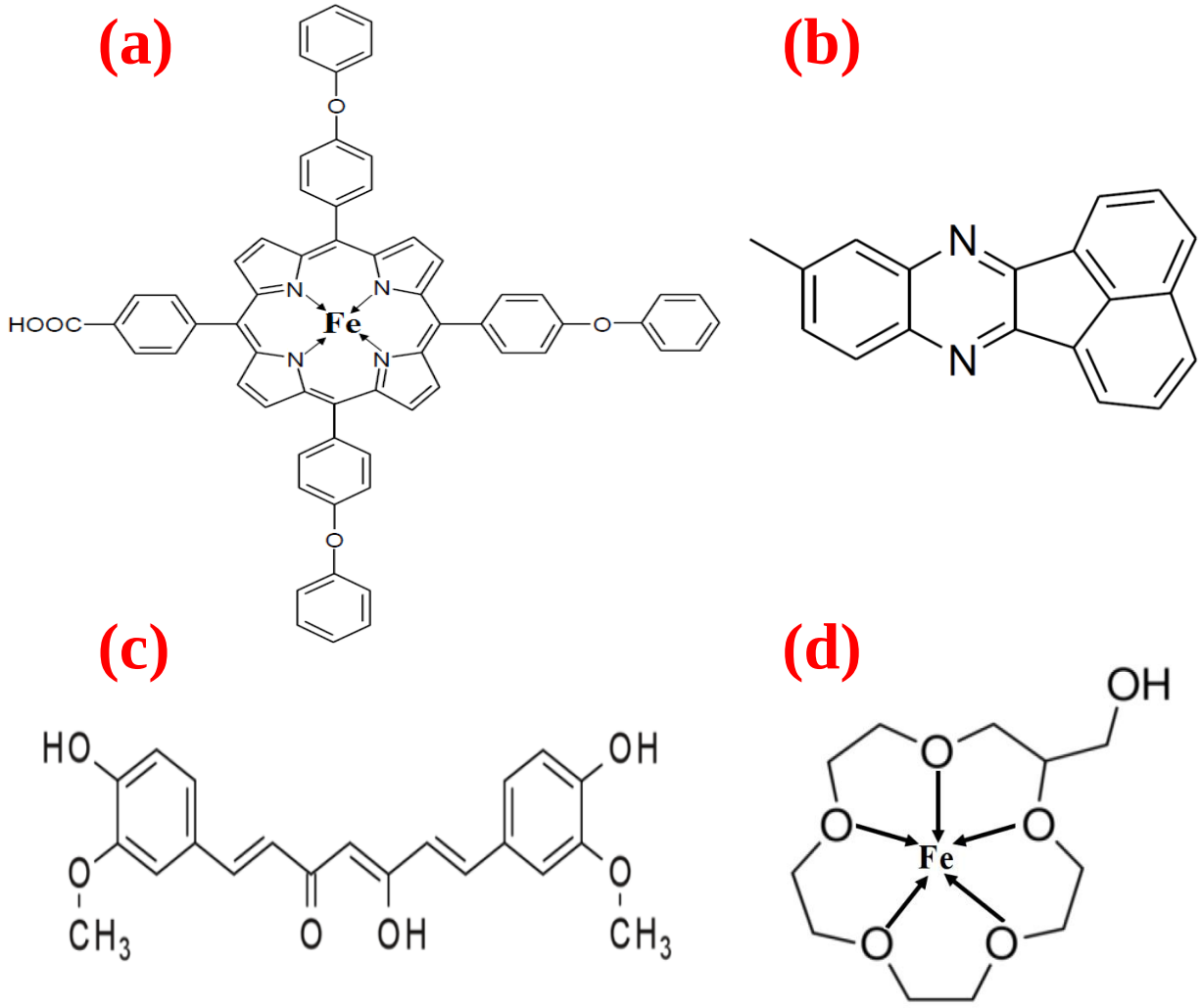

Figure 1.12 (a-d). The structures of the ionophores applied in references 31, 33, 29, and 161, respectively, and the proposed binding to Fe^{3+} for some of them.

Iron(III)-selective sensors were fabricated by Abbasi *et al* [125] based on seedless, highly aligned and vertical ZnO nanorods grown inside the pores of a nickel foam substrate. These ZnO nanorods were functionalized with trans-dinitro-dibenzo-18-6 crown ethers, a selective iron(III) ion ionophore. The cell assembly consisted of a two-electrode system: the functionalised seedless grown ZnO nanorods on nickel foam were used as the working electrode and a silver/silver

chloride (Ag/AgCl) electrode was employed as the reference electrode, as shown in figure 1.13. The sensor electrode showed high linearity with a wide Fe(III) detection range (from 0.005 mM to 100 mM). The low limit of detection of the proposed ion selective electrode was found to be 0.001 mM and it had a quick response time of less than 10 s. Besides, it was observed that the sensor electrode exhibited almost constant electrochemical response for a wide range of pH (from 5–12) demonstrating its potential usability for a wide range of applications. The wide Fe(III) ion concentrations detection range could be attributed to the 3D morphology of the ZnO nanorods on nickel foam which provided maximum surface area for the attachment of the ionophore molecules and later on for the binding of iron ions. Due to this morphology, rapid equilibrium could be established between the Fe(III) ions in solution and Fe(III)-selective ionophore-complex formation, which led to higher sensitivity and lower limit of detection [125].

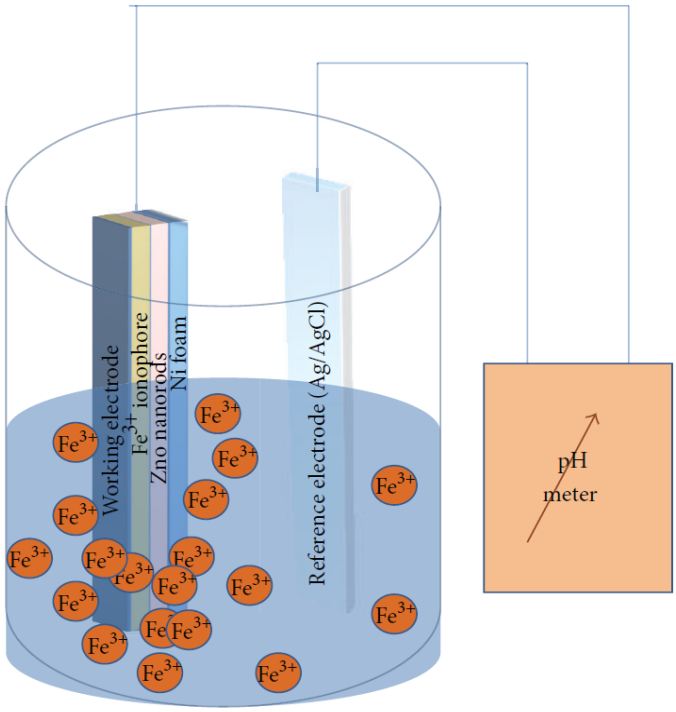

Figure 1.13. Schematic diagram of the fabricated iron(III) ion sensor based on ZnO nanorods on nickel foam. Adapted from open access Ref. [125], [http://dx.doi.org/10.1155/2013/382726]. Copyright © [2013] Abbasi *et al.*

1.16. Objective of the Thesis

The objective of the first part of this study was to design a novel Cr(III)-selective potentiometric sensor based on GBHA adsorbed on nanostructured TiO_2 electrodes, and to compare the performance of the fabricated sensor with some of the best previously reported Cr(III)-selective sensors, as reviewed in section 1.15.1.

The main goal of the second part of this work was to introduce novel solid state Fe(III)-selective potentiometric sensors based on desferal physisorbed and chemisorbed on nanostructured TiO_2 electrodes. The results of the designed sensors were then compared with each other and also with some of the best ferric-selective reported sensors based on other researchers' studies, as reviewed in section 1.15.2.

Also, for both developed ion-selective sensors, the principal analytical parameters have been studied including linear response range, calibration slope, detection limit, selectivity, and working pH range of the sensors. These objectives were successfully fulfilled as will be shown in the context of the next chapters.

2. Experimental Techniques

In this chapter, all methodologies for performing the experiments as well as the techniques and procedures used for the preparation of the materials and samples are described in details. In addition, characterization and measurement protocols are presented. These experimental procedures are then referred to in the following chapters as part of the discussion.

2.1. Preparation of Materials

The nitrate, chloride and sulphate salts of all cations used were from Sigma Aldrich, Merck, and Alfa Aesar and were of the highest purity available. Hence, they were used without any further purification. All employed acids and bases were of analytical reagent grade. Doubly distilled and deionized water was used throughout this work.

The following stock solutions were prepared: a)100.0 mL of a 1.0000×10^{-1} mol L^{-1} of chromium chloride hexahydrate ($CrCl_3.6\ H_2O$), b) 100.0 mL of a 6.0000×10^{-1} mol L^{-1} of ferric nitrate nonahydrate ($Fe(NO_3)_3.9\ H_2O$), as well as c) 100.0 mL of a 1.0000×10^{-1} mol L^{-1} of all other metal salts employed. The stock solutions were prepared by transferring the appropriate amounts of salts to a 100.0 mL volumetric flask and diluting to the mark with DI water. All other solutions of different concentrations were made by serial dilutions of the 1.0000×10^{-1} mol L^{-1} stock solutions.

The glyoxal-bis-(2-hydroxyanil) (GBHA) ligand was synthesized in Prof. P. G. Potvin's lab, Department of Chemistry, York University. In order to prepare 100.0 mL of a 1.000×10^{-2} M

stock solution of the GBHA ligand, about 0.2400 grams was weighed and then transferred to a 100.0 mL volumetric flask. GBHA was diluted to the mark with absolute ethanol. All the other GBHA solutions used for the UV-Vis as well as for surface coatings experiments were made by diluting the 1.000×10^{-2} M stock solution with ethanol.

The deferoxamine (desferal) ligand was synthesized by our collaborator, Dr. M. Elhabir's lab, Department of Chemistry and Bioorganic Medicine, European school of Chemistry, Polymers and Materials (ECPM), University of Strasbourg, Strasbourg, France. In order to prepare 100.0 mL of a 1.000×10^{-2} mol L^{-1} stock solution of the desferal ligand, ca. 0.6600 g was weighed, transferred to a 100.0 mL volumetric flask, and diluted to the mark with DI water. All the other desferal solutions used for the UV-Vis and for surface coatings experiments were made by diluting the 1.000×10^{-2} mol L^{-1} stock solution with DI water.

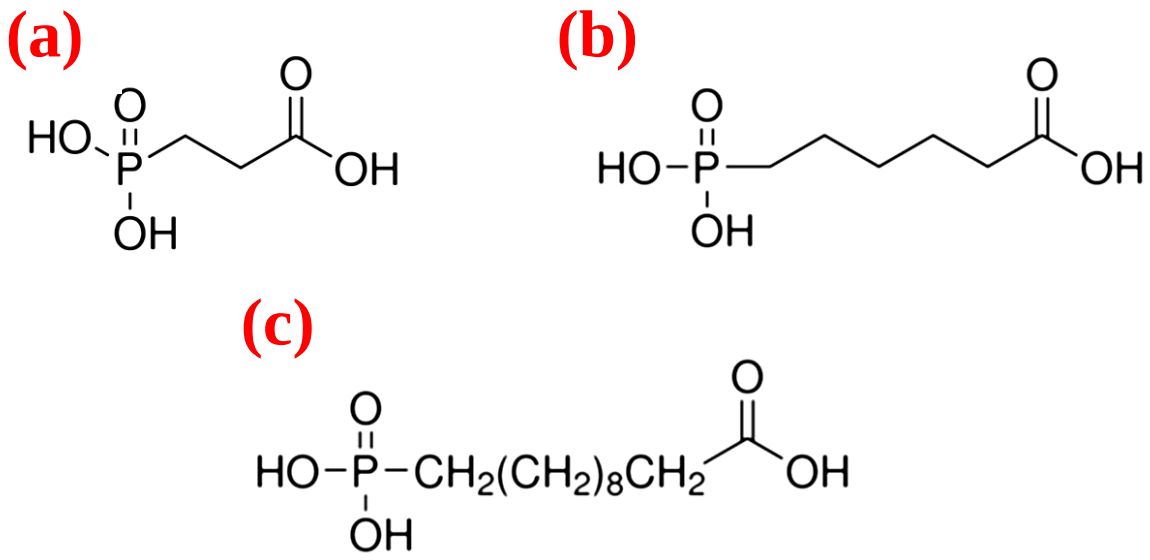

Figure 2.1. The chemical structures of: **(a)** 3-Phosphonopropionic acid, **(b)** 6-Phosphonohexanoic acid, and **(c)** 11-Phosphonoundecanoic acid.

Phosphonic acids (PAs) with different alkyl chain lengths were employed for surface functionalization, namely 3-Phosphonopropionic acid (94.0% purity), 6-Phosphonohexanoic acid (97.0% purity), as well as 11-Phosphonoundecanoic acid (96.0%purity), having 3, 6, and 11 carbons in their alkyl chain, respectively (Sigma-Aldrich).Their structures are depicted in figure 2.1. As seen in the structures of the applied PAs, the terminal functional parts of these linkers contain carboxylic acid (-COOH) groups, which can be activated to interact with the free amine ($-NH_2$) groups on the desferal ligand to stably immobilize it onto the surface of TiO_2 electrodes.

The following solvents were also used for the preparation of the PAs' solutions, *in-situ* immobilization of the desferal ligand on the surface of TiO_2 electrodes, and the synthesis of TiO_2 nanoparticles: absolute ethanol (Commercial Alcohols Inc.,), tetrahydrofuran (THF) (Sigma-Aldrich, 99.0% purity), acetonitrile (Sigma-Aldrich, LC-MS grade), and dichloromethane (Sigma-Aldrich, 99.5% purity). Titanium (IV) isopropoxide (Reagent grade, 97% purity) was obtained from Sigma-Aldrich.

The stock solutions (1.000×10^{-2} mol L^{-1}) of the three PAs were prepared by transferring the appropriate amount of their powders in a volumetric flask and the solutions were quantitatively made by adding pure ethanol to 3-C and 6-C PAs, and 3 : 1 ethanol : THF for 11-C PA.

N,*N*′-Dicyclohexylcarbodiimide (DCC) (99.0% purity), *N*-Hydroxysuccinimide (NHS) (98.0% purity), and potassium bicarbonate (bicarb) (99.7% purity) were purchased from Sigma-Aldrich.

2.2. Preliminary UV-Vis Spectroscopic Studies

In order to investigate the feasibility of using GBHA and desferal, as chromium(III) and iron(III) selective ionophores, respectively, we did some preliminary studies based on UV-Vis spectroscopic titrations. In this regard, complexation of the GBHA and desferal were studied with most of the first row transition metals in an ethanol solution and aqueous solution, respectively. The analyses were performed using a Varian Carry 100 Bio UV-Vis spectrometer, and the spectra were collected in the range of 200 - 800 nm.

As for the primary studies on the fabrication of Cr(III)-selective sensors based on GBHA, complexation studies were performed for Cr^{2+}, Cr^{3+}, Mn^{2+}, Fe^{2+}, Fe^{3+}, Co^{2+}, Ni^{2+}, Cu^{2+}, and Zn^{2+} using UV-Vis spectroscopic titrations at 25.0 ± 0.1ºC. The UV-Vis titration analyses were conducted with the aim of studying the existence of any interactions between GBHA and the first row transition metals. For these analyses, 3.00 mL of a 5.000×10^{-4} mol L^{-1} GBHA in ethanol solution was titrated in a step-wise fashion with microliters amounts of 1.000×10^{-2} mol L^{-1} aqueous solutions of metal ions (up to the final concentration of 1.000×10^{-3} mol L^{-1}) and the UV-Vis absorbance spectra were recorded.

For the preliminary studies with regard to designing Fe(III)-selective sensors based on desferal, complexation studies were carried out for Fe^{2+}, Fe^{3+}, Cr^{2+}, Mn^{2+}, Co^{2+}, Ni^{2+}, Cu^{2+}, and Zn^{2+} using UV-Vis spectroscopic titrations at 25.0 ± 0.1ºC. The objective of these studies was to investigate the interactions of desferal ligand with the first row transition metals. For these analyses, 3.00 mL of a 5.000×10^{-4} mol L^{-1} desferal solution in water was titrated in a step-wise manner with microliters amounts of 1.000×10^{-2} mol L^{-1} aqueous solutions of metal ions (up to the final concentration of 1.000×10^{-3} mol L^{-1}) and the UV-Vis absorbance spectra were obtained.

2.3. Synthesis of TiO_2 Nanoparticles

In this work, TiO_2/FTO glasses modified with GBHA (physisorbed), as well as desferal (physisorbed and chemisorbed) as anchoring ligands were assembled and investigated for Cr(III)- and Fe(III)-selective sensing measurements, respectively.

The first key component of the proposed potentiometric sensors is the working electrode. TiO_2/FTO glass substrate was chosen as the working electrode material. In order to synthesize TiO_2 nanoparticles, the following procedure was employed: a round bottom flask was filled with 69.0 mL of anhydrous ethanol and 69.0 mL of deionized water (Millipore, Milli-Q gradient 10) in order to make a 1:1 ethanol: water solution. Afterwards, 12.4 mL of titanium(IV) isopropoxide was added to 56.0 mL of anhydrous ethanol and transferred to a dropping funnel. The prepared solution of titanium(IV) isopropoxide was added dropwise to the flask using a dropping funnel as depicted in figure 2.2. (a). After the completion of gel formation (as shown in figure 2.2. (b)), the materials were suction filtered and rinsed several times with ethanol while filtering. The filtered materials were placed in the oven over night at 110 °C to dry (figure 2.3. (a)); the dried materials were then ground by pestle and mortar. The obtained fine powders of TiO_2 were calcinated in an electrical furnace at 450 °C for 2 hours (figure 2.3 (b)). This general route was repeated three times to prepare more samples.

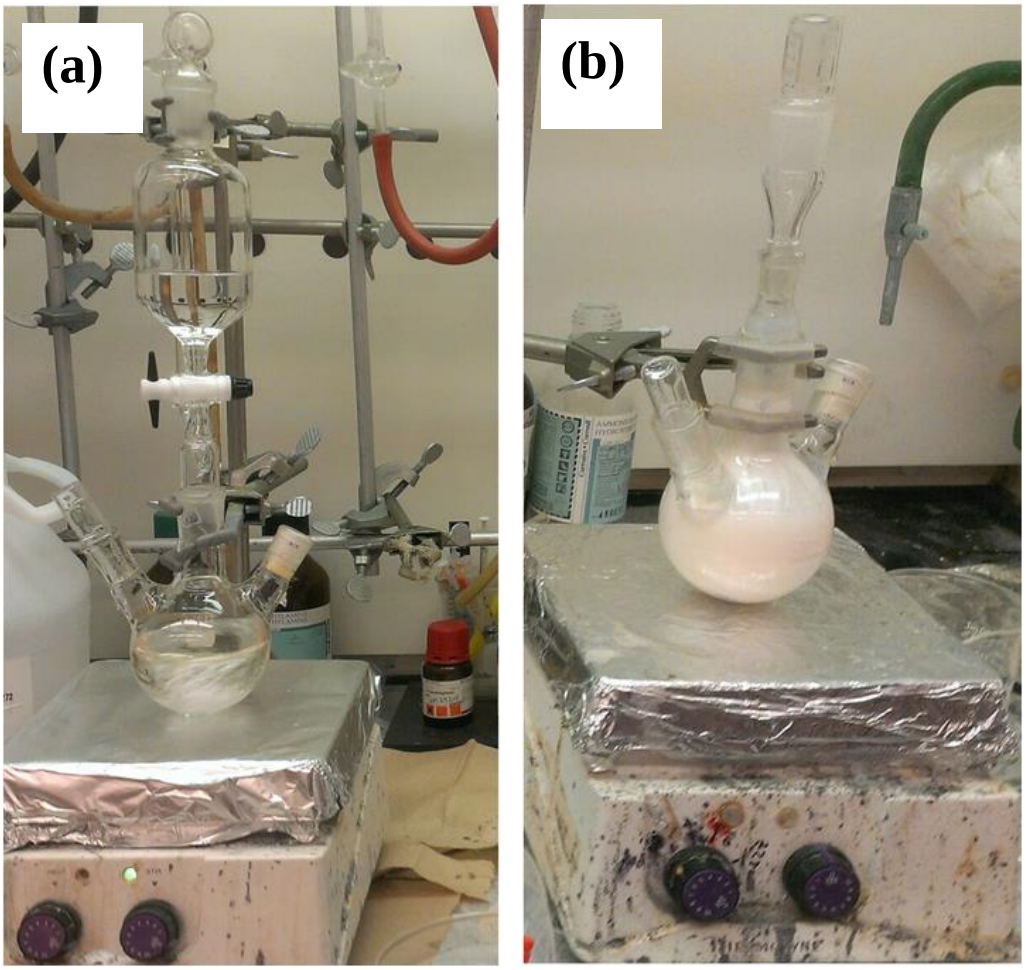

Figure 2.2. The experimental steps for the synthesis of TiO_2 nanoparticles. **(a)** The initial set-up, **(b)** The formation of a gel.

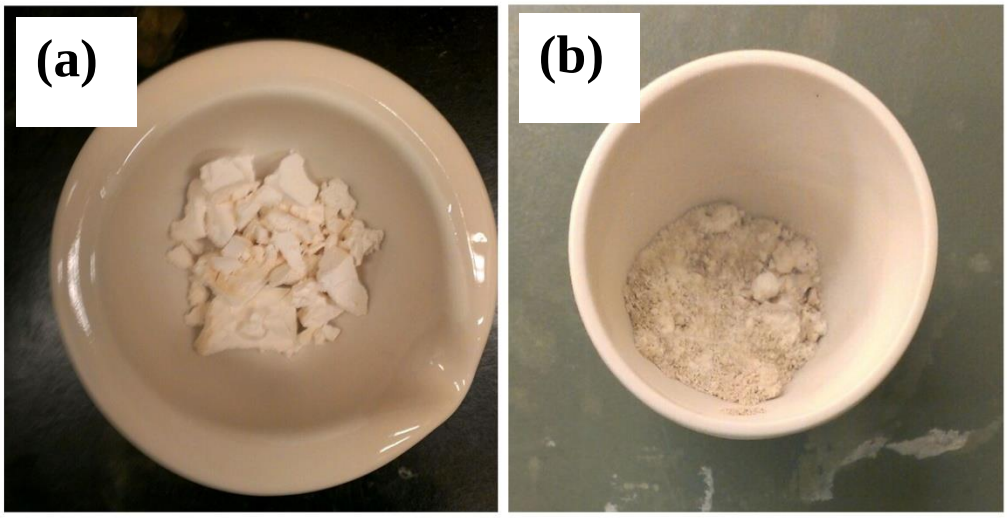

Figure 2.3. The experimental steps for the synthesis of TiO_2 nanoparticles: **(a)** The suction filtered materials, and **(b)** Fine powders of TiO_2 after calcination.

2.4. Preparation of TiO_2 Electrodes

The TiO_2 films were fabricated following a technique described elsewhere [162]. The first step involves the preparation of a TiO_2 suspension with approximately 2.00 g of powders and 7.00 mL of water, which was added gradually followed by the addition of 0.60 mL of acetyl-acetone (Fluka, 99.5%) as the dispersing agent or stabilizer. The mixture was then sonicated in an ultrasound bath for one hour. The resultant suspension was stirred on a magnetic stirrer for half an hour while it was cooled down with ice. The stirring/sonicating procedure was repeated several times to get a homogeneous suspension.

Fluorine-doped SnO_2 conductive glass (Tec 7 FTO, Pilkington Co., 8Ohm/cm^2) was cut in 13.5 cm × 6 cm pieces and rinsed with soap and water twice, following by rinsing with ethanol. Afterwards, they were carefully rinsed with DI water and dried by compressed air flow. The dried glasses were sonicated in isopropyl alcohol for half an hour following by careful drying with compressed air flow. The clean FTO plates were then coated with the TiO_2 suspension with a glass rod, using the "doctor blade" technique to distribute the particles evenly (figure 2.4). The films were left to dry in air and then sintered in an air atmosphere for one hour at 450°C to assure good connectivity between the particles and also to burn all the organic chemicals.

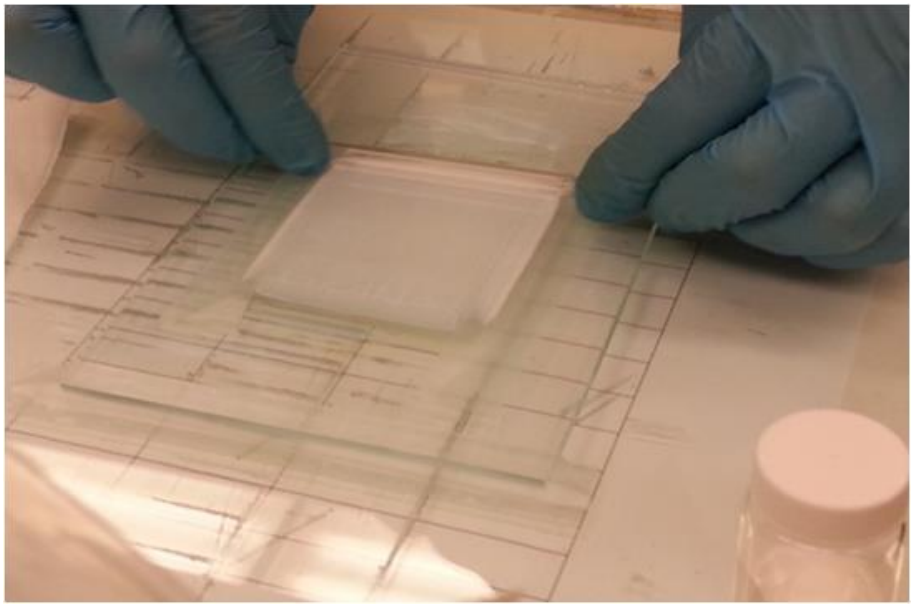

Figure 2.4. Preparation of TiO_2 Electrodes using "doctor blade" technique.

2.5. Surface Modification of TiO_2 Electrodes with Ionophores

The second key component of any sensor is the ionophore, which as explained in chapter one, imparts the selectivity to a particular analyte.

2.5.1. Cr(III)-selective Sensors

In order to fabricate Cr(III)-selective sensors, GBHA was used as the ionophore. In this regard, the TiO_2 substrates were modified with GBHA ionophores by immersing the electrodes into a 1.000×10^{-2} mol L^{-1} GBHA and ethanol solution for 24 hours. The substrates modified

with physisorbed GBHA were then removed from the solution and rinsed with ethanol to prevent aggregations of GBHA, and used for the detection of chromium(III) ions(figure 2.5).

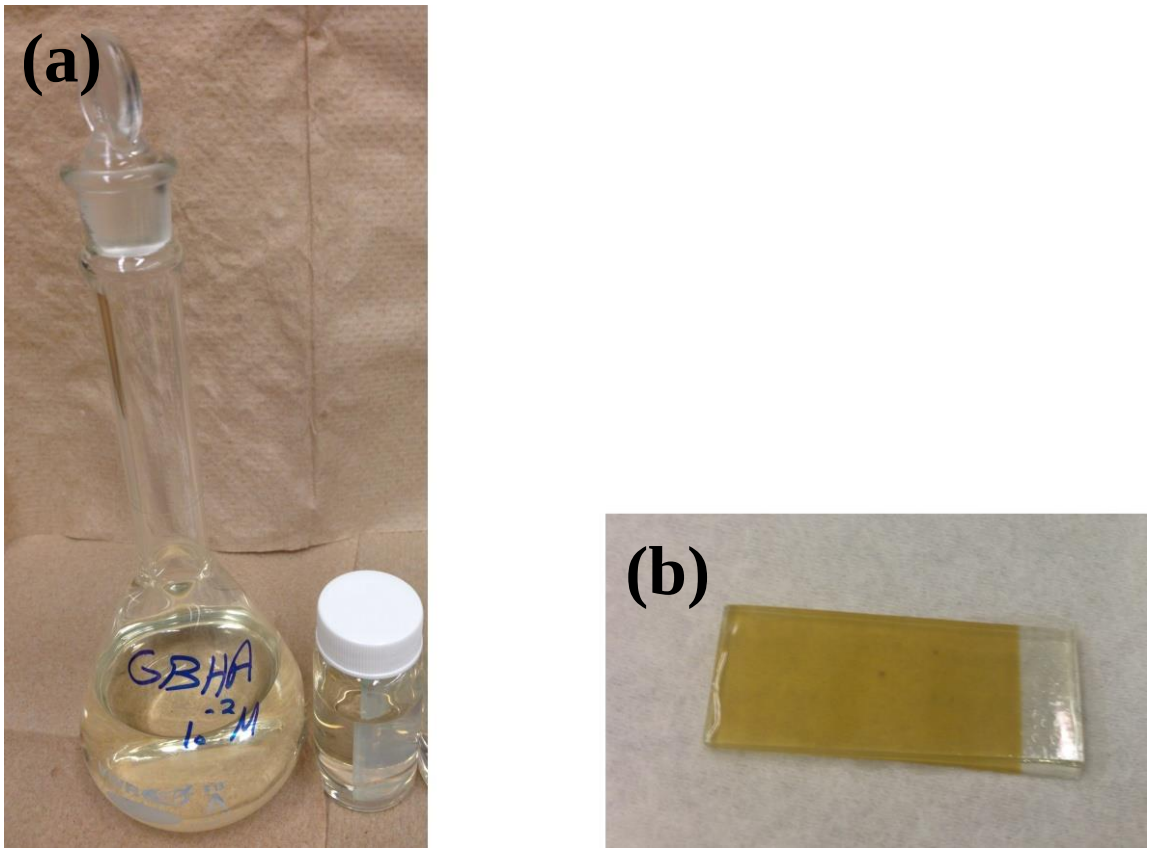

Figure 2.5. Experimental procedures for the preparation of a GBHA-modified TiO_2 electrode for the fabrication of a Cr(III)-selective sensor include: **(a)** the immersion process, and **(not shown)** rinsing of the modified TiO_2 electrode after its removal from the solution. **(b)** Appearance of the electrode after completion of the preparation process.

2.5.1.1. Fabrication of Cr(III)-Sensor, EMF measurements

The two-electrode potentiometric experiment set-up is shown in figure 2.6, using a GBHA-modified TiO_2 as the working electrode, and a saturated calomel electrode (SCE) (purchased from Fisher Scientific™ accumet™) as the reference electrode. The potentials of the varying concentration of the Cr(III) solutions were then read at 25 ± 0.1 °C form a voltmeter (Fluke 79-3 True RMS Multimeter) upon changing the chromium test solutions form the lowest to the highest concentrations (1.000×10^{-8} - 1.0000×10^{-1} mol L^{-1} of $CrCl_3.6H_2O$). The solutions were stirred and potential was recorded when it had reached a stable value.

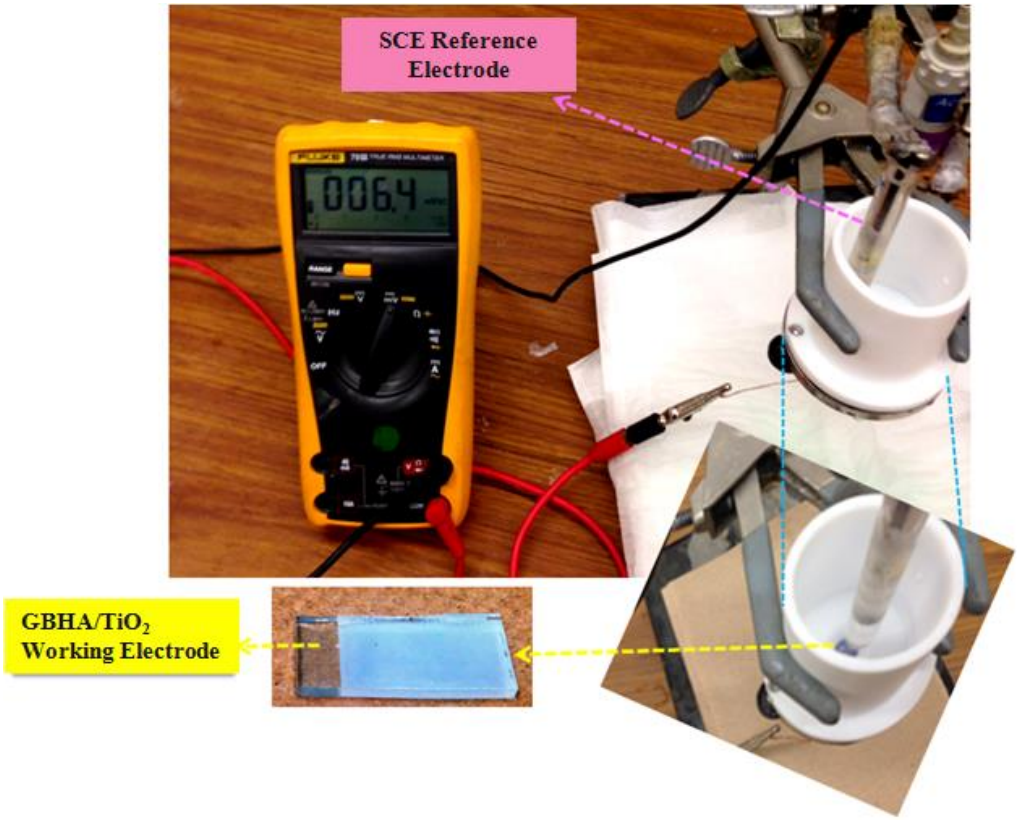

Figure 2.6. The two-electrode potentiometric experiment set-up, for designing a Cr^{3+} selective sensor.

2.5.2. Fe(III)-selective Sensors

Fe(III)-selective sensors were fabricated using desferal as the recognition element. Two strategies were applied for designing such sensors, namely the physisorption of desferal on TiO_2, as well as desferal chemisorption on TiO_2 electrodes using click chemistry.

2.5.2.1. Fe(III)-selective Sensors Based on Desferal Physisorbed on TiO_2 Electrodes

In order to fabricate Fe(III)-selective sensors based on desferal physisorbed on TiO_2 substrates, the electrodes were immersed into a 1.00×10^{-2} mol L^{-1} desferal aqueous solution for 24 hours. Afterwards, the modified electrodes were rinsed with water to eliminate aggregation prior to metal cation binding, and used for the detection of iron(III) ions.

2.5.2.2. Fe(III)-selective Sensors Based on Desferal Chemisorbed on TiO_2 Electrodes

For the assembly of Fe(III)-selective sensors based on desferal chemisorbed on TiO_2 substrates, the electrodes were first modified with SAMs of PA molecules. Afterwards the PA-modified TiO_2 electrodes were used for the immobilization of desferal ligands. The experimental procedure will be explained in the following sections.

2.5.2.2.1. Surface Modification of TiO_2 Electrodes with SAMs of Phosphonic Acids

The modification procedure used in the experiments described herein is a solution deposition method, which will be described in details in this section.

As the cleanness of the TiO_2 electrodes plays a key role in the quality of SAMs organization onto the substrates, prior to deposition, TiO_2 substrates were rinsed with ethanol 3 times, followed by rinsing with copious amounts of DI water. Afterwards the samples were blow-dried in a nitrogen stream. This process was repeated three times right before the assembly process. Following the cleaning steps, the substrates were immediately fully immersed in 10.0 mM PA and ethanol solution with the samples facing upward. The electrodes were left in the PAs solutions for 72 hours, which allowed the substrates to react well with the PA molecules in solutions. Therefore the PA molecules were transferred to the surface in an organized fashion (figure 2.7).

This process was followed by rinsing the substrates with ethanol and placing the electrodes in an oven (~ 120 °C) for 24 hours. This is to complete the heterocondensation reaction of the phosphonic acids onto the surface, giving a strongly bound, ordered alkylphosphonate film. It is shown that the subsequent heat treatment increases the covalent character of the bond between the TiO_2 substrate and the phosphonate anchor groups [163, 164]. After heating, the substrates were rinsed with a 5% triethylamine/ethanol solution, followed by rinsing with absolute ethanol 3 times to remove unbound or weakly bound PA molecules and to minimize the PAs aggregations on the TiO_2 electrodes.

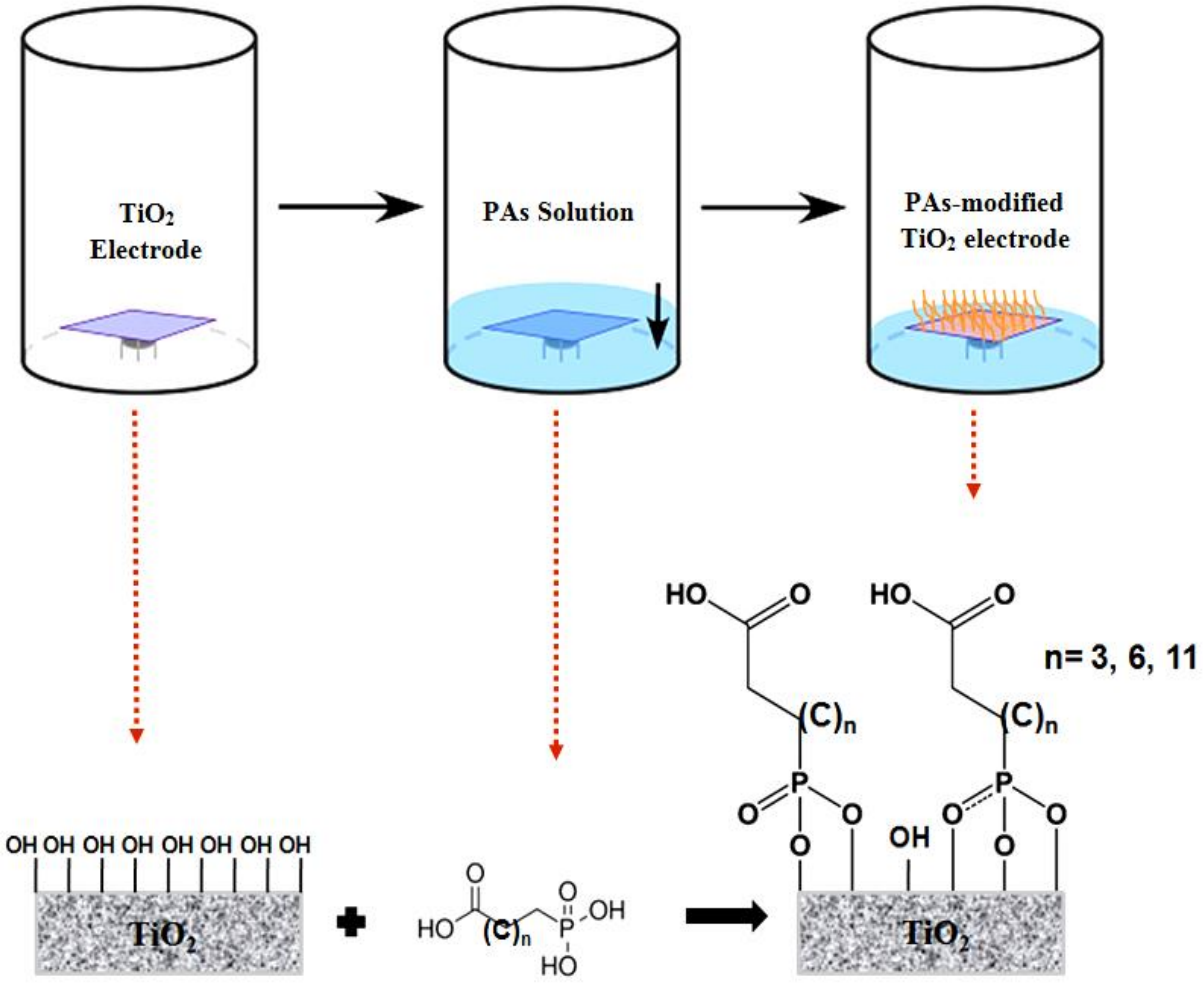

Figure 2.7. The experimental set-up showing the different steps of the chemical deposition method for modifying the TiO_2 surface with SAMs of phosphonic acids.

One of the advantages of utilizing phosphonic acids is that the formation of multilayers as seen for silanes is less likely to occur because the homocondensation of P–OH and P–O bonds does not occur under mild conditions and/or in aqueous conditions [149]. Additionally the extent of hydrolysis does not have an impact on the quality of the modification, so milder conditions can be applied when using phosphonic acids with respect to silanes. Other advantages of using

phosphonic acids are their ambient stability over long periods of time, and the fact that the formation of robust, complete monolayers which is dependent on the presence of functional groups on the surface of the metal oxides (e.g. hydroxyl groups which are already present on the surface of TiO_2), is much easier than the case of SiO_2 which requires chemical treatment to introduce Si-OH groups on the surface.[149].

2.5.2.2.2. Immobilization of Desferal ligand onto PAs-modified TiO_2 Electrodes

Carbodiimide compounds provide the most popular and versatile method for labeling or cross-linking to carboxylic acids [165] and N,N'-Dicyclohexyl carbodiimide (DCC) is the most readily available and commonly used carbodiimide for non-aqueous organic synthesis methods. DCC is an organic-soluble cross-linker that activates carboxyl groups (-COOH) for spontaneous amide-bond formation with primary amines ($-NH_2$) [166]. N-hydroxysuccinimide (NHS) is a chemical used to form semi-stable, but reactive esters from carboxylic acids [167]. NHS is typically used in conjunction with a dehydrating reactant, often a carbodiimide such as DCC [167].

In this study, we aimed for *in-situ* immobilization of the amino-terminated desferal ligands onto the surface of TiO_2 electrodes through binding to the carboxyl terminal groups of the phosphonic acid linkers. The procedure was carried out as follows. The PA-modified TiO_2 electrodes were rinsed with methanol followed by acetonitrile, and put in a vial (with a stir bar) containing fresh acetonitrile:dichloromethane (DCM) 9:1. Afterwards the base (bicarb) in excess amount was poured in the vial, and the solution was stirred for 15 minutes. The solution was then

treated with DCC:NHS (1.2:1) while stirring for one hour. The amino-terminated desferal ligand, pre-dissolved in methanol (pH was adjusted to 7.5 by NaOH), was then added to the solution, and the mixture was stirred overnight (considering that the DCC:NHS:PA:desferal ratio was 1.2:1:0.9:1). The experimental procedure are depicted in figures 2.8. The substrate was then removed from the solution mixture and rinsed with methanol in order to remove all the urea type by-products.

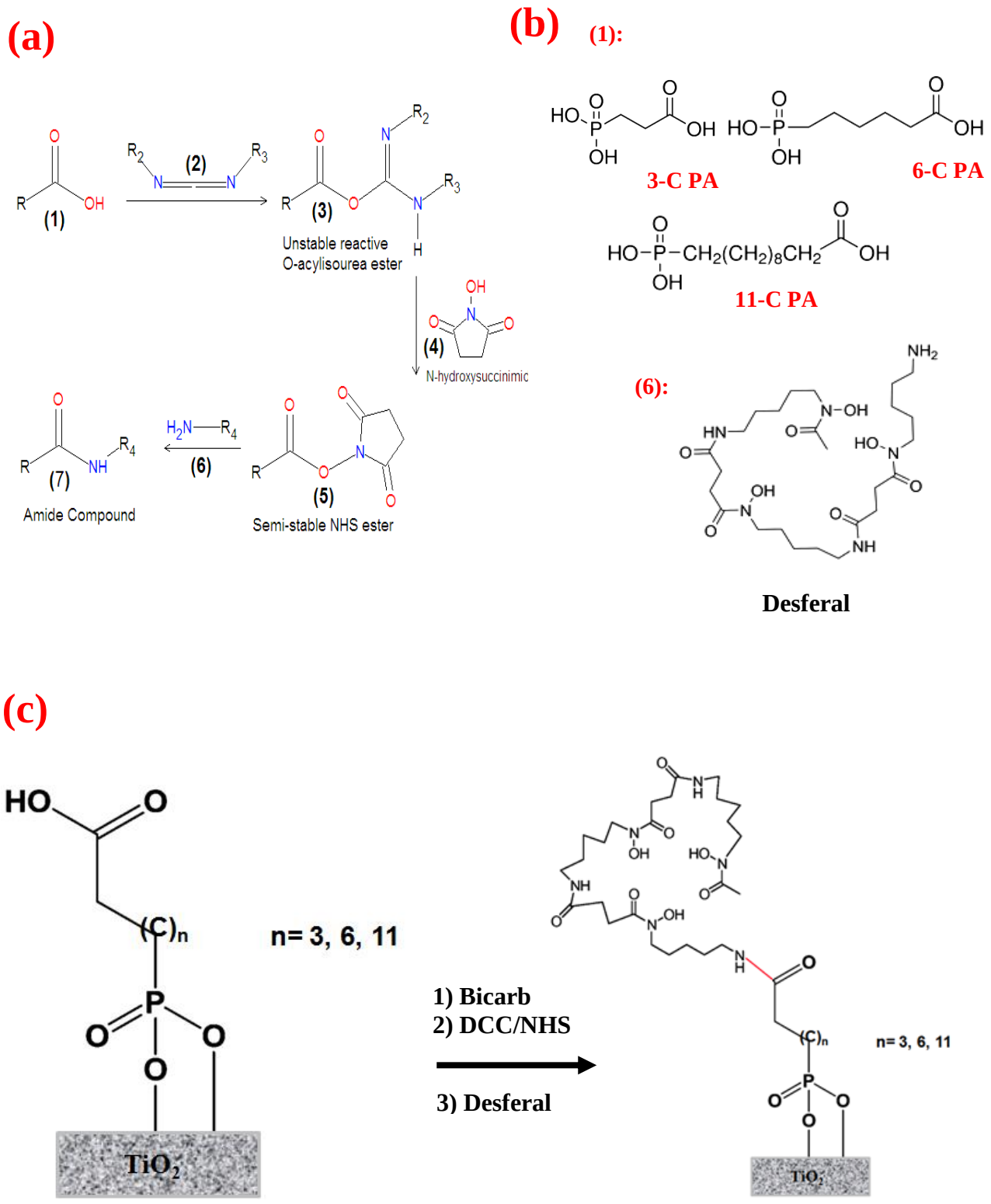

Figure 2.8. The experimental procedure for the immobilization of desferal ligand onto PAs-modified TiO_2 electrodes. **(a)** Coupling of a carboxylic acid and a primary amine using DCC and NHS [167]**. (b)** The chemical structures of the applied carboxylic acid-terminated PAs as well as amino-terminated ligand. **(c)** The schematic of the experimental procedure for chemisorption of desferal on TiO_2 electrodes through phosphonic acid linkers.

2.5.2.3. Fabrication of Fe(III)-Sensor, EMF measurements

After assembling the physisorbed desferal/TiO_2, and chemisorbed desferal-PA/TiO_2 electrodes, potentiometric measurements were performed. For these measurements, the same two-electrode potentiometric experiment set-up was applied as shown in figure 2.6, using a desferal-modified TiO_2 as the working electrode and a saturated calomel electrode (SCE) as the reference electrode. Afterwards, the potentials of the varying concentration solutions of Fe(III) were read at 25 ± 0.1 °C from the voltmeter upon changing the iron test solutions form the lowest to the highest concentrations (1.000×10^{-8} - 6.0000×10^{-1} mol L^{-1} of $Fe(NO_3)_3.9H_2O$). The solutions were stirred and the potential was recorded when a stable value was obtained.

We carried out four sets of emf measurements experiments, one based on physisorbed desferal and three based on chemisorbed desferal. The latter being carried out for various length of the alkyl chain on the PA linker (i.e., 3-C, 6-C, and 11-C PAs). These measurements will allow us to access their performance as iron(III)-selective sensors.

2.6. Characterization Methods

In order to study the surface functionalization of TiO_2 electrodes with SAMs of PAs, and also the immobilization of the desferal ligands onto the PAs-modified TiO_2 electrodes, the following characterization methods were applied: Fourier Transform Infrared Spectroscopy (FTIR), ^{31}Phosphorous Nuclear magnetic resonance (NMR) Spectroscopy, Scanning Electron Microscopy-Energy Dispersive X-ray Spectroscopy (SEM-EDX), and Atomic Force Microscopy

(AFM) imaging. The principles and the experimental parameters of each method will be explained in the following sections.

2.6.1. Fourier Transform Infrared Spectroscopy

2.6.1.1. Principles of IR Spectroscopy

Infrared spectroscopy (IR spectroscopy or vibrational spectroscopy) is a type of spectroscopic technique that deals with the infrared region of the electromagnetic spectrum (from 0.78 μm to 1000 μm), that is light with a longer wavelength and lower frequency than visible light. "wavenumbers", in units of cm^{-1} are commonly used. The most useful IR region lies between 670 to 4000 cm^{-1}. As know, molecules have several types of vibrations and rotations. In general, a molecule with N atoms has 3N-5 (for linear molecules) and 3N-6 (for non-linear molecules) normal modes of vibration associated with the internal bonds. Some (not all) of these vibrations are IR active [168].

In infrared spectroscopy, IR radiation is passed through a sample. Some of the infrared radiation is absorbed by the sample molecules at a characteristic energy (frequency/wavelength) which leads to increasing the amplitude of molecular vibrations, and therefore providing molecular information [169]. Some of the radiated IR is passed through (transmitted). The resulting spectrum represents the molecular absorption and transmission, creating a molecular fingerprint of the sample and therefore allowing the identification of the molecules present in the sample (qualitative analysis). Also the amount of energy absorbed per unit volume depends on the

concentration, i.e., the IR signal intensities reflect how much of the sample is present (quantitative analysis).

2.6.1.2. FTIR Spectroscopy

FTIR technique was developed with the goal of overcoming the limitations encountered with conventional IR instruments, such as slow scanning process. Nowadays all IR instruments are of the Fourier Transform Interferometer design. This spectrometer is capable of collecting high resolution spectral data over several wavelengths simultaneously. FTIR is currently used to obtain an infrared spectrum of absorption or emission of a solid, liquid or gaseous samples [170-171].

The development of FTIR technique started in the late 1960s by analytical chemists borrowing from early work of physicists. This technique takes advantage of a very simple optical device called an interferometer. The interferometer produces a unique type of signal which has all of the infrared frequencies “encoded” into it. The signal can be measured very quickly, usually on the order of one second or so. Thus, the time required to fully characterize a sample is reduced to a matter of a few seconds rather than several minutes [170].

2.6.1.3. FTIR Spectroscopic Measurements

Diffuse reflectance FTIR-spectra were recorded for our research with Thermo Scientific Nicolet 6700 spectrometer equipped with a cricket diffuse reflectance accessory from Harrick

scientific Products, using an MCT detector. The spectra were recorded in the 500 – 4000 cm^{-1} range. Typically 32 scans were acquired per spectrum at resolution 4 cm^{-1}. For all the FTIR measurements, the unmodified FTO glass was used as reference.

FTIR measurements were conducted at different stages of the preparations of the ligand-modified electrodes, to investigate the physisorption and chemisorption of desferal ligands onto the surface of TiO_2 electrodes, study the effect of Fe^{3+} chelation on the FTIR spectra of the free ligand, and also to confirm the binding of carboxyalkyl-phosphonic acids to the surface of TiO_2 supports. Four sets of experiments were carried out, starting from the FTIR measurements of the bare TiO_2 electrodes in each set. The first set of experiments proceeded by modifying the surface of TiO_2 with desferal ligand physisorbed onto it. The IR spectra of the modified electrode was then recorded following by immersing the modified electrode in a 1.000×10^{-4} M aqueous solution of Fe(III) to be analyzed for FTIR measurements. The second, third, and forth sets of experiments were conducted starting from recording the FTIR spectra of the bare TiO_2 electrodes, proceeding with modifying the electrodes with the 3-C, 6-C, and 11-C PA molecules, respectively, as explained in section 2.5.2.2.1. The IR spectra of the modified samples were also recorded and the PA-modified samples were used for immobilization of desferal ligand onto the surface of TiO_2 electrodes (as explained in section 2.5.2.2.2.). The desferal immobilized-PA-modified TiO_2 substrates were also analyzed for the FTIR measurements before and after immersing them in a 1.000×10^{-4} M aqueous solution of Fe(III).

2.6.2. ^{31}Phosphorus (^{31}P) NMR Spectroscopy

2.6.2.1. Principles of ^{31}P NMR Spectroscopy

^{31}P NMR spectroscopy is an analytical technique which can be carried out either in solution-phase or in solid-state phase. Solution ^{31}P NMR is a very routine technique, due to the fact that ^{31}P has an isotopic abundance of 100% and a relatively high magnetic ratio. ^{31}P is a medium sensitivity nucleus that has a spin of 1/2, making the spectra relatively easy to interpret [172]. ^{31}P-NMR spectroscopy is useful to assay purity and to assign structures of phosphorus-containing compounds because these signals are well resolved and often occur at characteristic frequencies. The ordinary range of chemical shifts for ^{31}P-NMR is from -250 to 250 ppm, which is much wider than that of ^{1}H NMR [173].

2.6.2.2. ^{31}P Magic Angle Spinning (MAS) NMR Spectroscopy

Solution-phase NMR spectra consist of a series of very sharp transitions due to averaging of anisotropic NMR interactions by rapid random tumbling. Solid-state NMR spectra are very broad because of anisotropic or orientation-dependent interactions in the spectrum. High-resolution NMR spectra are capable of providing the same type of information on chemistry, structure and dynamics that is available from corresponding solution NMR spectra, but a number of special techniques/equipment are needed, including magic-angle spinning [174].

In MAS NMR technique, dipolar interactions (nuclear dipole-dipole interactions between magnetic moments of nuclei, D (θ) is directly proportional to "3 $\cos^2\theta$-1", (D (θ) $\propto$ 3 $\cos^2\theta$-1). By

spinning the sample (usually at a frequency of 1 to 100 kHz) at the magic angle $\theta_m \approx 54.74°$ with respect to the direction of the magnetic field, where $\cos^2\theta_m=1/3$, these interactions are averaged to zero and normally broad lines become narrower. This results in increasing the resolution and therefore better identification and analysis of the spectrum [175].

2.6.2.3. ^{31}P NMR Spectroscopic Measurements

The solution phase ^{31}P NMR spectroscopic measurements were recorded at 7 T on a 1 D Bruker Avance 300 spectrometer. The spectrometer was operating at 121.496 MHz, using a 5 mm Auto Tune & Match (ATM) probe. Typically 32 scans were acquired per spectrum with 64.000 data points and a spinning rate of 2 Hz (line broadening). The phosphonic acids were externally referenced against phosphoric acid ($\delta = 0$ ppm).

The solid-state ^{31}P MAS NMR (SSNMR) spectra were collected on an Agilent DD2 700 spectrometer equipped with 1.6 mm double resonance T3-HX MAS Solids Balun probe. Each sample was ground into a fine powder using a mortar and pestle. The samples were packed into 1.6 mm O.D. Zirconia rotors for 1D ^{31}P spectra acquisition. The spectrometer was operating at 283.365 MHz and spectra were collected with 512 scans, flip angle of 45 degree, relaxation delay of 10 seconds, and spinning rate of 20 kHz. The solid state spectra were processed with a 200 Hz line broadening function. ^{31}P chemical shifts of the PAs-modified TiO_2 electrodes were externally referenced to the line at -148.89 ppm from $NaPF_6$ sample.

2.6.3. Scanning Electron Microscopy-Energy Dispersive X-ray Spectroscopy

2.6.3.1. Principles of SEM and EDX

Scanning Electron Microscopy (SEM) is a type of electron microscopy technique that uses focused beam of electrons for producing high-resolution images of samples.

In this technique, a beam of incident electrons is generated in an electron column above the sample chamber. The electrons are produced by a thermal emission source, such as a heated tungsten filament, or by a field emission cathode. The energy of the incident electrons can be as low as 100 eV or as high as 30 keV depending on the evaluation objectives. The incident electrons then interact with atoms in the sample, producing various signals that contain information about the sample's surface topography and composition. The electron beam is generally scanned in a raster pattern over the surface, and the beam's position in combination with the detected signal produces an image. The most conventional detection mode in SEM is detection of secondary electrons emitted by atoms excited via the electron beam. By scanning the sample and collecting the secondary electrons that are emitted from very close to the specimen surface using a special detector, a high-resolution image displaying the topography of the surface is created. SEM can achieve resolutions better than 1 nanometer [176, 177].

Energy dispersive X-ray (EDX) spectroscopy is a powerful analytical technique used for elemental analysis or chemical characterization of a sample. Qualitative and quantitative analysis is possible using an energy dispersive X-ray spectrometer (EDS) with the SEM. Characteristic X-rays are emitted when the electron beam removes an inner shell electron from the sample its interacting with, causing a higher-energy-electron to fill the shell and release energy. These

characteristic X-rays are used for identification of the composition and estimation the abundance of elements in the sample [176].

2.6.3.2. SEM and EDX Analysis

The SEM images were acquired using a high resolution FEI Quanta 3D Dual-Beam Field Emission-Focused Ion Beam (FEG-FIB) microscope with attached EDAX X-ray detector. The modified and unmodified TiO_2 electrodes were gold sputter coated before imaging, and were imaged under high vacuum mode. The elemental composition of the functionalized TiO_2 substrates were analyzed by energy dispersive X-ray spectrometry (EDX = EDAX GENESIS).

2.6.4. Atomic Force Microscopy

2.6.4.1. Principles of AFM

Atomic force microscopy (AFM) is a type of scanning probe microscopy, which is arguably one of the most versatile and powerful microscopy techniques for studying a wide range of samples at the nanoscale [178]. The basic configuration of AFM consists of a cantilever-tip assembly, a scanner, a deflection detecting system, a control system that includes a feedback loop, and a sample holder. The technique works by scanning the tip line-by-line (in a raster manner) over the sample using a very sharp nanofabricated tip mounted at the end of a flexible cantilever (i.e., probe), providing surface features and other information [179]. The scanner controls the tip movement over nanometer scale using a feedback system to adjust the tip vertical

position. As the tip scans over the surface, the changes in topology of the sample surface influence the deflection of the cantilever. A laser beam is used to detect cantilever deflections towards or away from the surface. By reflecting an incident beam off the flat top of the cantilever, any cantilever deflection will cause slight changes in the direction of the reflected beam, which will be recorded by a position-sensitive four-quadrant photodiode detector (PSPD). A controller attached to a computer with display screen for adjusting parameters, viewing and analyzing images controls the electronics. The three common topographical modes are contact mode, tapping mode and non-contact modes. Other non-topographical modes of experiments are available which allows for measurement of mechanical, magnetic electrical and thermal properties of sample. Contact mode is highly suitable for imaging of flat and hard samples. However, since the tip is in contact with the sample, damage to soft samples due to strong lateral force can occur; Tapping mode is used for imaging of soft molecules, because of the smaller applied force. The advantage of tapping mode is that lateral force is eliminated leading to better lateral resolution [180].

2.6.4.2. AFM Analysis

The AFM images were obtained using a Dimension 3100 (Veeco Digital microscope by Bruker) equipped with a NanoScope IIIa controller. Tapping mode AFM images in air were obtained using a silicon cantilever-tip assembly with a resonance frequency of 200 - 350 kHz. Images were viewed and were subjected to first order flattening using V614r1 Nanoscope program.

3. Designing a Potentiometric Sensor Based on Glyoxal-bis(2-hydroxyanil) adsorbed onto Nanostructured Titanium Dioxide for the Analysis of Chromium(III) Ions in Solution

As mentioned in the experimental part (section 2.2), the UV-Vis spectroscopic titration analysis were conducted as a preliminary experiment, to study the complexation of the GBHA ligand with most of the first row transition metal ions, and also to probe its selectivity towards those ions. These studies could also help us decide if this ligand can be a good ionophore in the assembly of an ISE.

3.1. UV-Vis Titration Analysis

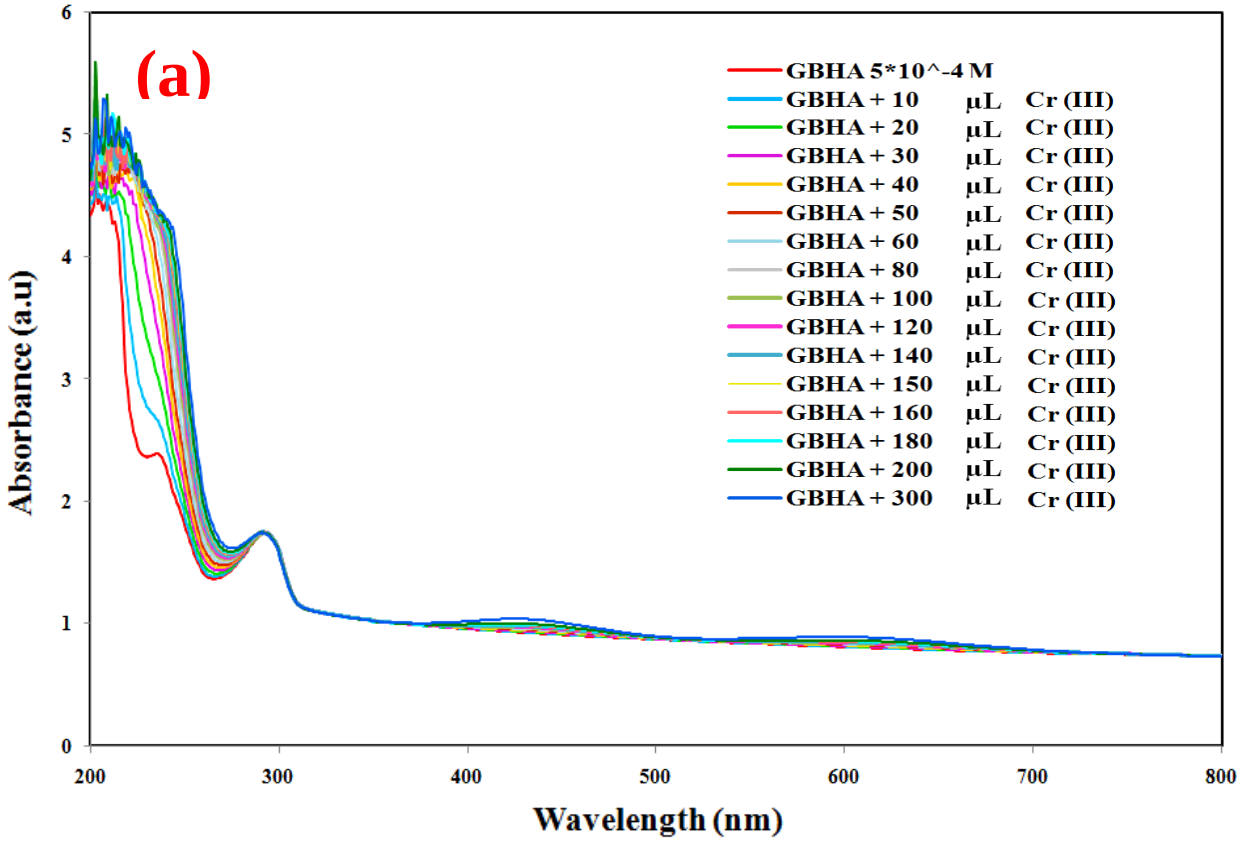

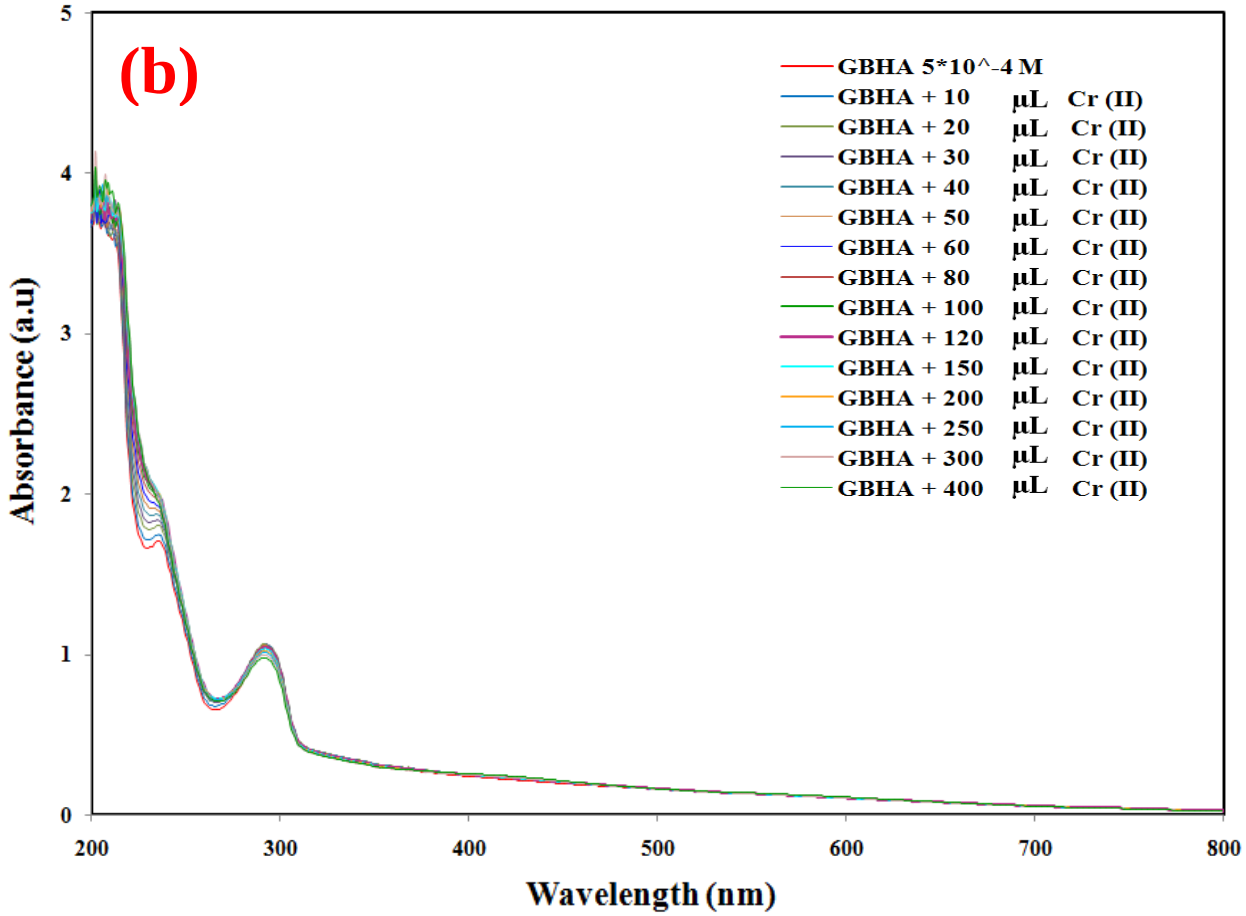
(b)
GBHA 5*10^-4 M
GBHA + 10 µL Cr (II)
GBHA + 20 µL Cr (II)
GBHA + 30 µL Cr (II)
GBHA + 40 µL Cr (II)
GBHA + 50 µL Cr (II)
GBHA + 60 µL Cr (II)
GBHA + 80 µL Cr (II)
GBHA + 100 µL Cr (II)
GBHA + 120 µL Cr (II)
GBHA + 150 µL Cr (II)
GBHA + 200 µL Cr (II)
GBHA + 250 µL Cr (II)
GBHA + 300 µL Cr (II)
GBHA + 400 µL Cr (II)
Absorbance (a.u)
Wavelength (nm)
0
1
2
3
4
5
200
300
400
500
600
700
800

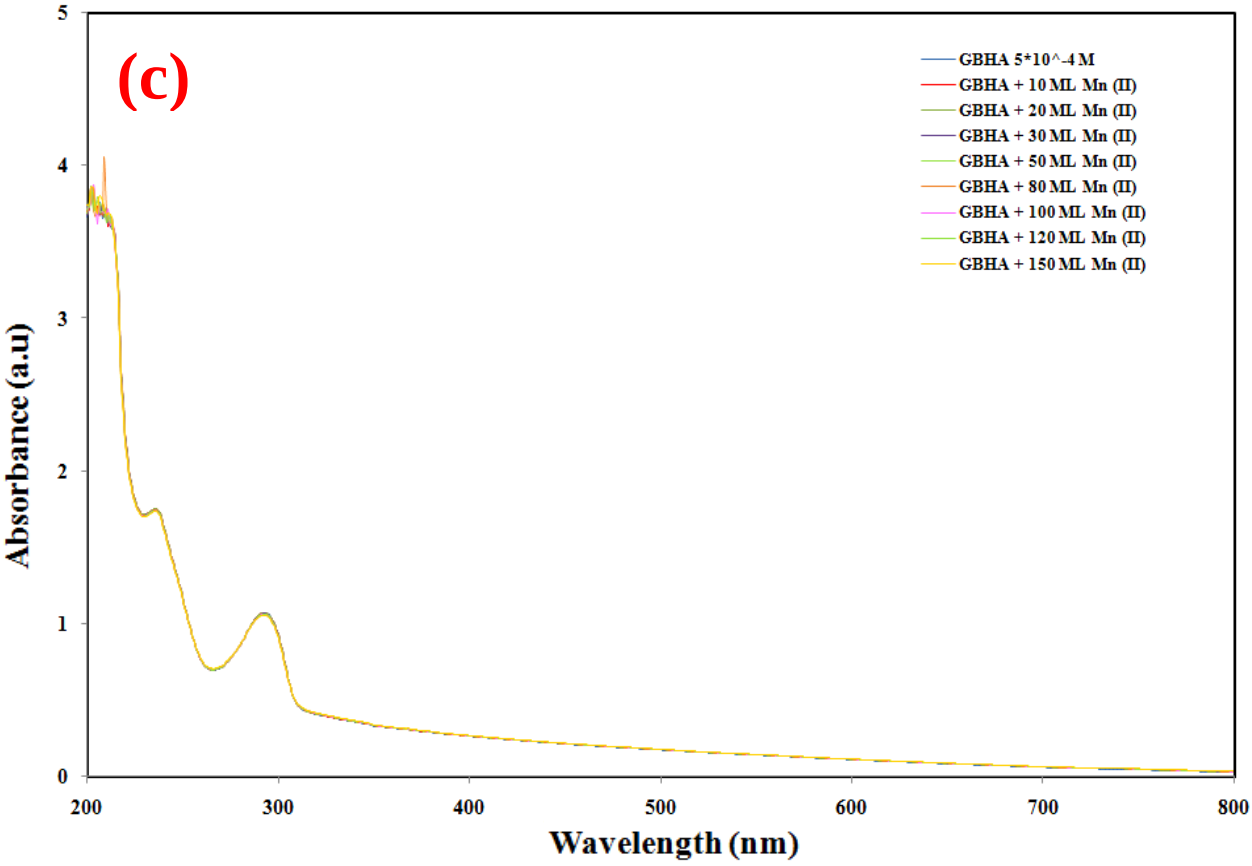
(c)
GBHA 5*10^-4 M
GBHA + 10 ML Mn (II)
GBHA + 20 ML Mn (II)
GBHA + 30 ML Mn (II)
GBHA + 50 ML Mn (II)
GBHA + 80 ML Mn (II)
GBHA + 100 ML Mn (II)
GBHA + 120 ML Mn (II)
GBHA + 150 ML Mn (II)
Absorbance (a.u)
Wavelength (nm)
0
1
2
3
4
5
200
300
400
500
600
700
800

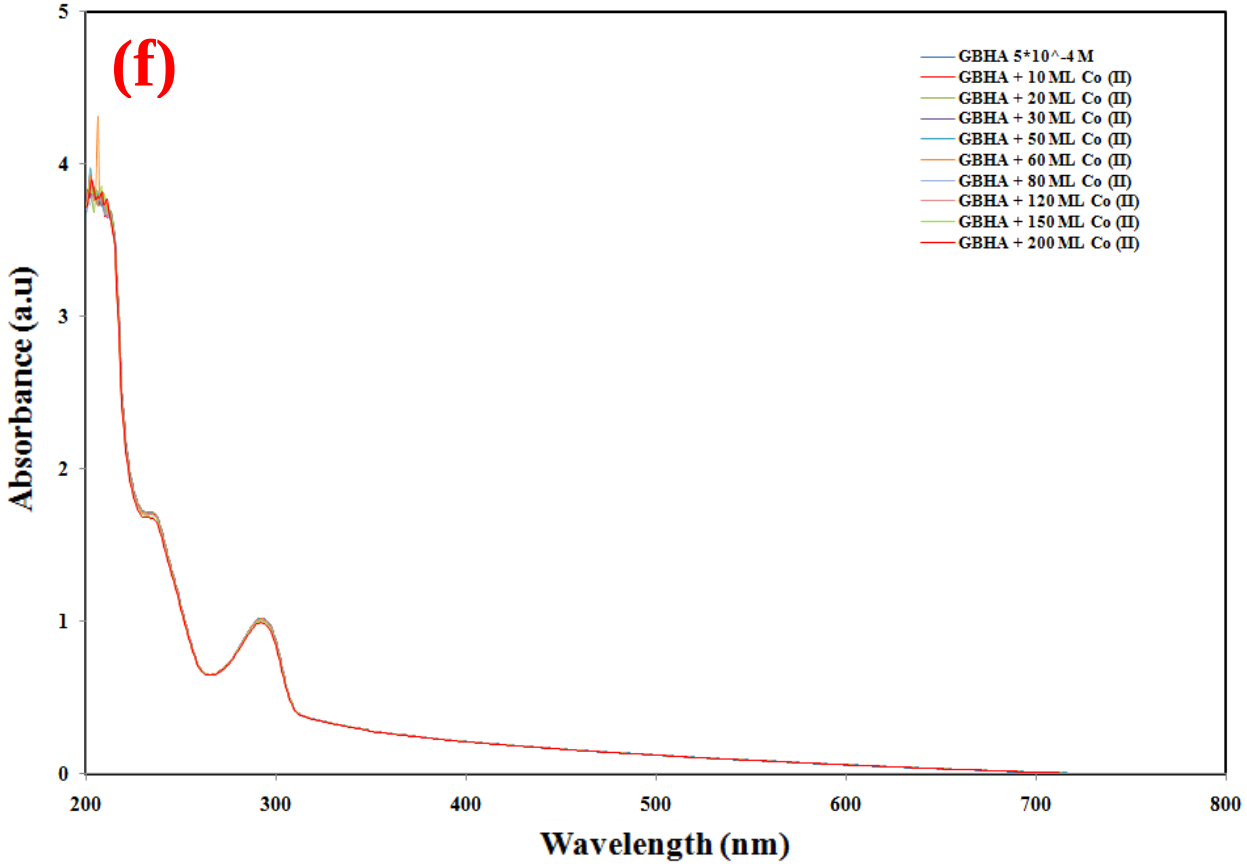
(f)
GBHA 5*10^-4 M
GBHA + 10 ML Co (II)
GBHA + 20 ML Co (II)
GBHA + 30 ML Co (II)
GBHA + 50 ML Co (II)
GBHA + 60 ML Co (II)
GBHA + 80 ML Co (II)
GBHA + 120 ML Co (II)
GBHA + 150 ML Co (II)
GBHA + 200 ML Co (II)
Absorbance (a.u)
Wavelength (nm)
0
1
2
3
4
5
200
300
400
500
600
700
800

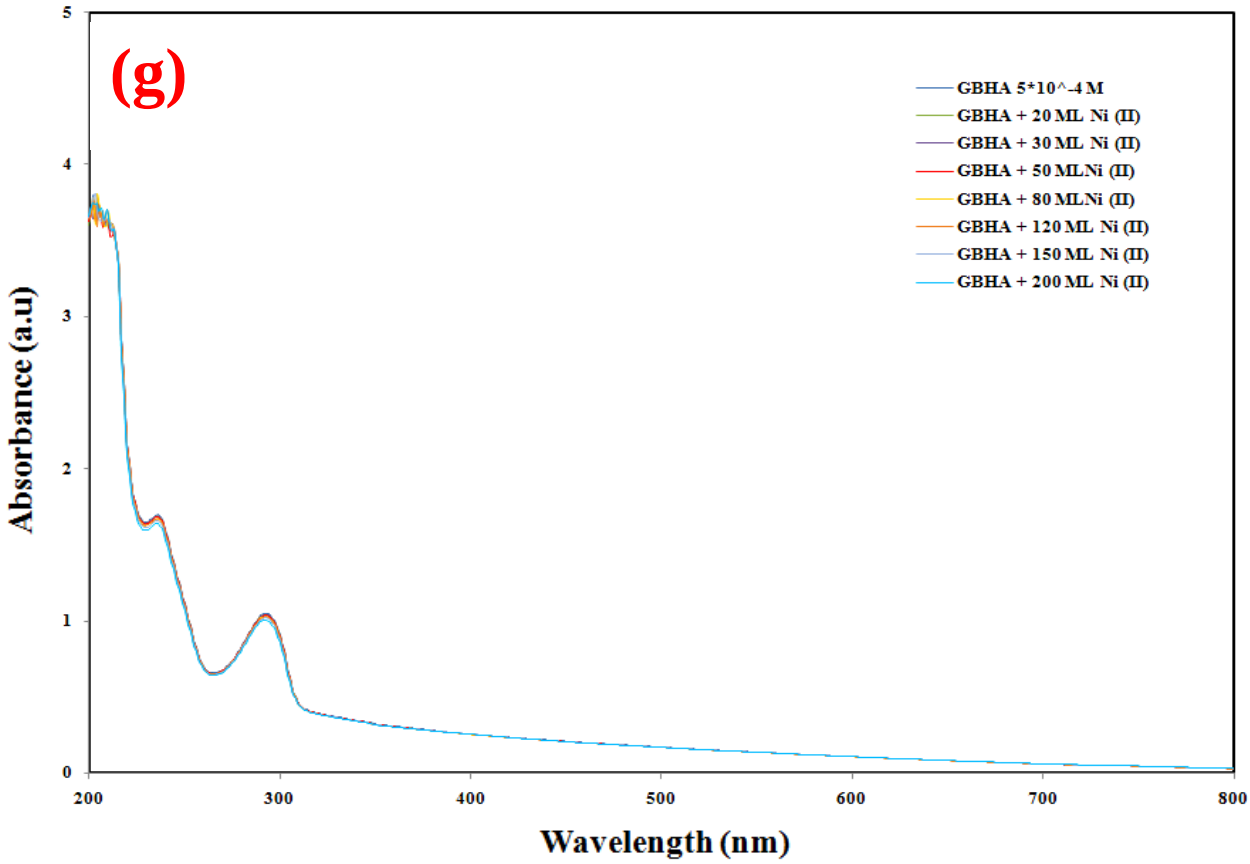
(g)
GBHA 5*10^-4 M
GBHA + 20 ML Ni (II)
GBHA + 30 ML Ni (II)
GBHA + 50 MLNi (II)
GBHA + 80 MLNi (II)
GBHA + 120 ML Ni (II)
GBHA + 150 ML Ni (II)
GBHA + 200 ML Ni (II)
Absorbance (a.u)
Wavelength (nm)
0
1
2
3
4
5
200
300
400
500
600
700
800

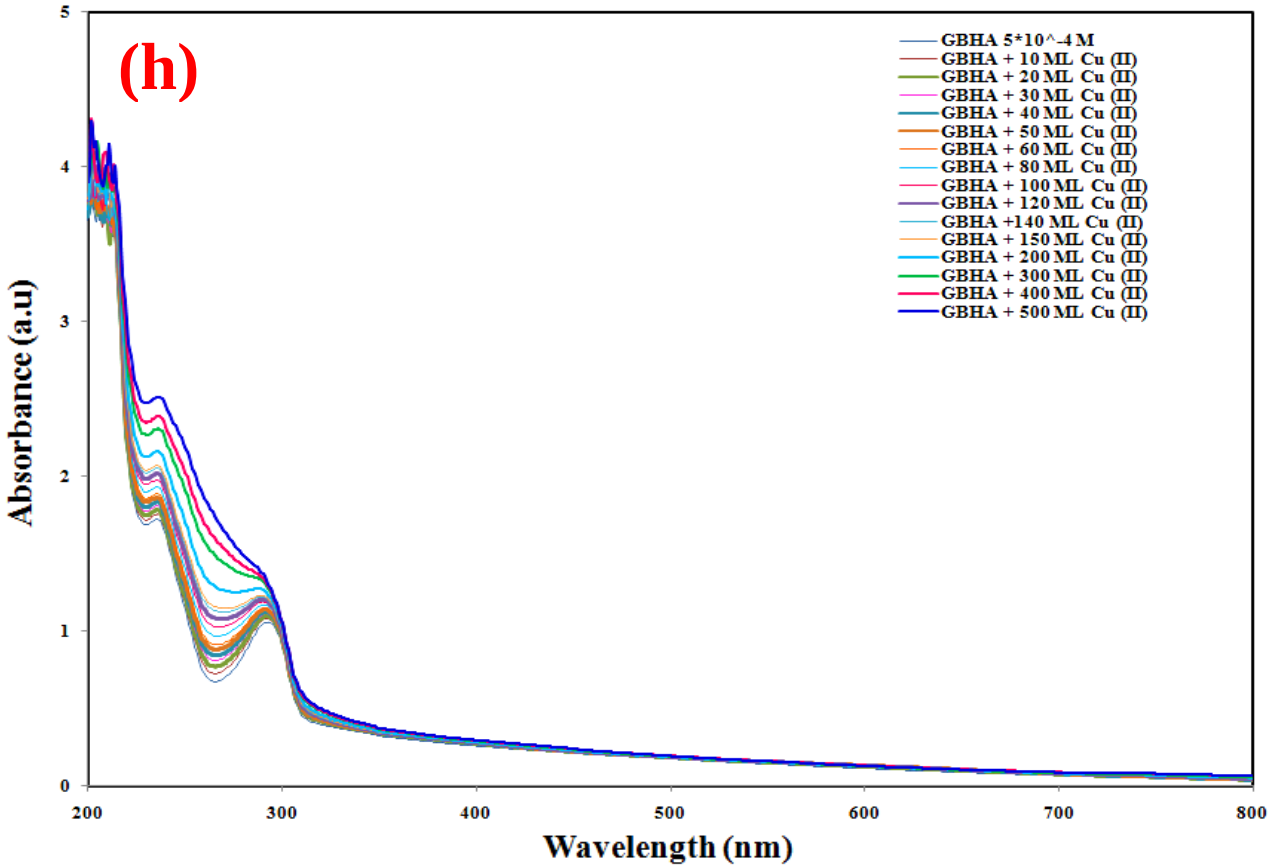

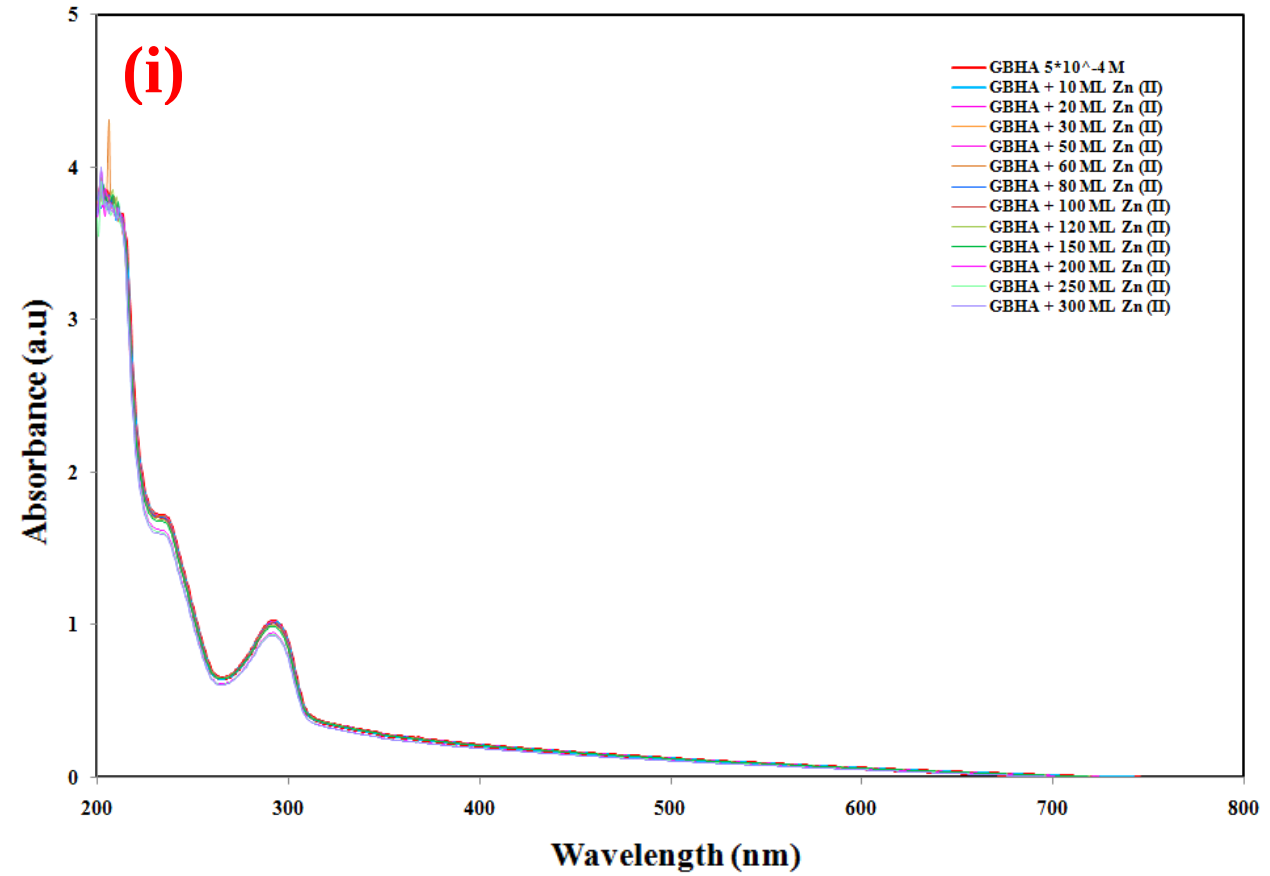

Figure 3.1 (a-i). UV-Vis titration spectra of 3.00 mL of a 5.000 $\times 10^{-4}$ M GBHA in ethanol, titrated with microliters amounts of 1.000 $\times$ 10^{-2} M aqueous solution of first row transition metal ions at 25ºC. The transition metal ion used is stated in each graph together with the volume employed.

Figures 3.1 (a-i) are characteristic UV-Vis titration spectra of 3.00 mL of a 5.000×10^{-4} M GBHA in ethanol, titrated with microliters amounts of 1.000×10^{-2} M aqueous solution of the first row transition metal ions Cr^{3+}, Cr^{2+}, Mn^{2+}, Fe^{2+}, Fe^{3+}, Co^{2+}, Ni^{2+}, Cu^{2+}, and Zn^{2+} at 25.0 ± 0.1ºC (see figure 3.1 for volumes used).

The UV-Vis spectrum of the free GBHA shows two main peaks around 235 nm and 290 nm, which can be assigned to the n to pi star ($n \rightarrow \pi^*$), and pi to pi star ($\pi \rightarrow \pi^*$) transitions, respectively. According to figure 3.1 (a), upon coordination of Cr(III) with GBHA, the peak associated with $n \rightarrow \pi^*$ transition is red shifted, which suggests that the lone pairs on the nitrogen as well as oxygen atoms of the GBHA ligand are participating in the coordination of this ligand with Cr(III). Also the peaks observed around 290 nm after the addition of Cr(III), could be related to the ligand-to-metal charge transfer (LMCT). Also the two peaks appeared around 420 and 580 nm were related to d–d transition in the Cr^{3+}. Based on these results, it can be concluded that coordination with chromium(III) caused the largest red shift to the wavelength of the GBHA ligand, which refers to the strong complexation of this ligand with the these ions.

The binding strength order of the transition metal ions studied besides Cr(III) is very similar and indicative of very weak or no complexation between the tested ions and the GBHA ligand. As seen in figures 3.1 (a-i), Cu(II) is found to induce the most change besides Cr(III). This makes GBHA a very good candidate to be used as the ionophore in designing Cr(III)-selective potentiometric sensors, due to its good selectivity towards Cr(III) ions in comparison with all the other first row transition metal ions. Possible interference from Cu(II) and other metal ions were tested and the sensor's response will be discussed later in this chapter.

Therefore, in this work, we took advantage of the high sensitivity of the GBHA ligand for binding with Cr(III) ions to fabricate an Cr(III)-selective potentiometric sensor based on nanostructured-TiO_2 electrodes.

In order to see the UV-Vis spectrum of free Cr(III) in the absence of the GBHA ligand, the UV-Vis titrations of 3.00 mL of ethanol with microliters amounts of a 1.000×10^{-2} M aqueous solution of Cr(III) was performed (Figure 3.2). According to the figure 3.2, the two peaks attributed to d-d transition in the free $Cr(H_2O)_6$ are still present, while there is no red-shifts to the spectrum of ethanol; therefore we concluded that the red-shifts caused by the microliters titrations of the free ligand with Cr(III) ions, are in fact due to the coordination of Cr(III) with the GBHA ligand.

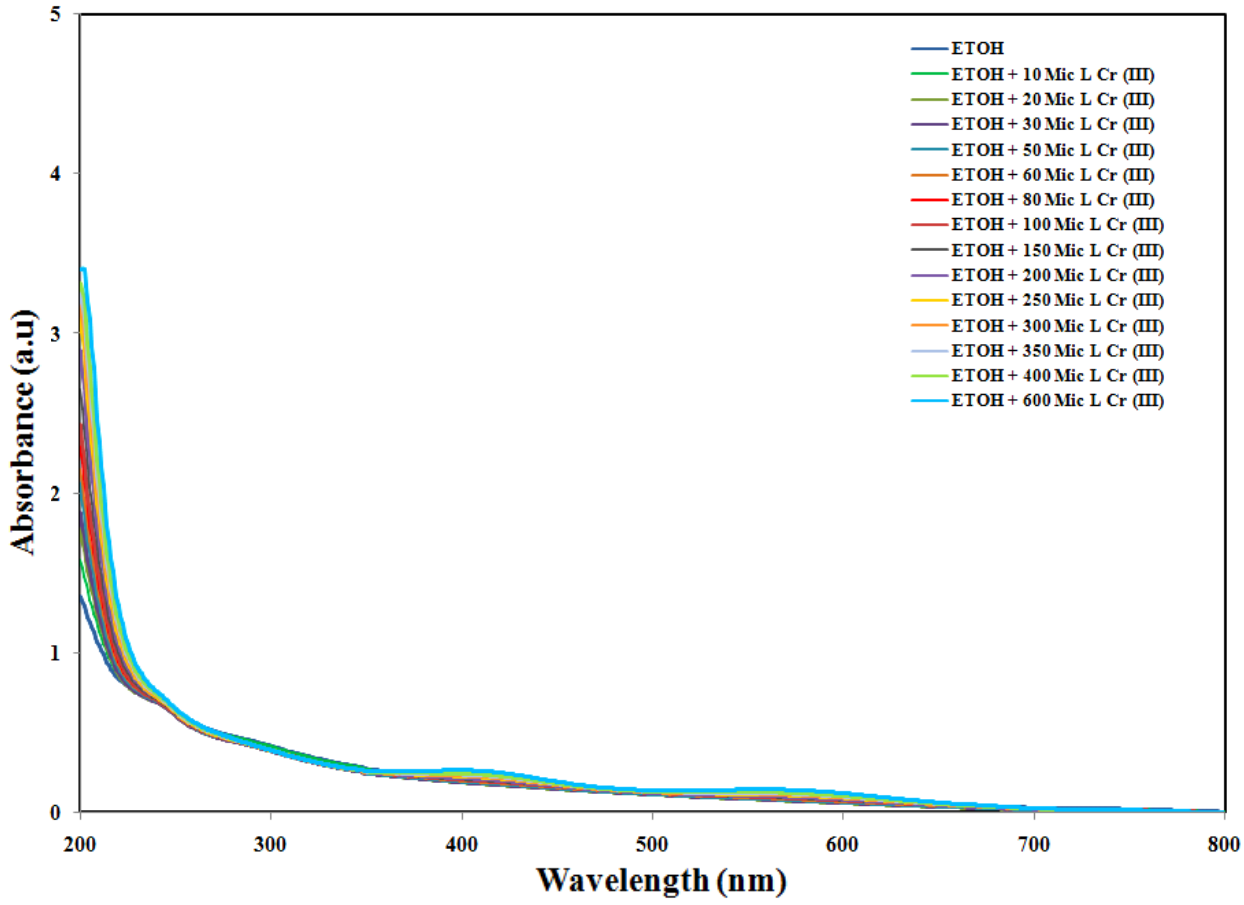

Figure 3.2. UV-Vis titrations of 3.00 mL of ethanol with microliters amounts of a 1.000×10^{-2} M aqueous solution of Cr(III) at 25ºC.

3.2. EMF Measurements

The emf response of the Cr(III)-selective sensor fabricated based on GBHA physisorbed onto the surface of TiO_2 electrodes for varying concentration of Cr^{3+} ions was recorded. Three potentiometric measurements were performed at each concentration of Cr(III), and the calibration plot showing all measurements is seen in figure 3.3. For this purpose, the Cr^{3+}concentration was varied from 1.000×10^{-8} o 1.000×10^{-1} M. The resulting calibration plot indicated a linear range from 1.000 (± 0.040) $\times 10^{-7}$ to 1.000 (± 0.020) $\times 10^{-2}$ M. The absolute value for the slope of the calibration plot was 19.45 ± 0.44 mV per decade of Cr^{3+} concentration. It should be noted that due to the fact that the systematic error of each concentration in all 3 repetitive measurements is equal, the same symbols are used for all the calibration plots represented in this thesis.

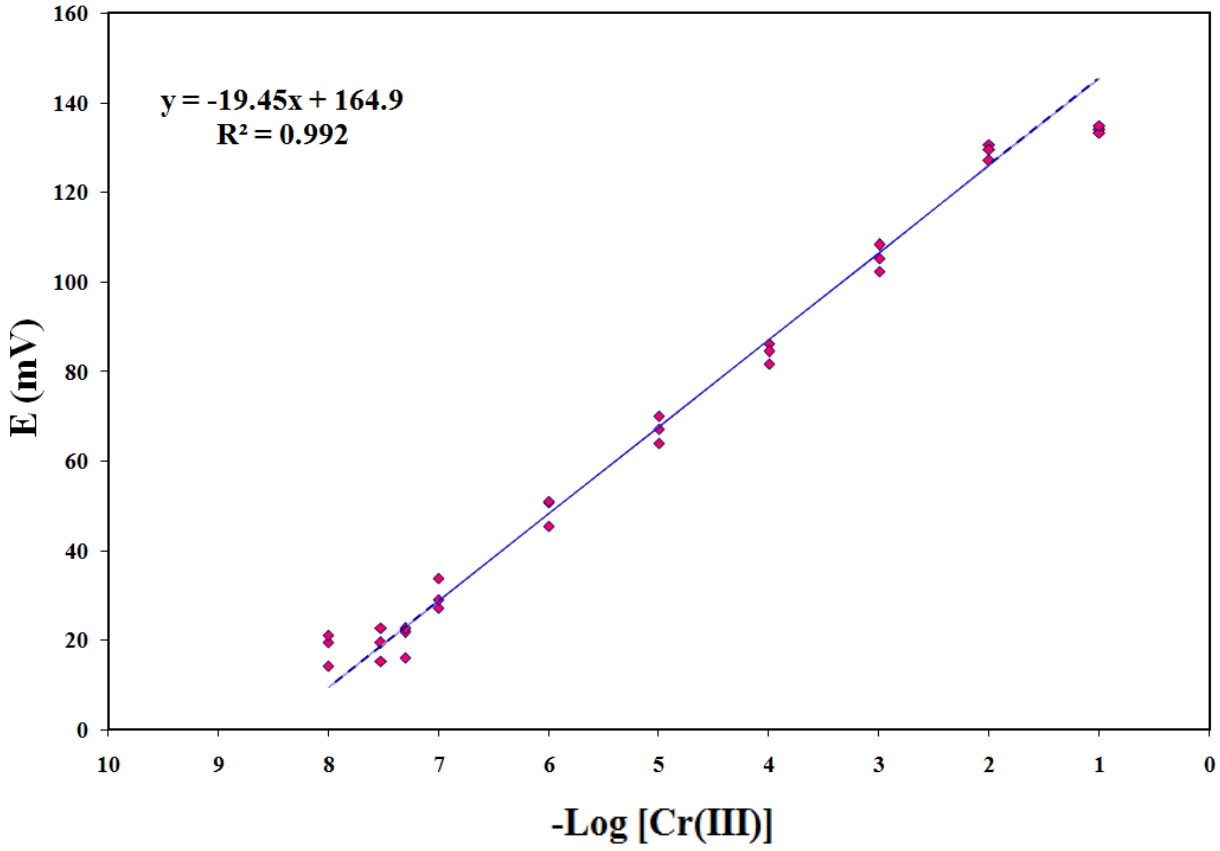

Figure 3.3. Calibration plot for chromium(III) ion selective electrode based on GBHA modified TiO_2 electrodes.

3.2.1. Error Analysis

In this section we will analyze the errors on the chromium concentrations and the measured potential values as obtained using the sensors. The errors were calculated for the chromium concentration as well as potential values; these error analyses are of great significance as they play a key role in defining the performance of the sensors as well as the accuracy of the potentiometric measurements. The error calculations for the concentration and potential values will be described.

3.2.1.1. Calculation of Error in the Concentration of Chromium

In order to calculate the errors in the chromium concentration values, the following method was applied:

$$M = \frac{m}{V} \qquad => \qquad \frac{\Delta M}{M} = \frac{\Delta m}{m} + \frac{\Delta V}{V}$$

in which:

M = Concentration of Cr(III) (mol L^{-1})

ΔM = Error in M (mol L^{-1})

m = moles of Cr(III)

Δm = Error in m

V = Volume of volumetric flask (mL)

ΔV = Error in V (mL)

The stock solution of chromium(III) was prepared by making a 1.0000×10^{-1} M aqueous solution of chromium(III) chloride hexahydrate ($CrCl_3.6\ H_2O$) (M_W =266.4500 ± 0.0001 g/mol) in a 100.0 ± 0.1 mL volumetric flask. So, the error in the concentration of chromium solution (ΔM_1) can be calculated as follows:

$$\Delta m = 0.0001\ g \times \frac{1\ mol}{266.4500\ g} = 3.7530 \times 10^{-7} mol$$

$$\frac{\Delta M_1}{M_1} = \frac{3.75 \times 10^{-7} mol}{1\ mol} + \frac{0.1\ mL}{100\ mL} \quad => \quad \frac{\Delta M_1}{M_1} = 0.0010 \quad => \quad \Delta M_1 = (0.0010 \times 0.1) = 1 \times 10^{-4}\ mol\ L^{-1}$$

$$M_1 = \left[Cr^{3+}\right] = 0.1000 \pm (1 \times 10^{-4})\ mol\ L^{-1}$$

$$\Delta log_b\ x \cong \frac{\Delta x}{x \times ln\ b} \quad => \quad \Delta log_{10}\ M_1 \cong \frac{\Delta M_1}{M_1 \times ln\ 10} \cong \frac{1 \times 10^{-4}}{0.1 \times 2.3} \cong 4.3478 \times 10^{-4}$$

$$\boldsymbol{X - axis = -log\ M_1 = (1.0000 \pm (4 \times 10^{-4}))}\ \textbf{\textit{(for } M_1 = 1.0000 \times 10^{-1}\ M\textit{)}}$$

The next solution of chromium (M_2) was a 1.000×10^{-2} M $CrCl_3.6\ H_2O$ aqueous solution that was prepared using a 100.0 L ± 0.1 mL volumetric flask by diluting the 1.0000×10^{-1} M stock solution of chromium, and adding water up to the mark. The error for this solution was calculated as follows:

$$M_1V_1 = M_2V_2 \ => \ V_1 = \frac{0.01000 \times 100.00}{0.10000} = 10.00\ mL$$

$$\frac{\Delta M_2}{M_2} = \frac{\Delta M_1}{M_1} + \frac{\Delta V_1}{V_1} + \frac{\Delta V_2}{V_2} \ => \ \Delta M_2 = \left(\frac{1 \times 10^{-4}\ \text{M}}{1.0000 \times 10^{-1}\ \text{M}} + \frac{0.01}{10.00} + \frac{0.1\ mL}{100.0\ mL}\right) \times 1.000 \times 10^{-2}\ mol\ \text{L}^{-1} \quad =>$$

$$\Delta M_2 = 3 \times 10^{-5}\ \text{M}$$

$$\text{M}_2 = 0.01000 \pm (3 \times 10^{-5})\ \text{mol}\ L^{-1} \quad =>$$

$$\Delta log_{10} M \cong \frac{\Delta M_2}{M_2 \times ln\,10} \cong \frac{3 \times 10^{-5}}{0.01 \times 2.3} \cong 1.3043 \times 10^{-3}$$

$$\boldsymbol{X - axis = -log\, M_2 = (2.000 \pm (1 \times 10^{-3}))} \quad \textit{(for } \boldsymbol{M_2 = 1.000 \times 10^{-2}}\textit{ M)}$$

Consequently, all the other solutions of lower concentrations of chromium were made by serial dilutions of the 1.000 × 10^{-2} M solutions with DI water. The errors for these solutions having the concentrations of 1.000 × 10^{-3} M to 1.000 × 10^{-8} M (M_3 to M_{10}) were calculated using the same method as shown above. Table 3.1 summarizes the calculated error in the concentration of chromium(III) for the calibration plot shown in figure 3.3.

$[Cr^{3+}]$ (M)		**-Log $[Cr^{3+}]$ (X-axis)**	**Error in the values of the X-axis**
M_{10}	1.000 × 10^{-8}	8.000	0.008
M_9	3.000 × 10^{-8}	7.520	0.007
M_8	5.000 × 10^{-8}	7.300	0.006
M_7	1.000 × 10^{-7}	7.000	0.006
M_6	1.000 × 10^{-6}	6.000	0.005
M_5	1.000 × 10^{-5}	5.000	0.004
M_4	1.000 × 10^{-4}	4.000	0.003
M_3	1.000 × 10^{-3}	3.000	0.002
M_2	1.000 × 10^{-2}	2.000	0.001
M_1	1.0000 × 10^{-1}	1.0000	0.0004

Table 3.1. Calculated errors in the concentration of chromium(III) for the calibration plot shown in figure 3.3.

3.2.1.2. Calculation of Error in the Potential Values

In order to calculate the errors in the potential values for the calibration plot as shown in figure 3.3, the standard deviations of the mean of three repetitive potentiometric measurements at each Cr(III) concentration were calculated (table 3.2) based on the following equations:

$$S = \sqrt{\frac{\sum_{i=1}^{N}(X_i - \bar{X})}{N-1}}$$ where S is the sample standard deviation

$$S_{mean} = \frac{1}{\sqrt{N}} S$$ where S_{mean} is the standard deviation of the mean

$[Cr^{3+}]$	Potential (E (mV)) (Y-axis)				S_{sample} in E (mV)	S_{mean} in E (mV)
	Measurement 1	Measurement 2	Measurement 3	Average		
M_{10}	19.42	14.18	21.00	18.20	3.57	2.06
M_9	19.34	15.32	22.75	19.14	3.72	2.15
M_8	21.72	16.14	22.53	20.13	3.48	2.01
M_7	27.17	33.83	29.00	30.00	3.44	1.99
M_6	50.65	45.45	50.92	49.00	3.08	1.78
M_5	69.97	67.11	63.82	66.97	3.08	1.78
M_4	81.54	86.05	84.41	84.00	2.28	1.32
M_3	105.13	108.22	102.36	105.24	2.93	1.69
M_2	127.03	130.50	129.49	129.00	1.78	1.03
M_1	133.99	133.30	134.80	134.03	0.75	0.43

Table 3.2. Calculated errors in the measured potential values for the calibration plot shown in figure 3.3.

3.2.1.3. Calculation of Uncertainty in the Slope of the Calibration Plot

For the analysis of uncertainties in the slope of the calibration plot as shown in figure 3.3, we used the "LINEST" complete linear least squares curve fitting routine. This approach takes into account all the measured values (here the potentiometric measurements are recorded in 3 measurements sets (noted as measurements 1-3 and shown in table 3.2)), and uses them on a single plot to compute a single slope, intercept, and unbiased uncertainties.

Measurements (-Log [Cr^{3+}])	**Potential (E (mV))**
Measurement 1	
7	27.17
6	50.65
5	69.97
4	81.54
3	105.13
2	127.03
Measurement 2	
7	33.83
6	45.45
5	67.11
4	86.05
3	108.22
2	130.5
Measurement 3	
7	29
6	50.92
5	63.82
4	84.41
3	102.36
2	129.49

LINEST output			
slope	-19.4502	164.8953	**Intercept**
Uncertainty in Slope	0.442901	2.131762	**Uncertainty in Intercept**
R^2	0.991772	3.209124	**S(y)**
F	1928.564	16	**Degree of Freedom**
Regression SS	19861.27	164.7756	**Residual SS**

Table 3.3. The output of the LINEST function using the potential data recorded in 3 measurements for the linear concentration range of the calibration plot shown in figure 3.3.

The rationale for this is that all three potential data at each concentration are equally reliable, and it is their scatter that determines the value and uncertainty in the slope and intercept.

Table 3.3 shows the potential values used, as well as the output of the LINEST function for the linear concentration range of the calibration plot (1.000 (± 0.04) $\times 10^{-7}$ M to 1.000 (± 0.02) $\times 10^{-2}$ M, as shown in figure 3.3.) As explain previously in section1.12.1, the LOD is defined as the concentration of chromium ions obtained when the linear region of the calibration plot was extrapolated to the base line. For our sensor this value was measured to be 3.000 (± 1.600) $\times 10^{-8}$ M (as shown below in figure 3.4).

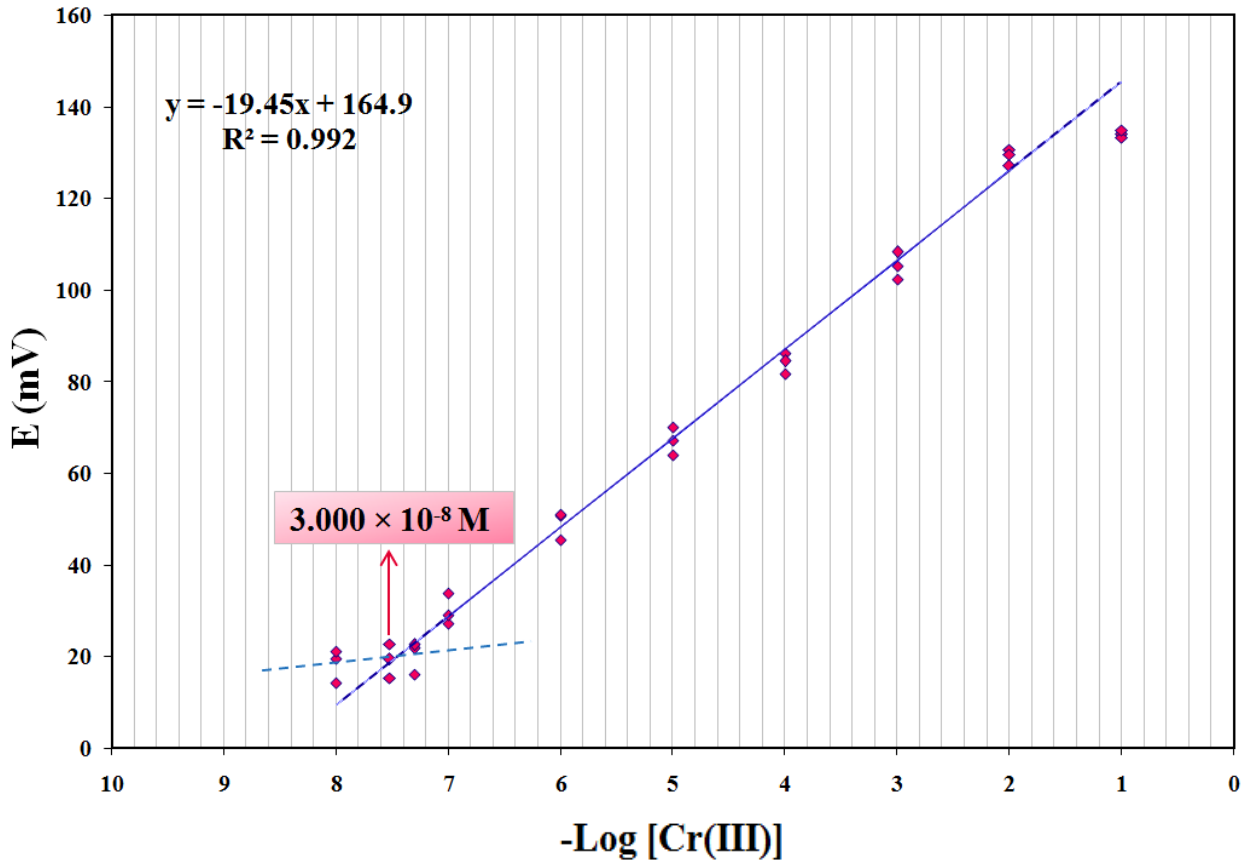

Figure 3.4. Calculations of LOD based on the extrapolation of the linear region of the calibration plot to the base line, for the calibration plot shown in figure 3.3.

In the absence of the ion exchanger the electrode may function due to impurities. For this reason, we recorded the potentials of varying concentrations of Cr(III) test solutions using a nanostructured TiO_2 electrode with no ionophore, as the working electrode. The potentiometric response of the electrode is then plotted as shown in figure 3.5. As this graph reveals, there is no emf response to the concentration of Cr(III) ions for an electrode without the GBHA ionophore.

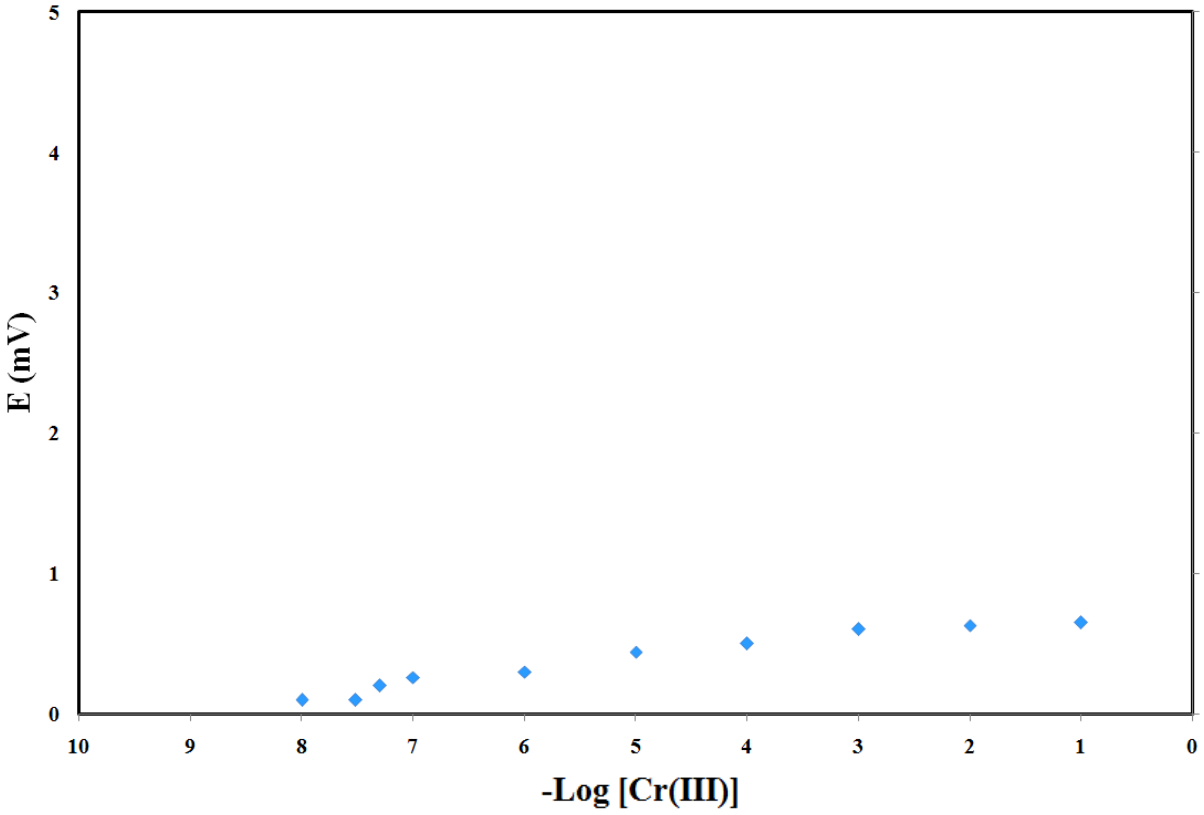

Figure 3.5. The potentiometric response to Cr(III) ions for a TiO_2 electrode without the GBHA ionophore.

3.3. Reproducibility

As the reproducibility of an ion selective electrode is important for the observation of a relatively similar response to another electrode prepared under similar set of conditions, six independent sensor electrodes were fabricated and functionalised with GBHA and tested for potentiometric measurements in a 1.000×10^{-4} M aqueous solution of Cr(III).

Figure 3.6 illustrates the histogram of potentiometric measurements correlated with each of the fabricated electrodes tested in a 1.000×10^{-4} M aqueous solution of Cr(III). The sensor electrode revealed good reproducibility with less than 1% relative standard deviation.

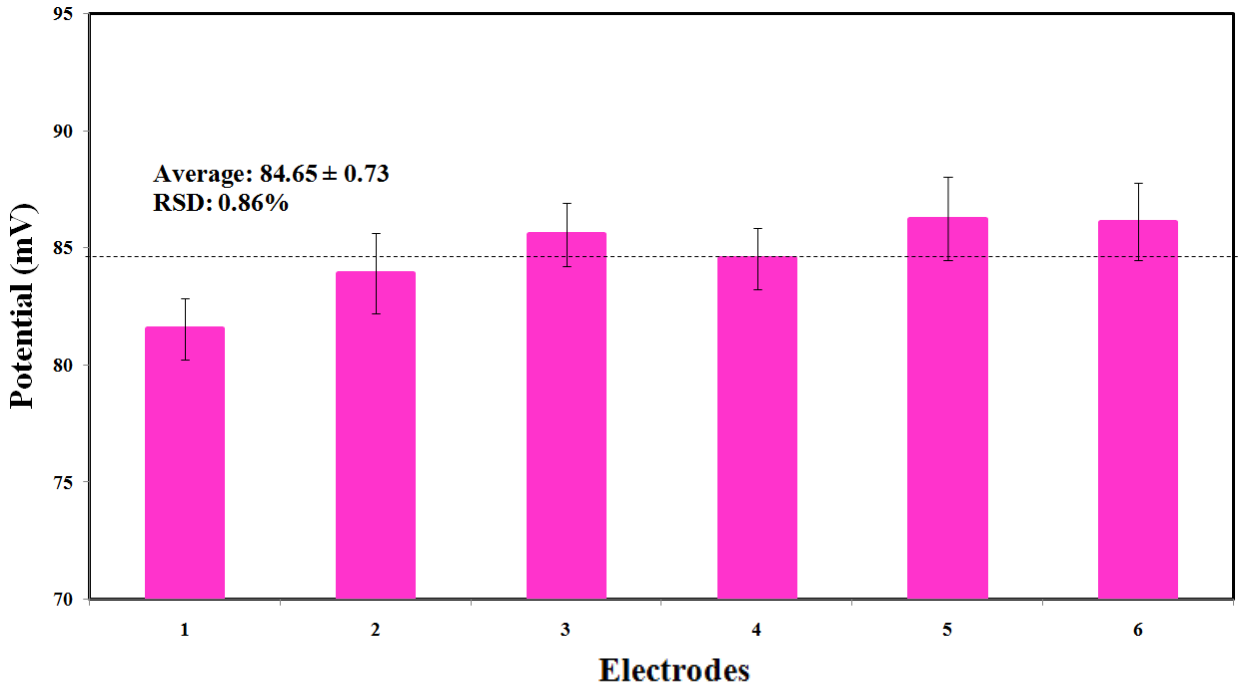

Figure 3.6. Histogram of potentiometric measurements correlated with the fabricated electrodes tested in a 1.000×10^{-4} M aqueous solution of Cr(III).

3.4. Potentiometric Selectivity

As mentioned in the introduction chapter, the selectivity of the ISEs is the back bone parameter for defining their behaviour in the presence of common interfering ions. The potential response of 16 various ISEs based on GBHA was investigated for some alkali, alkaline earth, heavy metals, and several transition metal ions (figure 3.7). Among these ions, Cr^{3+} with more sensitive response seems to be suitably determined with a nanostructured TiO_2 electrode modified with GBHA.

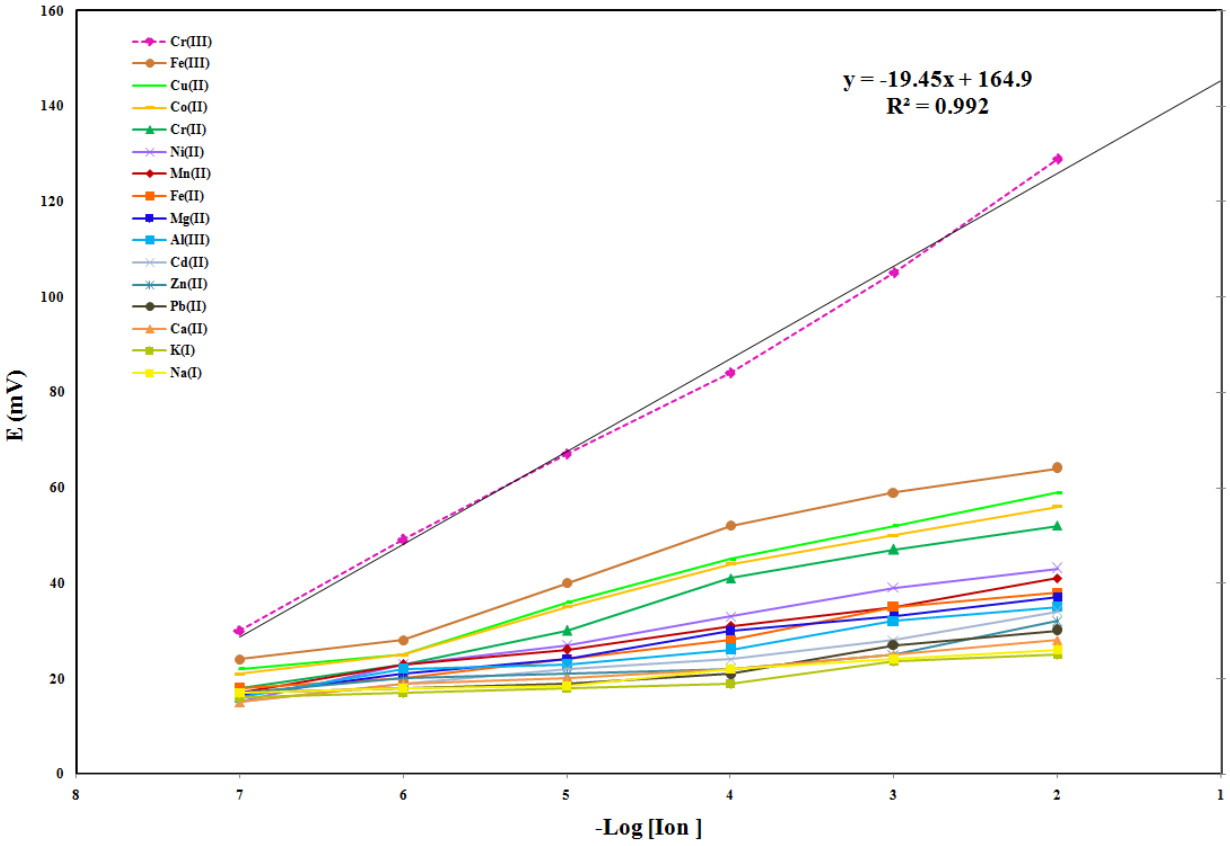

Figure 3.7. Potential response of ion-selective electrode based on GBHA for various metal ions.

Based on figure 3.7, it is clear that the resulting Cr^{3+} potential response showed a Nernstian behaviour in the concentration range of 1.000×10^{-7} to 1.000×10^{-2} M Cr^{3+}ions, with a slope of 19.45 ± 0.44 mV per decade of Cr^{3+} concentration. This is in contrast to the slopes of the linear part of the emf responses for other cations (potential/-log [Ion] plots), where much lower slopes than those expected by the Nernst equation were obtained. This behaviour may be considered to be the result of the selectivity of the GBHA ionophore to Cr^{3+} in comparison with other metal ions, and the rapid exchange kinetics of the resulting GBHA-Cr^{3+} complex between the aqueous and electrode phases.

The potentiometric selectivity coefficients, representing the preference of the GBHA-based sensor for the chromium ions (denoted A), relative to an interfering ion (denoted B) were calculated based on the Matched Potential Method (MPM) (as explained in section 1.12.2). For these measurements, the reference solution was chosen to be 9 mL of water. In order to have a 1.000×10^{-6} mol L^{-1} aqueous solution of Cr(III), 1 mL of a 1.000×10^{-5} mol L^{-1} aqueous solution of Cr(III) was added to this reference solution and its potential was recorded (potential at C_A, where C_A is the concentration of Cr(III) ion). Subsequently, for each studied interfering ion, different amounts of different concentration of those ions were added to the same reference solution (9 mL water) until the same potential value as obtained at C_A, was measured. Table 3.4 summarizes the resulting values for the proposed chromium(III) ISE measured based on MPM.

Interfering Ion (B)	Concentration of B (C_B) (M)	$K^{MPM} = C_A/C_B$
Fe^{3+}	4.545×10^{-5}	2.200×10^{-2}
Cu^{2+}	2.800×10^{-4}	3.571×10^{-3}
Co^{2+}	7.600×10^{-4}	1.316×10^{-3}
Cr^{2+}	2.857×10^{-3}	3.500×10^{-4}
Ni^{2+}	3.182×10^{-2}	3.143×10^{-5}
Mn^{2+}	4.839×10^{-2}	2.066×10^{-5}
Fe^{2+}	5.000×10^{-2}	2.000×10^{-5}
Mg^{2+}	6.625×10^{-2}	1.509×10^{-5}
Al^{3+}	7.429×10^{-2}	1.346×10^{-5}
Cd^{2+}	9.174×10^{-2}	1.090×10^{-5}
Zn^{2+}	1.429×10^{-1}	6.998×10^{-6}
Pb^{2+}	1.818×10^{-1}	5.500×10^{-6}
Ca^{2+}	2.174×10^{-1}	4.600×10^{-6}
Na^{+}	4.193×10^{-1}	2.385×10^{-6}
K^{+}	5.2631×10^{-1}	1.900×10^{-6}

Table 3.4. Selectivity coefficients of the developed Cr^{3+}-selective sensor. (C_A: concentration of Cr(III) was 1.000×10^{-6} mol L^{-1}, and C_B: concentration of the interfering ion).

As shown in table 3.4, for the alkali, alkaline earth, and heavy metal ions used as interfering ions, the selectivity coefficients are on the order of 3.500×10^{-4} or smaller, which shows that these ions would not affect the sensor behaviour toward chromium. Also, the selectivity coefficients for

the Fe^{3+}, Cu^{2+}, and Co^{2+} ions are relatively small (2.200×10^{-2} to 1.316×10^{-3}), which refers to the fact that they would not very significantly disturb the functioning of the Cr^{3+}-selective sensor. Therefore, the electrode could be used for the Cr^{3+} ions detection in the presence of the studied interfering ions.

3.5. Dynamic Response Time

The practical dynamic response time of the proposed GBHA-modified TiO_2 electrode was recorded by changing the Cr^{3+} concentration solution over a concentration range of 1.000×10^{-7} to 1.000×10^{-2} M. The potential versus time traces are shown in figure 3.8. Four potential readings were recorded at each Cr(III) concentration at 10-seconds intervals. As can be seen on the resulting potential versus time curve, the electrode reached its equilibrium responses in a short time ($\leq$29 seconds) over the entire linear concentration range. This can be attributed to the fast exchange kinetics of association-dissociation of Cr^{3+} ions with the GBHA ionophore at the test solution-electrode interface.

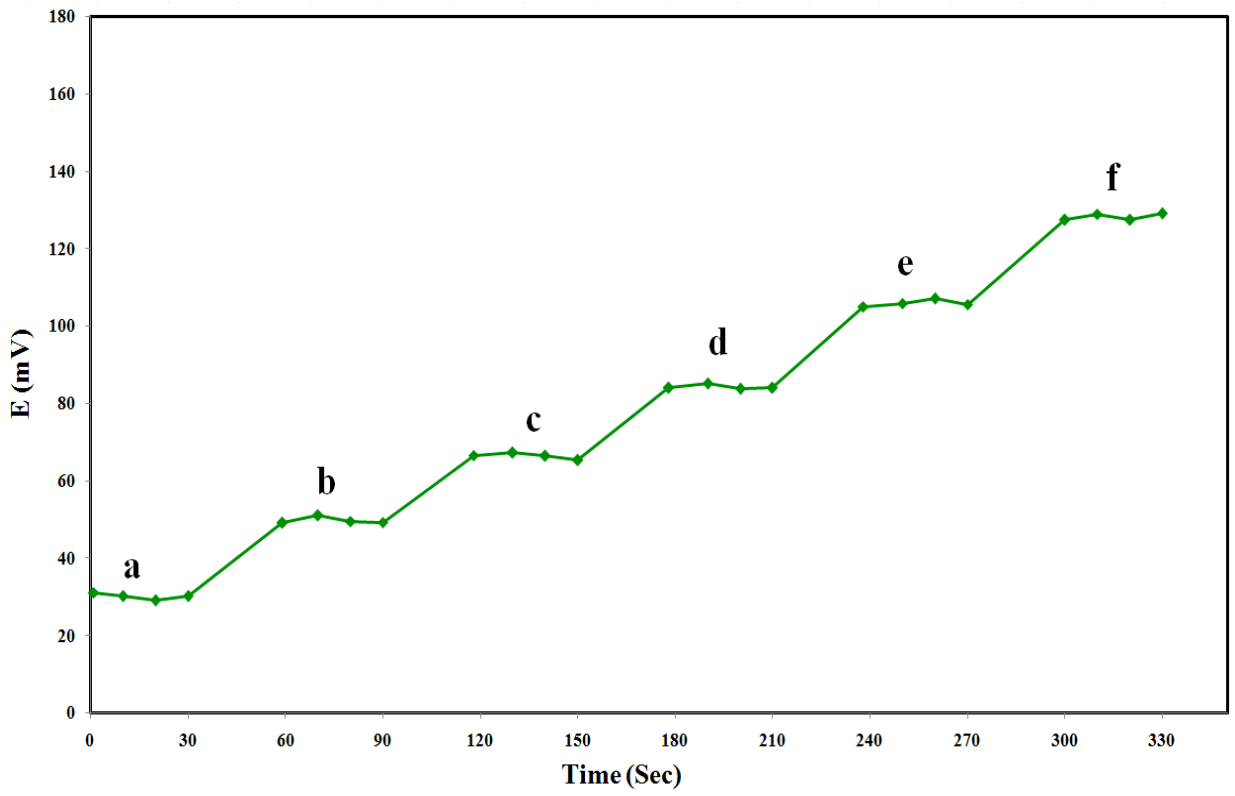

Figure 3.8. Dynamic response of the electrode for step changes in the concentration of Cr^{3+}: **(a)** 1.000×10^{-7} M, **(b)** 1.000×10^{-6} M, **(c)** 1.000×10^{-5} M, **(d)** 1.000×10^{-4} M, **(e)** 1.000×10^{-3} M, **(f)** 1.000×10^{-2} M.

0.6. Reversibility of the Electrode Response

For studying the reversibility behavior of the sensor's electrode, a similar procedure as conducted for the studies of the dynamic response time, was carried out in the opposite direction. These measurements were performed in several sequences of high-to-low (from 1.000×10^{-2} to 1.000×10^{-3} M) Cr(III) concentrations and the results are depicted in figure 3.9.

According to the observed trend, we could conclude that the potentiometric responses of the electrode was reversible, although the time required by the electrode to reach equilibrium values (≤40 seconds) was longer than that of low-to-high sample concentrations.

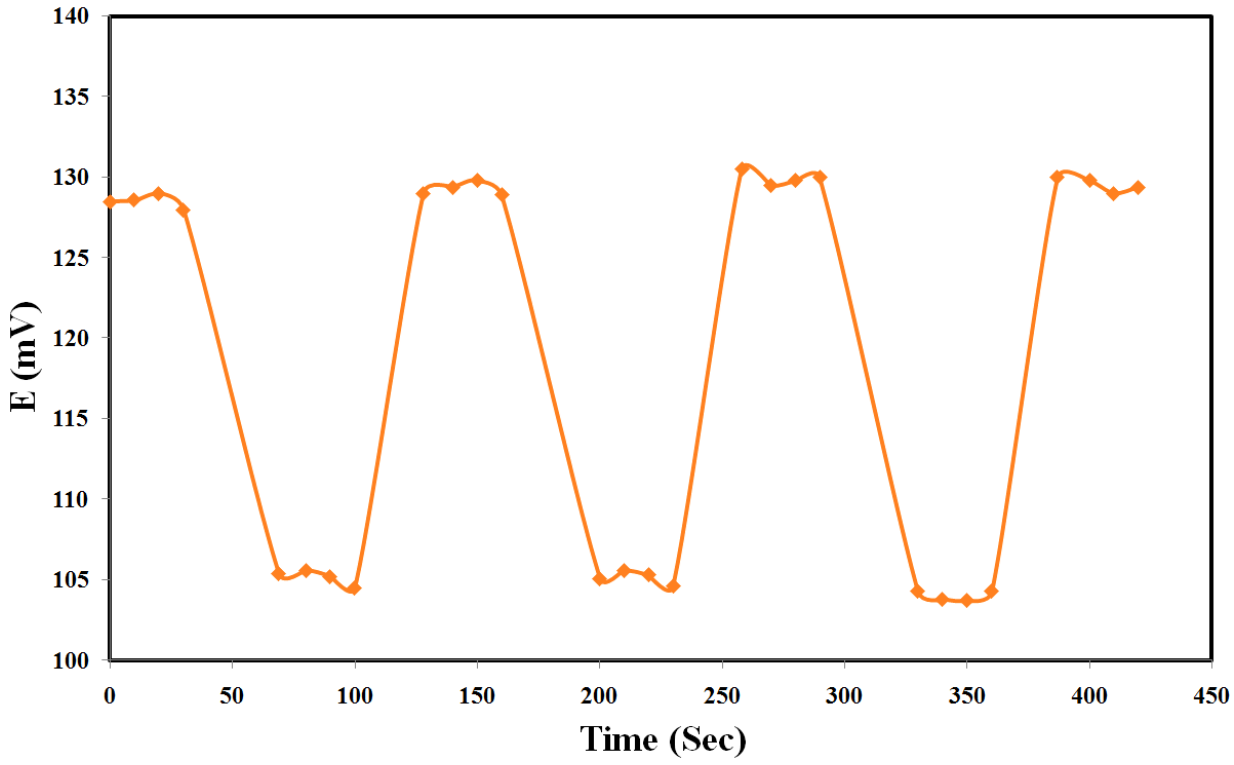

Figure 3.9. Dynamic response characteristics of the Cr(III)-selective sensor for several high-to-low sample cycles.

0.7. Effect of pH on the Potential Response of the Electrode

The pH dependence of the electrode response was tested in the range of 1.5 to 7.5 at two Cr(III) concentrations of 1.000×10^{-3} and 1.000×10^{-4} M. The pH was adjusted with dilute hydrochloric acid and sodium hydroxide solutions. The potential of the sensors were determined as a function of pH and the results are shown in figure 3.10. As noted, the potential remained constant over the pH range of 2.5 - 6.3, which may be taken as the working pH range of the GBHA-modified TiO_2-based sensor assembly.

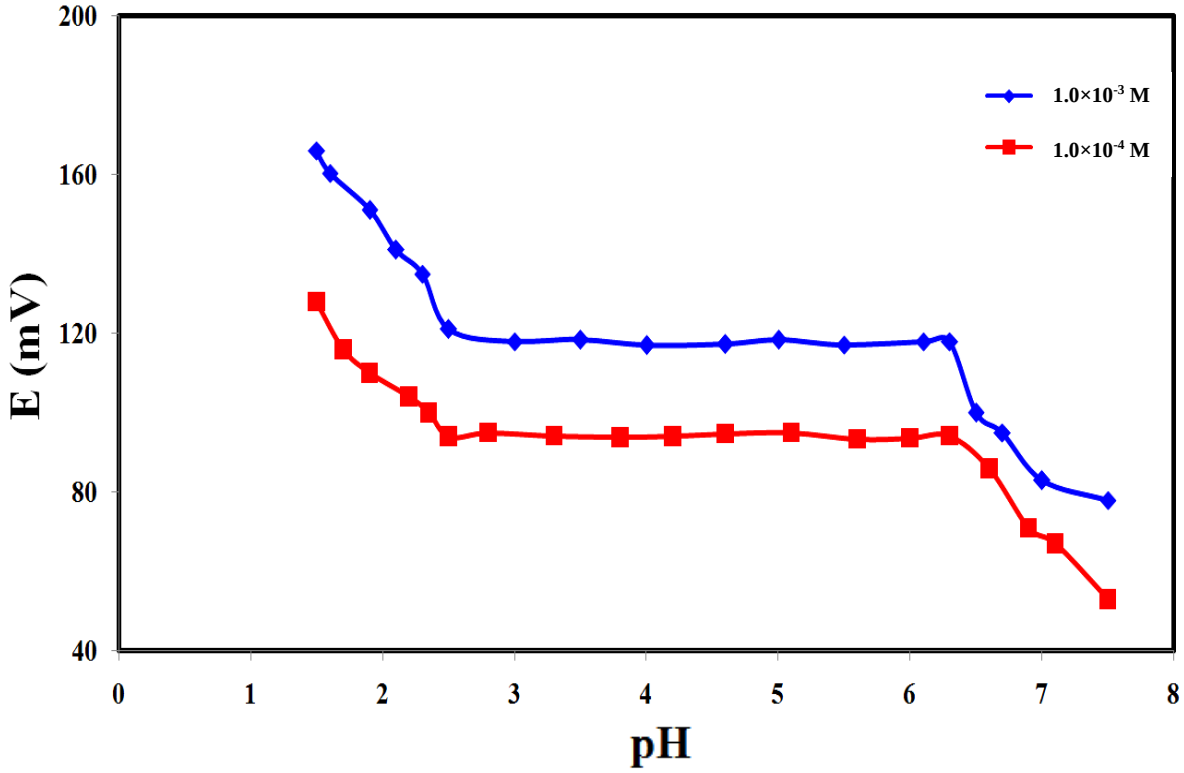

Figure 3.10. Effect of pH of test solutions on the potential response of Cr(III)-selective electrode based on GBHA-modified TiO_2 electrode over two concentrations of 1.000×10^{-4} M and 1.000×10^{-3} M Cr^{3+}.

It is reported that in this working pH range of the electrode, trivalent chromium remains in the solution and is present in the forms of Cr^{3+} and $Cr(OH)^{2+}$ [78]. On the one hand, at pH higher than 6.3, the formation of a chromium hydroxide precipitate ($Cr(OH)_3(s)$) due to Cr(III) complexation with OH^- ions occurs. This reaction decreases the amount of Cr^{3+} in solution and therefore the electrode potential decreases. On the other hand, at the lower pH values, we observed an increase in the measured potential. Although increasing the potential of the electrode at low pH values has been observed in some rare cases [18, 22, 23], for most ion-selective electrodes studied so far the potential of the electrode decreases at lower pH values. The observed increase in the measured potential at highly acidic pH values can be indicative of the fact that at this pH range, the GBHA-modified TiO_2 electrode responds to some other ion in addition to Cr^{3+} ions, such as Ti^{4+} ions from the TiO_2 crystalline structure.

0.8. Sensors' Stability and Lifetime

For the studies of the stability and lifetime of the fabricated Cr(III)-selective sensors based on GBHA-modified TiO_2 electrodes, three fabricated electrodes were tested over a period of 9 weeks and the results are summarized in table 3.5. The results indicated that no considerable variation in any of the response characteristics (recorded potential as well as the slope of the calibration graph) were observed over a period of 57 days for the potentiometric titanium dioxide-based Cr(III)-selective nanosensor modified with GBHA as the ionophore. During this time, the nanostructured sensors could be used without observing any significant divergence in the potential (mV). Also the detection limit and the slope of the electrode responses remained almost constant. However after this period changes were observed in the recorded potentials, the slope of

the calibration graph, and the detection limit, which can be attributed to the instability of the GBHA ligand onto the surface of TiO_2.

Week	Slope (mV decade^{-1})	Equation of the Line	Limit of Detection (M)
1	19.45 ± 0.44	y= -19.45 x +164.9	3.000 (± 1.600) × 10^{-8}
2	19.42 ± 0.47	y= -19.42 x +164.7	3.130 (± 2.200) × 10^{-8}
3	19.40 ± 0.45	y= -19.40 x +163.6	3.240 (± 2.300) × 10^{-8}
4	19.32 ± 0.33	y= -19.32 x +163.4	3.470 (± 2.300) × 10^{-8}
5	19.30 ± 0.35	y= -19.30 x +162.8	3.610 (± 2.600) × 10^{-8}
6	19.14 ± 0.39	y= -19.14 x +161.9	4.120 (± 3.000) × 10^{-8}
7	19.05 ± 0.41	y= -19.05 x +161.2	4.470 (± 3.400) × 10^{-8}
8	18.96 ± 0.44	y= -18.96 x +160.9	4.780 (± 4.000) × 10^{-8}
9	16.10 ± 0.49	y= -16.10 x +143.2	1.120 (± 3.100) × 10^{-7}

Table 3.5. Weekly-based potentiometric studies for estimating the lifetime of the Cr(III)-selective sensor based on 3 tested GBHA-modified TiO_2 electrodes.

3.9. Short-term Stability

For evaluating the short-term stability of the fabricated Cr(III)-selective sensors, the potentiometric measurements were carried out daily (the electrode was employed 1 hour per day) using three GBHA-modified TiO_2 electrodes.

;

Day	Slope (mV decade^{-1})	Equation of the Line	Limit of Detection (M)
1	19.45 ± 0.44	y= -19.45 x +164.9	3.000 (± 1.600) × 10^{-8}
2	19.45 ± 0.45	y= -19.45 x +165.8	3.000 (± 1.700) × 10^{-8}
3	19.45 ± 0.40	y= -19.45 x +163.6	3.000 (± 1.900) × 10^{-8}
4	19.44 ± 0.34	y= -19.44 x +165.7	3.060 (± 2.200) × 10^{-8}
5	19.44 ± 0.48	y= -19.44 x +164.5	3.060 (± 2.100) × 10^{-8}
6	19.44 ± 0.43	y= -19.44 x +165.7	3.060 (± 2.200) × 10^{-8}
7	19.44 ± 0.32	y= -19.44 x +164.9	3.060 (± 2.200) × 10^{-8}
SD_{mean} (Slope): 0.002			
Day	**Slope (mV decade^{-1})**	**Equation of the Line**	**Limit of Detection (M)**
8	19.42 ± 0.47	y= -19.42 x +165.0	3.130 (± 2.200) × 10^{-8}
9	19.42 ± 0.39	y= -19.42 x +164.9	3.130 (± 2.200) × 10^{-8}
10	19.41 ± 0.41	y= -19.41 x +164.9	3.180 (± 2.200) × 10^{-8}
11	19.41 ± 0.40	y= -19.41 x +165.4	3.180 (± 2.200) × 10^{-8}
12	19.41 ± 0.42	y= -19.41 x +165.2	3.180 (± 2.200) × 10^{-8}
13	19.40 ± 0.34	y= -19.40 x +165.0	3.240 (± 2.300) × 10^{-8}
14	19.40 ± 0.43	y= -19.40 x +165.1	3.240 (± 2.300) × 10^{-8}
SD_{mean} (Slope): 0.003			

Day	Slope (mV decade^{-1})	Equation of the Line	Limit of Detection (M)
50	18.94 ± 0.49	y= -18.94 x +161.8	4.780 (± 4.000) × 10^{-8}
51	18.92 ± 0.29	y= -18.92 x +161.8	4.840 (± 4.000) × 10^{-8}
52	18.92 ± 0.41	y= -18.92 x +162.0	4.840 (± 4.000) × 10^{-8}
53	18.91 ± 0.38	y= -18.91 x +162.3	4.880 (± 4.200) × 10^{-8}
54	18.90 ± 0.34	y= -18.90 x +162.2	4.910 (± 4.300) × 10^{-8}
55	18.88 ± 0.44	y= -18.88 x +161.9	5.990 (± 4.000) × 10^{-8}
56	18.88 ± 0.53	y= -18.88 x +161.2	5.990 (± 4.000) × 10^{-8}
SD_{mean} **(Slope)**: 0.008			

Table 3.6. Daily-based potentiometric studies for estimating the lifetime of the Cr(III)-selective sensor based on 3 tested GBHA-modified TiO_2 electrodes.

. These measurements were performed during the first two weeks as well as the last week of the sensors reliable functioning time (according to table 3.5). The standard deviation in the slopes of the calibration graphs in each week was then calculated as reported in table 3.6. Table 3.6 summarizes the results of the slopes and intercepts of the calibration graphs as well as the LODs obtained based on daily potentiometric measurements, carried out during weeks 1, 2, and 8 for the Cr(III)-selective sensors designed based on GBHA-modified TiO_2 electrodes.

As is apparent from this table, the values of standard deviation in the mean of the slopes of the calibration graphs are very small, which refers to high short-term stability of the fabricated sensors. These studies rule out the necessity to record the potentials on a daily basis and validated the weekly potentiometric measurements for the studies of sensors' stability and lifetime, as explained in section 3.8.

3.10. Comparisons With the Reported Sensors

The working concentration range, slope, response time, detection limit, working pH range, and lifetime of the proposed potentiometric sensors are compared with the corresponding values for some of the best (in terms of the performance factors) previously reported chromium ISEs based on different ionophores [18, 21-23], and the results are summarized in table 3.7.

Ref.	Working Concentration Range (M)	Slope (mV/decade of Concentration)	LOD (M)	pH Range	Lifetime (days)
18	4.000×10^{-6} -1.000×10^{-1}	20.0 ± 0.1	2.000×10^{-7}	2.8 – 5.1	150
22	1.000×10^{-7} -1.000×10^{-1}	20.0 ± 0.5	5.000×10^{-8}	3.0 - 8.0	30
23	2.000×10^{-7} -1.000×10^{-1}	19.8 ± 0.2	9.000×10^{-8}	2.2 - 5.0	90
21	7.500×10^{-6} -1.000×10^{-2}	20.1 ± 0.6	1.800×10^{-6}	4.5 – 7.7	NA
This Work	$1.000 (\pm 0.040) \times 10^{-7}$ - $1.000 (\pm 0.020) \times 10^{-2}$	19.45 ± 0.44	$3.000 (\pm 1.600) \times 10^{-8}$	2.5 - 6.3	57

Table 3.7. Comparison of the working concentration range, slope, limit of detection, working pH range, and lifetime of present Cr(III)-selective sensors and previous studies of other research groups.

From the data summarized in table 3.7 we concluded that:

1) Although the Cr(III)-selective sensor reported in Ref. [18] showed the longest lifetime among all the reported works, its linear concentration range and working pH range are narrower than our fabricated Cr(III)-selective sensor. In addition its LOD is bigger than the LOD obtained in our work.

2) The Cr(III)-selective sensor reported in Ref. [22] indicated the widest working concentration range and its working pH range is wider than that of our sensor. However our sensor is superior in terms of offering smaller LOD and longer lifetime.

3) Although the Cr(III)-selective sensor reported in Ref. [23] had a longer lifetime than that of our fabricated sensor, our sensor showed wider working pH range, and lower LOD, in addition to its limit of quantification is lower than that of Ref. [23].

4) In comparison with the Cr(III)-selective sensor reported in Ref. [21], our sensor exhibited superior behavior in terms of having a wider linear concentration range, wider working pH range, and lower LOD.

In summary according to table 3.7, the GBHA derived sensor possesses the best detection limit in comparison to those reported previously, while its linear range and working pH range are better than most of the previously reported Cr(III)-selective sensors.

Throughout my PhD studies, we were searching for strategies to improve the stability of the fabricated nanostructured TiO_2-based Cr(III)-selective sensor based on GBHA molecular receptors physisorbed onto the surface of TiO_2. Although immobilization of this ligand onto the surface of TiO_2 through appropriate linkers (chemisorption) was considered to be a good solution, it required some modifications of the GBHA molecule. This could have included the introduction of some functional groups to the benzene rings of the GBHA ionophores, which could then bind to the terminal groups of a linker self-assembled on the surface of TiO_2 (such as SAMs of silanes or phosphonic acids). We faced many challenges proceeding in this direction, such as finding the appropriate chemistry to introduce carboxyl groups on the benzene rings without affecting the rest of the ligand. This strategy also introduced other difficulties, such as the need to protect and deprotect the hydroxyl groups involved in ion complexation during surface attachment of the ligand. We also considered *in-situ* synthesis of the functionalized-GBHA ligand directly on the

TiO_2 surface, first by creating a SAM with the desired anchoring group, and then introducing in solution the ligand building blocks. Due to the challenges involved working with the GBHA ligand, we decided to shift to other classes of molecules that could enable us to fulfill our research goals. Desferal was a very good option because it has an NH_2 group that can be used for surface attachment without interference with the metal ion binding.

0.11. Conclusion

In conclusion, for the first time we fabricated a highly selective potentiometric sensor for quantification analysis of Cr^{3+} ions, using GBHA molecular receptors physisorbed onto nanostructured TiO_2 electrodes. The proposed sensor showed the best response characteristics with Nernstian behaviour for Cr^{3+} (Nernstian slope of 19.45 $\pm$ 0.44 mV per decade of Cr^{3+} concentration) over a wide working concentration range of 1.000×10^{-7} to 1.000×10^{-2} M, and a low detection limit of 3.000×10^{-8} M. The sensor worked well in the pH range of 2.5 – 6.3, had a relatively fast response time of $\leq$ 29 seconds, and could be used for at least 57 days without any considerable divergence in potential. The fabricated sensor showed good selectivity against Cr^{3+} in comparison with variety of other cations, and could be used for the determination of this ion in the presence of considerable concentrations of common interfering ions. This assembled nanostructured TiO_2 based Cr(III)-selective sensor offered simplicity, rapidity, reproducibility, and reliability as a portable analytical tool.

In addition, our results showed that except for Fe^{3+}, for all other ions tested, the selectivity coefficients are on the order of 10^{-3} to 10^{-6}.This is much smaller in comparison with the selectivity coefficients obtained based on MPM in the cited works (the reported values are in the

orders of 10^{-2} to 10^{-3} in Ref. [23], and 10^{-2} to 10^{-3} in Ref. [22]). Based on these facts, our fabricated sensor has an improved selectivity towards Cr^{3+} with respect to all the other tested ions.

4. Functionalization of Nanostructured Titanium Dioxide Surface with Self Assembled Monolayers (SAMs) of Alkanephosphonic Acids, and the comparisons of the Performances of the Fe(III)-Selective Sensors Fabricated Based on Desferal-Physisorbed and Chemisorbed on TiO_2 Electrodes

The structure of this chapter will be very similar to the previous chapter, and involves similar types of measurements in order to assess the performance of a novel desferal-based iron(III)-selective potentiometric sensor.The UV-Vis spectroscopic titration analysis were performed as a preliminary experiment for studying the complexation of the desferal ligand with most of the first row transition metal ions, and also for probing its selectivity towards those ions. These studies were necessary to help us decide if this ligand can be a good candidate a good candidate to be used as an ionophore in the assembly of an ISE.

4.1. UV-Vis Titration Analysis

Figure 4.1.(a-c) show desferal ligand in water, the analyte, Fe^{3+}, and the complex formed in solution when Fe^{3+} was reacted with the desferal reagent and formed a coloured complex that absorbs strongly in the visible region of the electromagnetic spectrum.

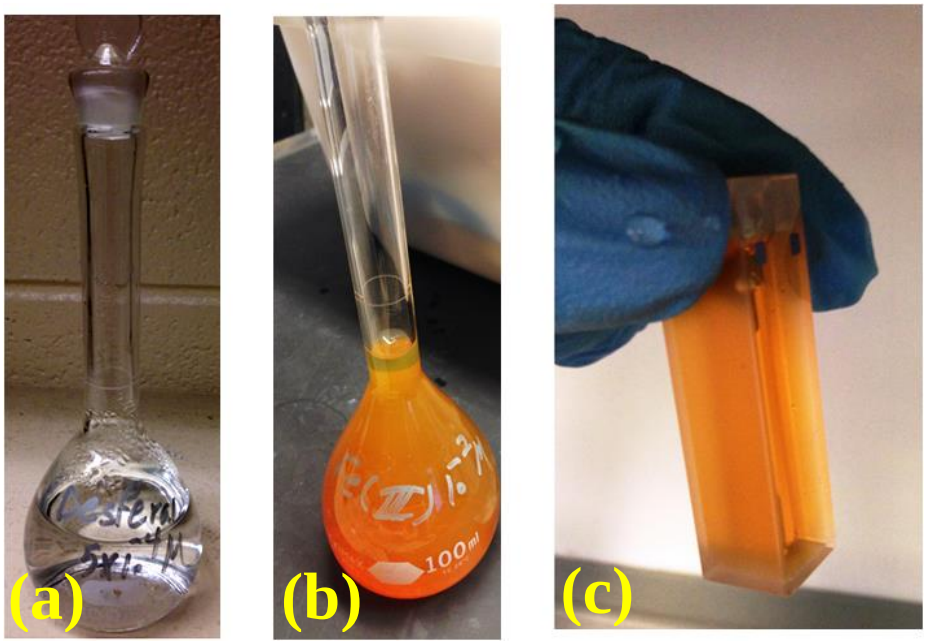

Figure 4.1. (a) 5.000 × 10^{-4} M aqueous solution of desferal, **(b)** 1.000 × 10^{-2} M aqueous solution of Fe^{3+}, and **(c)** the formed Fe(III)-desferal complex.

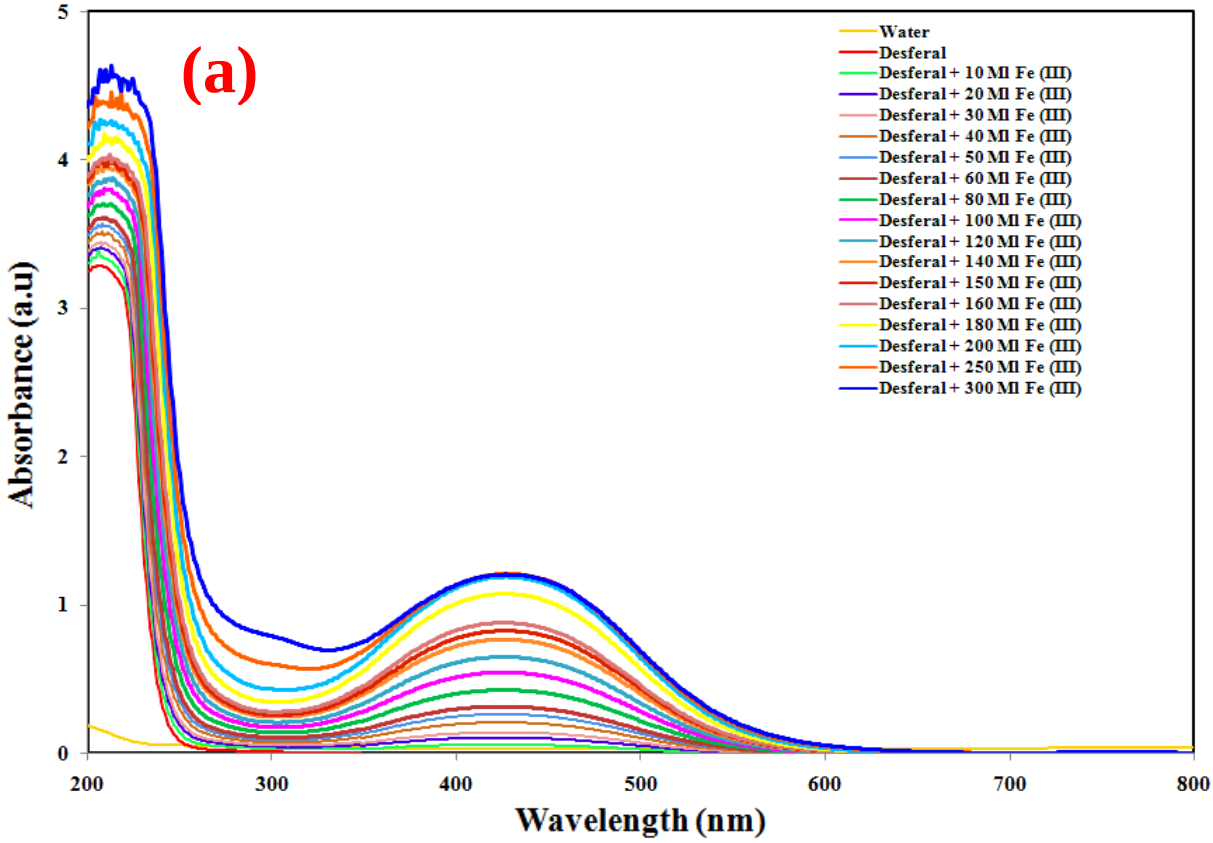

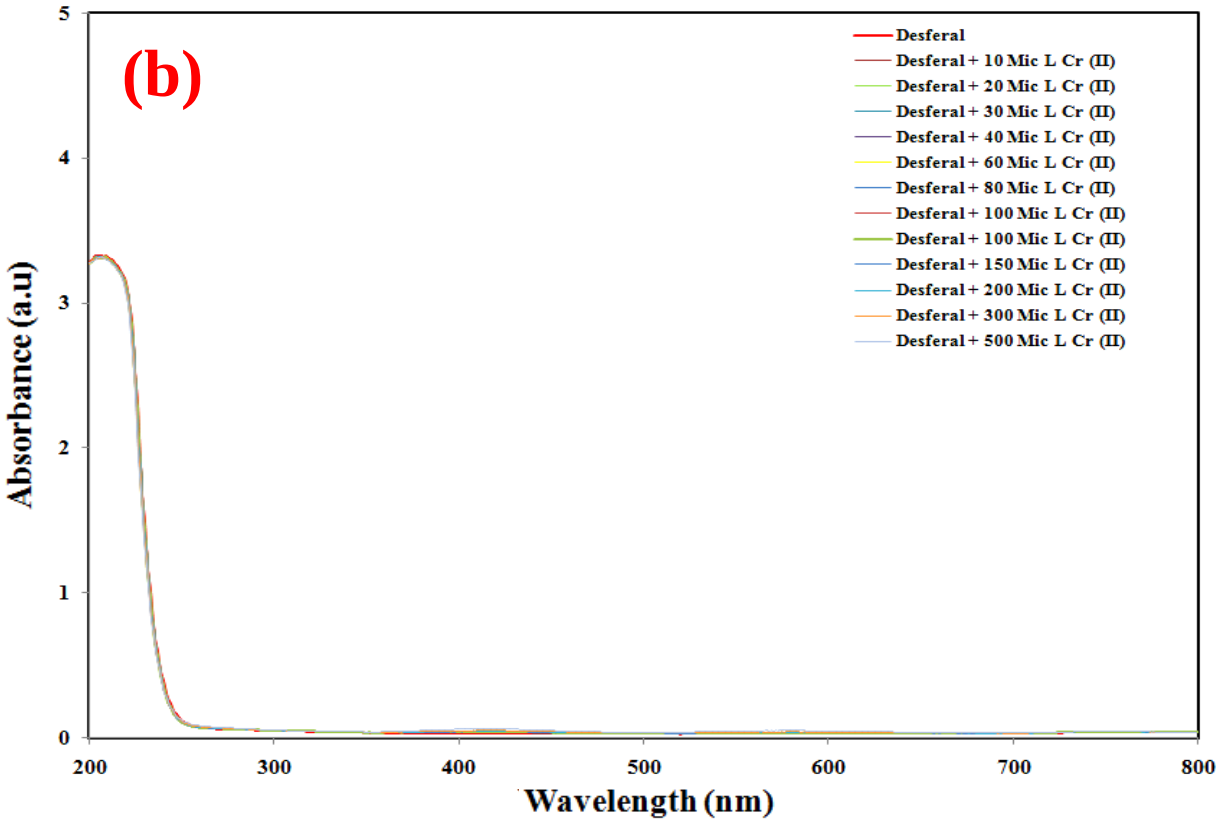
(b)
Desferal
Desferal + 10 Mic L Cr (II)
Desferal + 20 Mic L Cr (II)
Desferal + 30 Mic L Cr (II)
Desferal + 40 Mic L Cr (II)
Desferal + 60 Mic L Cr (II)
Desferal + 80 Mic L Cr (II)
Desferal + 100 Mic L Cr (II)
Desferal + 100 Mic L Cr (II)
Desferal + 150 Mic L Cr (II)
Desferal + 200 Mic L Cr (II)
Desferal + 300 Mic L Cr (II)
Desferal + 500 Mic L Cr (II)
Absorbance (a.u)
Wavelength (nm)
0
1
2
3
4
5
200
300
400
500
600
700
800

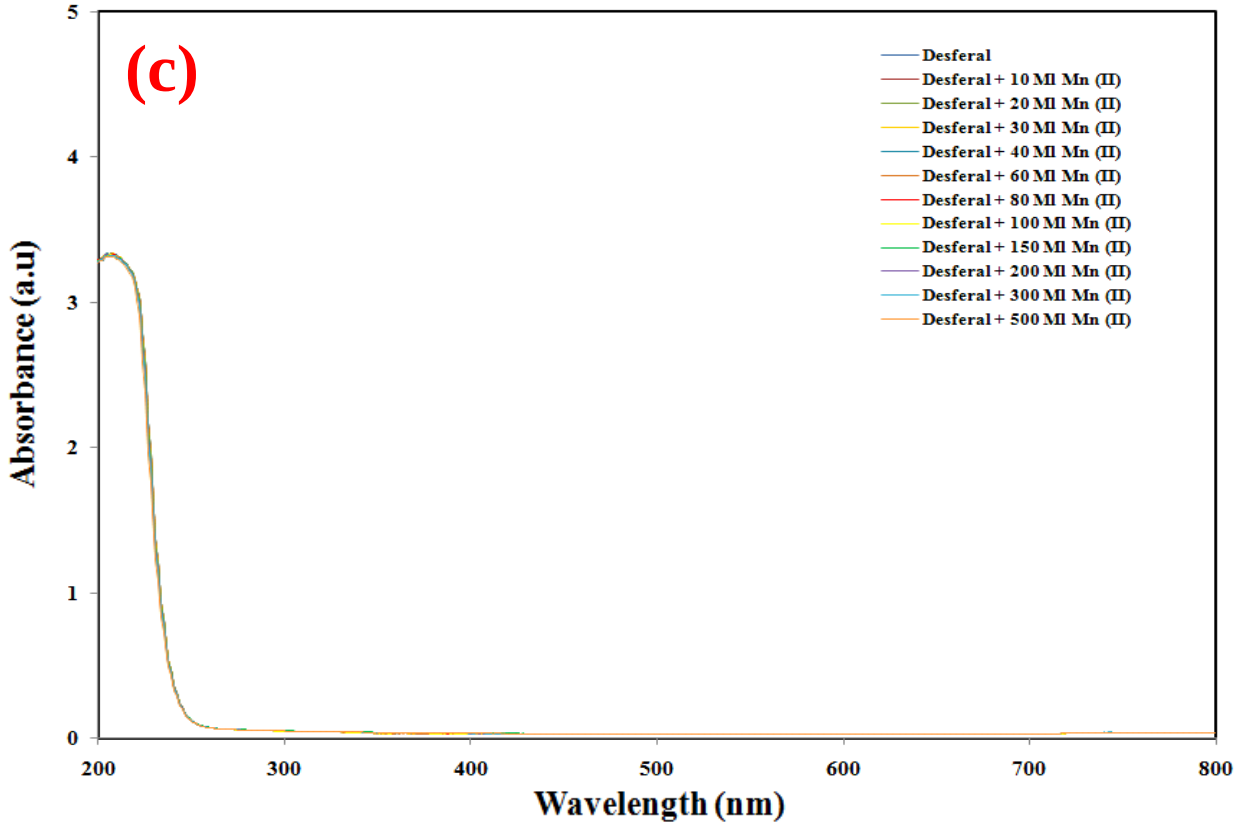
(c)
Desferal
Desferal + 10 Ml Mn (II)
Desferal + 20 Ml Mn (II)
Desferal + 30 Ml Mn (II)
Desferal + 40 Ml Mn (II)
Desferal + 60 Ml Mn (II)
Desferal + 80 Ml Mn (II)
Desferal + 100 Ml Mn (II)
Desferal + 150 Ml Mn (II)
Desferal + 200 Ml Mn (II)
Desferal + 300 Ml Mn (II)
Desferal + 500 Ml Mn (II)
Absorbance (a.u)
Wavelength (nm)
0
1
2
3
4
5
200
300
400
500
600
700
800

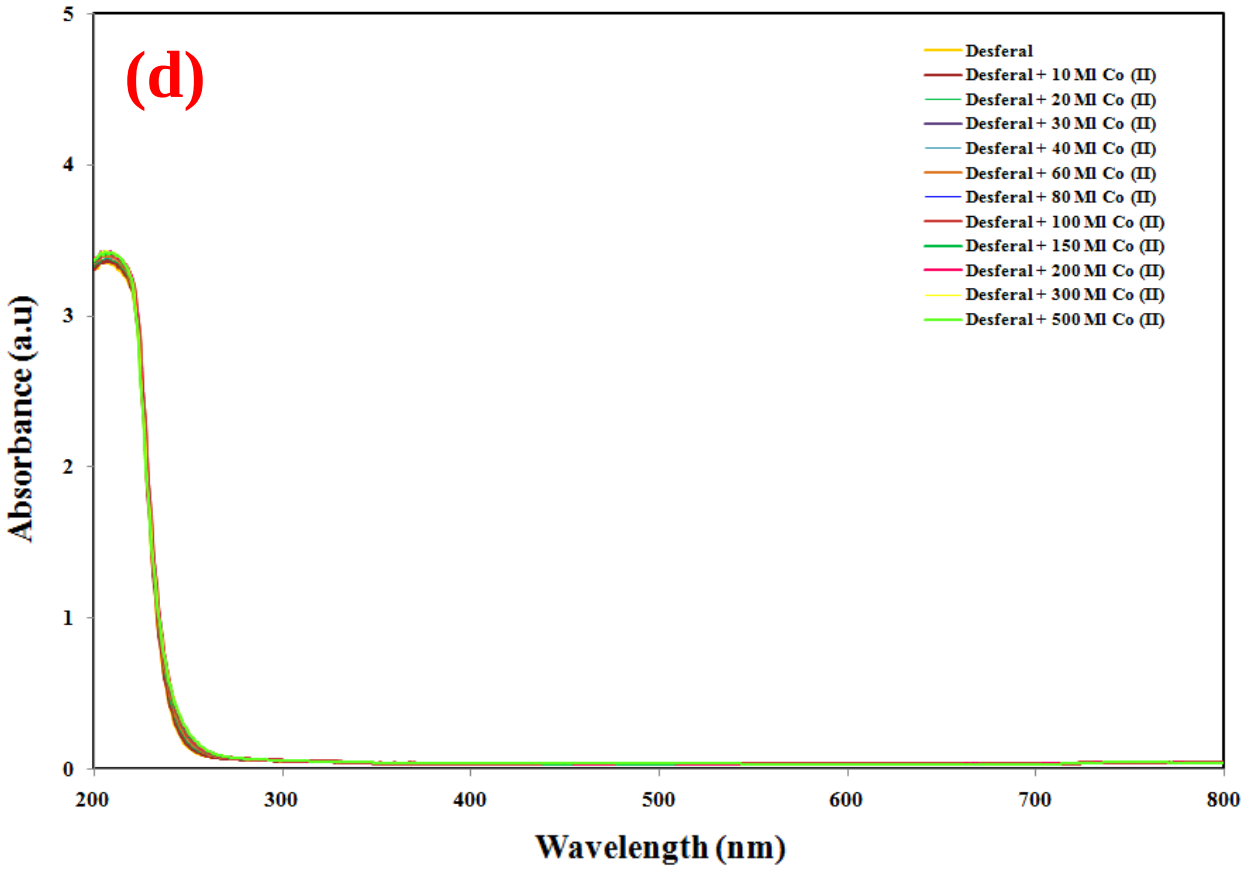
(d)
Absorbance (a.u)
Wavelength (nm)
Desferal
Desferal + 10 Ml Co (II)
Desferal + 20 Ml Co (II)
Desferal + 30 Ml Co (II)
Desferal + 40 Ml Co (II)
Desferal + 60 Ml Co (II)
Desferal + 80 Ml Co (II)
Desferal + 100 Ml Co (II)
Desferal + 150 Ml Co (II)
Desferal + 200 Ml Co (II)
Desferal + 300 Ml Co (II)
Desferal + 500 Ml Co (II)

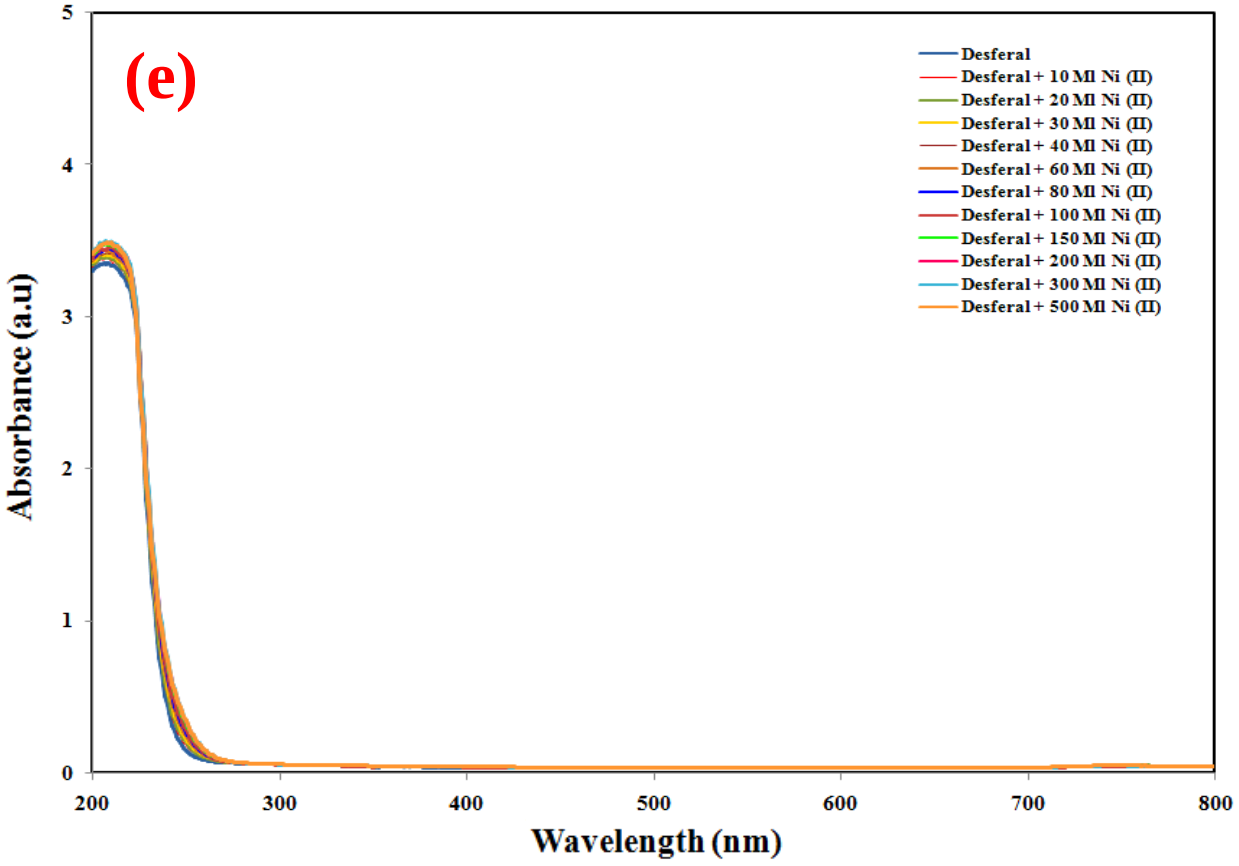
(e)
Absorbance (a.u)
Wavelength (nm)
Desferal
Desferal + 10 Ml Ni (II)
Desferal + 20 Ml Ni (II)
Desferal + 30 Ml Ni (II)
Desferal + 40 Ml Ni (II)
Desferal + 60 Ml Ni (II)
Desferal + 80 Ml Ni (II)
Desferal + 100 Ml Ni (II)
Desferal + 150 Ml Ni (II)
Desferal + 200 Ml Ni (II)
Desferal + 300 Ml Ni (II)
Desferal + 500 Ml Ni (II)

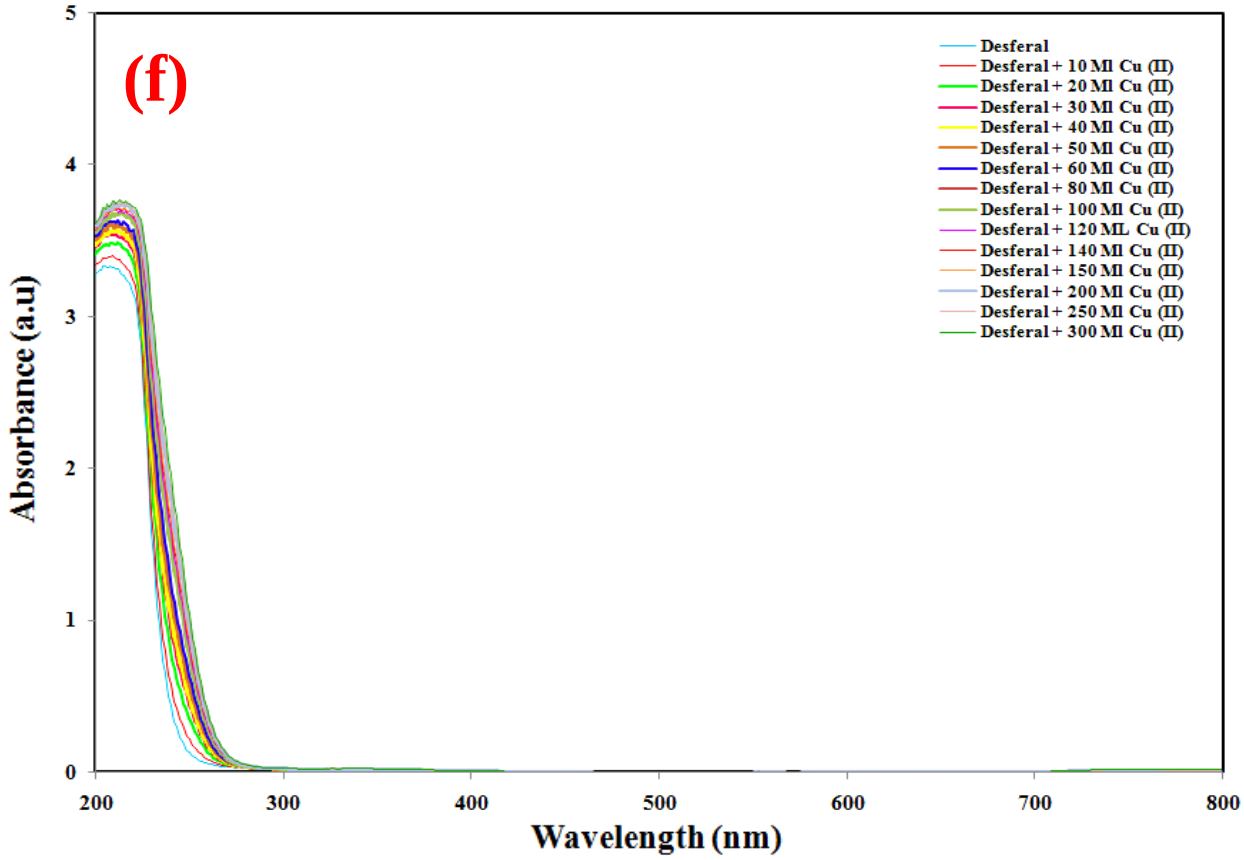

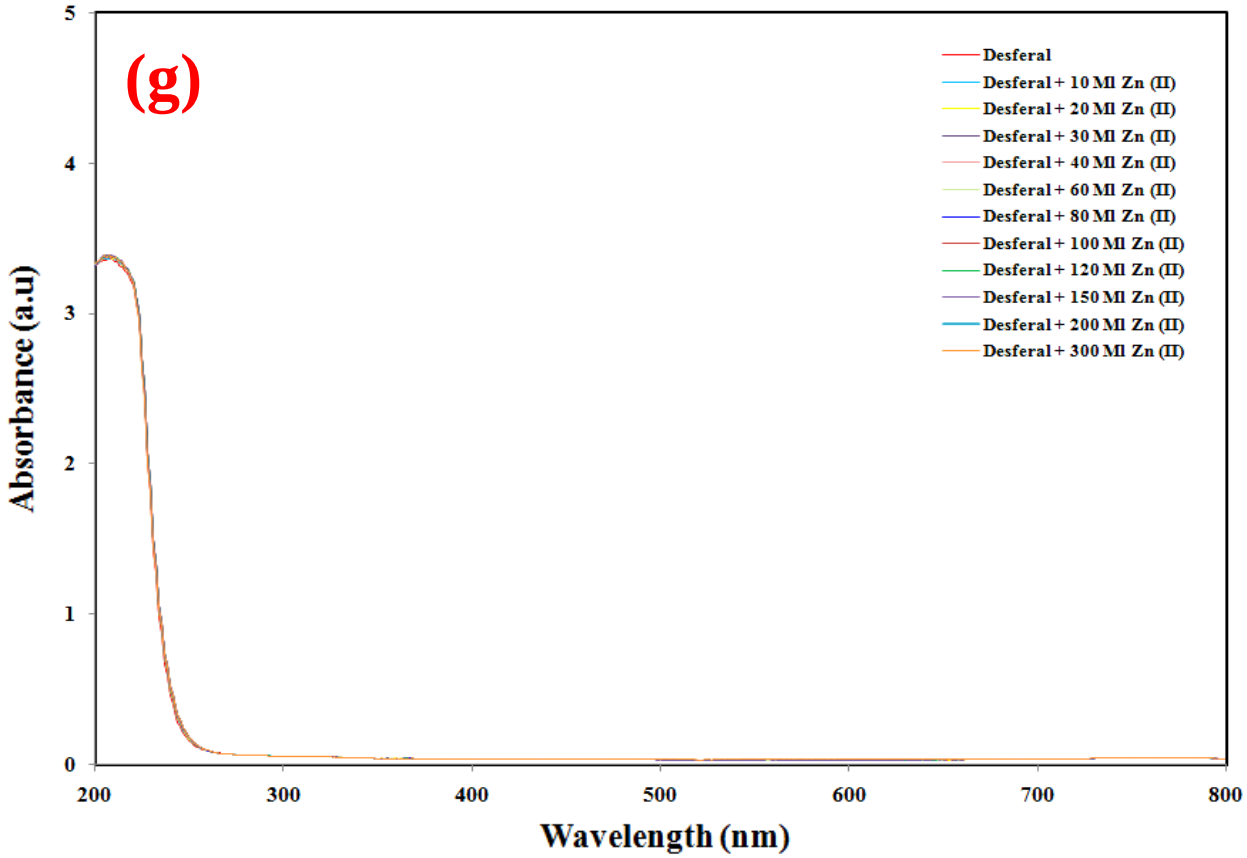

Figure 4.2 (a-h). UV-Vis titration spectra of 3.00 mL of a 5.000 $\times 10^{-4}$ M desferal in water, titrated with microliters amounts of 1.000 $\times$ 10^{-2} M aqueous solution of first row transition metal ions at 25ºC. The transition metal ion used is stated in each graph together with the volume employed.

Figures 4.2 (a-h) are characteristic UV-Vis titration spectra of 3.00 mL of a 5.000 $\times 10^{-4}$ M desferal in water, titrated with microliters amounts of 1.00 $\times$ 10^{-2} M aqueous solution of the first row transition metal ions Cr^{3}, Fe^{3+}, Cr^{2+}, Mn^{2+}, Co^{2+}, Ni^{2+}, Cu^{2+}, and Zn^{2+} at 25.0 ± 0.1ºC. Although the UV-Vis spectrum of the free desferal does not show any significant peaks, upon coordination of Fe(III) with this ligand, an intense peak appeared in the visible region (350 - 600 m), which could be related to LMCT (figure 4.2 (a)).

Based on these results, it could be concluded that among all the tested cations, the microliters titrations of desferal ligand with iron(III) ions caused an appearance of the largest peaks in the visible region of the electromagnetic spectrum, which referred to a strong complexation of desferal ligand with these ions. These studies showed that desferal could be a very good candidate to be used as the ionophore in designing Fe(III)-selective potentiometric sensors, due to the high selectivity of this ligand for Fe(III) ions comparing with all the other tested ions. Therefore, in this work, we took advantage of the high sensitivity of the desferal ligand for binding with Fe(III) ions, to fabricate a Fe(III)-selective potentiometric sensor based on nanostructured-TiO_2 electrodes.

In order to see the UV-Vis spectrum of free Fe(III) in the absence of the desferal ligand, the UV-Vis titrations of 3.00 mL of water with microliters amounts of a 1.000 $\times 10^{-2}$ M aqueous solution of Fe(III) were also recorded (figure 4.3).

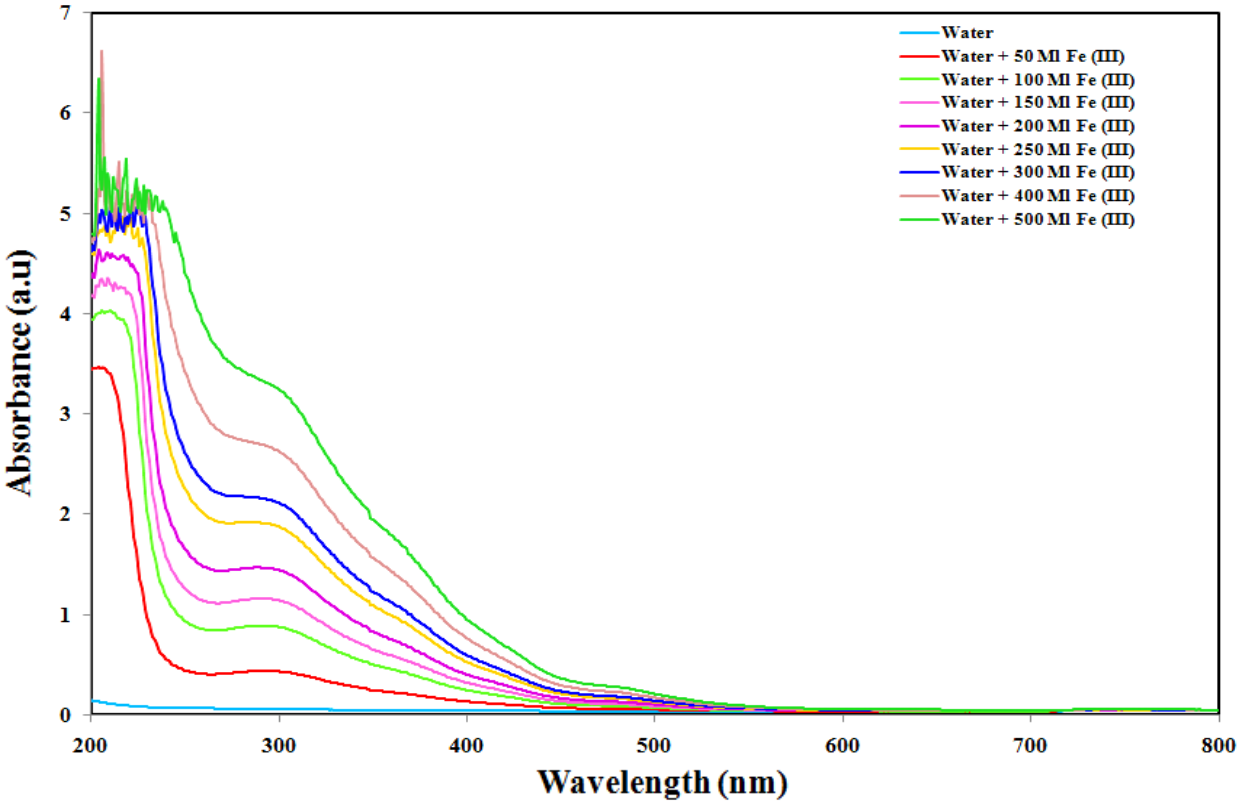

Figure 4.3. UV-Vis titrations of 3.00 mL of water with microliters amounts of a 1.000×10^{-2} M aqueous solution of Fe(III) at 25ºC.

As seen in figure 4.3, the peaks around 350-400 nm are associated with d-d transition in Fe^{3+}, while the peaks assigned to LMCT in figure 4.2 (a), are absent. This further confirmed the coordination of Fe(III) with the desferal ligand.

4.2. EMF measurements for Fe(III)-Selective Sensors Based on Desferal-Physisorbed on TiO_2 Electrodes

As previously explained, it is very important for a good potentiometric sensor to have a broad linear response. The linear response to the concentration of Fe^{3+} ions was investigated for the potentiometric sensors fabricated based on physisorbed ligand onto the surface of TiO_2 electrodes. Figure 4.4 is indicative of the resulting calibration plot for the Fe(III)-selective sensor prepared based on desferal-physisorbed on TiO_2 electrodes. As seen from this figure, a Nernstian response was obtained for the concentration range of 5.300 (± 0.030) × 10^{-6} to 1.000 (± 0.020) × 10^{-1} M. The absolute value in the slope of the calibration plot was measured to be 19.14 ± 0.35 mV per decade of Fe^{3+} concentration.

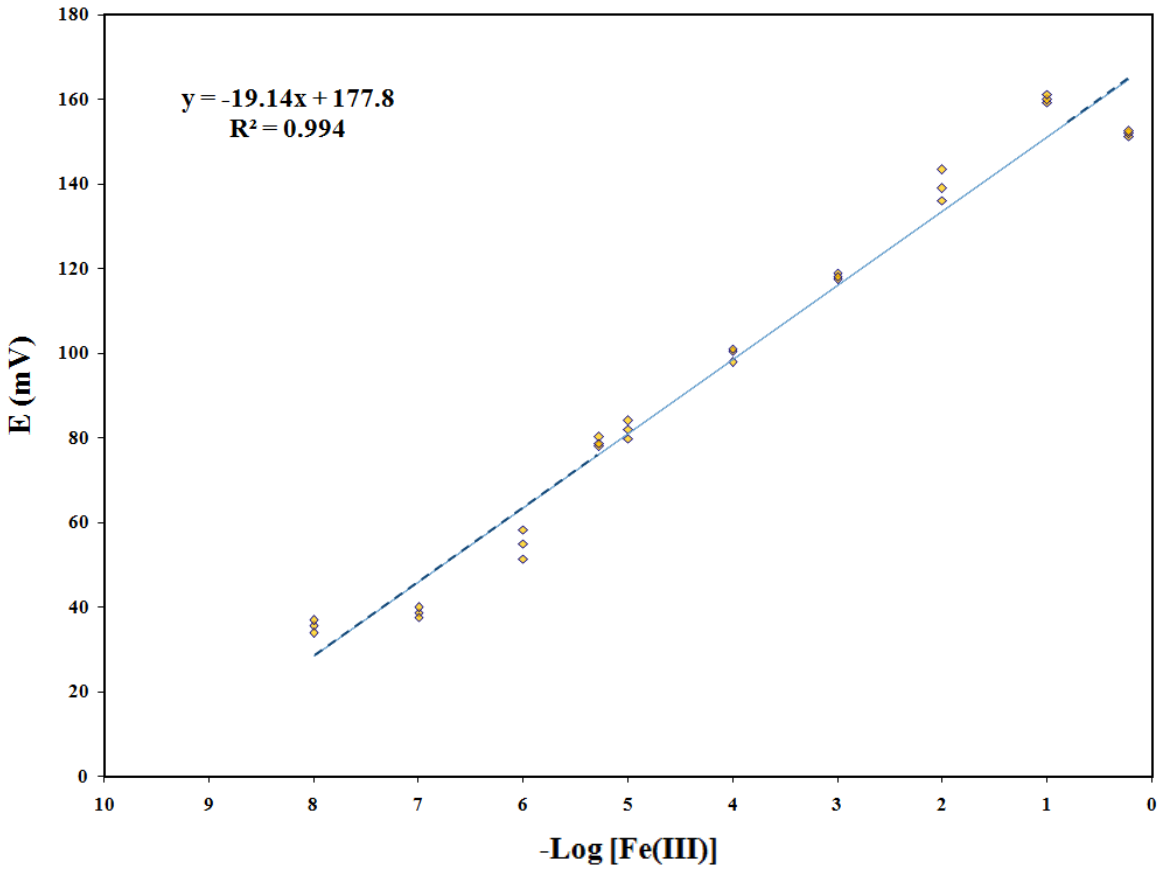

Figure 4.4. Calibration plot for iron(III) ion selective electrode based on desferal-physisorbed onto TiO_2 electrodes.

4.2.1. Error Analysis

The errors were calculated in the concentration of Fe(III), the recorded potential values, as well as the slope of the calibration plot as seen in figure 4.4, using the same method as explained previously in chapter 3 (section 3.2). Table 4.1 is indicative of the calculated errors on the concentration of Fe(III) for the calibration plot shown in figure 4.4.

$[Fe^{3+}]$ (M)		-Log $[Fe^{3+}]$ (X-axis)	Error in the values of the X-axis
M_{10}	1.000×10^{-8} M	8.000	0.008
M_9	1.000×10^{-7} M	7.000	0.007
M_8	1.000×10^{-6} M	6.000	0.006
M_7	5.300×10^{-6} M	5.276	0.006
M_6	1.000×10^{-5} M	5.000	0.005
M_5	1.000×10^{-4} M	4.000	0.004
M_4	1.000×10^{-3} M	3.000	0.003
M_3	1.000×10^{-2} M	2.000	0.002
M_2	1.000×10^{-1} M	1.000	0.001
M_1	6.0000×10^{-1} M	0.2218	0.0004

Table 4.1. Calculated errors in the concentration of iron(III) for the calibration plot shown in figure 4.4.

In order to calculate the errors in the potential values, the standard deviations in the mean of three repetitive potentiometric measurements at each Fe(III) concentration were calculated (as summarized in table 4.2.)

$[Fe^{3+}]$	Potential (E (mV)) (Y-axis)				S_{sample} in E (mV)	S_{mean} in E (mV)
	Measurement 1	Measurement 2	Measurement 3	Average		
M_{10}	35.57	41.82	33.92	37.10	4.17	2.41
M_9	38.68	44.33	37.61	40.21	3.61	2.08
M_8	58.29	55.7	51.42	55.14	3.47	2.00
M_7	80.24	75.63	78.68	78.18	2.345	1.35
M_6	79.79	82.51	84.04	82.11	2.15	1.24
M_5	100.45	103.58	97.9	100.64	2.84	1.64
M_4	117.45	122.34	118.14	119.31	2.65	1.53
M_3	136.08	139.01	143.41	139.50	3.69	2.13
M_2	159.26	158.43	161.15	159.61	1.39	0.80
M_1	151.21	153.14	152.57	152.31	0.99	0.57

Table 4.2 Calculated errors in the measured potential values for the calibration plot shown in figure 4.4.

Using the LINEST complete linear least squares curve fitting routine for the analysis of uncertainty in the slope of the calibration plot (as shown in figure 4.4), the slope of this plot was measured to be 19.14 ± 0.35 mV per decade of Fe^{3+} concentration.

The LOD defined as the concentration of ferric ions obtained when the linear region of the calibration graphs was extrapolated to the base line, was measured to be 3.160 (± 1.500) × 10^{-8} M for the sensors designed based on desferal-physisorbed onto TiO_2 electrodes (as shown below in figure 4.5).

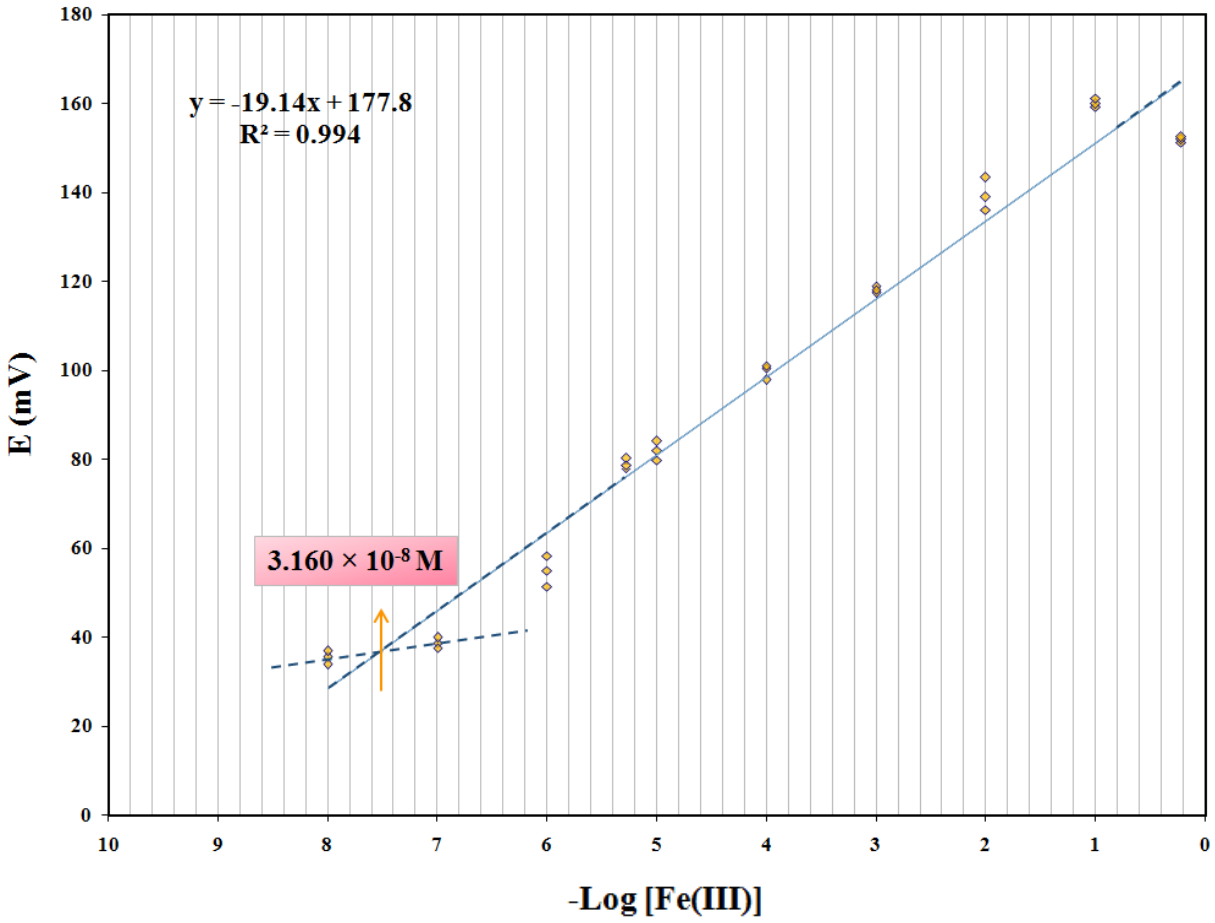

Figure 4.5. Calculations of LOD based on the extrapolation of the linear region of the calibration plot to the base line, for the calibration graph shown in figure 4.4

The potentials of varying concentrations of Fe(III) test solutions were recorded using a nanostructured TiO_2 electrode without the desferal ionophore, as the working electrode. The potentiometric response of the electrode in the absence of the ion exchanger is plotted as shown

in figure 4.6. As this graph indicates, there is no emf response to the concentration of Fe(III) ions for an electrode without the desferal ionophore.

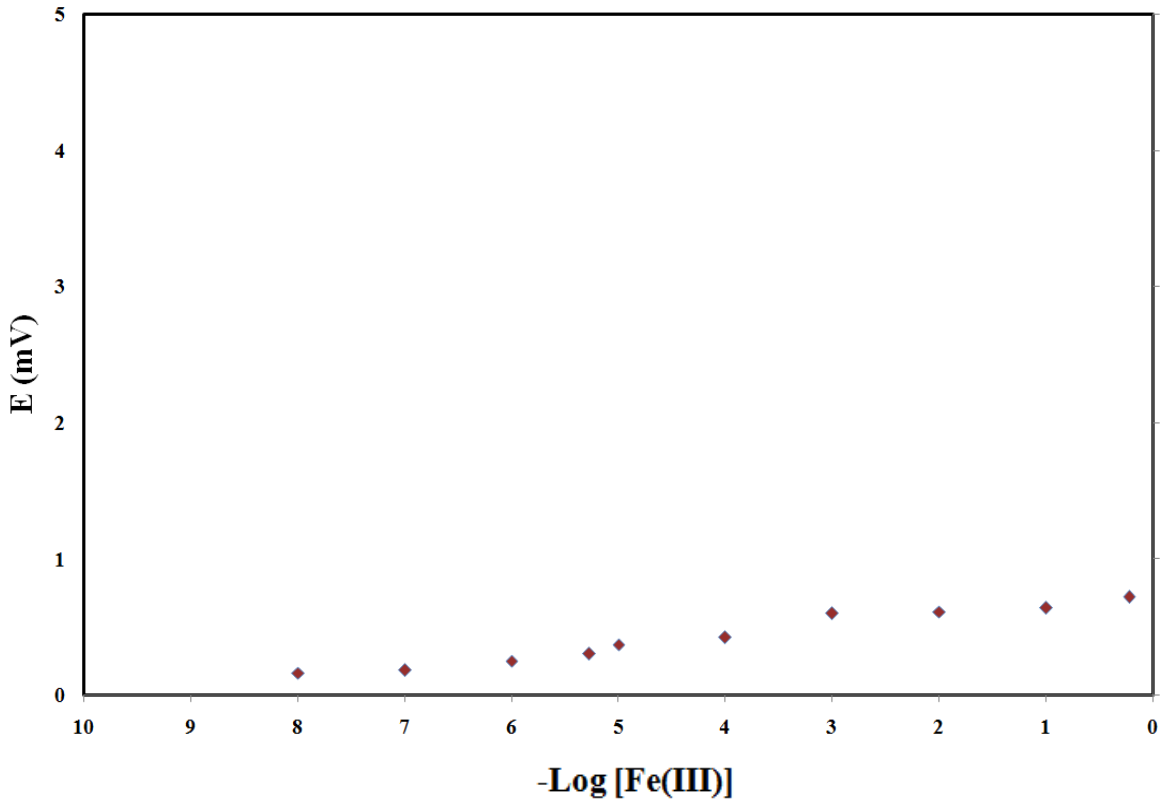

Figure 4.6. The potentiometric response to Fe(III) ions for a TiO_2 electrode without the desferal ionophore.

Although we were able to successfully fabricate a highly sensitive potentiometric sensor for quantification analysis of Fe^{3+} ions using desferal molecular receptors physisorbed onto the surface of nanostructured TiO_2 electrodes, we were looking for ways to improve the performance of our designed sensor in terms of getting a broader linear concentration range, lower detection limit, higher stability, and longer lifetime (see tables 4.12 and 4.14 for the results of the stability and lifetime studies of the sensors fabricated based on desferal-physisorbed onto TiO_2 electrodes).

These demands persuaded us to look for ways to chemically attach the desferal ligands onto the surface of nanostructured TiO_2 electrodes to see the effect of chemisorption on the performance of the sensor.

As mentioned before, in the present study, we used phosphonic acid molecules as linkers that self assemble onto the surface of TiO_2, to immobilize desferal ligands onto these electrodes. The functionalization of the TiO_2 substrates using SAMs of PAs of different alky chain lengths (short chain (3-C PA), medium chain (6-C PA), and long chain (11-C PA)) was studied in terms of preparation methodology, characterization, and their impact on the performance of the iron(III)-selective sensors.

4.3. ^{31}P NMR Spectroscopic Measurements

^{31}P Magic-Angle Spinning (MAS) NMR was used to investigate the binding of the phosphonic acid molecules employed to functionalize the surface of TiO_2 electrodes. solution phase ^{31}P NMR spectra of the parent phosphonic acids (3-C, 6-C, and 11-C PAs) in an ethanol solution were recorded. These experiments were followed by measuring the solid state ^{31}P MAS NMR spectra of the TiO_2 functionalized phosphonic acids (see figure 4.7).

It is noteworthy to mention that ^{31}P is a very sensitive nucleus with a spin of $\frac{1}{2}$, which makes it most strongly affected by the chemical shielding interactions. Chemical shifts in phosphonate compounds are sensitive to the number of titanium second neighbours. Hence each condensation between P-OH and Ti-OH groups should lead to an upfield shift, while the interactions of the P=O groups with surface Lewis acidic sites should lead to a downfield shift [181], also ^{31}P chemical shifts are sensitive to variations in the O-P-O bond angles.

Although SSNMR spectra are expected to be broad by nature, according to figure 4.7, our SSNMR spectra are significantly broad and seem to be overlay of a few lines, which is expected for phosphorous in a range of different environments [182]. As for the surface-bounded PAs, there exist multiple phosphorus sites. The broadening caused by the anisotropy produced severe overlap between the different environments which prevented unambiguous resolution of the different sites. Thus it is not possible to ascribe chemical shift values to different P-O-Ti, P=O, and P-OH sites, draw conclusions about percentages of these sites, and comment on different binding modes of the attached PA molecules on TiO_2.

For the surface-bonded PAs, the signals for the main resonance spectra (25.9-26.9 ppm) are shielded (shifted upfield) in comparisons with those of the correlated parent phosphonic acids (27.2-29.7 ppm), which can be indicative of condensations between P-OH and Ti-OH groups. Also, because the peaks are very broad, the downfield shifted expected peaks may overlap with the up-field shifted peaks corresponding to the binding of P=O with Ti atoms. The upfield component observed in the ^{31}P MAS NMR of the 3-C PA, (at - 6.5 ppm) might be attributed to bulk titanium phosphonates ($Ti(H_2PO_3)_2$) due to a dissolution-precipitation process, which may compete with surface modification even in the case of chemically stable TiO_2 [183]. Considering the excellent stability and low solubility of TiO_2, there results were ascribed to the cleavage of Ti-O-Ti bonds by 3-C-PA.

In 2008, Gervais *et al*. applied Gaussian-Lorentzian shapes to simulate the ^{31}P MAS NMR spectra of dodecylphosphonic acid monolayers on titania with a minimum number of resonances [155]. The results of the simulated spectra indicated the presence of at least three sites on the surface of titania [155]. As it was not possible to ascribe the simulated chemical shifts to each possible phosphorous site, the authors took advantage of high field ^{17}O MAS NMR (17.6 T) to study the attachment and binding modes of the ^{17}O enriched dodecylphosphonic acid.

This technique offered an excellent resolution between the different oxygen sites, P-O-H, P=O, and P-O-Ti, thus greatly facilitating their quantification [155].

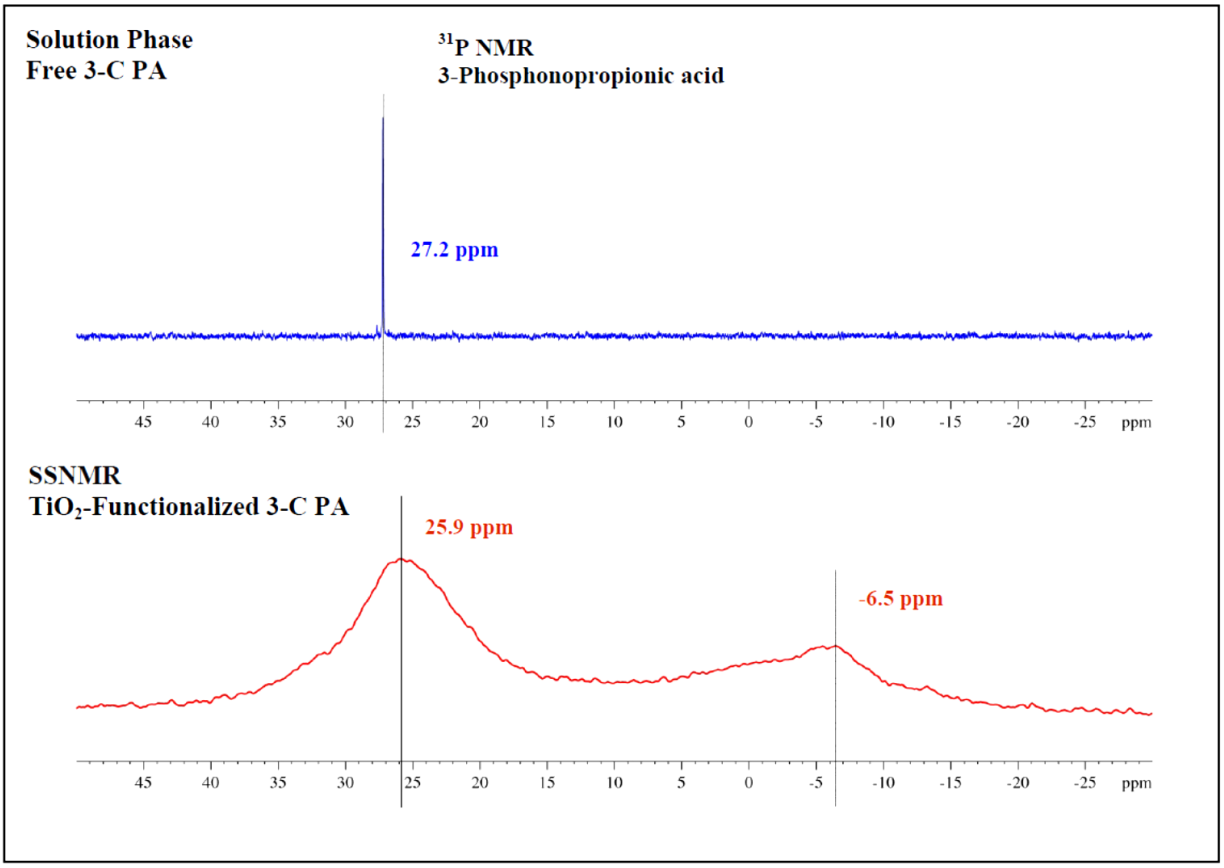

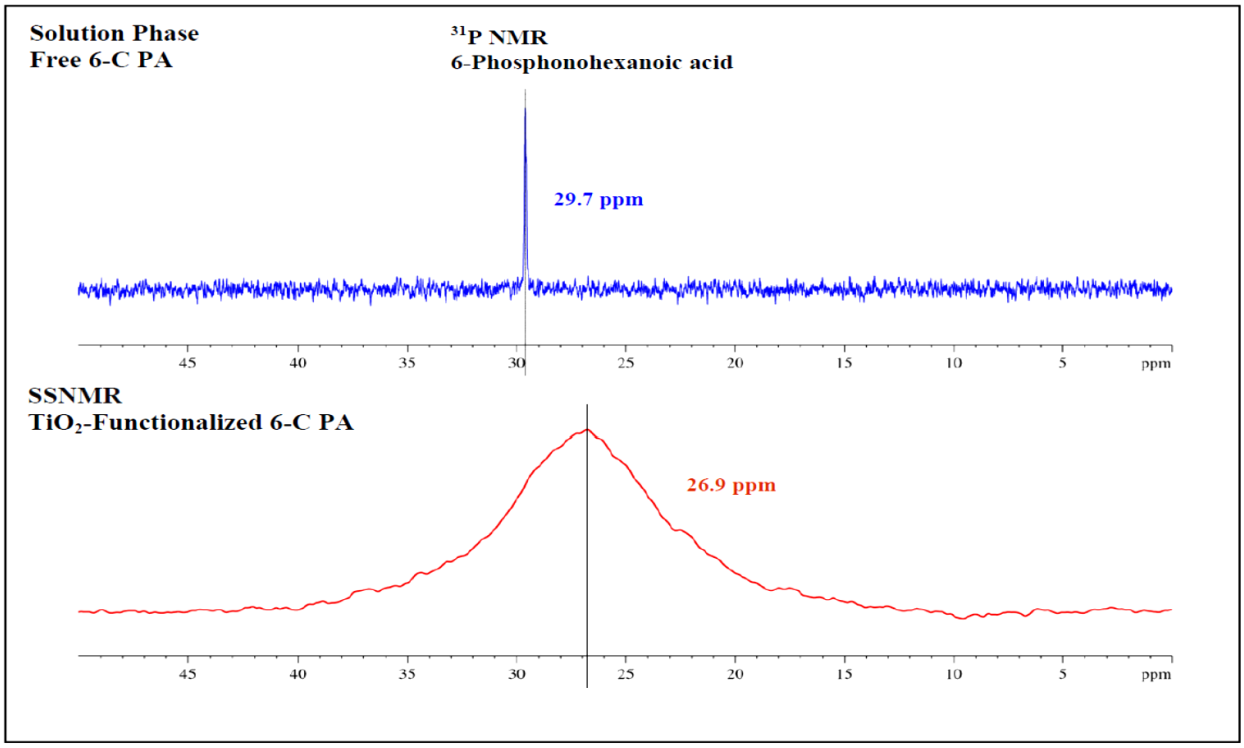

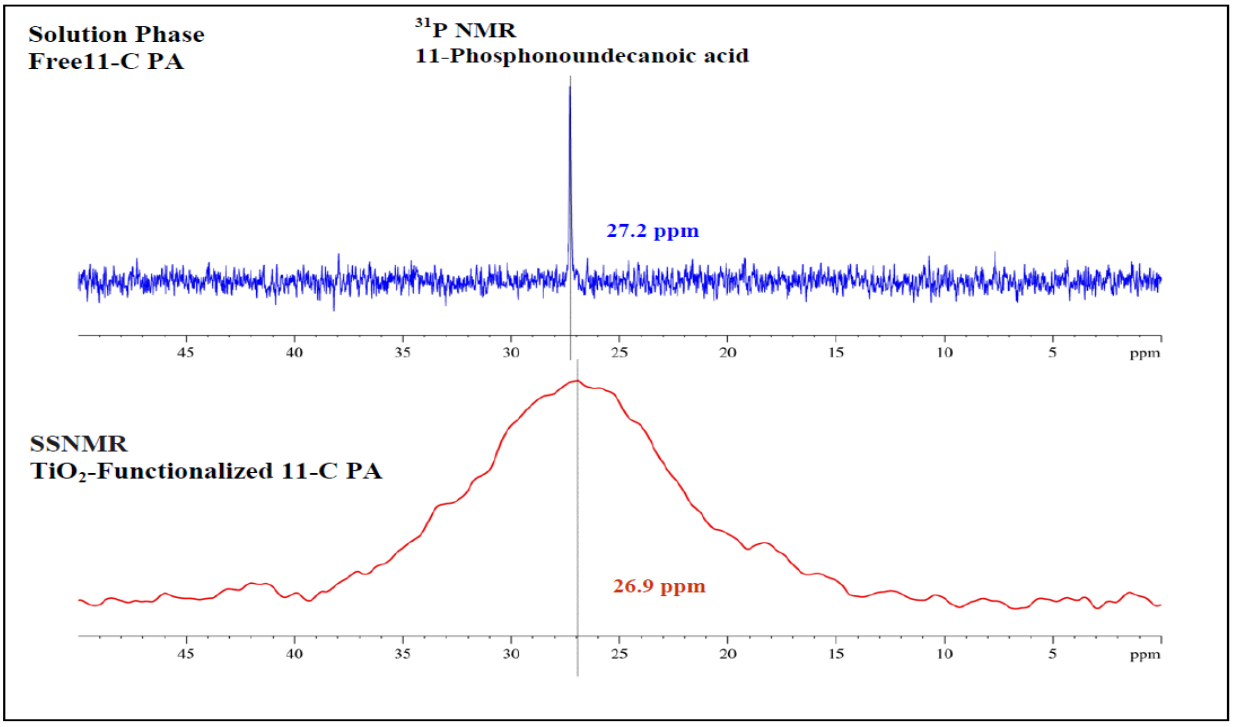

Figure 4.7. ^{31}P NMR spectra of the solution phase (blue), and TiO_2 bounded (red) phosphonic acids, for **(a)** 3-Phosphonopropionic acid, **(b)** 6-Phosphonohexanoic acid, **(c)** 11-Phosphonoundecanoic acid.

According to the results of ^{31}P NMR analysis, we can say that the SSNM spectra confirmed the presence of grafted phosphonate species.

4.4. SEM and EDX Analysis

The morphology of the unmodified and PA-modified TiO_2 electrodes were studied by scanning electron microscopy (SEM), in order to assure that the TiO_2 particles formed homogenous porous films, and also for comparison purposes (figures 4.8-4.11). As seen in the SEM images, in the case of the 11-C PA functionalized-TiO_2, some features were observed that were indicative of the aggregations of these molecules on the surface of TiO_2. This was not observed in the case of the 3-C as well as 6-C PA molecules.

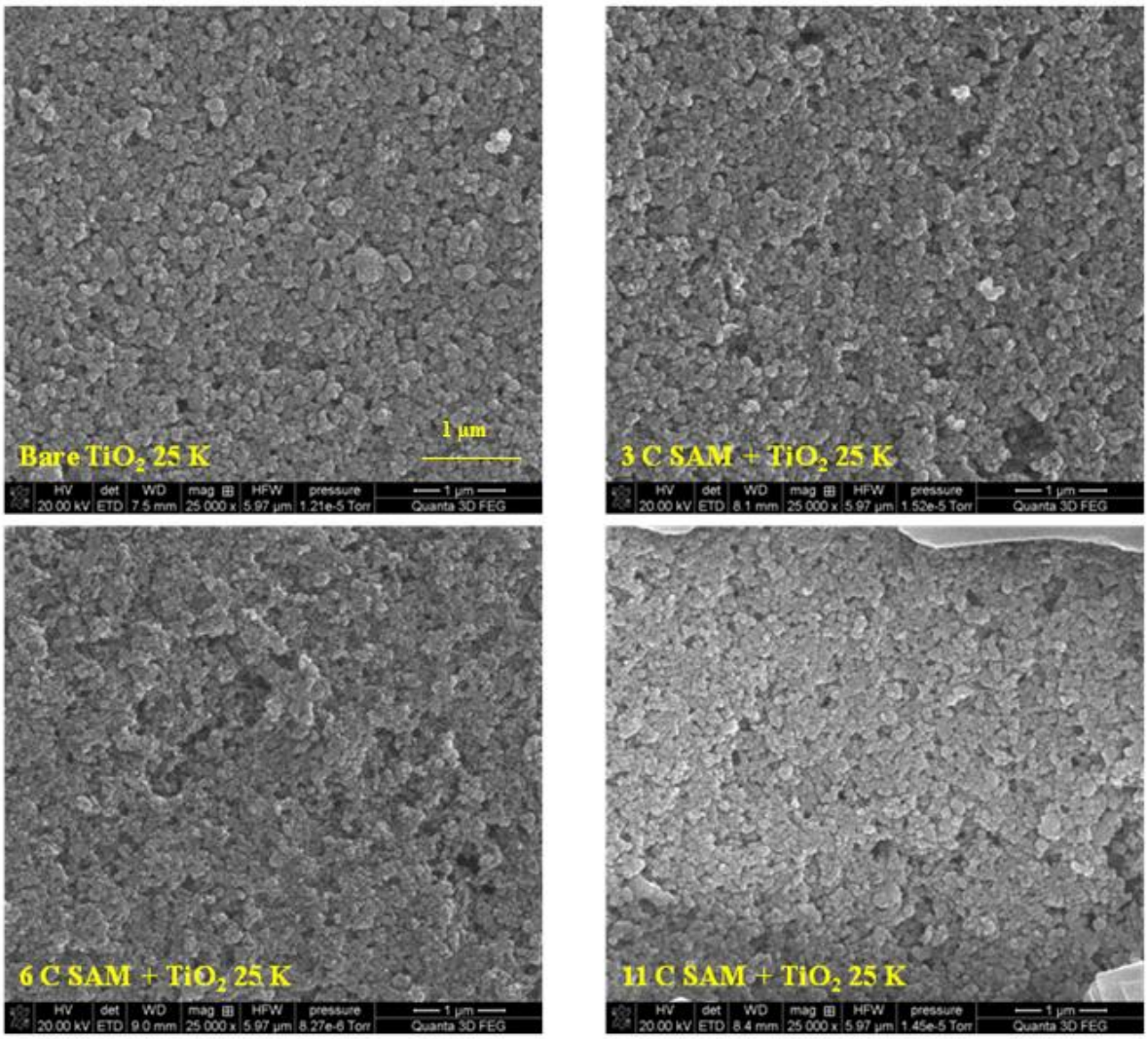

Figure 4.8. SEM images of bare TiO_2, as well as 3-C, 6-C, and 11-C PAs functionalized-TiO_2 electrodes, with 25 K magnification.

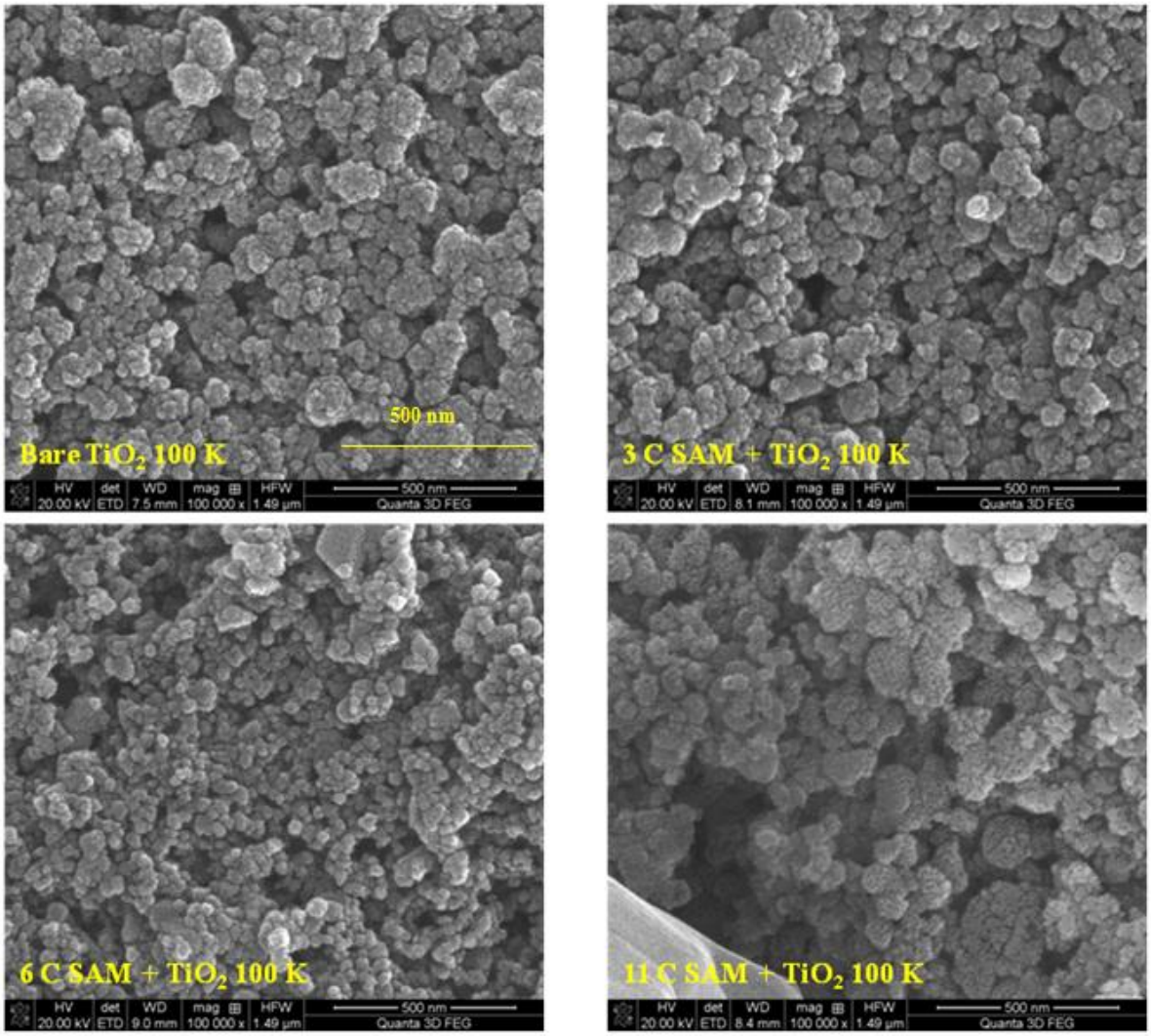

Figure 4.9. SEM images of bare TiO_2, as well as 3-C, 6-C, and 11-C PAs functionalized-TiO_2 electrodes, with 100 K magnification.

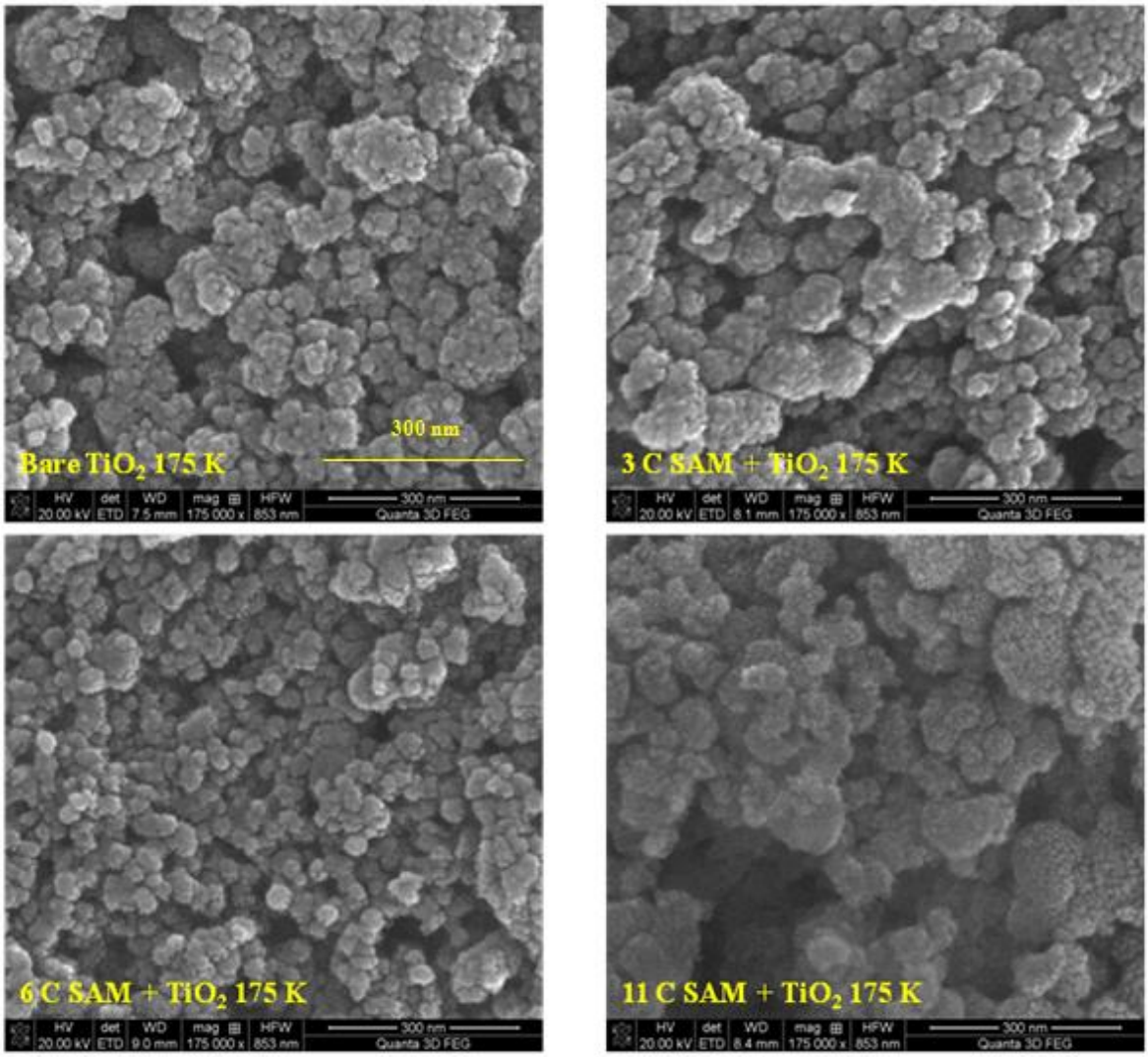

Figure 4.10. SEM images of bare TiO_2, as well as 3-C, 6-C, and 11-C PAs functionalized-TiO_2 electrodes, with 175 K magnification.

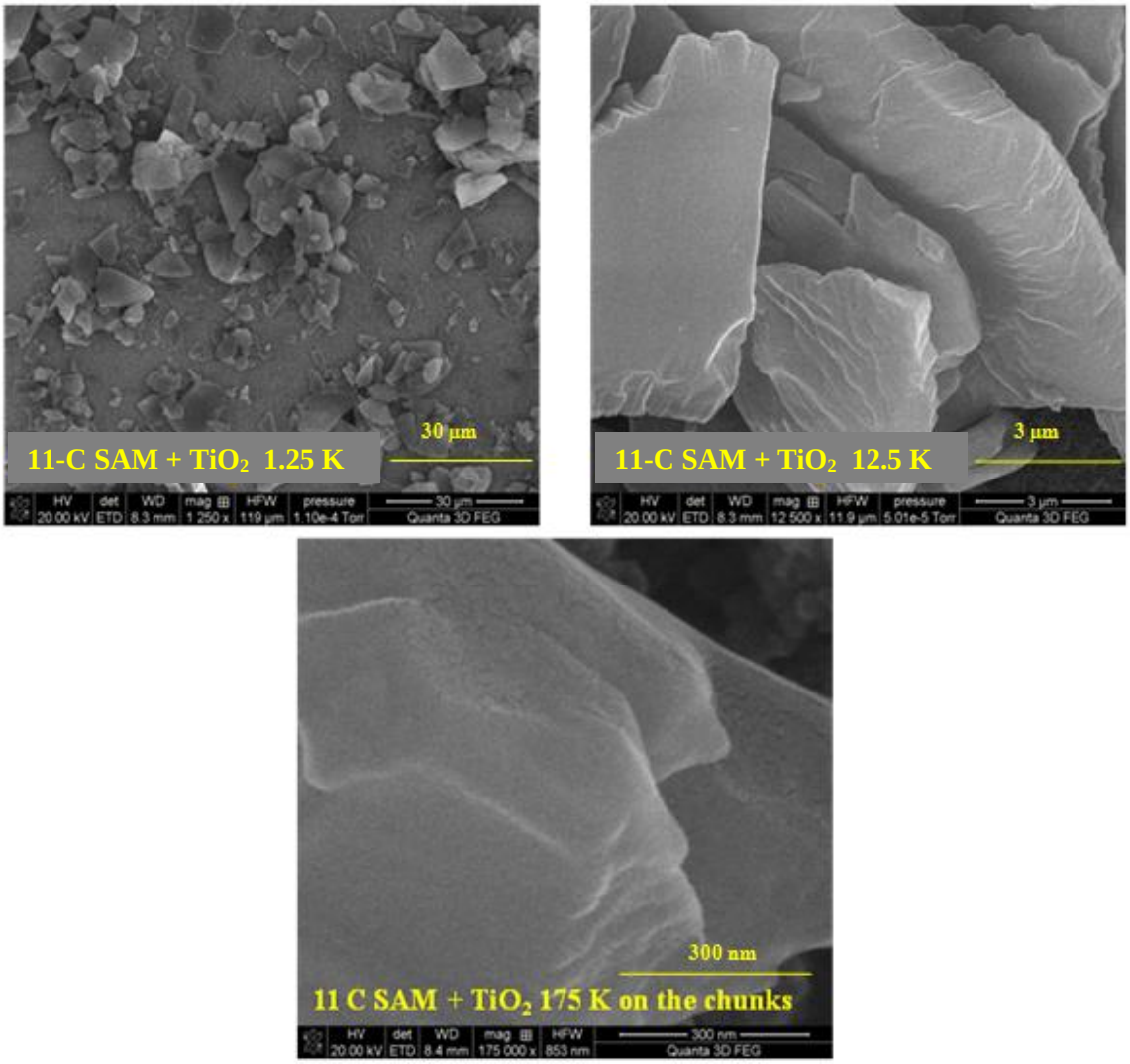

Figure 4.11. SEM images of 11-C PAs functionalized-TiO_2 electrodes with **(a)** 12.5 K, **(b)** 1.25 K, and **(c)** 175 K magnification.

The EDX analysis were performed by the same instrument used for SEM measurements and at the same time that the SEM images were recorded. As seen in the EDX spectra of the bare TiO_2, the titanium peaks are remarkably intense compared to the other peaks, and there are no peaks attributed to phosphorous and carbon. In addition, for the phosphonic acid-functionalized TiO_2 samples, the EDX patterns were different and indicative of the presence of phosphorous as well as carbon atoms on the surface. As seen, the intensities of both phosphorous and carbon peaks increase upon increasing the alkyl chain lengths of the phosphonic acid modifiers from 3 to 6, to 11 carbons (figure 4.12).

The increase in the intensity of the carbon peaks is in a good conformity with increasing the alkyl chain lengths of the phosphonic acids. Also according to the EDX analysis, it can be concluded that as the length of the alkyl chains increases, the amount of the phosphorous atoms also increases. This can be related to the fact that the longer chains are better able to self-assemble on the surface of TiO_2, as the reaction of long-chain alkylphosphonic acids with metal oxide supports leads to dense, well-ordered SAMs [143, 184]. This could be indicative of PA molecules aggregation at the surface of the TiO_2.

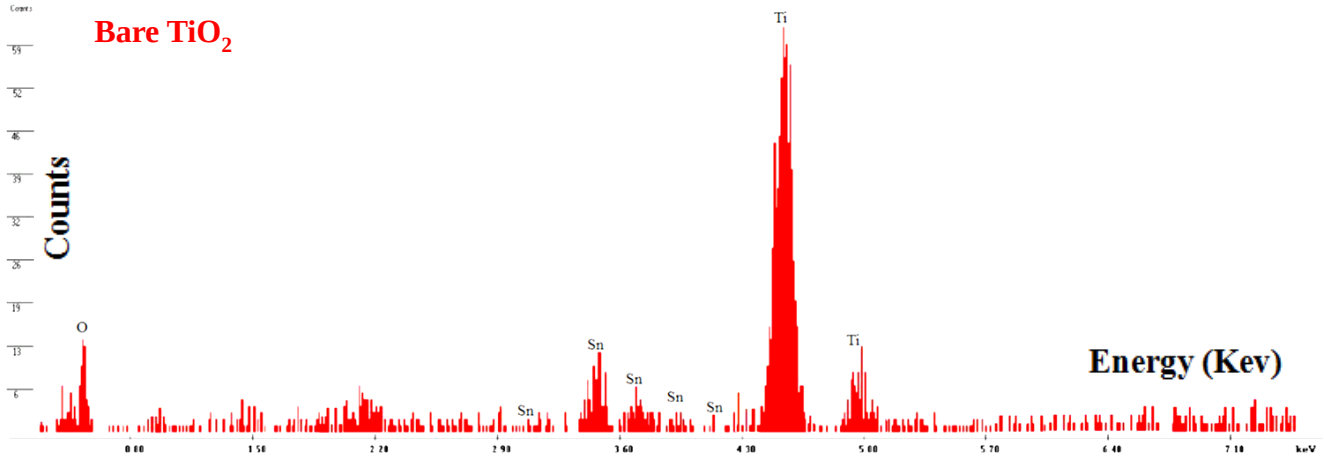

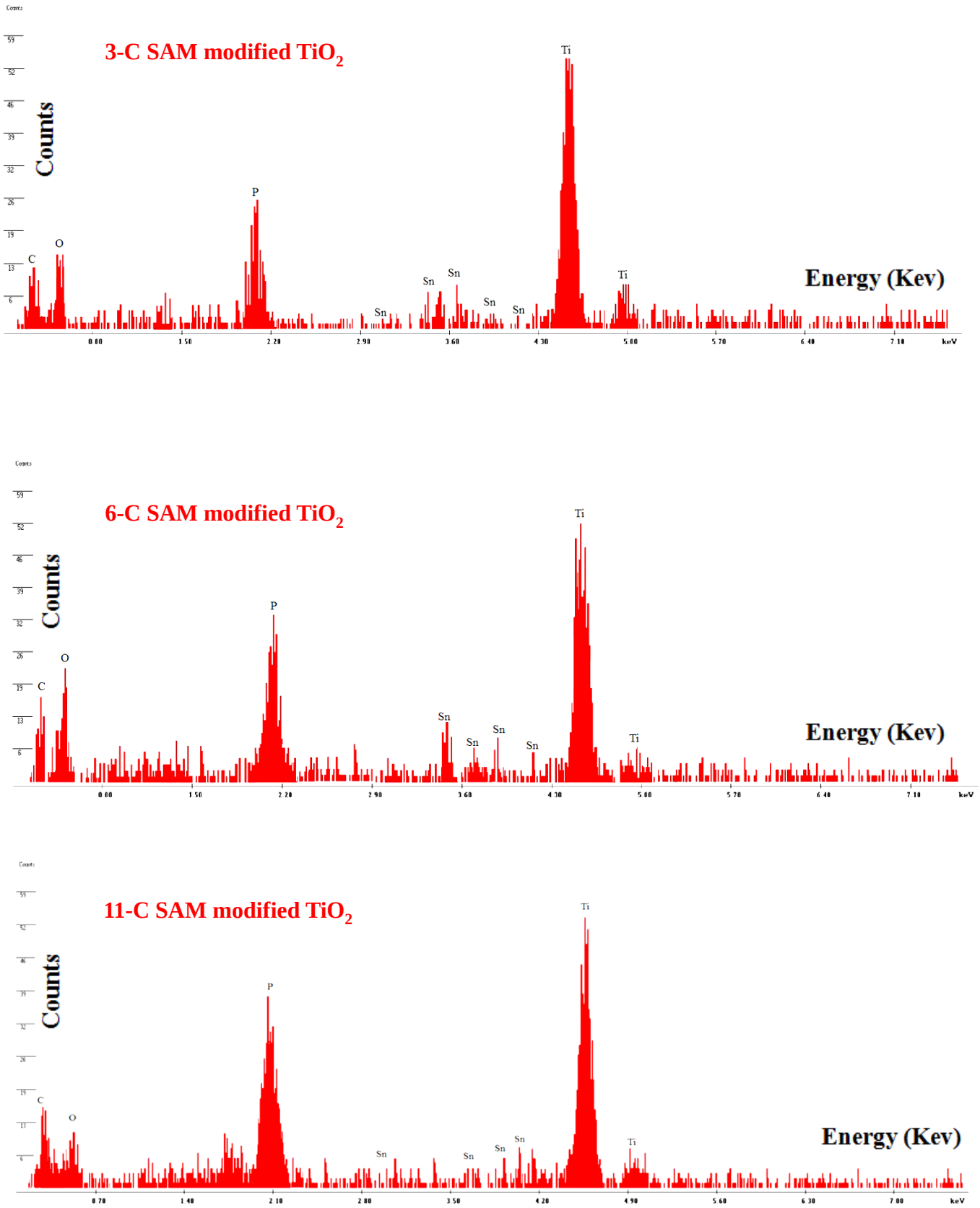

Figure 4.12. EDX spectroscopy measurements for bare TiO_2, as well as 3-C, 6-C, and 11-C PAs functionalized-TiO_2 electrodes.

It is important to note that EDX is a chemical-sensitive analysis technique. However, it is not always quantitative. In the case of porous substrates is it only semi-quantitative unless proper standards are used. EDX signal intensities for different elements also depend on different factors such as: 1) homogeneity of the substrate (as the variations in the surface density can cause variations in signal intensities); 2) chemical environment of the elements; and 3) the lower detection limit of each element in EDX. This is because the detection of the EDX signal depends on the ability of each element to absorb high-energy electrons and emit X-rays that are detectable under these experimental conditions.

4.5. AFM Measurements

Atomic Force Microscopy was used to study self-assembly of the applied phosphonic acids on TiO_2 electrodes. The AFM images of the bare TiO_2, as well as PAs-modified TiO_2 electrodes were obtained, and their surface morphologies were compared. As the AFM micrographs illustrate, it is clear that the morphology of the TiO_2 electrodes change due to their surface modification with phosphonic acids of various alkyl chain lengths (figure 4.13).

The height histograms show that the average measured height of the surfaces increased upon increasing the alkyl chain lengths of the modifiers.

Bare TiO_2

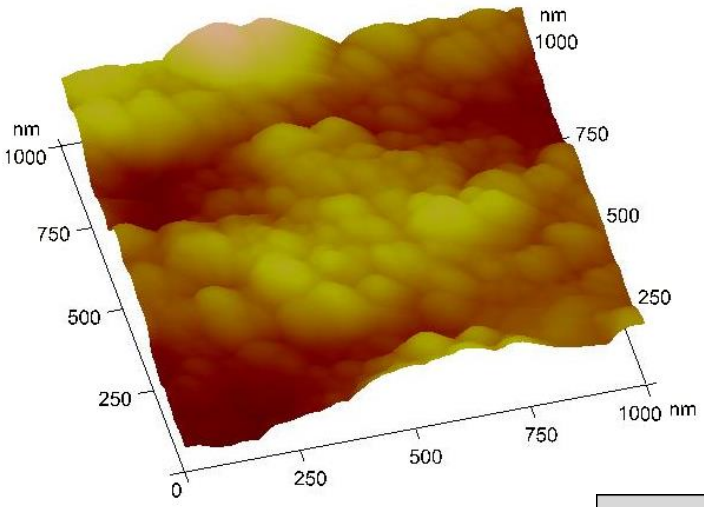

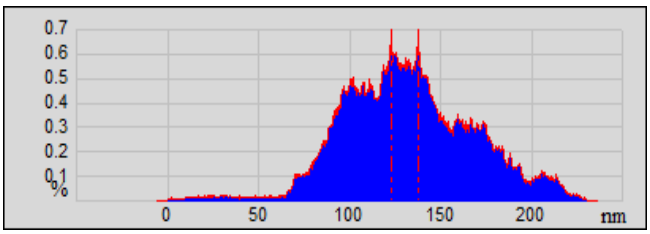

Depth at histogram maximum : 128.639 nm

3-C SAM modified TiO_2

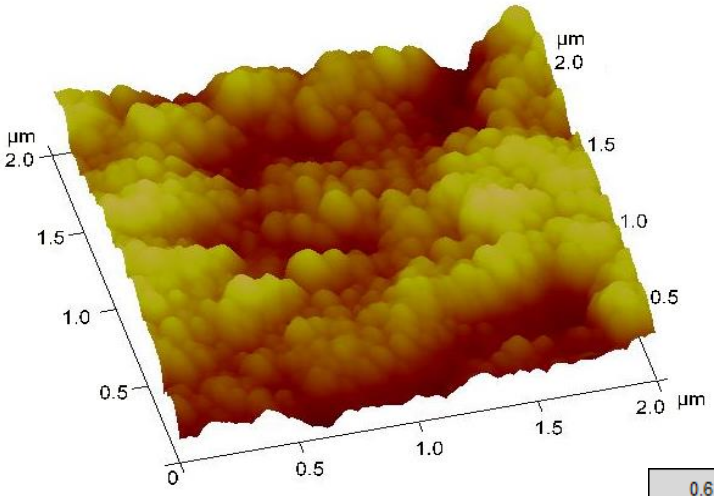

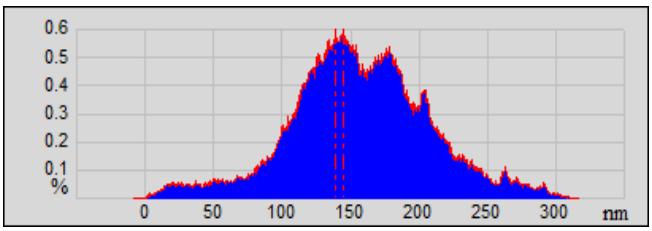

Depth at histogram maximum : 146.609 nm

6-C SAM modified TiO_2

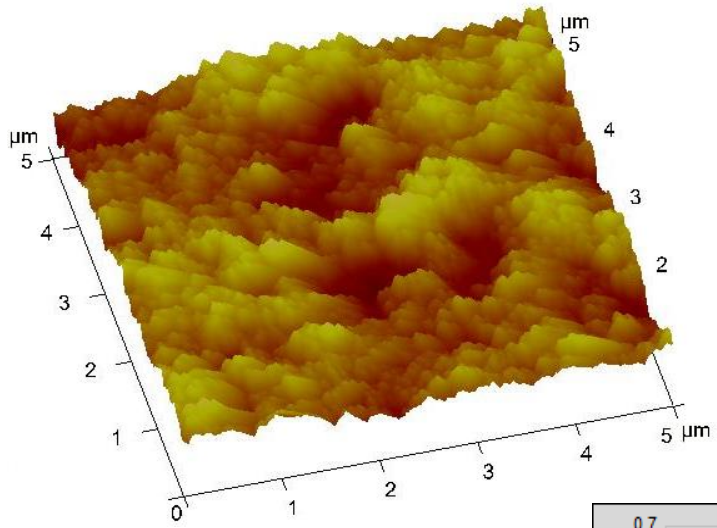

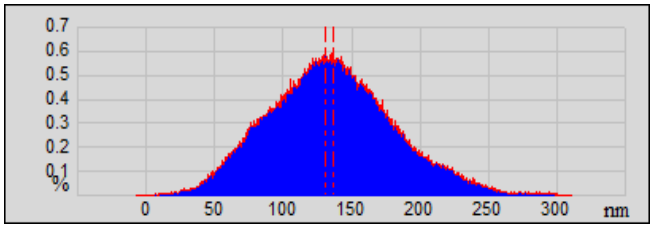

Depth at histogram maximum : 152.231 nm

11-C SAM modified TiO_2

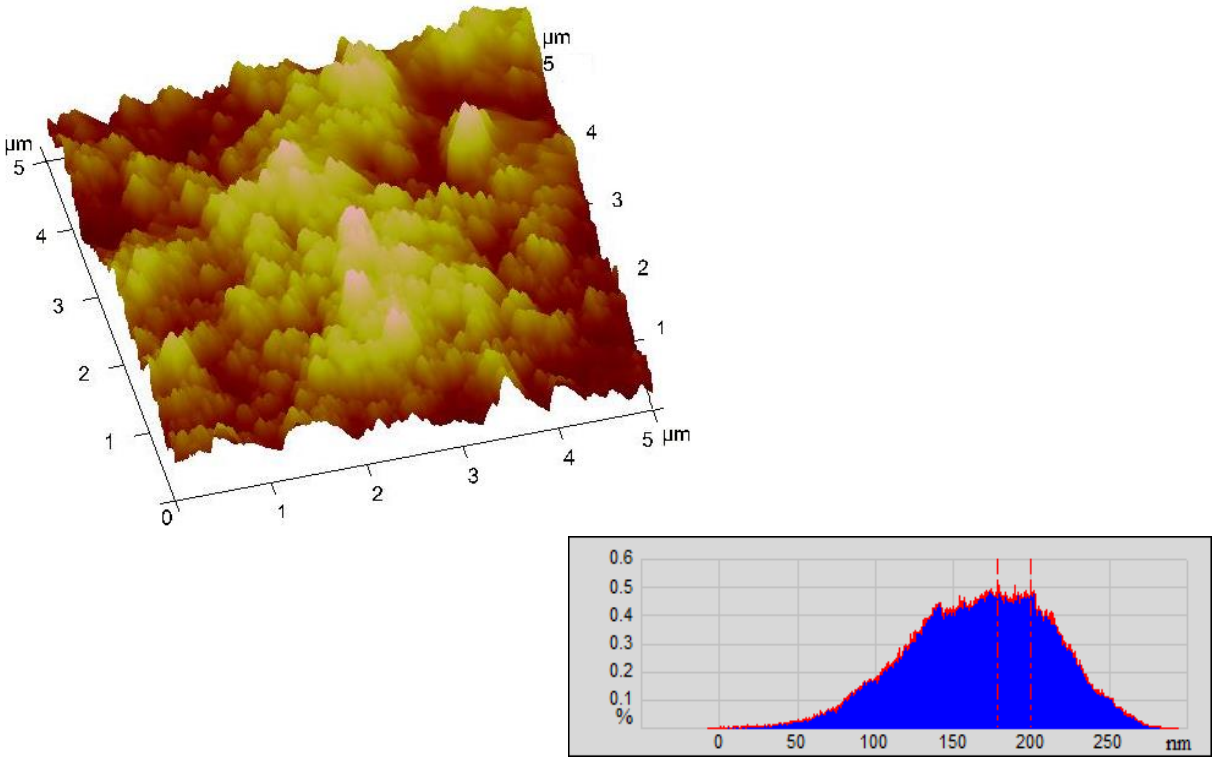

Depth at histogram maximum : 185.755 nm

Figure 4.13. AFM images of bare TiO_2, as well as 3-C, 6-C, and 11-C PAs functionalized-TiO_2-electrodes.

From these images we could not successfully confirm the adsorption of the short, medium, and long alkyl chain phosphonic acids on the surface of TiO_2 electrodes since individual molecules cannot be imaged. However, the lack of changes in the sample morphology between the bare TiO_2 and the surfaces modified with 3-C and 6-C indicates that the layers formed are homogeneous. The change in morphology observed for the surface modified with 11-C supports our conclusion that multilayers and aggregation occurs for that sample. The impact of using

different PAs and the surface aggregations on the performance of our Fe(III)-selective sensor was studied as will be shown in the following sections.

4.6. FTIR Spectroscopic Measurements

As mentioned earlier in the experimental section, the first set of FTIR experiments was carried out by recording the IR spectra of the bare TiO_2 as well as desferal-physisorbed TiO_2 electrodes, followed by immersing the modified electrode into a 1.000×10^{-4} M aqueous solution of Fe(III) to be analyzed for FTIR measurements. Figure 4.14 shows the IR spectrum (in nujol mull) of 3-phosphonopropionic acid (3-C PA) solid sample according to Spectral Database for Organic Compounds (SDBS).

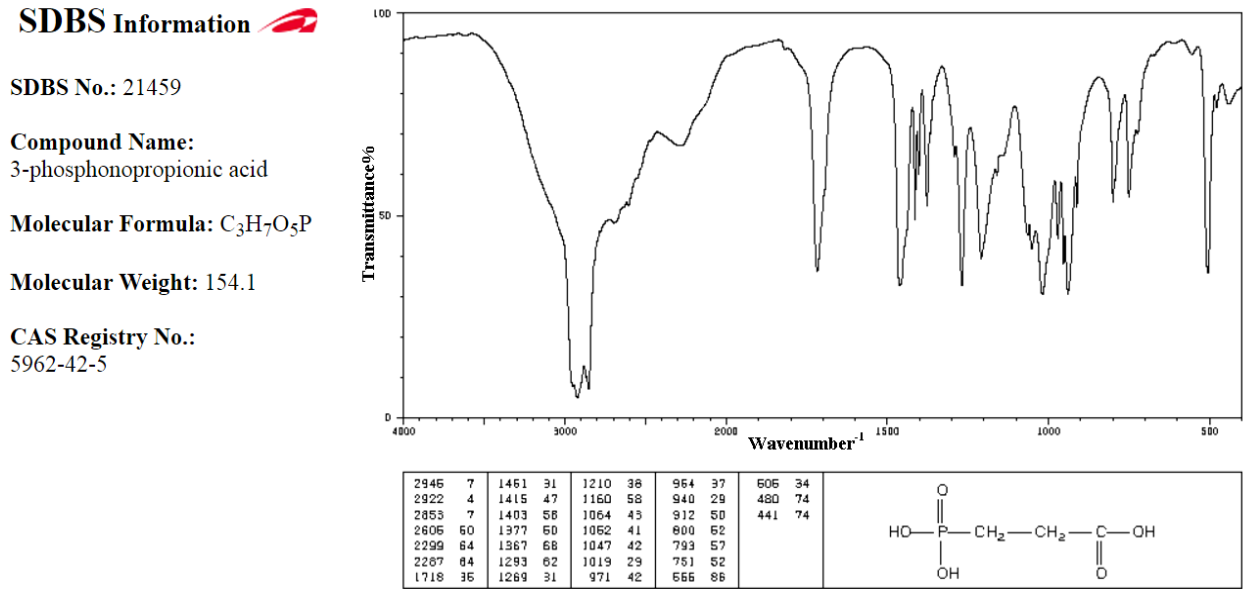

Figure 4.14. IR spectra of 3-phosphonopropionic acid (3-C PA) powder based on SDBS [185].

Figure 4.15 (a) is indicative of the FTIR spectra of every step taken in the preparation of desferal-physisorbed TiO_2 substrates as well as the effect of Fe^{3+} complexation on the spectra of desferal-physisorbed TiO_2 electrode. This figure includes the FTIR spectra of bare TiO_2 electrode, the free ligand (desferal) as a powder, desferal-modified TiO_2 electrode, and the latter sample upon immersing in iron solution. Table 4.3 shows the band assignments as well as the correlated frequencies associated with the labeled peaks in figure 4.15 (a).

Upon Fe^{3+} chelation, oxygen atoms of the hydroxamate groups bind to iron (as shown in the index of figure 4.15 (a)), three hydroxyls are deprotonated, and three identical asymmetrical chelation rings are formed, creating a distorted octahedron centered on the Fe ion [112]. As seen in the FTIR spectra in figure 4.15 (a), the most conspicuous effect of iron chelation on the spectra is a decrease in the frequency of the band assigned to the stretching vibrations of hydroxamate C=O bond (peaks G) from 1626 cm^{-1} to 1620 cm^{-1}, which is in a good agreement with the structure of the desferal-iron complex. This decrease in the frequency of the carbonyl band of the hydroxamate group, can be related to the resonance in the chelating ring, which gives rise to its single bond (C-O) character.

Label	Band Assignment	Frequency (Wavenumber, cm^{-1})
A	O-H Stretch of water molecules and free surface O-H on the surface of TiO_2	3000 - 3550
B	-Ti-O-Ti Bending vibrations (Broad band)	600-900
C	N-H Stretch from Amide (2^o) hydrated	3313
D	O-H Stretch from N-OH	3100
E	CH_2 Stretch	2850 & 2972
F	C=O Stretch (Secondary amide)	1684-1690
G	C=O Stretch (Hydroxamate)	1620-1626
H	C-N-H Bending (Secondary amide)	1564
I	C-H Bending	1458
J	C-N Stretch N-H Bend (Secondary amide)	1250
K	C-N Stretch (Amine & Amide)	1159
L	N-O Stretch	963
M	Ti-O-H Bending vibrations	1020-1091

Table 4.3. FTIR band assignments for the peaks labelled on figure 4.15 (a).

The second, third and fourth sets of experiments were conducted starting from recording the FTIR spectra of the bare TiO_2 electrodes, continuing with modifying the electrodes with the 3-C, 6-C, and 11-C PA molecules, respectively, and recording their IR spectra. Afterwards, the PA-

modified samples were used for immobilization of desferal ligand onto the surface of TiO_2 electrodes and the samples were analyzed for the FTIR measurements before and after immersing them in an iron solution, and the results are shown in figures 4.15 (b, c, d) for 3-C, 6-C, and 11-C PA modifiers, respectively. These figures consist of the FTIR spectra of bare TiO_2 electrodes, the PAs-modified electrodes, the ligand immobilized-PAs-modified electrodes, and the latter samples upon immersing in a 1.000×10^{-4} M aqueous solution of Fe(III). Tables 4.4-4.6 show the band assignments as well as the correlated frequencies associated with the labeled peaks in figures 4.15 (b-d), respectively.

Label	Band Assignment	Frequency (Wavenumber, cm^{-1})
A_1	O-H Stretch of water molecules and free surface O-H on the surface of TiO_2	3000 - 3550
B_1	–Ti-O-Ti Bending vibrations (Broad band)	600-900
C_1	CH_2 Stretch	2880 & 2952
D_1	C=O Stretch (Carboxylic acid)	1740
E_1	C-H Bending	1423
F_1	C-O Stretch (Carboxylic acid)	1313
G_1	P=O	1250
H_1	Ti-O-P Bending vibrations	900-954
I_1	Overlapping of C=O Stretch (Hydroxamate) & C=O Stretch (Secondary amide) (broad band)	1553-1650

Table 4.4. FTIR band assignments for the peaks labelled on figure 4.15 (b).

According to figure 4.15 (b) and table 4.4, we can conclude that firstly the intensity of the D_1 peak, which appeared due to the C=O stretching vibrations from the carboxyl terminus of the 3-C PA molecules, decreases upon its anchoring to the desferal ligand. This supports the hypothesis that many of those carboxyl functional groups have attached to the $-NH_2$ functional groups from the desferal ligand molecules by forming an amide bond. Secondly, the broad peak labeled I_1 on the FTIR spectra of desferal chemisorbed-3-C PA-modified TiO_2. This is expected to be an overlap of stretching vibrations of C=O bonds from hydroxamate as well as that of amide secondary amide groups, shifts to lower frequencies (from 1600 cm^{-1} to 1553 cm^{-1}) upon immersing the electrode in a 1.000×10^{-4} M aqueous solution of Fe(III), which confirms the complexation of iron with the desferal immobilized-TiO_2 electrode. Thirdly the peak labeled M that was ascribed to Ti-O-H bending vibrations (1020 - 1091 cm^{-1}) in figure 4.15 (a), shifted to lower frequencies. This peak was labeled H_1 in figure 4.15(b) (900-954 cm^{-1}) and it is assigned to the formation of Ti-O-P bonds, and confirmed the chemisorption of the 3-C PA molecules on the surface of TiO_2. [127].

Label	Band Assignment	Frequency (Wavenumber, cm^{-1})
A_2	O-H Stretch of water molecules and free remained surface O-H on the surface of TiO_2	3000 - 3550
B_2	–Ti-O-Ti Bending vibrations (Broad band)	600-900
C_2	CH_2 Stretch	2885 & 2920
D_2	C=O Stretch (Carboxylic acid)	1747
E_2	C-H Bending	1400
F_2	C-O Stretch (Carboxylic acid)	1305
G_2	P=O	1231
H_2	Ti-O-P Bending vibrations	876-900
I_2	Overlapping of C=O Stretch (Hydroxamate) & C=O Stretch (Secondary amide) (broad band)	1550-1689

Table 4.5. FTIR band assignments for the peaks labeled on figure 4.15 (c).

One can also observe that upon changing the phosphonic acid modifiers from short (3-C PA) to medium (6-C PA), and to long (11-C PA) chain molecules, the intensity of the peaks associated with the CH_2 stretching vibrations increases (from C_1 in the FTIR spectra of the 3-C PA-modified TiO_2 to C_2 in the FTIR spectra of the 6-C PA-modified TiO_2, and to C_3 in the FTIR spectra of the11-C PA-modified TiO_2). These observations are consistent with the chemical structures of the PA molecules and the increase in their alkyl chain length.

Label	Band Assignment	Frequency (Wavenumber, cm^{-1})
A_3	O-H Stretch of water molecules and free remained surface O-H on the surface of TiO_2	3000 - 3550
B_3	⁻Ti-O-Ti Bending vibrations (Broad band)	600-900
C_3	CH_2 Stretch	2889 & 2945
D_3	C=O Stretch (Carboxylic acid)	1750
G_3	P=O	1249
H_3	Ti-O-P Bending vibrations	883-900
I_3	Overlapping of C=O Stretch (Hydroxamate) & C=O Stretch (Secondary amide) (broad band)	1552-1625

Table 4.6. FTIR band assignments for the peaks labelled on figure 4.15 (d).

As can be seen in the FTIR spectra, the M peak in figure 4.15 (a), (due to the Ti-O-H bending vibrations (1091 cm^{-1})), was also shifted to lower frequencies due to the chemisorption of 6-C PA as well as 11-C PA molecules on the surface of TiO_2, which was labeled as H_2 and H_3 in figures 4.15 (c) and 4.12 (d), respectively (as it was the case for 3-C PA). These shifts can be indicative of the formation of Ti-O-P bonds.

Also as seen in the cases of the desferal-physisorbed TiO_2 electrode and desferal immobilized-3-C PA-modified TiO_2 electrode (figures 4.15 (a, b)), the frequency of the bands associated with the stretching vibrations of C=O bonds from the hydroxamate groups decreased

upon chelation of the desferal immobilized-6-C (and -11-C)-modified TiO_2 substrates with Fe^{3+} (as is clear from bands I_2 and I_3, in figures 4.15 (c) and (d), respectively).

The data reported here give direct evidence of the extensive formation of Ti-O-P bonds in the surface modification of titania by phosphonic acids, and also confirm that the complexation of iron by desferal ligand takes place from the oxygen atoms of the hydroxamate groups. This is whilst due to the multiplicity of the functional groups and significant overlapping of their related IR bands, it is hard to identify every single characteristic bands in the recorded FTIR spectra. For example the O-H stretching vibrations on P-O-H bond generally show a broad IR band around 1600-1740 cm^{-1} [127], which remarkably overlaps with the band associated with C=O stretching vibrations as well as bending mode of amide groups (NH), Therefore it is impossible to comment on the presence of residual P=O and P-O-H sites and draw conclusions on the binding modes of PAs on TiO_2 only on the basis of FTIR spectroscopy studies.

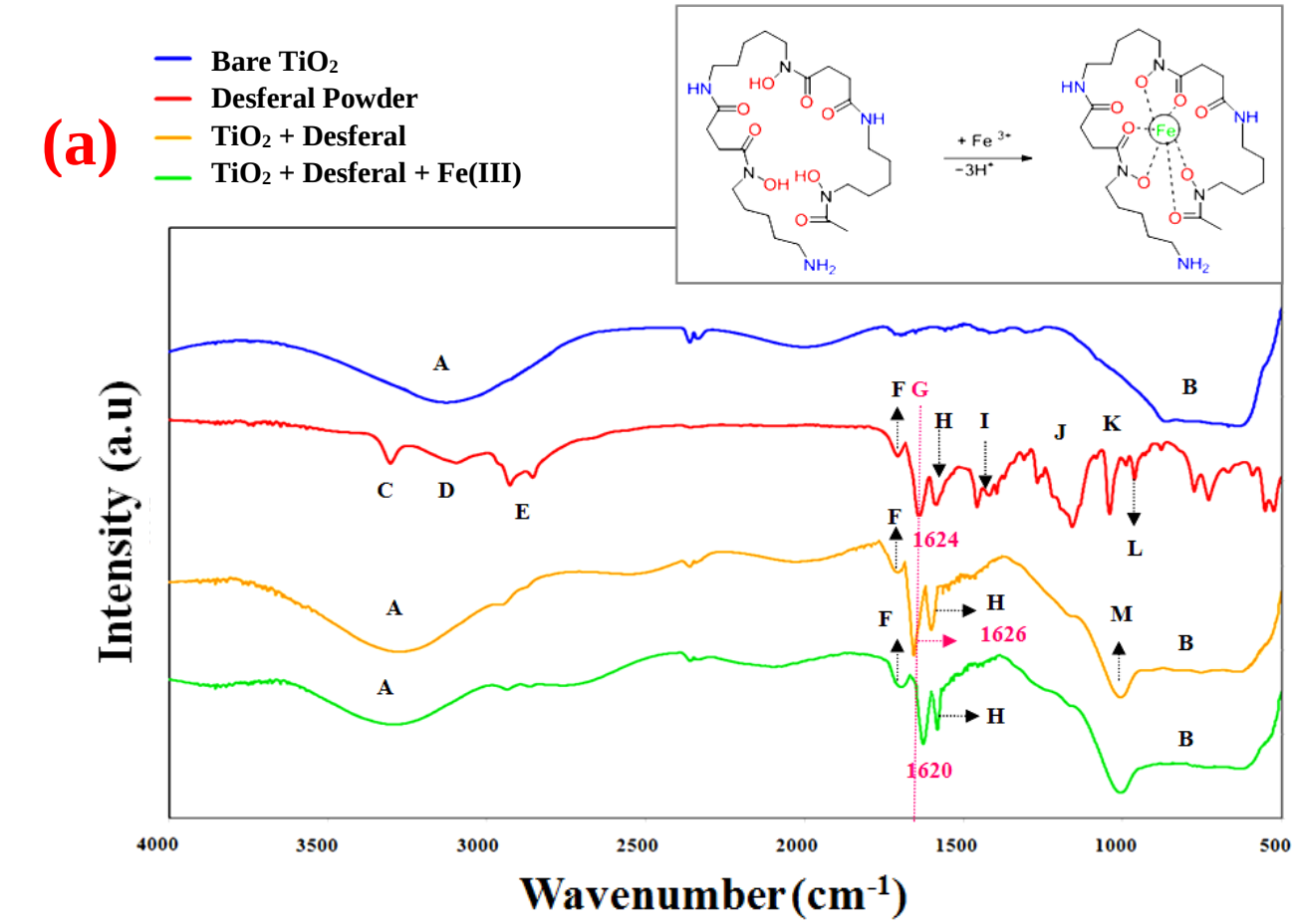
(a)
Bare TiO2
Desferal Powder
TiO2 + Desferal
TiO2 + Desferal + Fe(III)
+ Fe 3+
−3H+
Intensity (a.u)
Wavenumber (cm-1)
4000
3500
3000
2500
2000
1500
1000
500
1624
1626
1620

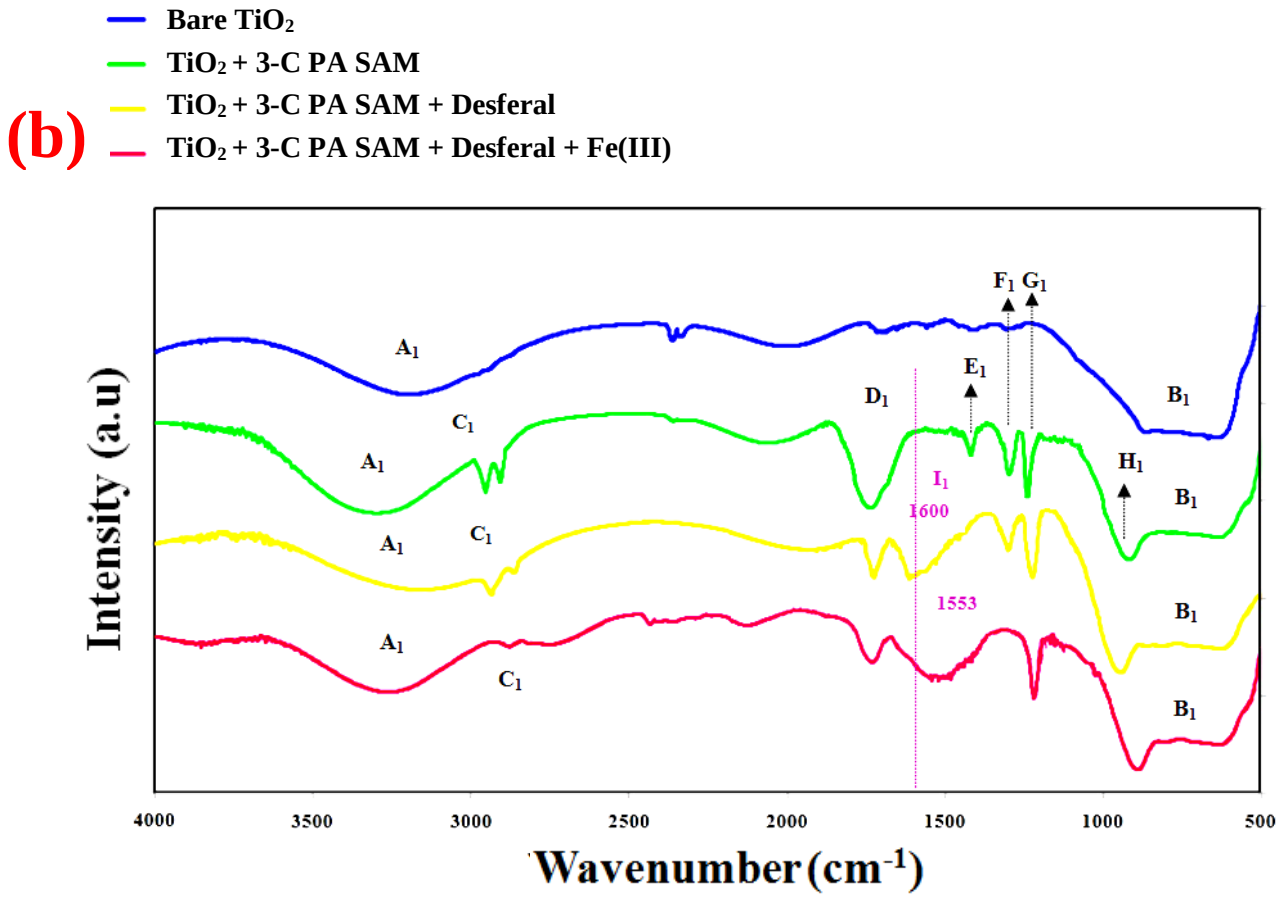
(b)
Bare TiO2
TiO2 + 3-C PA SAM
TiO2 + 3-C PA SAM + Desferal
TiO2 + 3-C PA SAM + Desferal + Fe(III)
Intensity (a.u)
Wavenumber (cm-1)
4000
3500
3000
2500
2000
1500
1000
500
1600
1553

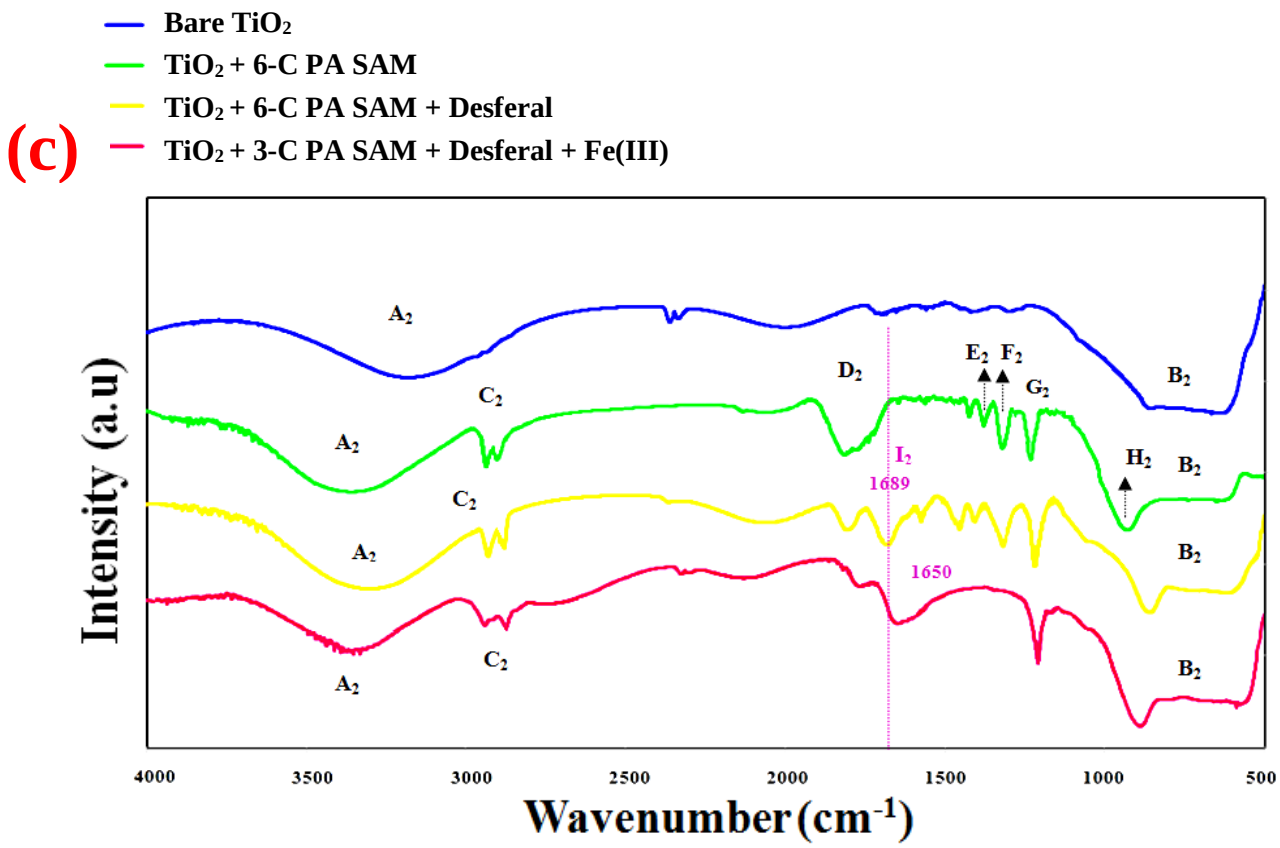

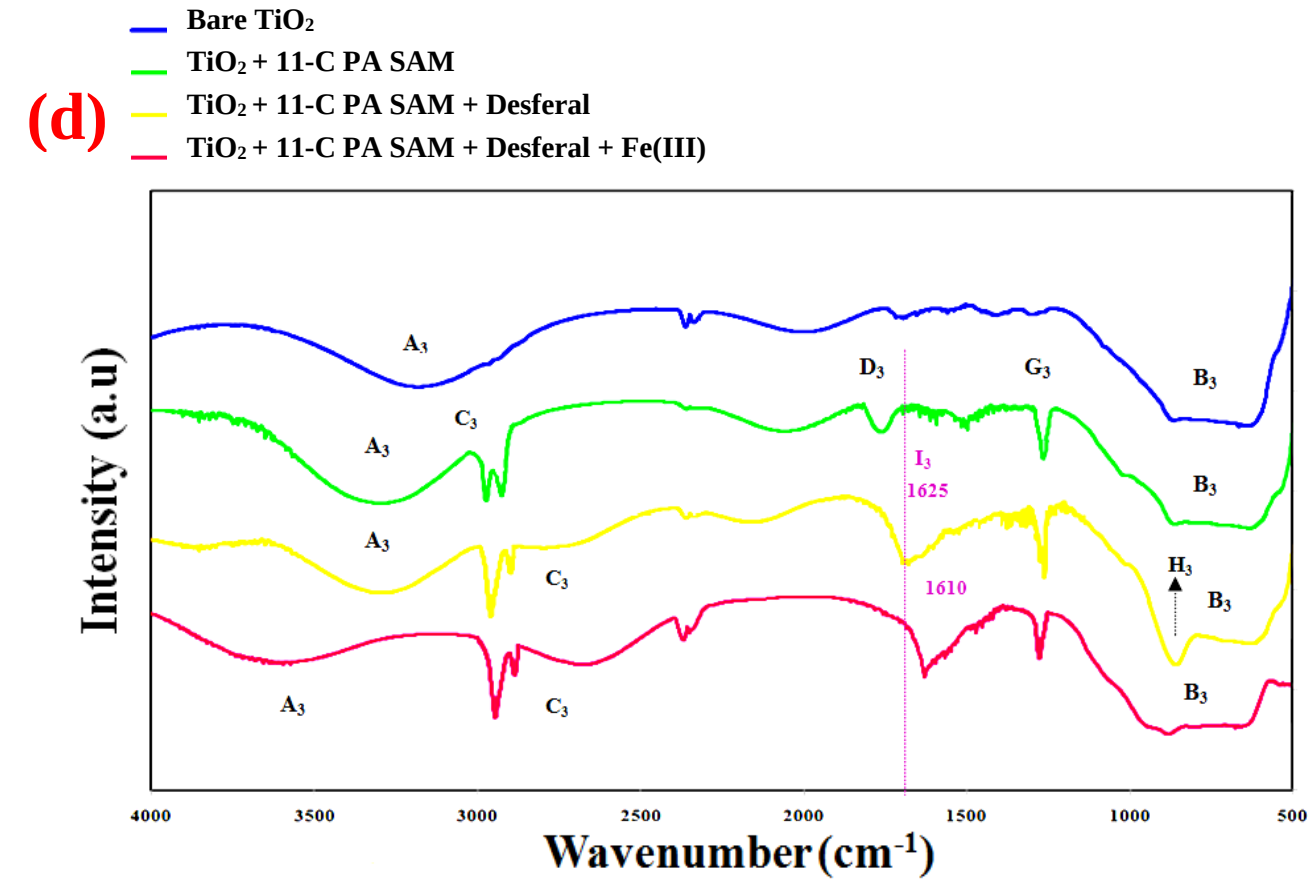

Figure 4.15. FTIR spectra of different experimental steps taken in the preparation of **(a)** desferal-physisorbed TiO_2, **(b-d)** desferal chemisorbed-TiO_2 via 3-C, 6-C, and 11-C PAs linkers, respectively, as well as the effect of Fe^{3+} chelation on their IR spectra.

4.7. EMF measurements for Fe(III)-Selective Sensors Based on Desferal-Chemisorbed on TiO_2 Electrodes

Using the electrodes based fabricated on the chemisorbed ionophores, the potentiometric measurements were repeated, using the same strategy as employed in chapter 3. The EMF measurements as a function of logarithm of Fe(III) concentrations for the 3-C-, 6-C-, and 11-C-PA modified TiO_2 electrodes revealed linear potential responses (as reported in figures 4.16-4-18 and summarized in table 4.10).

Figure 4.16 is indicative of the potentiometric response of the Fe(III)-selective sensor designed based on desferal-chemisorbed onto TiO_2 electrodes via 3-C PA linker assemblies.

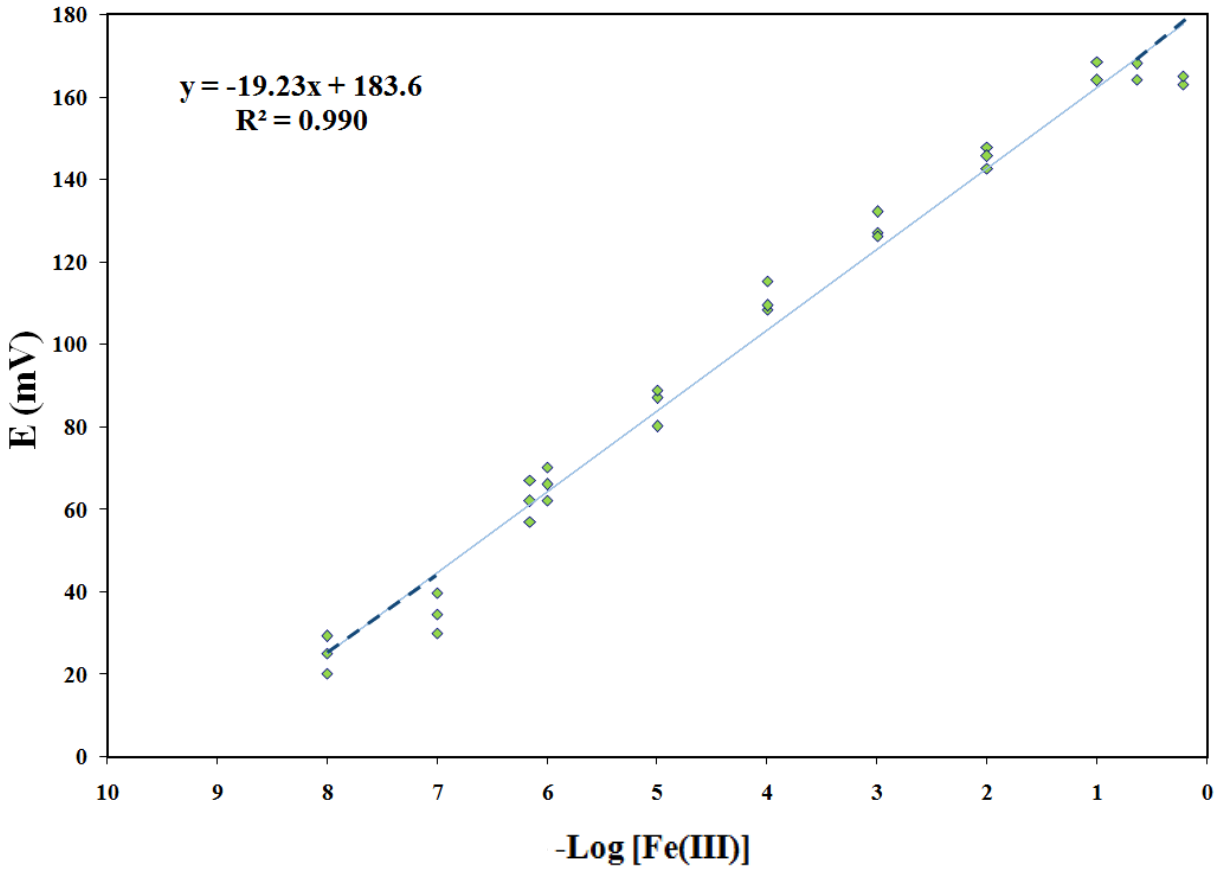

Figure 4.16. Calibration plot for iron(III) ion selective electrode based on desferal-chemisorbed onto TiO_2 electrodes via 3-C PA linker.

As the graph shows, the Nernstian response was obtained in the iron concentration range of 7.000 (± 0.040) × 10^{-7} to 2.300 (± 0.02) × 10^{-1} M, and the absolute value of the slope of this plot was measured to be 19.23 ± 0.48 mV per decade of Fe^{3+} concentration. The limit of detection of iron was determined to be 1.000 (± 0.500) × 10^{-8} M for the sensors fabricated based on desferal chemisorbed onto TiO_2 electrodes via 3-C-PA linkers. The values of X and Y errors shown on this calibration graph (figure 4.16) are summarized in table 4.7. As expected the error in the concentration is negligible in comparison with the error on the potential.

[Fe^{3+}]		**Error in the values of the X-Axis**	**SD_{sample} in the values of the Y-Axis**	**SD_{mean} in the values of the Y-Axis**
1.000 × 10^{-8} M	M_{11}	0.009	4.50	2.60
1.000 × 10^{-7} M	M_{10}	0.008	4.56	2.63
7.000 × 10^{-7} M	M_9	0.007	5.01	2.88
1.000 × 10^{-6} M	M_8	0.006	3.95	2.28
1.000 × 10^{-5} M	M_7	0.006	4.65	2.68
1.000 × 10^{-4} M	M_6	0.005	3.69	2.13
1.000 × 10^{-3} M	M_5	0.004	3.12	1.80
1.000 × 10^{-2} M	M_4	0.003	2.66	1.54
1.000 × 10^{-1} M	M_3	0.002	1.91	1.10
2.300 × 10^{-1} M	M_2	0.001	2.74	1.58
6.0000 × 10^{-1} M	M_1	0.0004	1.47	0.85

Table 4.7. Calculated errors in the X and Y values for the calibration graph shown in figure 4.16.

The emf response of the Fe(III)-selective potentiometric sensor fabricated based on desferal chemisorbed onto TiO_2 electrodes via 6-C PA linker is shown in figure 4.1

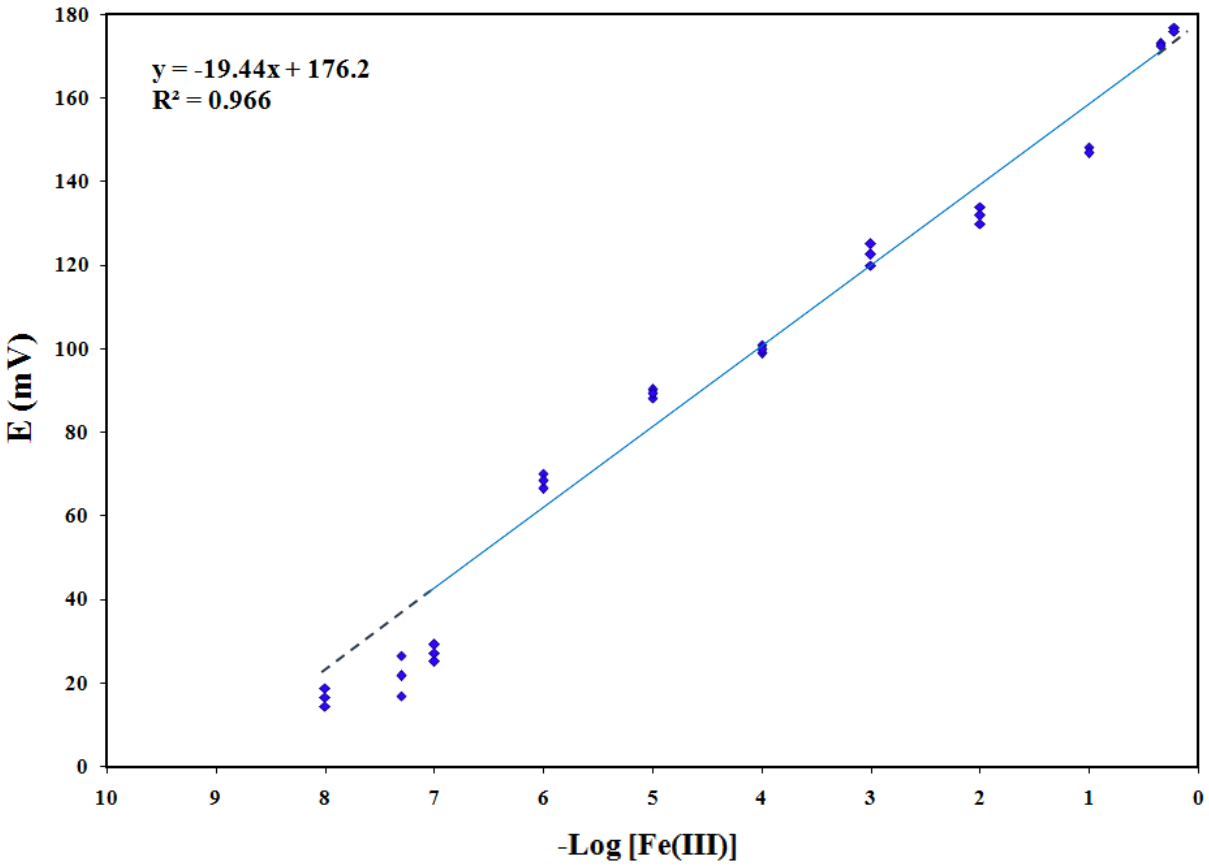

Figure 4.17. Calibration plot for iron(III) ion selective electrode based on desferal-chemisorbed onto TiO_2 electrodes via 6-C PA linker.

Similarly to the results obtained for 3-C PA, the calibration graph displays Nernstian behaviour in a broader concentration range of 1.000 (± 0.020) × 10^{-7} to 4.500 (± 0.010) × 10^{-1} M, and the absolute value of the slope of this plot was measured to be 19.44 ± 0.46 mV per decade of Fe^{3+} concentration.

The LOD of iron was determined to be 2.820 (± 1.600) × 10^{-9} M for the sensors fabricated based on desferal chemisorbed onto TiO_2 electrodes via 6-C-PA linkers. The values of X and Y errors shown on this calibration graph (figure 4.17) are summarized in table 4.8.

[Fe^{3+}]		**Error in the values of the X-Axis**	**SD_{sample} in the values of the Y-Axis**	**SD_{mean} in the values of the Y-Axis**
1.000 × 10^{-8} M	M_{11}	0.009	4.45	2.57
5.000 × 10^{-8} M	M_{10}	0.008	4.86	2.81
1.000 × 10^{-7} M	M_9	0.007	3.66	2.11
1.000 × 10^{-6} M	M_8	0.006	3.30	1.91
1.000 × 10^{-5} M	M_7	0.006	4.78	2.76
1.000 × 10^{-4} M	M_6	0.005	3.61	2.08
1.000 × 10^{-3} M	M_5	0.004	2.92	1.68
1.000 × 10^{-2} M	M_4	0.003	3.51	2.03
1.000 × 10^{-1} M	M_3	0.002	3.14	1.81
4.500 × 10^{-1} M	M_2	0.001	0.85	0.49
6.0000 × 10^{-1} M	M_1	0.0004	0.72	0.42

Table 4.8. Calculated errors in the X and Y values for the calibration graph shown in figure 4.17.

Figure 4.18 represents the potentiometric response of the Fe(III)-selective sensor designed based on desferal chemisorbed onto TiO_2 electrodes via 11-C-PA linkers.

In this case, the Nernstian slope was observed in the iron concentration range of 4.500 (± 0.040) × 10^{-6} to 8.000 (± 0.030) × 10^{-2} M and the LOD of iron was measured to be 4.780 (± 2.500) × 10^{-8} M for the sensors fabricated based on desferal chemisorbed onto TiO_2 electrodes via 11-C-PA linkers. The absolute value of the slope of this plot was measured to be 18.85 ± 0.51 mV per decade of Fe^{3+} concentration.

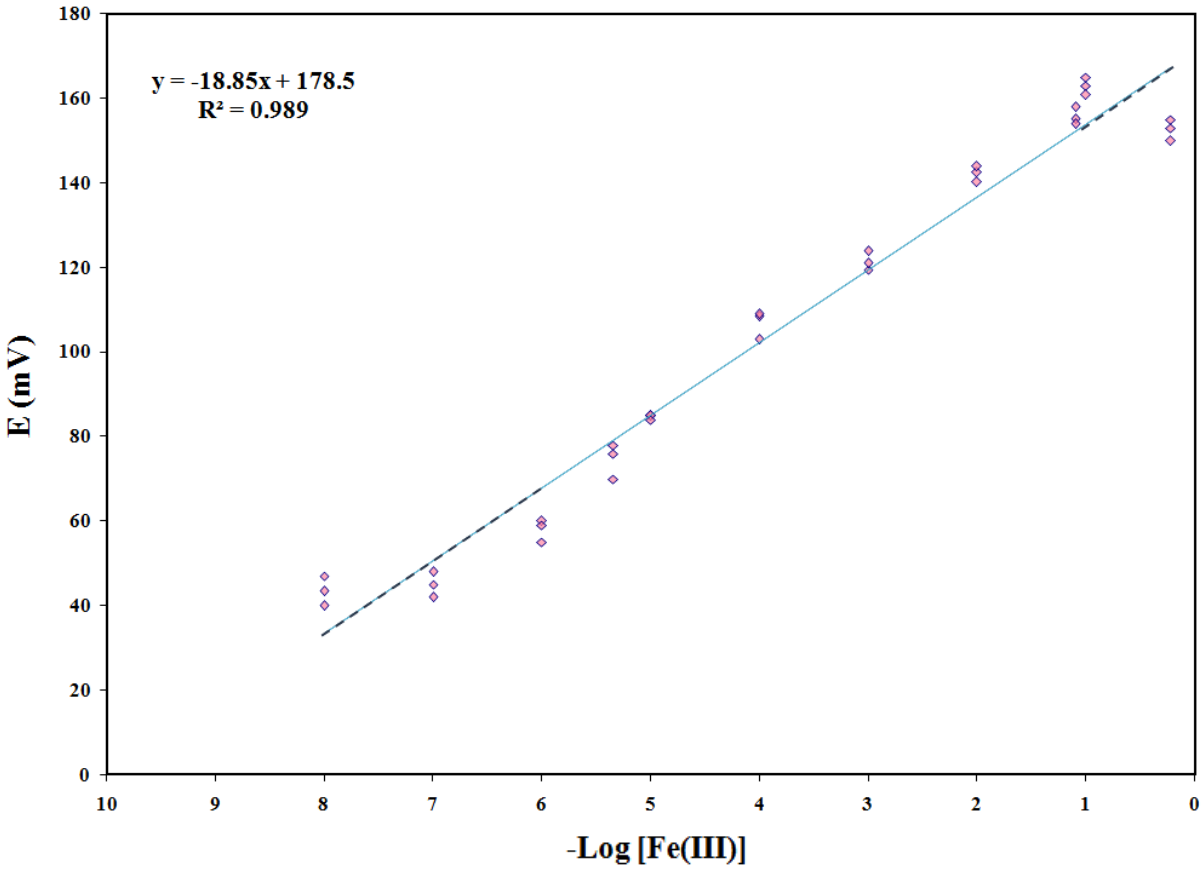

Figure 4.18. Calibration plot for iron(III) ion selective electrode based on desferal-chemisorbed onto TiO_2 electrode via 11-C PA linker.

The values of X and Y errors shown on this calibration graph (figure 4.18) are summarized in table 4.9.

$[Fe^{3+}]$		Error in the values of the X-Axis	SD_{sample} in the values of the Y-Axis	SD_{mean} in the values of the Y-Axis
1.000×10^{-8} M	M_{11}	0.009	6.03	3.48
1.000×10^{-7} M	M_{10}	0.008	5.03	2.91
1.000×10^{-6} M	M_9	0.007	4.46	2.58
4.500×10^{-6} M	M_8	0.006	3.21	1.86
1.000×10^{-5} M	M_7	0.006	2.89	1.67
1.000×10^{-4} M	M_6	0.005	3.17	1.83
1.000×10^{-3} M	M_5	0.004	2.47	1.42
1.000×10^{-2} M	M_4	0.003	1.24	0.72
8.000×10^{-2} M	M_3	0.002	1.62	0.94
1.000×10^{-1} M	M_2	0.001	1.58	0.91
6.0000×10^{-1} M	M_1	0.0004	0.58	0.33

Table 4.9. Calculated errors in the X and Y values for the calibration graph shown in figure 4.18.

Electrode Type	Slope (mV/decade)	Concentration Range (M)	LOD (M)
Desferal Physisorbed-TiO_2	19.14 ± 0.35	$5.300 (\pm 0.030) \times 10^{-6}$ - $1.000 (\pm 0.020) \times 10^{-1}$	$3.160 (\pm 1.500) \times 10^{-8}$
Desferal Chemisorbed -3-C PA-Modified TiO_2	19.23 ± 0.48	$7.000 (\pm 0.040) \times 10^{-7}$ - $2.300 (\pm 0.020) \times 10^{-1}$	$1.000 (\pm 0.500) \times 10^{-8}$
Desferal Chemisorbed -6-CPA-Modified TiO_2	19.44 ± 0.46	$1.000 (\pm 0.020) \times 10^{-7}$ - $4.500 (\pm 0.010) \times 10^{-1}$	$2.820 (\pm 1.600) \times 10^{-9}$
Desferal Chemisorbed -11-CPA-Modified TiO_2	18.85 ± 0.51	$4.500 (\pm 0.040) \times 10^{-6}$ - $8.000 (\pm 0.030) \times 10^{-2}$	$4.780 (\pm 2.500) \times 10^{-8}$

Table 4.10. Comparison of performance of the Fe (III)-selective electrodes based on physisorbed and different chemisorbed ionophores (errors are calculated based on 3 measurements).

As it is shown in table 4.10 and figures 4.4 and 4.16-4.18, the sensor fabricated based on desferal-chemisorbed onto TiO_2 electrode via 6-C PA linker showed the best Nernstian behaviour over a wider concentration range, as well as the smallest LOD in comparisons with all other tested electrodes. Therefore this electrode was used as the optimized substrate for all other complementary experiments reported in this chapter.

A comparison of the electrodes based on desferal-physisorbed onto TiO_2 substrate and the one prepared based on desferal-chemisorbed onto TiO_2 via 3-C PA linker showed superior behaviour (wider working concentration range and smaller LOD) of the latter. A similar comparison of the electrodes based on desferal-physisorbed onto TiO_2 substrate and the one prepared based on desferal-chemisorbed onto via 11-C PA linker indicated that the latter possessed an inferior behaviour (narrower working concentration range and bigger LOD).

4.8. Reproducibility

In order to study the reproducibility of our Fe(III)-selective electrode, six independent sensor electrodes modified with 6-C PA linker were fabricated and functionalised with desferal ionophore and their response were further tested in a 1.000×10^{-4} M aqueous solution of Fe(III). Figure 4.19 illustrates the histogram of potentiometric measurements correlated with each of the fabricated electrodes tested in a 1.000×10^{-4} M aqueous solution of Fe(III). The sensor electrode revealed good reproducibility with about 0.5% relative standard deviation.

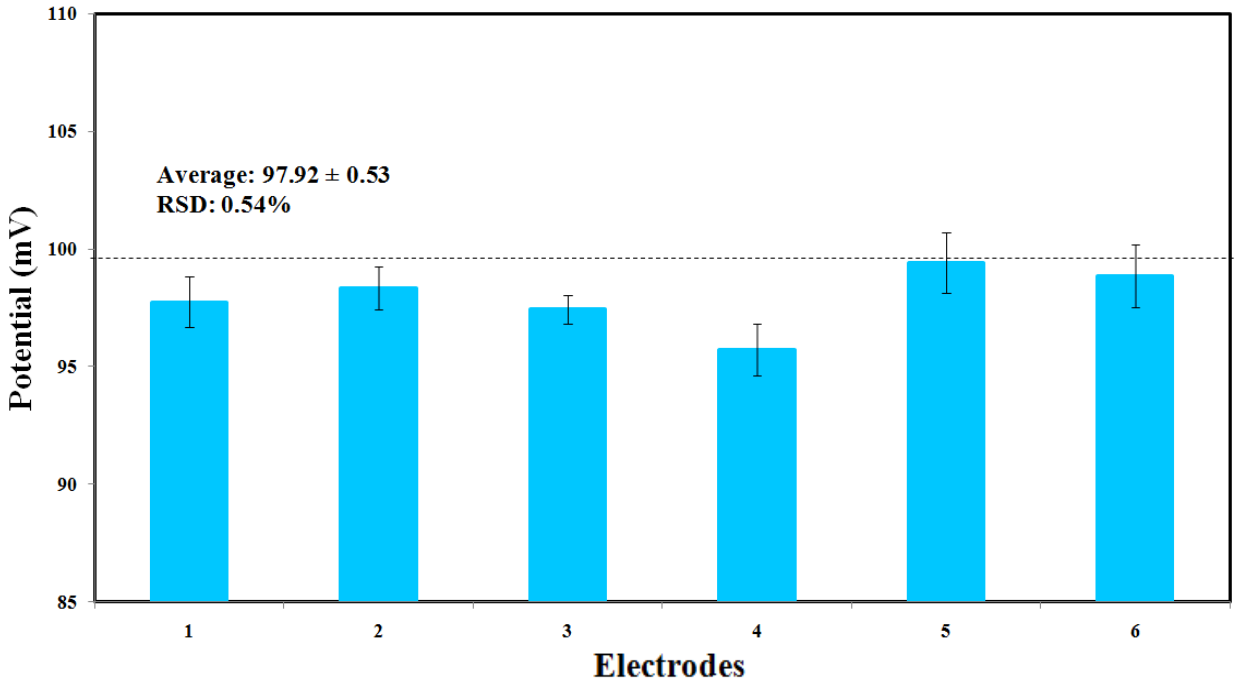

Figure 4.19. Histogram of potentiometric measurements correlated with the fabricated electrodes tested in a 1.000×10^{-4} M aqueous solution of Fe(III).

4.9. Potentiometric Selectivity

In order to have a clear picture about the selectivity of the desferal ligand for various metal ions, the sensor was tested against a number of metal ions, including some alkali, alkaline earth, heavy metals, and several transition metal ions. The methodology employed was the same as described in section 3.4. The potential responses of the 15 tested ISEs based on desferal are shown in figure 4.20. Among all these ions, the sensor showed the most sensitive response towards Fe^{3+}.

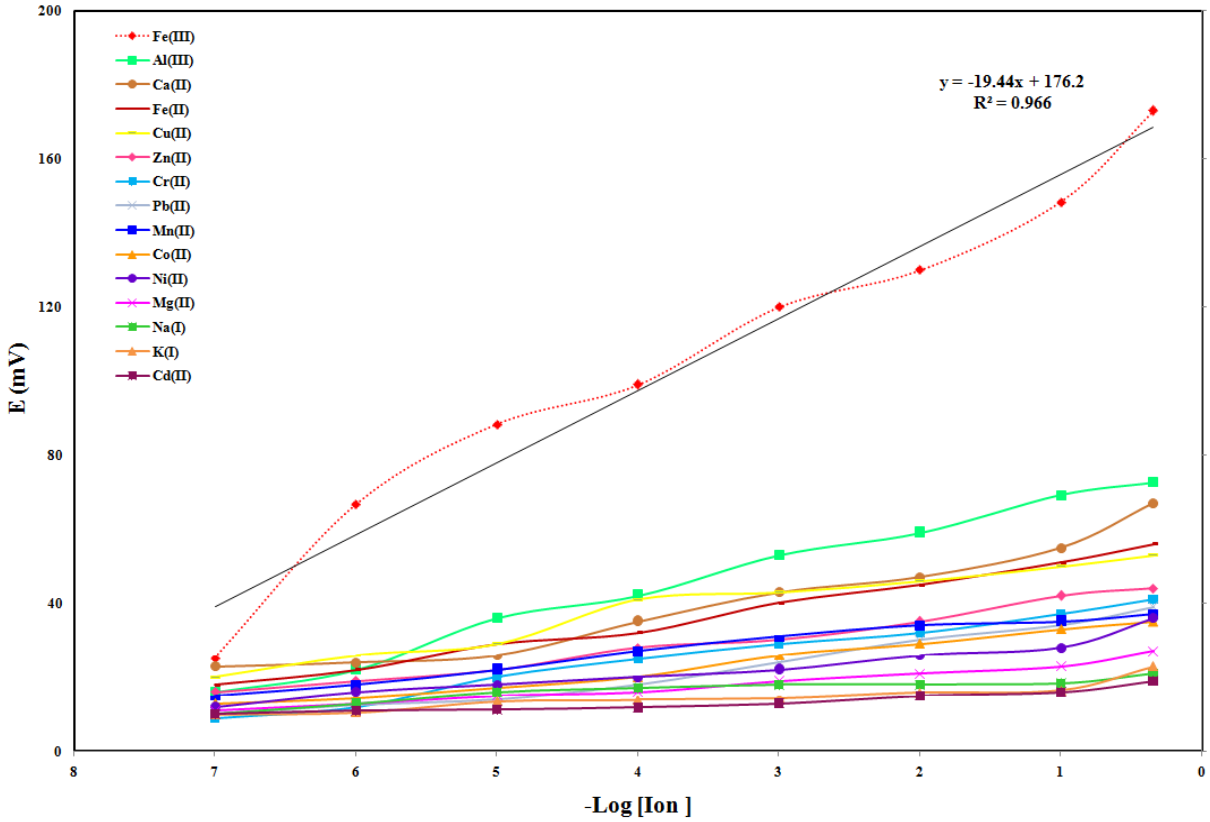

Figure 4.20. Potential response of ion-selective electrode based on desferal for various metal ions.

As can be seen from figure 4.20, it can be concluded that with the exception of the Fe^{3+} ions, all slopes of the corresponding potential/-log [Ion] plots differed greatly from the expected Nernstian slope and the plots also suffer from limited linear ranges. However, the Fe(III) ion results display good Nernstian behaviour with a slope of 19.44 ± 0.46 mV decade^{-1} of Fe^{3+} concentration, in the concentration range of 1.000×10^{-7} to 4.500×10^{-1} M. This is probably due to both the selective behaviour of the desferal ionophore against Fe^{3+} in comparison with other cations and rapid exchange kinetics of the cation between the aqueous and electrode phases.

Interfering Ion (B)	Concentration of B (C_B) (M)	$K^{MPM} = C_A/C_B$
Al^{3+}	2.800×10^{-3}	3.571×10^{-4}
Ca^{2+}	1.428×10^{-2}	7.003×10^{-5}
Fe^{2+}	1.589×10^{-2}	6.293×10^{-5}
Cu^{2+}	1.812×10^{-2}	5.519×10^{-5}
Zn^{2+}	1.089×10^{-1}	9.182×10^{-6}
Cr^{2+}	1.346×10^{-1}	7.429×10^{-6}
Pb^{2+}	1.429×10^{-1}	6.998×10^{-6}
Mn^{2+}	1.743×10^{-1}	5.737×10^{-6}
Co^{2+}	1.892×10^{-1}	5.285×10^{-6}
Ni^{2+}	1.964×10^{-1}	5.091×10^{-6}
Mg^{2+}	2.857×10^{-1}	3.500×10^{-6}
K^{+}	3.333×10^{-1}	3.000×10^{-6}
Na^{+}	4.944×10^{-1}	2.023×10^{-6}
Cd^{2+}	7.692×10^{-1}	1.300×10^{-6}

Table 4.11. Selectivity coefficients of the developed Fe^{3+}-selective sensor. (C_A: concentration of Fe(III) was 1.000×10^{-6} mol L^{-1}, and C_B: concentration of the interfering ion).

The potentiometric selectivity coefficients, describing the preference of the desferal-based sensor for the iron ion (A), relative to an interfering ion (B), were determined based on the MPM (see section 1.12.2), and the resulting values are listed in table 4.11. For these measurements, the reference solution was chosen to be 9 mL of water. In order to have a 1.000×10^{-6} mol L^{-1} aqueous solution of Fe(III), 1 mL 1.000×10^{-5} mol L^{-1} aqueous solution of Fe(III) was added to

this reference solution and its potential was recorded (potential at C_A, where C_A is the concentration of Fe(III) ion). Subsequently, for each studied interfering ion, different amounts of different concentration of those ions were added to the same reference solution (9 mL water) until the same potential value as obtained at C_A, was measured.

Table 4.11 summarizes the resulting values for the proposed iron(III) ISE measured based on MPM. As seen in this table, the selectivity coefficients for the alkali, alkaline earth, transition metals, and heavy metal ions used as interfering ions are on the order of 3.571×10^{-4} or smaller, suggesting they would not disturb significantly the response of the iron(III)-selective electrode due to their negligible interference.

4.10. Dynamic Response Time

In this work, the dynamic response time was recorded using the optimized electrode (desferal chemisorbed-6-C PA-modified TiO_2 electrode), by immediate repeatedly changing the Fe(III) aqueous solution from 1.000×10^{-7} to 4.500×10^{-1} M. Four potential readings were recorded at each of the Fe(III) concentrations with 10s intervals. The potential versus time plot is shown in figure 4.21. As seen, the electrode reaches its equilibrium response in a short time ($\leq$35seconds) over the whole linear concentration range. This can be related to the fast exchange kinetics of association-dissociation of Fe^{3+} ions with the desferal ionophore at the test solution-electrode interface.

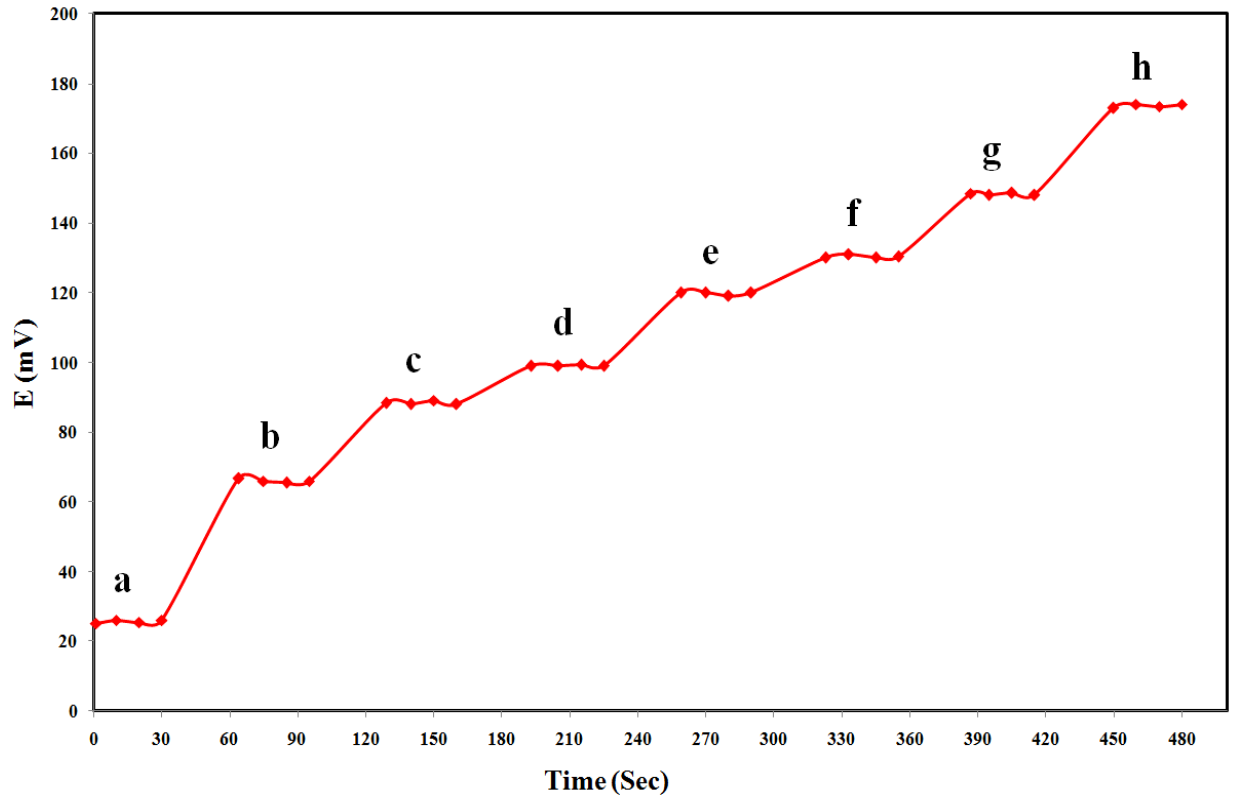

Figure 4.21. Dynamic response of the electrode for step changes in concentration of Fe^{3+}: **(a)** 1.000×10^{-7} M, **(b)** 1.000×10^{-6} M, **(c)** 1.000×10^{-5} M, **(d)** 1.000×10^{-4} M, **(e)** 1.000×10^{-3} M, **(f)** 1.000×10^{-2} M, **(g)** 1.000×10^{-1} M., **(h)** 4.500×10^{-1} M.

4.11. Reversibility of the Electrode Response

In order to evaluate the reversibility of the electrode, a similar procedure as done for the studies of the dynamic response time, was conducted but this time by going from a high to a low concentration, i.e., from 1.000×10^{-2} to 1.000×10^{-3} M Fe(III) concentrations. The results showed that the potentiometric response of the electrode was reversible. Although the time needed to reach an equilibrium potential values (≤45 seconds) was longer than that of the experiment

shown previously where the concentration was changed from a low to a high Fe(III)concentration (see figure 4.22).

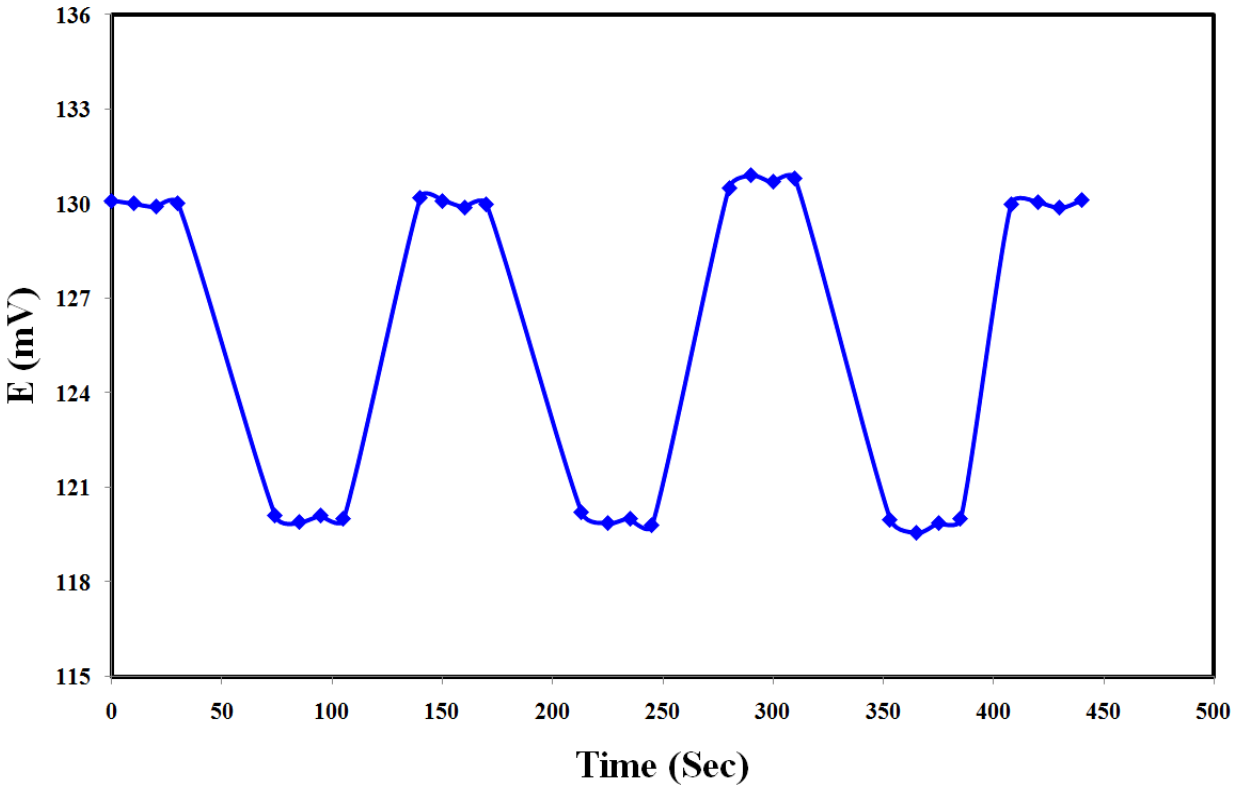

Figure 4.22. Dynamic response characteristics of the Fe(III)-selective sensor for several high-to-low sample cycles.

4.12. Effect of pH on the Potential Response of the Electrode

The effect of pH of the test solutions on the electrode's potential response was studied in the pH range of 1.5 - 8.5 (adjusted with either HCl or NaOH) for two different Fe(III) ions concentrations, namely 1.000×10^{-3} and 1.000×10^{-4} M. The results are shown in figure 4.23. For

the two concentration studied, the potential is independent of pH in the range of 2.6 - 7.5, which can be taken as the suitable working pH range of the desferal-chemisorbed-6-C PA-modified TiO_2 electrode system.

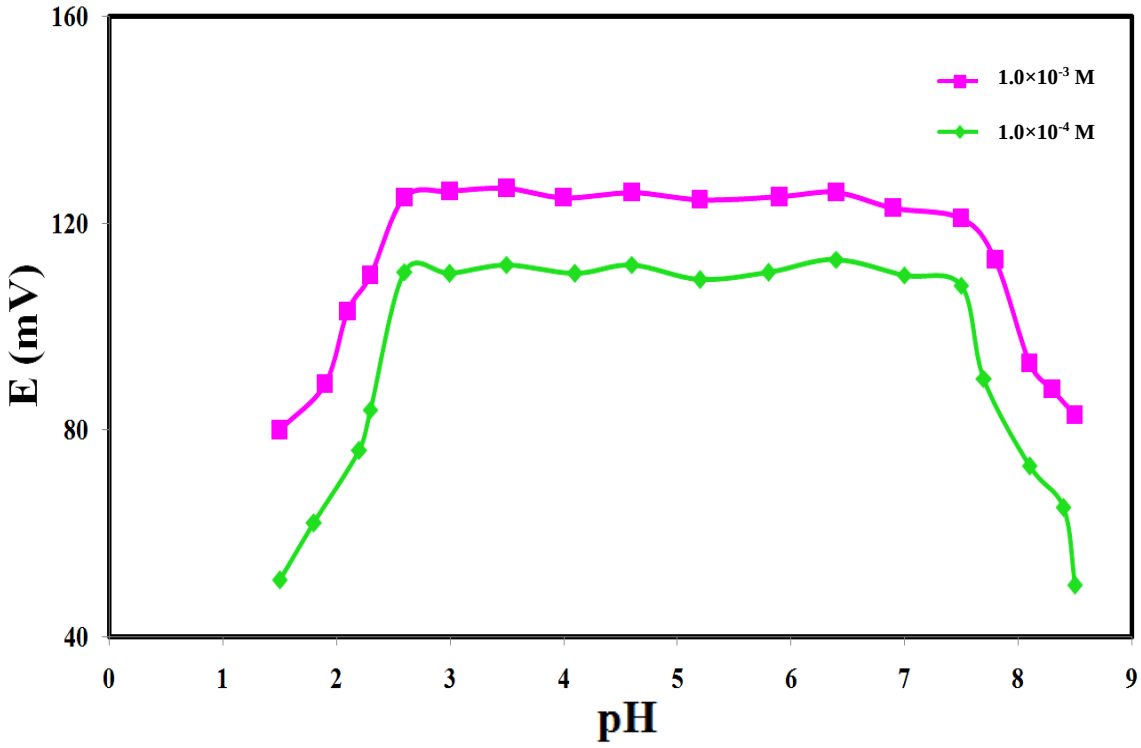

Figure 4.23. Effect of pH of test solutions on the potential response of Fe(III)-selective electrode based on desferal-chemisorbed 6-C PA modified-TiO_2 over two concentrations of 1.000×10^{-4} M and 1.000×10^{-3} M Fe^{3+}.

At higher pH values the Ti-O-P bonds can be hydrolyzed, which leads to instability and further detachment of the 6-Phosphonohexanoic acid modifier molecules from the surface of TiO_2, leading to a decrease in the electrode potential. In addition at pH values higher than 7.5, hydroxyl complexes of Fe^{3+} can be formed, which decreases the amount of Fe^{3+} in solution due to the complexation with hydroxyl ions and hence the electrode potential drops. This is while at

lower pH values the observed decrease in potential is probably due to the protonations of the binding oxygen atoms from the hydroxamate groups of the desferal ligand.

The same experiments were carried out using desferal-physisorbed TiO_2 electrodes, which demonstrated that the working pH range of the fabricated electrode is 2.4 - 7.9 (figure 4.24), which is somewhat wider than that of the desferal-chemisorbed-6-C PA-modified TiO_2 electrodes (2.6 - 7.5).

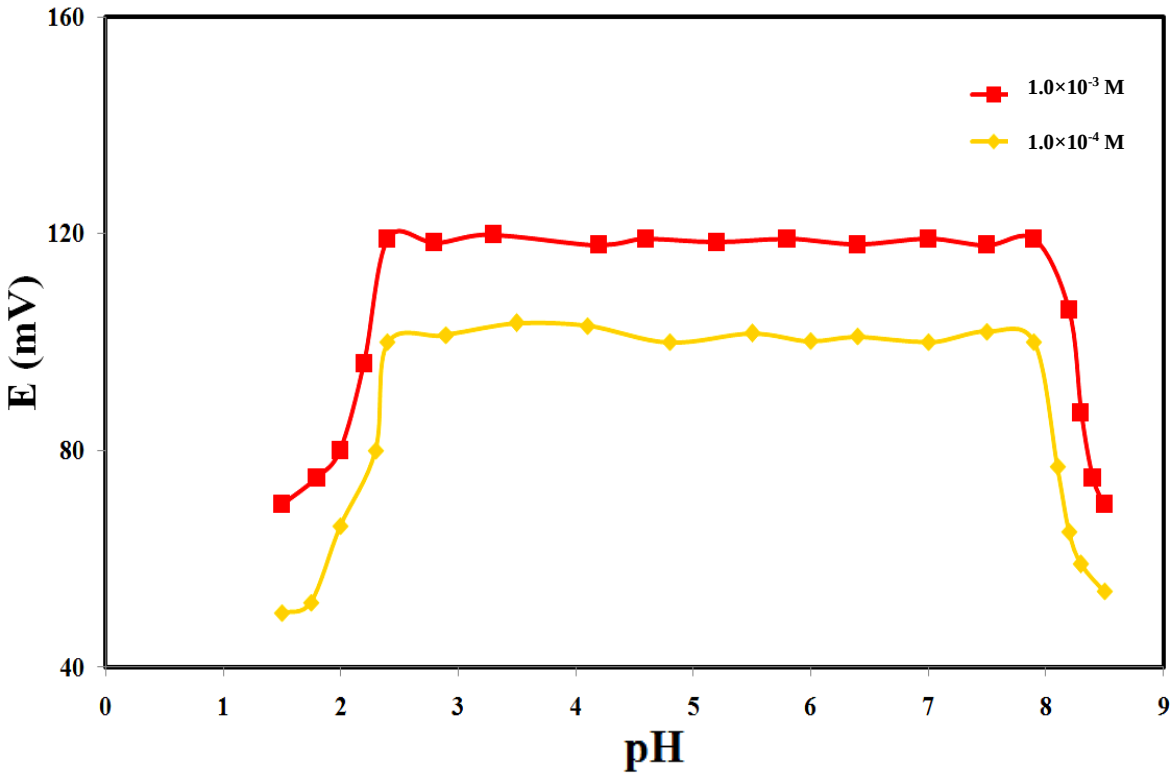

Figure 4.24. Effect of pH of test solutions on the potential response of Fe(III)-selective electrode based on desferal-physisorbed TiO_2 over two concentrations of 1.000×10^{-4} M and 1.000×10^{-3} M Fe^{3+}.

The fact that the fabricated sensors based on desferal-physisorbed TiO_2 showed a wider working pH range especially in the slightly alkaline solutions in comparisons with the sensors designed based on desferal-chemisorbed-6-C PA-modified TiO_2, can be related to the hydrolysis

of the Ti-O-P bonds in alkaline pH values, which leads to the instability and detachment of the 6-C-PA molecules from the surface of TiO_2.

4.13. Sensors' Stability and Lifetime

For the investigations of the stability and lifetime of the fabricated Fe(III)-selective sensors based on desferal-physisorbed TiO_2 and desferal-chemisorbed-6-C PA-modified TiO_2 electrodes, three electrodes of each type were tested over a period of 7 and 13 weeks and the results are summarized in table 4.12 and table 4.13, respectively. The main factor limiting the lifetime of an ion-selective sensor in potentiometric measurements is the stability of ionophore onto the electrode's surface.

The experiment results showed that the proposed titanium dioxide-based nanosensor based on the physisorbed ionophore was stable for 44 days, while the fabricated sensor based on the chemisorbed ionophore (6-C PA) could be used for at least 86 days (almost three months), which is almost twice the lifetime of the sensor fabricated based on physisorbed ligand. During these time periods, the nanostructured sensors could be used without observing any divergence in their characteristic responses (E (mV) measured). Also the limit of detection and the slope of the electrode responses remained almost constant. After these days changes were observed in the slopes and detection limits.

According to table 4.12, we can say that using the Fe(III)-selective potentiometric sensors based on desferal-physisorbed onto TiO_2 electrodes within its reliable functioning duration, the absolute value of the slope of the calibration graph was between 19.14 .± 0.35 mV and 18.41 ± 0.44 $decade^{-1}$ of iron concentration.

Also based on table 4.13, it can be concluded that using the Fe(III)-selective potentiometric sensors fabricated based on desferal-chemisorbed-6-C PA-TiO_2 electrodes during its reliable functioning time, the absolute value of the slope of the calibration graph was between 19.44± 0.46 and 18.42 ± 0.45 mV $decade^{-1}$ of iron concentration. This clearly indicate that the mode of adsorption of the ionophore, i.e., physisorbed versus chemisorbed does not affect its potentiometric response to Fe(III). In addition, the improvement in the lifetime of the fabricated Fe(III)-selective sensor (from 44 days for the sensors fabricated based on desferal-physisorbed onto TiO_2 electrodes, to 86 days for the fabricated sensor based on desferal-chemisorbed-6-C PA-TiO_2 electrodes) can be related to increasing the stability of desferal ligand onto the surface of TiO_2 electrodes due to the stronger chemisorbed assembly on the TiO_2 surface in comparison to the weaker ionophore-surface interactions that exist when physical adsorption is employed to prepare the sensor.

Week	**Slope (mV $decade^{-1}$)**	**Equation of the Line**	**Limit of Detection (M)**
1	19.14 ± 0.35	y= -19.14 x +177.8	3.160 (± 1.500) × 10^{-8}
2	19.09 ± 0.41	y= -19.09 x +177.6	3.330 (± 1.600) × 10^{-8}
3	19.05 ± 0.43	y= -19.05x +177.4	3.480 (± 1.500) × 10^{-8}
4	18.95 ± 0.39	y= -18.95 x +176.7	3.810 (± 1.700) × 10^{-8}
5	18.88 ± 0.51	y= -18.88 x +176.2	4.100 (± 1.900) × 10^{-8}
6	18.41 ± 0.44	y= -18.41 x +174.2	5.220 (± 1.900) × 10^{-8}
7	16.23 ± 0.62	y= -16.23x +163.3	0.820 (± 2.400) × 10^{-7}

Table 4.12. Weekly-based potentiometric studies for estimating the lifetime of the Fe(III)-selective sensor based on 3 tested desferal-physisorbed-TiO_2 electrodes.

Week	Slope (mV decade^{-1})	Equation of the Line	Limit of Detection (M)
1	19.44 ± 0.46	y= -19.44 x +176.2	2.820 (± 1.600) × 10^{-9}
2	19.39 ± 051	y= -19.39 x +175.9	3.060 (± 1.700) × 10^{-9}
3	19.34 ± 056	y= -19.34x +175.7	3.210 (± 1.700) × 10^{-9}
4	19.27 ± 0.53	y= -19.27 x +175.1	3.430 (± 1.600) × 10^{-9}
5	19.05 ± 0.53	y= -19.05 x +173.9	4.210 (± 1.800) × 10^{-9}
7	18.92 ± 0.46	y= -18.92 x +173.3	4.740 (± 1.500) × 10^{-9}
8	18.83 ± 0.64	y= -18.83 x +172.7	5.270 (± 1.600) × 10^{-9}
9	18.60 ± 052	y= -18.60 x +171.6	5.860 (± 1.800) × 10^{-9}
10	19.00 ± 0.52	y= -19.00 x +173.6	4.450 (± 1.800) × 10^{-9}
11	18.47 ± 0.47	y= -18.47 x +170.8	6.320 (± 1.900) × 10^{-9}
12	18.42 ± 0.45	y= -18.42 x +170.6	6.500 (± 2.000) × 10^{-9}
13	16.52 ± 0.62	y= -16.52 x +159.2	1.000 (± 2.600) × 10^{-8}

Table 4.13. Weekly-based potentiometric studies for estimating the lifetime of the Fe(III)-selective sensor based on 3 tested desferal-chemisorbed-6-C PA-TiO_2 electrodes.

4.14. Short-term Stability

For the studies of the short-term stability of the fabricated Fe(III)-selective sensors based on desferal-physisorbed TiO_2 and desferal-chemisorbed-6-C PA-modified TiO_2 electrodes, the potentiometric measurements of three electrodes of each type were carried out on a daily basis during the first two weeks as well as the last week of the sensors reliable functioning time (based on tables 4.12 and 4.13). The standard deviation in the mean of the slopes of the calibration graphs in each week was then calculated as reported in tables 4.14 and 4.15.

Table 4.14 and 4.15 show the results of the slopes and intercepts of the calibration graphs as well as the LODs according to daily-based potentiometric measurements carried out during weeks 1-2, and 6 for the sensors designed based on desferal-physisorbed TiO_2 , and during weeks 1-2, and 12 for the sensors assembled based on desferal-chemisorbed-6-C PA-modified TiO_2 electrodes, respectively.

Day	Slope (mV decade^{-1})	Equation of the Line	Limit of Detection (M)
1	19.14 ± 0.35	y= -19.14 x +177.8	3.160 (± 1.500) × 10^{-8}
2	19.13 ± 0.34	y= -19.13 x +177.7	3.190 (± 1.500) × 10^{-8}
3	19.11 ± 0.39	y= -19.11 x +177.7	3.270 (± 1.500) × 10^{-8}
4	19.12 ± 0.33	y= -19.12 x +177.7	3.230 (± 1.600) × 10^{-8}
5	19.11 ± 0.35	y= -19.11 x +177.7	3.270 (± 1.500) × 10^{-8}
6	19.10 ± 0.29	y= -19.10 x +177.5	3.300 (± 1.600) × 10^{-8}
7	19.10 ± 0.33	y= -19.10 x +177.6	3.300 (± 1.600) × 10^{-8}
***SD*$_{mean}$ (Slope)**: 0.006			
8	19.09 ± 0.41	y= -19.09 x +177.6	3.330 (± 1.600) × 10^{-8}
9	19.09 ± 0.44	y= -19.09 x +177.5	3.330 (± 1.600) × 10^{-8}
10	19.09 ± 0.37	y= -19.09 x +177.6	3.330 (± 1.600) × 10^{-8}
11	19. 08 ± 0.29	y= -19.08 x +177.4	3.370 (± 1.600) × 10^{-8}
12	19.08 ± 0.32	y= -19.08 x +177.3	3.370 (± 1.600) × 10^{-8}
13	19.07 ± 0.38	y= -19.07 x +177.2	3.400 (± 1.700) × 10^{-8}
14	19.07 ± 0.40	y= -19.07 x +177.2	3.400 (± 1.700) × 10^{-8}
***SD*$_{mean}$ (Slope)**: 0.004			
36	18.41 ± 0.44	y= -18.41 x +174.6	5.220 (± 1.900) × 10^{-8}
37	18.41 ± 0.38	y= -18.41 x +174.5	5.220 (± 1.900) × 10^{-8}
38	18.40 ± 0.28	y= -18.40 x +174.5	5.260 (± 2.000) × 10^{-8}
39	18.40 ± 0.33	y= -18.40 x +174.4	5.260 (± 1.900) × 10^{-8}
40	18.38 ± 0.43	y= -18.38 x +174.4	5.330 (± 2.200) × 10^{-8}
41	18.38 ± 0.37	y= -18.38 x +174.3	5.330 (± 2.100) × 10^{-8}
42	18.37 ± 0.31	y= -18.37 x +174.3	5.380 (± 2.300) × 10^{-8}
***SD*$_{mean}$ (Slope)**: 0.006			

Table 4.14. Daily-based potentiometric studies for estimating the lifetime of the Fe(III)-selective sensor based on 3 tested desferal-physisorbed-TiO_2 electrodes.

Day	Slope (mV decade^{-1})	Equation of the Line	Limit of Detection (M)
1	19.44 ± 0.46	y= -19.44 x +176.2	2.820 (± 1.600) × 10^{-9}
2	19.43 ± 0.44	y= -19.43 x +176.1	2.870 (± 1.600) × 10^{-9}
3	19.42 ± 0.43	y= -19.42 x +176.0	2.910 (± 1.500) × 10^{-9}
4	19.42 ± 0.42	y= -19.42 x +176.0	2.910 (± 1.500) × 10^{-9}
5	19.42 ± 0.43	y= -19.42 x +176.0	2.910 (± 1.500) × 10^{-9}
6	19.41 ± 0.41	y= -19.41 x +176.0	2.940 (± 1.700) × 10^{-9}
7	19.41 ± 0.44	y= -19.42 x +175.9	2.940 (± 1.700) × 10^{-9}
***SD*$_{mean}$ (Slope)**: 0.004			
8	19.39 ± 0.51	y= -19.39 x +175.9	3.060 (± 1.700) × 10^{-9}
9	19.39 ± 0.53	y= -19.39 x +175.8	3.060 (± 1.600) × 10^{-9}
10	19.39 ± 0.47	y= -19.39 x +175.9	3.060 (± 1.700) × 10^{-9}
11	19.38 ± 0.46	y= -19.38 x +175.8	3.120 (± 1.800) × 10^{-9}
12	19.38 ± 0.48	y= -19.38 x +175.8	3.120 (± 1.800) × 10^{-9}
13	19.37 ± 0.53	y= -19.37 x +175.6	3.120 (± 1.700) × 10^{-9}
14	19.37 ± 0.51	y= -19.37 x +175.7	3.120 (± 1.700) × 10^{-9}
***SD*$_{mean}$ (Slope)**: 0.003			
78	18.42 ± 0.45	y= -18.42 x +170.6	6.500 (± 2.000) × 10^{-9}
79	18.42 ± 0.47	y= -18.42 x +170.6	6.500 (± 2.000) × 10^{-9}
80	18.42 ± 0.44	y= -18.42 x +170.6	6.500 (± 2.100) × 10^{-9}
81	18.41 ± 0.46	y= -18.41 x +170.5	6.560 (± 2.200) × 10^{-9}
82	18.40 ± 0.51	y= -18.40 x +170.4	6.570 (± 2.100) × 10^{-9}
83	18.40 ± 0.40	y= -18.40 x +170.5	6.570 (± 2.200) × 10^{-9}
84	18.40 ± 0.41	y= -18.40 x +170.4	6.570 (± 2.200) × 10^{-9}
***SD*$_{mean}$ (Slope)**: 0.004			

Table 4.15. Daily-based potentiometric studies for estimating the lifetime of the Fe(III)-selective sensor based on 3 tested desferal-chemisorbed-6-C PA-TiO_2 electrodes.

It is clear that the values of standard deviations in the mean of the slopes of the calibration graphs in weeks 1-2 and 6 for the sensors designed based on desferal-physisorbed TiO_2 electrodes, and also in weeks 1-2 and 12, for the sensors designed based on desferal-chemisorbed-6-C PA-modified TiO_2 electrodes, are very small, indicating high short-term stability of the fabricated sensors. Therefore for the evaluation of the sensors' stability and lifetime, the potentiometric measurements were performed on a weekly basis, as explained in section 4.13.

4.15. Comparisons With the Reported Sensors

The working concentration range, slope, response time, limit of detection, working pH range, and lifetime of the proposed potentiometric sensors are compared with the corresponding values for some of the best previously reported ferric ion-selective electrodes based on different neutral ion carriers [29, 31, 33, 161], and the results are summarized in table 4.16.

Ref.	Working Concentration Range (M)	Slope (mV/decade of Concentration)	LOD (M)	pH Range	Life-time (days)
29	4.300×10^{-7} - 1.000×10^{-2}	18.5 ± 0.9	4.300×10^{-7}	1.8 - 6	55
31	1.000×10^{-7} - 1.000×10^{-1}	21.6 ± 0.7	8.600×10^{-8}	2 - 3.8	42
33	2.300×10^{-7} - 5.000×10^{-2}	19.5 ± 0.3	9.600×10^{-8}	2.9 - 7.1	150
161	8.000×10^{-6} - 1.000×10^{-1}	90.92	1.200×10^{-6}	3 - 7	60
This Work	$1.000 (\pm 0.020) \times 10^{-7}$ - $4.500 (\pm 0.010) \times 10^{-1}$	19.44 ± 0.46	$2.820 (\pm 1.600) \times 10^{-9}$	2.6 - 7.5	86

Table 4.16. Comparison of the working concentration range, slope, limit of detection, working pH range, and lifetime of present Fe(III)-selective work and previous studies of other research groups.

According to table 4.16 it could be concluded that:

1) Comparing with Ref. [29], our Fe(III)-selective sensor is superior since it showed a wider linear concentration range as well as a wider working pH range, also the LOD obtained by our sensor is much smaller than that of Ref. [29]. In addition, our sensor had a longer lifetime.

2) Our sensor is superior compared with the work reported in Ref. [31], as it showed a wider working concentration range, a much wider working pH range, a smaller LOD, and more than twice longer lifetime.

3) Although the Fe(III)-selective sensor reported in Ref. [33] showed the longest lifetime among all the reported works, comparing with our sensor, its working concentration range is narrower. Besides its LOD is bigger than the LOD obtained in our work.

4) Our fabricated sensor also showed improved performance compared to the Fe(III)-selective sensor reported in Re. [161], as it showed a wider linear concentration range, a much smaller LOD, as well as a longer lifetime.

4.16. Conclusion

In this work, we were interested in modifying the surface of nanostructured TiO_2 electrodes to improve the properties of our Fe(III)-selective sensor. This was achieved by using a self-assembled anchoring group to immobilize the desferal ligands onto the surface of these electrodes. we took advantage of three different phosphonic acid molecules with different alkyl chain lengths (short chain (3-C), medium chain (6-C), and long chain (11-C)) as surface linkers. Using ^{31}P as well as FTIR spectroscopic measurements, SEM and EDX analysis, and AFM images it was shown that it is possible to use TiO_2 as a platform to form stable alkyl phosphonic

acids self-assembled layers and then achieve effective and stable ligand immobilization on top of the SAM using simple chemistry.

Based on the ^{31}P NMR and FTIR spectroscopic measurements, it was proved that the attachment of these PAs takes place through their phosphonic end groups, although it was impossible to draw conclusions on the binding modes of these modifiers on TiO_2 electrodes.

The FTIR analysis also showed that the desferal ligand had been immobilized onto the surface of TiO_2 by chemical binding of its terminal amino-groups to the carboxylic terminal functional groups of the PAs SAM linkers. The performances of the desferal chemisorbed-(3-C, 6-C, and 11-C) PAs nanostructured TiO_2 electrodes were compared with that of desferal physisorbed-nanostructured TiO_2 substrates by comparing the Nernstian slopes of the calibration graphs of the fabricated nanosensors' electrodes, as well as their LODs. It was concluded that by chemically anchoring the desferal ligand onto the surface of functionalized TiO_2 electrodes using the SAMs of medium alkyl chain length PAs (6-C), we could significantly improve the performance of the iron-selective potentiometric sensor. The lifetime and stability of this sensor was compared with that of desferal-physisorbed on TiO_2. The chemisorption of the ligand resulted in lifetimes that were almost twice as long. This was related to weak desferal-surface interactions in the case of the sensors prepared with physisorbed desferal ligands.

The sensor based on desferal-chemisorbed 6-C PA-modified TiO_2 electrode showed the best response characteristics with Nernstian behaviour for Fe^{3+} ions (Nernstian slope of 19.44 $\pm$ 0.46 mV per decade of Fe^{3+} concentration) over a wide working concentration range, 1.000×10^{-7} to 4.500×10^{-1} M, and a low detection limit of 2.820×10^{-9} M. The sensor could be used in the pH range of 2.6 – 7.5 and had a relatively fast response time of $\leq$35 seconds; and it could be used for at least 86 days without any considerable significant dropping in the potential.

The sensor showed good selectivity against Fe^{3+} in comparison with variety of other cations and could be used for the determination of this ion in the presence of considerable concentrations of common interfering ions. In addition, our Fe(III)-selective sensor showed that the selectivity coefficients for the alkali, alkaline earth, transition metals, and heavy metal ions used as interfering ions are on the order of 10^{-4} or smaller, which suggests that these ions would not disturb significantly the response of the iron(III)-selective electrode due to their negligible interference.

5. Conclusions and Final Remarks

During the course of this thesis work, two highly-selective solid-state ISEs based on nanostructured titanium dioxide, were designed for the analysis of Cr(III) and Iron(III) ions in solution. A Cr(III)-selective sensor was fabricated using GBHA ionophores physisorbed on the surface of TiO_2 electrodes. The sensor showed the best response characteristics with Nernstian behaviour for Cr^{3+} (Nernstian slope of 19.45 ± 0.44 mV per decade of Cr^{3+} concentration) over a wide working concentration range of 1.000×10^{-7} to 1.000×10^{-2} M, and a low detection limit of 3.000×10^{-8} M. The sensor worked well in the pH range of 2.5 – 6.3, had a relatively fast response time of ≤ 29 seconds, and could be used for at least 57 days without any considerable divergence in potential. It showed good selectivity against Cr^{3+} in comparison with a large variety of other cations, and could be used for the determination of this ion in the presence of considerable concentrations of common interfering ions.

Of all interfering ions, with the exception of Fe^{3+}, the selectivity coefficients are on the order of 10^{-3} to 10^{-6}. This is much smaller than the selectivity coefficients of Cr(III)-selective sensors previously reported by others. Based on these studies, we conclude that our fabricated sensor has an improved selectivity towards Cr^{3+} with respect to all the other tested ions.

The Fe(III)-selective sensors were fabricated using two methodologies, based on desferal molecular receptors either physisorbed, or chemisorbed on the surface of TiO_2 electrodes. Although we were able to successfully fabricate a highly sensitive potentiometric sensor for quantification analysis of Fe^{3+} ions using the firs methodology (i.e., desferal molecular receptors physisorbed onto the surface of nanostructured TiO_2 electrodes), we were looking for ways to improve the performance of our Fe(III) sensor. Therefore, we studied the application of three

different phosphonic acid molecules with different alkyl chain lengths (short chain (3-C), medium chain (6-C), and long chain (11-C)) as self-assembled anchoring groups to immobilize the desferal ligand onto the surfaces of nanostructured TiO_2 electrodes.

Different surface characterization techniques were used to study surface modifications of TiO_2 with PA molecules, and to confirm the immobilization of desferal ionophores via these linkers onto the surface of TiO_2 electrodes. According to these studies the following conclusions were drawn; 1) it is possible to use TiO_2 as a platform to form stable alkyl phosphonic acids self-assembled layers and then achieve effective and stable ligand immobilization on top of the SAM using simple chemistry; 2) the attachment of these PAs take place through their phosphonic end groups, although it was impossible to draw conclusions on the binding modes of these modifiers on TiO_2 electrodes; 3) the desferal ligand had been immobilized onto the surface of TiO_2 by chemical binding of its terminal amino-groups to the carboxylic terminal functional groups of the PAs SAM linkers.

The performances of the desferal chemisorbed-(3-C, 6-C, and 11-C) PAs nanostructured TiO_2 electrodes were compared with that of desferal physisorbed-nanostructured TiO_2 substrates by comparing the Nernstian slopes of the calibration graphs of the fabricated nanosensors' electrodes, as well as their LODs. It was concluded that by chemically anchoring the desferal ligand onto the surface of functionalized TiO_2 electrodes using the SAMs of medium alkyl chain length PAs (6-C), we could significantly improve the performance of the iron-selective potentiometric sensor. The lifetime and stability of this sensor was then compared with that of desferal-physisorbed on TiO_2. The chemisorption of the ligand resulted in lifetimes that were almost twice as long. This was related to weak desferal-surface interactions in the case of the sensors prepared with physisorbed desferal ligands.

The sensor based on desferal-chemisorbed 6-C PA-modified TiO_2 electrode showed the best response characteristics with Nernstian behaviour for Fe^{3+} (Nernstian slope of 19.44 ± 0.46 mV per decade of Fe^{3+} concentration) over a wide working concentration range, 1.000×10^{-7} to 4.500×10^{-1} M and a low detection limit of 2.820×10^{-9} M. The sensor worked well in the pH range of 2.6 – 7.5, had a relatively fast response time of ≤ 35 seconds, and could be used for at least 86 days without any considerable significant dropping in the potential. This sensor showed good selectivity against Fe^{3+} in comparison with variety of other cations and could be used for the determination of Fe^{3+} in the presence of considerable concentrations of common interfering ions. In addition our sensor showed that the selectivity coefficients for the alkali, alkaline earth, transition metals, and heavy metal ions used as interfering ions are on the order of 10^{-4} or smaller. This is much smaller than the selectivity coefficients of Fe(III)-selective sensors previously reported by others. Compared to other Fe(III)-selective sensors, our sensor showed smaller selectivity coefficients and therefore had improved selectivity.

In conclusion, by chemically anchoring desferal ligand onto the surface on TiO_2 electrodes using PA modifiers as linkers, we could significantly improve the performance of the fabricated Fe(III)-selective potentiometric sensors. The assembled nanostructured TiO_2 based ISEs offered simplicity, rapidity, reproducibility, and reliability as a portable analytical tool.

References

[1]. Kimmel, D. W.; LeBlanc, G.; Meschievitz, M. E. Cliffel, D. E. *Anal. Chem*. **2012**, *84(2)*, 685.

[2]. Bratovčić, A.; Odobašić, A.; Ćatić, A. *Agric. Conspe. Sci.* **2009**, *74 (3)*, 139.

[3]. Zamani, H. A.; Langroodi, S.; Meghdadi, S. *Int. J. Electrochem. Sci.* **2011**, *8*, 237.

[4]. Sharma, H. K.; Sharma, N. *Int. J. Electrochem. Sci.* **2009**, 6, 1139.

[5]. Zamani, H. A.; Zaferoni, M.; Meghdadi, S. *Int. J. Electrochem. Sci.* **2012**, *9*, 1941.

[6]. Gupta, V. K.; Goyal, R. N.; Sharma, R. A. *Anal. Chim. Acta*. **2009**, *647*, 66.

[7]. Faridbod, F.; Zamani, H. A.; Hosseini, M.; Pirali-Hamedani, M.; Ganjali, M. R.; Norouzi, P. *Int. J. Electrochem. Sci.* **2011**, *6*, 3694.

[8]. Norouzi, P.; Ganjali, M. R.; Faridbod, F.; Shahtaheri, S. J; Zamani, H. A. *Int. J. Electrochem. Sci.* **2012**, *7*, 2633.

[9]. Zamani, H. A. *Chin. Chem. Lett*. **2011**, *22*, 346.

[10]. Chandra, S.; Singh, D. R. *Mater. Sci. Eng. A* **2009**, *502*, 107.

[11]. Frant, M. S. *Analyst*. **1994**, *119*, 2293.

[12]. Mathew, S. Development of macrocyclics based electrochemical sensors. Ph.D Thesis, Cochin University, Kochi, India, 2012.

[13]. National institute of health. Strengthening Knowledge and Understanding of Dietary Supplements: Chromium Dietary Supplement Fact Sheet. http://ods.od.nih.gov/factsheets/Chromium-HealthProfessional/ (accessed Oct. 20, 2013).

[14]. Subcommittee on the Tenth Edition of the RDAs; Food and Nutrition Board; Commission on life Sciences; National Research Council. *Recommended Dietary Allowance*, 10th ed.; National Academy Press: Washington, D.C, 1989.

[15]. Gholivand, M. B.; Raheedayat, F. *Electroanalysis.* **2004**, *16*, *No. 16*, 1330.

[16]. Loyola Medicine. Chromium -blood test. http://loyolauniversity.adam.com/content.aspx?productId=101&pid=1&gid=003359 (accessed January 15, 2014).

[17]. Delaware health and social services. Chromium(III) and (VI). http://www.dhss.delaware.gov/dhss/dph/files/chromiumfaq.pdf (accessed Nov. 14, 2013).

[18]. Gupta, V. K.; Jain, A. K.; Kumar, P.; Agarwal, S.; Maheshwari, G. *Sens. Actuators B* **2006**, *113*, 182.

[19]. Singh, A. K.; Gupta, V. K.; Gupta, B. *Anal. Chim. Acta*. **2007**, *585(1)*, 171.

[20]. United States Environmental Protection Agency. Technology Transfer Network - Air Toxics Web Site: Chromium Compounds.
https://www3.epa.gov/airtoxics/hlthef/chromium.html (accessed Nov. 23, 2013).

[21]. Abu-Shawish, H. M.; Saadeh, S. M.; Hartani, K.; Dalloul, H. M. *J. Iran. Chem. Soc.* **2009**, 6 (4), 729.

[22]. Sadeghi, H. B.; Tamaddon, A.; Afifian, A.; Almasian, N.; Bozorgvar, F.; Mollaei, S. *Electroanalysis*. **2011**, *23 (10)*, 2472.

[23]. Kumar, P.; Sharma, H. K. *Electrochimica Acta.* **2013**, *87*, 925.

[24]. Singh, A. K.; Panwar, A.; Kumar, S.; Baniwal, S. *Analyst.* **1999**, *124*, 521.

[25]. Gholivand, M. B.; Sharifpour, F. *Talanta* **2003**, *60*, 707.

[26]. Singh, A. K.; Singh, R.; Saxena, P. *Sensors* **2004**, *4*, 187.

[27]. Zamani, H. A.; Rajabzadeh, G.; Ganjali, and M. R. *Sens. Actuators B* **2006**, 119, 41.

[28]. Greenwood, N. N.; Earnshaw, A. E. *Chemistry of the Elements*; Pergamon Press: Oxford, 1984.

[29]. Ali, T. A.; Mohamed, G. G.; Farang, A. H. *Int. J. Electrochem. Sci.* **2015**, *10*, 564.

[30]. Demir, E.; Kemer, B.; Bekircan, O.; Aboul-Enein, H. Y**.** *Curr. Anal. Chem.* **2015**, *11*, 29.

[31]. Vlascici, D.; Cosma, E. F.; Popa, I.; Chiriac, V.; Agusti, M. G. *Sensors* **2012**, *12*, 8193.

[32]. Goyer, R. A. Toxic effects of metals, in: C.D. Klaassen (Eds.), Casarett & Doull's Toxicology: the basic science of poisons, 5th ed; McGraw-Hill: NY, 1996.

[33]. Fakhari, A. R.; Alaghemand, M.; Shamsipur, M. *Anal. Lett*. **2001**, *34 (7)*, 1097.

[34]. Cairo, G., Pietrangelo, A. *Biochem. J*. **2000**, *352*, 241.

[35]. Porter, J. *Hematol. Oncol. Clin. North. Am*. **2005**, *19*, 7.

[36]. Andrews, N. C. *N Engl. J. Med*. **1999**, *341(26)*, 1986.

[37]. Cabantchik, Z. I.; Breuer, W.; Zanninelli, G.; Cianciulli, P. *Best Pract. Res. Clin. Haematol*. **2005**, *18*, 277.

[38]. Toyokuni, S. *Front. Pharmacol*. **2014**, *5*, 200.

[39]. Huang, X. *Lancet. Oncol*. **2008,** *9(8)*, 803.

[40]. Oliveira, A. F.; N´obrega, J. A.; Fatibello-Filho, O. *Talanta* **1999**, *49(3)*, 505.

[41]. Safavi, A.; Abdollahi, H.; Hormozi-Nezhad, M. R. *Talanta* **2002**, *56(4)*, 699.

[42]. Costa, R. C. D. C.; Ara´ujo, A. N. *Anal. Chim. Acta*. **2001**, *438(1-2)*, 227.

[43]. Ismael, M. R. C.; Carvalho, J. M. R. *Miner. Eng.* **2003**, *16*, 31.

[44]. Gholivand, M. B.; Raheedayat, F. *Electroanalysis.* **2004**, *16*, 1330.

[45]. Carneiro, J.M.T.; Dias A.C.B.; Zagatto E.A.G.; Honorato R.S. *Anal. Chim. Acta*. **2002**, *455*, 327.

[46]. Fakayode, S. O.; King, A. G.; Yakubu, M.; Mohammed, A. K.; Pollard, D. A. *J. Chem. Educ.* **2012**, *89 (1)*, 109.

[47]. Nagabhushana, B. N.; Chandrappa, G. T.; Nagappa, B.; Nagaraj, N. H. *Anal. Bioanal. Chem*. **2002**, *373*, 299.

[48]. Zolgharnein, J.; Abdollahi, H.; Jaefarifar, D.; Azimi, G. A. *Talanta* **2002**, *57*, 1067.

[49]. Zamani, H. A.; Ganjali, M. R., Norouzi, P.; Meghdadi, S. *Anal. Lett* **2008**, *41*, 902.

[50]. Gupta, V. K.; Sethi, B.; Upadhyay N.; Kumar, S.; Singh, R.; Sing, L. P. *J. Electrochem. Sci*. **2011**, *6*, 650.

[51]. Domaille, D. W.; Que, E. L.; Chang, C. J. *Nat. Chem. Biol*. **2008**, *4*, 168.

[52]. Zheng, T.; Nolan, E. M. *Metallomics*. **2012**, *4 (9)*, 866.

[53]. Cattrall, R. W. *Chemical Sensors*; Oxford Science Publications: NY, 1997.

[54]. Hulanicki, A.; Glab, S.; Ingman, F. *Pure & Appl. Chem.* **1991**, *63(9)*, 1247.

[55]. Oliva, S. U. Smart Chemical Sensors: Concepts and Application. Ph.D Thesis, University of Barcelona, Barcelona, 2012.

[56]. This images correspond to: Quadruple Pyroelectric detector with integrated filters from pyreos, Edinburgh; Electrochemical sensor from RAE systems, USA; Taguchi gas sensor (MOX) from Figaro engineering Inc., Japan; Paracube sensor, Servomex, USA; TCG-3880 sensor from Xensor inc., The Netherlands; Velocity of sound sensor from Anton Paar GmbH, Austria.

[57]. Sunandana, C. S. Introduction to Solid State Ionics: Phenomenology and Applications; CRC Press, Taylor & Francis Group: USA, 2015.

[58]. Wang, Y.; Xu, H.; Zhang, J.; Li, G. *Sensors* **2008**. *8*, 2043.

[59]. Stradiatto, N. R.; Yamanaka, H.; Zanoni, M. V. B. *J. Braz. Chem. Soc*. **2003**, *14(2)*, 159.

[60]. Leyendekkers, J. V. *Anal. Chem*. **1971**, *43*, 1835.

[61]. Eisenman, G. *Glass Electrodes for Hydrogen and other cations, Principles and Practice*; Marcel Dekker: NY, 1967.

[62]. Eisenman, G.; Reilley, C. W. *Advances in Analytical Chemistry and Instrumentation*; Wiley: NY, 1965.

[63]. Poduval, R.; Kurzatkowska, K.; Stobiecka, M.; Dehaen, W. F. A.; Dehaen, W.; Radecka, H.; Radecki, J. *Supramol. Chem*. **2010**, *22*, 413.

[64]. Buck, R. P.; Lindner, E. *Anal. Chem.*, **2001**, *73*, 88.

[65]. Young, C. C. *J. Chem. Educ*. **1977**, *74(2)*, 177.

[66]. Girish Kumar, K.; John, S.; Poduval, R.; Augustine, P. *The Chin. Pharm. Jour*. **2005**, *57*, 29

[67]. Girish Kumar, K.; Augustine, P.; John, S. *J. Appl. Electrochem.* **2010**, 40, 65.

[68]. Ganjali, M. R.; Norouzi, P.; Shamsolahrari, L.; Ahmadi, A. *Sens. Actuators B* **2006**, *114*, 713.

[69]. Girish Kumar, K.; John, S.; Augustine, P.; Poduval, R.; Beena. S. *Anal. Sci.* **2007**, *23*, 291.

[70]. Girish Kumar, K.; Saji John, K.; Indira, C. J. *Indian J. Chem. Tech*. **2006**, *13*, 13.

[71]. Shamsipur, M.; Soleymanpour, A.; Khond, M. A.; Sharghi, H.; Hasaninejad, A. R. *Sens. Actuators B* **2003**, *89*, 9.

[72]. Ardakani, M. M.; Salavati-Niasari M.; Jamshidpoor, M. *Sens. Actuators B* **2004**, *101*, 302.

[73]. Hassan, S. S. M.; Mahmoud, W. H.; Elmosallamy, M. A. F.; Almarzooqi, M. H. *J. Pharm. Biomed. Anal*. **2005**, *39*, 315.

[74]. Bakker, E.; Bühlmann, P.; Pretsch, E. *Chem. Rev.* **1997**, *97 (8)*, 3083.

[75]. Pretsch, E. *Trends Anal. Chem.* **2007**, *26(1)*, 45.

[76]. Gholivand, M.B.; Raheedayat, F. *Electroanalysis*. **2004**, *16*, 1330.

[77]. Hassan, S. S. M.; Elshahawi, M. S; Othman, A. M.; Mosaad, M. A. *Anal. Sci*. **2005**, *21*, 673.

[78]. Abbaspour, A.; Izadyar, A. *Talanta* **2001**, *53*, 1009.

[79]. Das, A.; Chen, T-C.; Yang, CM.; Lai, C-S. *Sens. Actuators B* **2014**, *198*, 225.

[80]. Ali, T. A.; Aglan, R. F.; Mohamed, G. G.; Mourad, M. A. *Int. J. Electrochem. Sci.* **2014**, *9*, 1812.

[81]. Ali, T. A.; Mohamed, G. G.; Al-Sabagh, A.; Migahed, M. *Chinese J. Anal. Chem*. **2014**, *42*, 565.

[82]. Frag, E. Y .Z.; Ali, T. A.; Mohamed, G. G.; Awad, Y. H. H. *Int. J. Electrochem. Sci.* **2012**, *7*, 4443.

[83]. Khaled, E.; Mohamed, G. G.; Awad, T. *Sens. Actuators B* **2008**, *135*, 74.

[84]. Mohamed, G. G.; Ali, T. A.; El-Shahat, M. F.; Al-Sabagh, A. M.; Migahed, M. A. *Electroanalysis*. **2010**, *22*, 2587.

[85]. Mohamed, G. G.; Ali, T. A.; El-Shahat, M. F.; Migahed, M. A.; Al-Sabagh, A. M. *Drug Test Anal*. **2012**, *4*, 1009.

[86]. Mohamed, G. G.; El-Shahat, M. F.; Al-Sabagh, A. M.; Migahed, M. A.; Ali, T. A. *Analyst*. **2011**, *136*, 1488.

[87]. Singh, A.K.; Singh, R.; Saxena, P. *Sensors* **2004**, *4*, 187.

[88]. Sharma, R.K.; Goel, A. *Anal. Chim. Acta*. **2005**, *534*, 137.

[89]. Li, M.; Gou, H.; Al-Ogaidi, I.; Wu, N. *ACS Sustain. Chem. Eng.* **2013**, *1 (7)*, 713.

[90]. Cui, L.; Wu, J.; Ju, H. *Biosens. Bioelectron.* **2015**, *63*, 276.

[91]. Pooyamanesh, M.; Zamani, H. A.; Rajabzadeh, G.; Ganjali, M. R.; Norouzi, P. *Anal. Lett*. **2007**, *40*, 1596.

[92]. Mashhadizadeh, M. H.; Sheikh-Shoaei, I.; Monadi, N. *Talanta* **2004**, *64*, 1048.

[93]. Gupta, V. K.; Jain, A. K.; Agarwal, S.; Maheshwari, G. *Talanta* **2007**, *71*, 1964.

[94]. Mizani, F.; Ganjali, M.R.; Faridbod, F.; Esmaeilnia, S. *Int. J. Electrochem. Sci.* **2013**, *8*, 10473.

[95]. Zamani, H. A.; Abedi, M. R.; Ganjali, M. R. *J. Chil. Chem. Soc*. **2009**, *54*, 186.

[96]. Ali, T. A.; Aglan, R. F.; Mohamed, G. G.; Mourad, M.A. *Int. J. Electrochem. Sci.* **2014**, *9*, 1812.

[97]. Ali, T. A.; Azzam, E. M. S.; Hegazy, M. A.; El-Farargy, A. F. M.; Abd-elaal, A. A. *J. Ind. Eng. Chem*. **2014**, *20*, 3320.

[98]. Jeitziner, M. Selectophore Ionophores, http://www.sigmaaldrich.com/technical documents/articles/analytix/selectophore-ionophores.html. AnalytiX, 6 *(4)*. (accessed May 07, 2015).

[99]. Kamata, S.; Bhale, A.; Fukunaga, Y.; Murata, H. *Anal. Chem.* **1988**, *60 (22)*, 2464.

[100]. Sousa, T. F. A.; Amorim, C. G.; Montenegro, M. C. B. S. M.; Araújo, A. N. *Sens. Actuators B* **2013**, *176*, 660.

[101]. Khun, K.; Ibupoto, Z. H.; Chey, C. O.; O. Nur, J. L.; Willander, M. *Appl. Surf. Sci*. **2013**, *268*, 37.

[102]. Lai, M. T.; Shih, J. S. *Analyst* **1986**, *111*, 891.

[103]. Paolesse, R.; Lvova, L.; Nardis, S.; Natale, C. D.; Amico, A. D.; Castro, F. L. *Microchim. Acta*. **2008**, *163*, 103.

[104]. Beer, P. D.; Gale, P. A.; Chen, G. Z. *J. Chem. Soc. Dalton Trans*. **1999**, *12*, 1897.

[105]. Boulas, P. L.; Gomeaz, K. M.; Echegoyen, L. *Angew. Chem.* **1998**, *11*, 216.

[106]. Bader, N. R. *Rasayan J. Chem*. **2010**, *3(4)*, 660.

[107]. Brodowska, K.; Lodyga-Chruscinska, E. *Chemik* **2014**, *68 (2)*, 129.

[108]. Cozzi, P. G. *Chem. Soc. Rev*. **2004**, *33*, 410.

[109]. Chu, B. C.; Garcia-Herrero, A.; Johanson, T. H.; Krewulak, K. D.; Lau, C. K.; Peacock, R. S.; Slavinskaya, Z.; Vogel, H. J. *Biometals*. **2010**, 601.

[110]. Miethke, M.; Marahiel, M. *Microbiol*. *Mol*. *Biol*. *Rev*. **2007**, *71 (3)*, 413.

[111]. Winkelmann, G.; Drechsel, H. *Biotechnology Set (2nd edition)*; Wiley: NY, 1999.

[112]. Freibach, H. S.; Yariv, S.; Lapides, Y.; Hadar, Y.; Chen, Y. *J. Agric. Food Chem.* **2005,** *53*, 3434.

[113]. Deferoxamine. https://www.drugs.com/cdi/deferoxamine.html (accessed Jan. 27, 2015).

[114]. Microbial iron scavengers. http://www.rsc.org/education/eic/issues/2009Jan/iron-antibiotic-siderophore-oxygen-microbe.asp (accessed March 08, 2015).

[115]. What is Nernst equation. http://www.liquisearch.com/what_is_nernst_equation (accessed Aug 14, 2013).

[116]. Nernst equation. http://www.science.uwaterloo.ca/~cchieh/cact/c123/nernsteq.html (accessed Oct. 27, 2013).

[117]. Atkins, P.; De Paula, J. *Physical Chemistry for the Life Sciences*; W.H. Freeman and Company: NY, 2006; p. 214.

[118]. Electrochemistry Dictionary. http://corrosion-doctors.org/Dictionary/Dictionary-N.htm (accessed Jan. 01, 2014).

[119]. All about Electrochemistry. http://www.chem1.com/acad/webtext/elchem/ec4.html (accessed March 03, 2014).

[120]. Rahman, M. M.; Ahammad, A. J. S.; Jin, J-H.; Ahn, S. J.; Lee, J-J. *Sensors* **2010**, *10*, 4855.

[121]. Liu, A. *Biosens. Bioelectron.* **2008**, *24*, 167.

[122]. Zhai, T.; Fang, X.; Liao, M.; Xu, X.; Zeng, H.; Yoshio, B.; Golberg, D. A. *Sensors* **2009**, *9*, 6504.

[123]. Huang, J.; Wan, Q. *Sensors* **2009**, *9 (12)*, 9903.

[124]. Ahammad, A. J. S.; Lee, J.-J.; Rahman, M. A. *Sensors* **2009**, *9*, 2289.

[125]. Abbasi, M. A.; Ibupoto, Z. H.; Khan,Y.; Khan, A.; Nur, O.; Willander, M. *Sensors* **2013**, *2013*, 382726.

[126]. Brett, C. M. A. *Pure Appl. Chem.* **2001**, *73 (12)*, 1969.

[127]. Iravani, E.; Allahyari, S. A.; Shojaei, Z.; Torab-Mostaedi, M. *J. Braz. Chem. Soc.* **2015**, *26 (8)*, 1608.

[128]. Palomares, E.; Vilar, R.; Durrant, *J. R. Chem. Commun*. **2004**, *4*, 362.

[129]. Nazeeruddin, M. K.; Di Censo, D.; Humphry-Baker, R.; Grätzel, M. *Adv. Funct. Mater*. **2006**, *16*, 189.

[130]. Faisal, M.; Ismail, A. A.; Harraz, F. A.; Bouzid, H.; Al-Sayari, S. A.; Al-Hajry, A. *Nanoscale Res. Lett*. **2014**, *9*, 62.

[131]. Vericat, C.; Vela, M. E.; Salvarezza, R. C. *Phys. Chem. Chem. Phys.* **2005**, *7 (18)*, 3258.

[132]. Buck, R. P.; Lindner, E. *Pure Appl. Chem*. **1994**, *66*, 2527.

[133]. Bayesian calibration of Ion-Selective Electrodes. https://raduresearchgroup.wordpress.com/about/projects/bayesian-calibration-of-ion-selective-electrodes/ (accessed July 24, 2015).

[134]. Muslinkina, L. *Molecular Recognition Studies With Ion-Selective Membranes: Complexation in the Bulk and Molecular Recognition on the Surface*, Ph.D. Thesis, Swiss Federal Institute of Technology, Zürich, Switzerland, 2004.

[135]. Umar, A.; Hahn, Y.-B. Metal *Oxide Nanostructures and their applications*; American Scientific Publishers: USA, 2010; vol.3,. pp.31-52.

[136]. Zamani, H.A.; Sahebnasagh, S. *Int. J. Electrochem. Sci.* **2013**, *8*, 3708.

[137]. Morf, W. E. *The Principles of Ion Selective Electrodes and of membrane transport*; Elsevier: NY, 1981.

[138]. IUPAC Gold Book. http://goldbook.iupac.org/R05346.html\ (accessed Feb 11, 2015).

[139]. Inczendy, J.; Lengyal, T.; Ure, A. M.; Gelencser, A.; Hulanicki, A. *Compendium of Analytical Nomenclature. Definitive Rules 1997*, 3rd Edition; Wiley-Blackwell Science Ltd: Great Britain, 1998.

[140]. Love, J. C.; Estroff, L. A.; Kriebel, J. K.; Nuzzo, R. G.; Whitesides, G. M. *Chem. Rev*. **2005**, *105*, 1103.

[141]. Whitesides, G. M.; Kriebel, J. K.; Love, J. C. *Science Progress*. **2005**, *88 (1)*, 17.

[142]. Vos, J. G.; Forster, R. J.; Keyes, T. E. *Interfacial Supramolecular Assemblies*, Wiley, John & Sons: NY, 2003, pp. 88.

[143]. Mastrangelo, F.; Fioravanti, G.; Quaresima, R.; Vinci, R.; Gherlone, E. *J Biomater Nanobiotechnol*. **2011**, *2*, 533.

[144]. Kaifer, A. E. Kaifer, M. G. *Supramolecular Electrochemistry*; Wiley VCH: USA, 2001; pp. 191.

[145]. Vericat, C.; Vela, M. E.; Salvarezza, R. C. *Phys. Chem. Chem. Phys*. **2005**, *7 (18)*, 3258.

[146]. Raman, A.; Quinones, R.; Barriger, L.; Eastman, R.; Parsi, A.; Gawalt, E. S. *Langmuir*, **2010**, *26 (3)*, 1747.

[147]. Patel, J. N.; Kaminska, B.; Gray, B.; Gates, B. D. *IEEE Eng. Med. Biol. Soc*.**2007**, *2007*, 2677.

[148]. Mandler, D.; Kraus-Ophir, S. *J. Solid State Electrochem*. **2011**, *15*, 1535.

[149]. Feng, G. *The Synthesis and Characterization of Phosphonic Acids for the Surface Modification Study on Indium Tin Oxide*. M.Sc. Thesis, Georgia Institute of Technology, Georgia, USA, 2012.

[150]. Mutin, P. H.; Guerrero, G.; Vioux, A. *J. Mater. Chem*. **2005**, *15*, 3761.

[151]. Hoque, E.; DeRose, J. A.; Kulik, G.; Hoffmann, P.; Mathieu, H. J.; Bhushan, B. *J. Phys. Chem. B.* **2006**, *110*, 10855.

[152]. Guerrero, G.; Mutin, P. H.; Vioux, A. *Chem. Mater.* **2001**, *13*, 4367.

[153]. McElwee, J.; Helmy, R.; Fadeev, A. Y. *J. Colloid. Interface. Sci.* **2005**, *285*, 551.

[154]. Galoppini, E. *Coord. Chem. Rev.* **2004**, *248*, 1283.

[155]. Severac, F. B.; Guerrero, G.; Maquet, J.; Florian, P.; Gervais, C.; Mutin, P. H. *Chem. Mater.* **2008,** *20,* 5191.

[156]. Gillaizeau-Gauthier, I.; Odobel, F.; Alebbi, M.; Argazzi, R.; Costa, E.; Bignozzi, C. A.; Qu, P.; Meyer, G. J. *Inorg. Chem.* **2001**, *40*, 6073.

[157]. Pawsey, S.; Yach, K.; Reven, L. *Langmuir* **2002**, *18*, 5205.

[158]. Randon, J.; Blanc, P.; Paterson, R. *J. Membr. Sci.* **1995**, *98*, 119.

[159]. Spori, D. M.; Venkataraman, N. V.; Tosatti, S. G.; Durmaz, F.; Spencer, N. D.; Zuercher, S.; *Langmuir* **2007**, *23(15)*, 8053.

[160]. Lundqvist, M. J.; Nilsing, M.; Lunell, S.; Aakermark, B.; Persson, P. *J. Phys. Chem. B* **2006**, *110*, 20513.

[161]. Isildak, O.; Durgun, O. *Int. J. Adv. Res. Eng. Appl. Sci.* **2015**, *2 (4)*, 1.

[162]. Sepehrifard, A.; Stublla, A.; Haftchenary, A.; Chen, A.; Potvin, P. G.; Morin, S. *J.* New *Mate. Electrochem. Syst*. **2008**, *11*, 281.

[163]. Adden, N.; Gamble, L. J.; Castner, D. G.; Hoffmann, A.; Gross, G.; Menzel, H. *Biomacromolecules* **2006**, *7 (9)*, 2552.

[164]. Clair, S.; Variola, F.; Kondratenko, M.; Jedrzejowski, P.; Nanci, A.; Rosei, F.; Perepichka, D. F. *J. Chem. Phys*. **2008**, *128 (14)*, 1.

[165]. Carbodiimide Crosslinker Chemistry https://www.thermofisher.com/us/en/home/life-science/protein-biology/protein-biology-learning-center/protein-biology-resource-library/pierce-protein-methods/carbodiimide-crosslinker-chemistry.html (accessed Nov. 20, 2015).

[166]. Chemistry of Crosslinking. https://www.thermofisher.com/us/en/home/life-science/protein-biology/protein-biology-learning-center/protein-biology-resource-library/pierce-protein-methods/chemistry-crosslinking.html (accessed Nov. 09, 2015).

[167]. N-hydroxysuccinimide. http://en.citizendium.org/wiki/N-hydroxysuccinimide (accessed Nov 09, 2015).

[168]. Reichenbacher, M.; Popp, J. *Challenges in Molecular Structure Determination*; Springer-Verlag: Germany, 2012

[169]. Stuart, B. *Infrared Spectroscopy: Fundamentals and Applications*; Wiley, John & Sons: NY, 2004.

[170]. Introduction to Fourier Transform Infrared Spectrometry. http://mmrc.caltech.edu/FTIR/FTIRintro.pdf (accessed March 04, 2016).

[171]. Paré, J. R. J.; Bélanger, J. M. R. *Instrumental Methods in Food Analysis*; Elsevier B.V: Netherlands, 1997; 18, pp 1.

[172]. Johnson, B. F. G.; McIndoe, J. S. Coord. Chem. Rev. **2000**, *200*, 901.

[173]. Gorenstein, D. G. *Phosphorous-31 NMR Principles and Applications*; Academic Press: USA, 1984.

[174]. Introduction to Solid State NMR http://www.emory.edu/NMR/web_swu/SSNMR_redor/ssnmr_schurko.pdf. (accessed March 22, 2016).

[175]. Andrew, E. R. *Philosophical Transactions. Series A, Mathematical and Physical Sciences*; Royal Society: Great Britain, 1981, 299 (1452);pp. 505.

[176]. Cheney, B. Introduction to Scanning Electron Microscopy http://www.sjsu.edu/people/anastasia.micheals/courses/MatE143/s1/SEM_GUIDE.pdf. (accessed April 08, 2016).

[177]. Scanning Electron Microscopy. http://www.mee-inc.com/hamm/scanning-electron-microscopy-sem/ (accessed April 10, 2016).

[178]. Last, J. A.; Russell, P.; Nealey, P. F.; Murphy, C. *Invest. Ophthalmol. Vis. Sci*. **2010**, *51*, 6083.

[179]. Meyer, G.; Amer N. M. *Appl. Phys. Lett*. **1988**, *53*, 1045.

[180]. Tamayo, J.; Garcia, R. *Langmuir*. **1996**, *12 (18)*, 4430-4435.

[181]. Osegovic, J. P.; Drago, R. S. *J. Phys. Chem. B.* **2000**, *104*, 147.

[182]. Triba, M.N.**;**Warschawski, D. E.; Devaux, P. F. *Biophys. J.* **2005**, *88(3)*, 1887.

[183]. Guerrero, G.; Mutin, P. H.; Vioux, A. *Chem. Mater.* **2001**, *11*, 3161.

[184]. Paz, Y. *Beilstein J. Nanotechnol.* **2011,** *2*, 845.

[185]. Spectral Database for Organic Compounds. http://sdbs.db.aist.go.jp/sdbs/cgi-bin/direct_frame_top.cgi (accessed March 13, 2016).